Biological cell–substrate interactions with few-layered nanomaterials

Rhiannon Wyn Harries

Submitted for the degree of Doctor of Philosophy
University of Sussex
March 2021

Declaration

I hereby declare that this thesis has not been and will not be submitted in whole or in part to another University for the award of any other degree.

Signature:

Rhiannon W. Harries

UNIVERSITY OF SUSSEX

Rhiannon W. Harries, Doctor of Philosophy

Biological cell–substrate interactions with few-layered nanomaterials

Biology, fundamental to understanding life, remains a vitally important area of research. There is still much left for humankind to understand even after decades of research. This is clear now more than ever; as I write this, research has been disrupted for about 12 months due to various COVID-19 restrictions. Biology, therefore, is ripe for the fresh, new advances that result from interdisciplinary collaboration. Recent years have seen the exciting development of new few-layered materials, providing new possibilities in biology, as well as other areas. To this end, the work presented herein considers the interactions between different cell lines and various synthesised nanomaterial substrates.

To distinguish effects due to the inherent biology of the cell and effects due to the nanomaterial substrate, well-defined substrates are crucial to interdisciplinary research. Thin films created by the Langmuir–Schaefer (L–S) deposition technique are a good candidate. This technique provides an easily controllable method of producing single-layer substrates. Here, a method resulting in improved understanding of the physical and chemical influences on L–S film formation is described. Surface pressure-surface coverage data can be normalised to nanosheet size to account for edge effects. This new approach allows the L–S film density to be determined from standard dispersion properties alone. In addition, this work produced the first demonstration of the production of single layer hexagonal boron nitride films using this method.

To test nanomaterial–cellular interactions, various cell lines were seeded onto MoS_2 L–S substrates. To the best of our knowledge, this study resulted in the first demonstration of the internalisation of MoS_2 through mechanotransduction. The material showed localisation to the endoplasmic reticulum, which combined with the innate fluorescence or Raman signal of the MoS_2 nanosheet, could lead to a new theranostic tool. This study was expanded to consider cell interactions with other transition metal dichalcogenide materials, WS_2 and $MoSe_2$, to investigate the difference between structure and chemistry seen by the cell. This work provides a step change to studying nanomaterial–cellular interactions, opening the door to new therapies and diagnostics.

Publications

Elements of this thesis have contributed (in part or in their entirety) to the following publications:

1. **Rhiannon W. Harries**, Christopher J. Brown, Sean P. Ogilvie, Matthew J. Large, Aline Amorim Graf, Keiran Clifford, Thomas Simon, Georgios Giamas, Alan B. Dalton, and Alice A. K. King, *Langmuir Films of Layered Nanomaterials: Edge Interactions and Cell Culture Applications.* J. Phys. Chem. B, 2020, **124** (33) pp. 7184–7193.

2. **Rhiannon W. Harries**, Christopher J. Brown, Lisa Woodbine, Aline Amorim Graf, Matthew J. Large, Keiran Clifford, Peter J. Lynch, Sean P. Ogilvie, Alan B. Dalton, and Alice A. K. King, *Cell–Substrate Interactions Lead to Internalization and Localization of Layered MoS_2 Nanosheets.* ACS Appl. Nano Mater., 2021, **4** (2) pp. 2002–2010

3. Christopher J. Brown, **Rhiannon W. Harries**, Peter J. Lynch, Aline Amorim Graf, Jonathan P. Salvage, Thomas Simon, Alan B. Dalton, Georgios Giamas, and Alice A. K. King, *Observations of spontaneous neovascularisation of glioblastoma on synthetic three-dimensional reduced graphene oxide scaffolds.* 2021 (submitted)

Acknowledgements

I never intended to complete an MPhys, let alone a PhD! But one serendipitous conversation with my supervisor-to-be, Alice, set me on the path that I have taken over the past few years. So thank you for asking me about my future plans and interests that day we were both invigilating for the summer school. I would have missed out on so much had it been someone else working with me that day! Thanks also to Maria for encouraging me to apply for the summer school in the first place, and to Jackie for being the ray of sunshine often needed on many gloomy afternoons. Thanks to Alan for fostering a sense of independence, and for teaching me the importance of networking (always much easier after a few drinks!).

Physics was brought alive to me at school by my teacher, Nia Ifans. Without sharing the knowledge from her 'epiphanies' (obtained while leaning in door frames) or the healthy competition for 'brownie points', things might be very different! Diolch am bopeth, Mrs Ifans.

I wouldn't have made it through this PhD without the unerring support I have received from Aline. She has always been there for me through thick and thin, and I can't emphasise enough how much her friendship has meant to me. You always have just the right advice, whether my problem is scientific or personal! Thank you.

Thank you to everyone else, past and present, who has made my time in the Materials Physics group so much fun: Matt, Peter, Sean, Manoj, Yuanyang, Manuela, Giuseppe, Marcus, Frank, Abdullah, Chris, Keiran, Hannah, Cencen, Adel, and Anne.

To my undergraduate friends at uni while I've been on this journey — Alex, Poppy, Sam, and Ewan — thank you for always brightening my day. Alex; I hope you don't think that the work presented herein is 'preliminary excrement' (!).

To Dani Hajas — thanks for your endless encouragement, and for still being here after seven years. I guess you didn't kill too many of my brain cells after walking me into that map? Soon we will be able to play a few more games of snapszer and cribbage (you'll have to teach me the rules all over again!).

To Ryan — thanks for being a constant in my life at the University of Sussex. Life wouldn't be the same without your jokes (or are they 'jokes'?).

To Mitch and Eleanor — thank you for the fun games nights and silly chat. Whoever knew there were so many cute tea cosy patterns? I promise I will eventually make one! It's been fantastic getting to know you both, long may it continue.

To The House of Slight Panic — Tom, Neelesh, and Gemma — I'm glad we're still in touch. Tom; thank you for being so interested in what I've been up to over the past few months, it has been so encouraging and has really meant a lot to me.

To the ‘Unofficial’ Star Trek Society — Charlotte, Will, and Dan — thank you for all the interesting discussions and insights. It’s always fun hearing madcap ideas from you guys, and I feel like if nothing else, I have learned the difference between a cruise ship and an ocean liner.

To the old guard from DocSoc: Ben, Susanna, George, Jake, Fridah, Laurence, Emily, Nick, Luke — what a family we have been. Thanks for creating an atmosphere where I always felt welcome and was always entertained. And to Rory — thanks for manning the fort for the past few years.

To everyone at Sussex Harmony — thank you for sharing this journey with me! It will be sad to move away, but I hope I will be able to visit and to sing with you on occasion. Rachel; thank you for being a good friend, and for being so willing to feed me for the past six years! Cynthia; thank you for your kindness, laughter, and advice over the years. It wouldn’t have been the same without the Brighton Bus. Though we may be apart, we can still create art...

To my friends from home — Jade, Chloe, Danny and Jai, Llŷr and Siâna, Siôn and Jess — diolch o waelod fy nghalon. Dych chi wedi nabod fi yn hirach nag unrhyw un arall, ac wedi fy helpu i drwy gymaint tra yn yr ysgol ac wrth i mi astudio yn y brifysgol. Dwi’n caru chi i gyd.

To my family — thank you for always being there with a ready ear when everything seemed too much and I needed to let it all out. Without your support, I would never have made it this far. Thank you for everything you have done for me all these years. To Sushi and Neil — thank you for being additional parents to me and for being so supportive of me as well as Andrew these past six years.

Finally, to Andrew. What can I say? You have always encouraged and supported me, and are a tireless cheerleader. You have always believed in me even when I haven’t, and it is no exaggeration to say that I wouldn’t be where I am now without your unending faith in me. Diolch, fy nghariad.

Contents

List of Figures

List of Tables

List of Abbreviations

| **A** | **B** | **C** | **D** | **E** | **F** | **G** | **I** | **L** | **M** | **N** | **O** | **P** | **Q** | **R** | **S** | **T** | **U**

#

0D zero-dimensional. 7, 52
1D one-dimensional. 7
2D two-dimensional. 3, 4, 6, 7, 10, 14, 15, 20, 32, 44, 45, 52, 55, 58, 61, 67, 70, 71, 73, 76, 78, 79, 82, 83, 91, 100, 101, 102, 221
3D three-dimensional. 4, 7, 9, 29, 33, 36, 102

A

AFM
1) atomic force microscope. 1, 36, 38, 40, 62, 77, 80, 81, 215, 218
2) atomic force microscopy. 36, 37, 38, 40, 62, 63, 73, 77, 215
AuNP gold nanoparticle. 14, 45, 46, 51

B

BN hexagonal boron nitride. 5, 7, 12, 13, 15, 22, 45, 52, 57, 58, 59, 61, 63, 64, 65, 67, 68, 69, 70, 73, 74, 100, 216, 218

C

CCD charge-coupled device. 32
CNT carbon nanotube. 7, 8, 15, 22, 45, 52
COVID-19 coronavirus disease 2019. 43, 49, 55, 104
CTAB cetyltrimethylammonium bromide. 46
CuNP copper nanoparticle. 14
CVD chemical vapour deposition. 11, 20, 77, 83, 91, 96

D

DI deionised. 20, 42, 43
DIC differential interference contrast. 29, 30, 40
DMEM Dulbecco's modified Eagle's medium. 42, 43
DNA deoxyribonucleic acid. 1, 45, 49

E

EDTA ethylenediaminetetraacetic acid. 42, 43
ER endoplasmic reticulum. 4, 75, 80, 82, 83, 84, 86, 87, 88, 89, 96, 102, 221

ESF European Science Foundation. 51

F

FCS fetal calf serum. 42, 43

G

GO graphene oxide. 9, 10, 44, 45, 53

I

IONP iron oxide nanoparticle. 46

L

L-gra larger-sized graphene flakes. 23, 59, 61, 63, 64, 65, 67, 68, 72, 215, 218
LCC liquid cascade centrifugation. 17, 18, 23
LPE
1) liquid-phase exfoliated. 11, 18, 33, 73, 96, 100
2) liquid-phase exfoliation by sonication. 14, 15, 16, 17, 19, 24, 57, 58, 59, 63, 77, 78, 79, 91, 92, 100
L–S Langmuir–Schaefer. 4, 5, 13, 22, 24, 59, 60, 67, 68, 73, 78, 79, 92, 101, 104

M

MEM minimum essential medium. 42, 43
MWCNT multi-walled carbon nanotube. 45
MXene transition metal carbide, nitride, or carbonitride. 52

N

NP nanoparticle. 14, 21, 22, 31, 43, 45, 46, 48, 49, 50, 51, 52, 54, 55, 56, 60, 66, 75, 89

O

OPL optical path length. 29, 30, 35

P

PBS phosphate-buffered saline. 41, 42
PTT photothermal therapy. 11, 12, 44, 47, 50, 51, 55, 88

Q

QD quantum dot. 7, 45, 46, 47, 48, 49, 55
QNM quantitative nanoscale mechanical. 40

R

rGO reduced graphene oxide. 10, 45

RNA ribonucleic acid. 49
RPM revolutions per minute. 17

S

SARS-CoV-2 severe acute respiratory syndrome coronavirus 2. 104
S-gra smaller-sized graphene flakes. 23, 59, 63, 64, 65, 67, 68, 71, 72, 216, 218
SWCNT single-walled carbon nanotube. 45

T

TMD transition metal dichalcogenide. 3, 4, 6, 7, 10, 11, 12, 15, 19, 20, 45, 52, 55, 57, 58, 68, 69, 70, 76, 88, 90, 91, 98, 99, 102, 103, 104

U

UPR unfolded protein response. 86, 88, 89, 102, 103
UV ultraviolet. 34, 35, 39, 62, 73

Chapter 1

Introduction

Nanotechnology is the study and application of matter at the nanoscale, which is about 1 to 100 nanometers. This encompasses a broad range of scientific disciplines, including surface science, organic chemistry, molecular biology, semiconductor physics, energy storage, and engineering. The field in its modern sense is still young, having been growing steadily over the past 50 years.

The term 'nano-technology' was first used by Norio Taniguchi at a conference in 1974 [1], but it was not until the invention of the scanning tunnelling microscope by Gerd Binnig and Heinrich Rohrer in 1981 [2, 3] and the atomic force microscope by Gerd Binnig, Calvin Quate and Christoph Gerber in 1986 [4] that nanotechnology research began to take off in earnest. These instruments enabled researchers to image and to manipulate individual atoms for the first time. Without these inventions, and those that followed, the emergent properties of materials on the nanoscale would not be known and investigated for the wide array of applications researched today.

Nanobiotechnology refers to the application of nanotechnologies in biological fields, for example development of a "lab-on-a-chip", real-time nano-sensors, drug delivery vectors, and tissue engineering [5, p. 1]. This is distinguished from bionanotechnology, which is the application of biological building blocks and tools for modern nanoscale technology, for example DNA nanotechnology (use of artificial nucleic acids for technology), or the use of peptide nanotubes or protein fibrils for the fabrication of physical elements at the nanoscale [5, p. 1]. According to the *MedLine* database, the

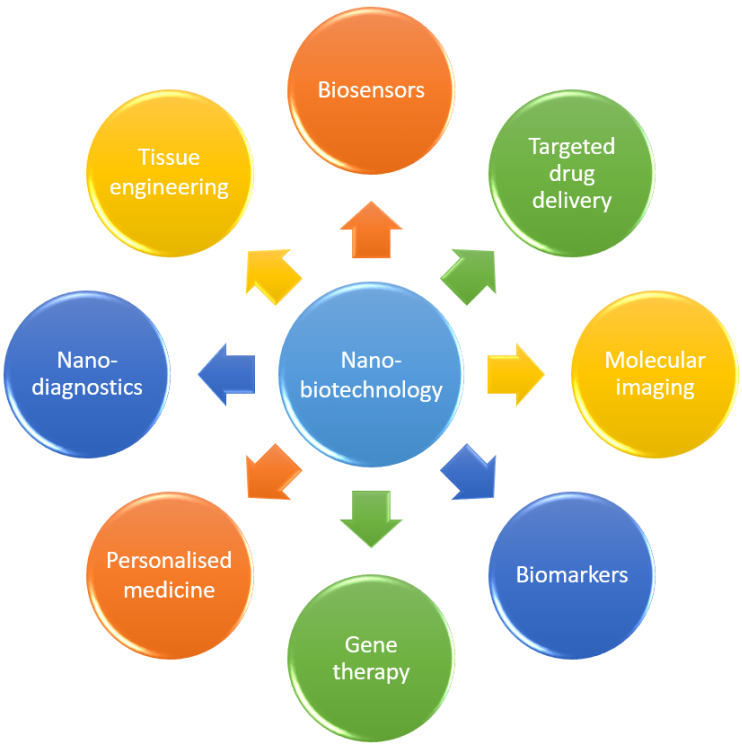

Figure 1.1: Nanobiotechnology applications.

term "nanobiotechnology" is first recorded in 2000 [5, p. 13]; this confirms that this is a young, interdisciplinary field which has gathered pace over the past few decades. Fresh perspectives from interdisciplinary collaboration could lead to new insights in several areas (Figure 1.1). These areas can be broadly categorised as being

- diagnostic,
- therapeutic, or
- "theranostic" (i.e. having combined therapeutic and diagnostic ability).

New inroads in these areas are in no small part attributable to the number of new nanomaterials and associated composites that have been synthesised and investigated since Geim and Novoselov's Nobel Prize-winning work on the isolation of monolayer graphene in 2004 [6].

A whole host of few-layered and low-dimensional nanomaterials with interesting properties could introduce new ammunition to the arsenal of existing diagnostics, treatments, and theranostics. These materials typically have different properties when compared to the bulk form. Many exhibit enhanced physical, chemical, and

biological functionality due to their uniform shapes, high surface-to-volume ratios, and high specific surface areas [7] (some key materials and their properties are discussed in 2.1). This makes different nanomaterials ideal for applications such as biomedical nanocomposites (high surface-to-volume could improve scaffold or implant properties) and drug delivery (high specific surface area allows large numbers of drug molecules to be adsorbed), among others (see Figure 1.1). Furthermore, materials could exhibit different toxicities at the nanoscale. Ensuring biocompatibility is clearly vital if there is to be wide-scale adoption of biomedical applications based on nanomaterials. The burgeoning research on few-layer and low-dimensional materials means that, even for the most well established nanomaterials, their interactions with living cells and tissues is still poorly understood. One way to tackle this is to create well-defined substrates for cell and tissue studies; this would allow potential biological responses to be separated from any changes in the substrate properties.

1.1 Thesis outline

Reviewing the current state-of-the-art in nanobiotechnology, it is clear that well-defined substrates are of great importance to cell–substrate interactions. This thesis seeks to address two main themes:

- Is it possible to define a methodology to ensure a controlled and tuneable production of two-dimensional (2D) thin film substrates?
- Most nano–bio studies introduce the nanomaterial to the cell by dispersion in the cell medium — can nanomaterials be introduced to the cell from the substrate alone? Does this change the effect on the cell?

Chapter 2 covers the properties and common processing methods of layered nanomaterials, and techniques used to characterise these materials. Particular attention will be given to the transition metal dichalcogenides (TMDs), as these are investigated in more depth in later chapters. Additionally, various applications of low-dimensional materials in diagnostics and therapeutics will be discussed.

In Chapter 3, the Langmuir–Schaefer (L–S) deposition technique is discussed in more detail. Particular focus is given to the edge interactions of monolayer nanosheets. A framework to account for material interactions is developed by normalising the film surface coverage to nanosheet size, allowing greater understanding of thin film densities, and leading to a generic film formation methodology. This has wide implications, as control over thin film creation is crucial for various applications. One such application is also explored in this chapter, that of repeatable production of sample substrates for biological studies. The significant modification in cancer cell growth is demonstrated by the edge density of the material substrate used.

Chapter 4 details cell experiments on molybdenum disulfide (MoS_2) substrates. While most nano–bio experiments introduce the nanomaterial to the cell by dispersion in the cell medium, this work introduced MoS_2 to the cell only via the thin film substrate onto which the cells were seeded. After a week of growth, bone carcinoma cells exhibited internalisation of the MoS_2, with material clearly present within the cell, localised in the endoplasmic reticulum (ER). This is confirmed by optical microscopy and by 2D and three-dimensional (3D) Raman spectroscopy. The innate fluorescence and Raman signal of monolayer MoS_2 lending itself to cell imaging, and its ability to target specific organelles, makes this an interesting phenomenon with potential theranostic applications.

This requires further investigation; Chapter 5 begins this work by considering the effect of other TMDs, tungsten disulfide (WS_2) and molybdenum diselenide ($MoSe_2$), on bone carcinoma cell growth. Cells were grown in the same conditions for one week to more easily compare with the work on MoS_2. The work showed that internalisation of the nanomaterial is not unique to MoS_2, but is also shown in WS_2. However, $MoSe_2$ was not visibly internalised within the cells. This suggests that the sulfur chemistry may play an important role in the internalisation process, although the reason for the lack of $MoSe_2$ internalisation has not been confirmed. It is uncertain whether the material was never internalised, or whether there was a rapid internalisation and excretion of the material in the 7 day growth window before

trypsinisation and reseeding for imaging. The claim that cell–substrate interactions are an important feature for uptake was reinforced by visible cell extensions of U2OS cells on $MoSe_2$ substrates, which showed active sensing processes at work.

This thesis introduces a generic methodology for the controlled production of L–S films, applicable to a range of layered nanomaterials. This work describes the first demonstration of the deposition of L–S films of hexagonal boron nitride (BN) (Chapter 3). MoS_2 nanosheets are shown to be internalised and localised within the cell by mechanotransduction, leading to a potential new theranostic agent.

Chapter 2

Few-layered and low-dimensional materials

The last few decades have been a boom time for research into few-layered low-dimensional nanomaterials, with good reason. These materials, their properties long known and well characterised at the macro scale, can exhibit vastly different properties at the nanoscale. This has made possible many new applications, and research into potential medical and biological uses is ongoing, as described in 2.4.

Greater understanding of these nanomaterials and their properties is vital for the realisation of future applications. The ability to characterise them thoroughly is therefore necessary. This chapter discusses the properties, synthesis and processing of materials used during the course of this thesis, and the characterisation techniques used to investigate their properties. Experimental details for Chapters 3–5 are also included.

2.1 Properties of layered materials

Graphene is perhaps the most well known two-dimensional (2D) layered nanomaterial — many people globally will have come into contact with its bulk form, graphite (in the form of pencil lead), at an early age. However, there is increasing interest in other low-dimensional nanomaterials; in particular the transition metal dichalcogenides

(TMDs) are hailed as the new 'wonder materials' [8]. The following subsections will discuss carbon-based nanomaterials (2.1.1) and TMDs (2.1.2) in more detail, and other nanomaterials such as hexagonal boron nitride (BN) (2.1.3) will also be discussed.

2.1.1 Carbon-based nanomaterials

The carbon family of nanomaterials spans from the zero-dimensional (0D) to the three-dimensional (3D). In addition to the 2D graphene, these materials include the 0D fullerenes (first predicted by Osawa in 1970 [9] and discovered by Kroto et al. in 1985 [10]); the 1D carbon nanotube (CNT), whose first discovery is contentious* [15]; and the 3D graphite, a layered material formed of stacks of graphene monolayers, natural deposits of which have been known and used for centuries. Together, these can be considered the graphitic family; graphene can be used as an initial building block for the formation of these other materials (Figure 2.1). Additionally, there are a range of other carbon nanomaterials including carbon quantum dots (QDs) [16, 17], carbon black [18], carbon nanofibres [19, 20], and the more exotic carbon nanohorns [21, 22] and carbon nano-onions [23, 24].

There has been a surge of research involving graphene since 2004, when the work for which Novoselov and Geim won their Nobel Prize was first reported [6]. This described the isolation of graphene nanosheets large enough to measure its remarkable electronic properties for the first time [6], detailed further in [25]. These properties are produced as a result of the structure of graphene.

Carbon atoms have four valence electrons, two in the 2s orbital and the other two in the $2p_x$ and $2p_y$ orbitals. When bonding with other atoms, one of the electrons in the 2s orbital is promoted to the $2p_z$ orbital, such that each orbital has one electron [27]. In graphene, only the 2s, $2p_x$, and $2p_y$ orbitals undergo hybridisation, forming three sp^2 orbitals [27]. These orbitals lie perpendicular to the remaining

*Single-walled CNTs were first discovered independently by Iijima and Ichihashi, and Bethune et al., in 1993 [11, 12]. The discovery of multi-walled CNTs is also frequently ascribed to Iijima [13]; while this work certainly brought CNTs wider attention in the scientific community, they were perhaps first observed in 1952 by Radushkevich and Lukyanovich [14].

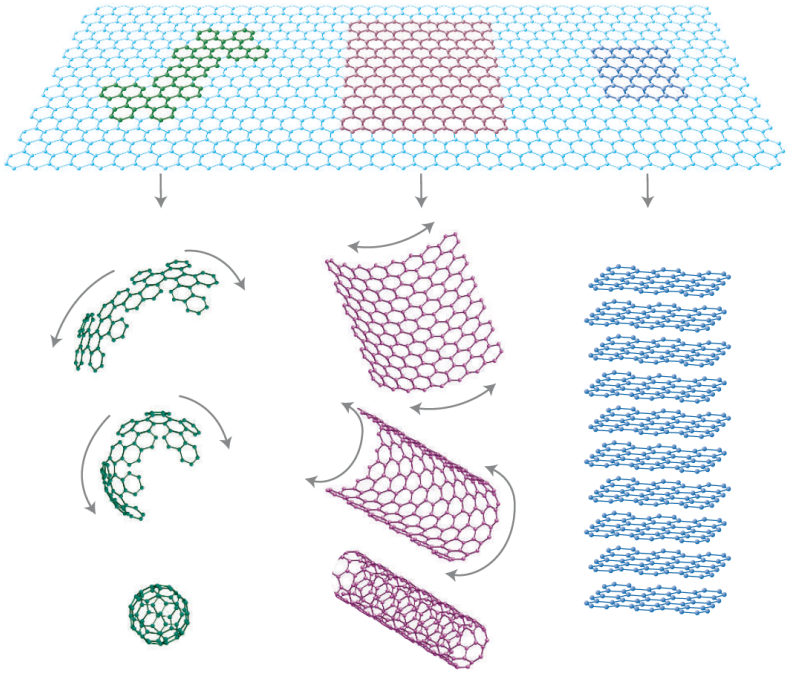

Figure 2.1: The iconic hexagonal structure of graphene is shown in blue (top). Graphene can be considered the initial building block for the graphitic family, comprising fullerenes (left), CNTs (centre), and graphite (right). Image from [26].

$2p_z$ orbital, forming covalent σ bonds in a trigonal planar geometry, resulting in graphene's familiar layered hexagonal lattice [25, 27]. This is shown in Figure 2.1. The $2p_z$ orbitals form π bonds between graphene sheets, and are the cause of the weak bonding which allows the easy exfoliation of graphite.

It is these σ and π bonds that give graphene its remarkable mechanical and electronic properties. The delocalised electron density associated with σ bonds ranks these among the strongest covalent bonds, giving graphene its extreme strength (intrinsic strength of 42 N/m in a defect-free sheet) [28]. This delocalisation also improves the electronic transport properties [27]. While the π bonds explain the weak, easily-broken bonding between sheets of graphene, they are also the cause of graphene's unique electronic properties [29].

A tight-binding model can be used to derive the energy dispersion relation of graphene [25, 30]. The band structure can therefore be visualised by plotting this relation, shown in Figure 2.2. The dispersion relation is linear at the K points, called the Dirac points, which correspond to the corners of the first Brillouin

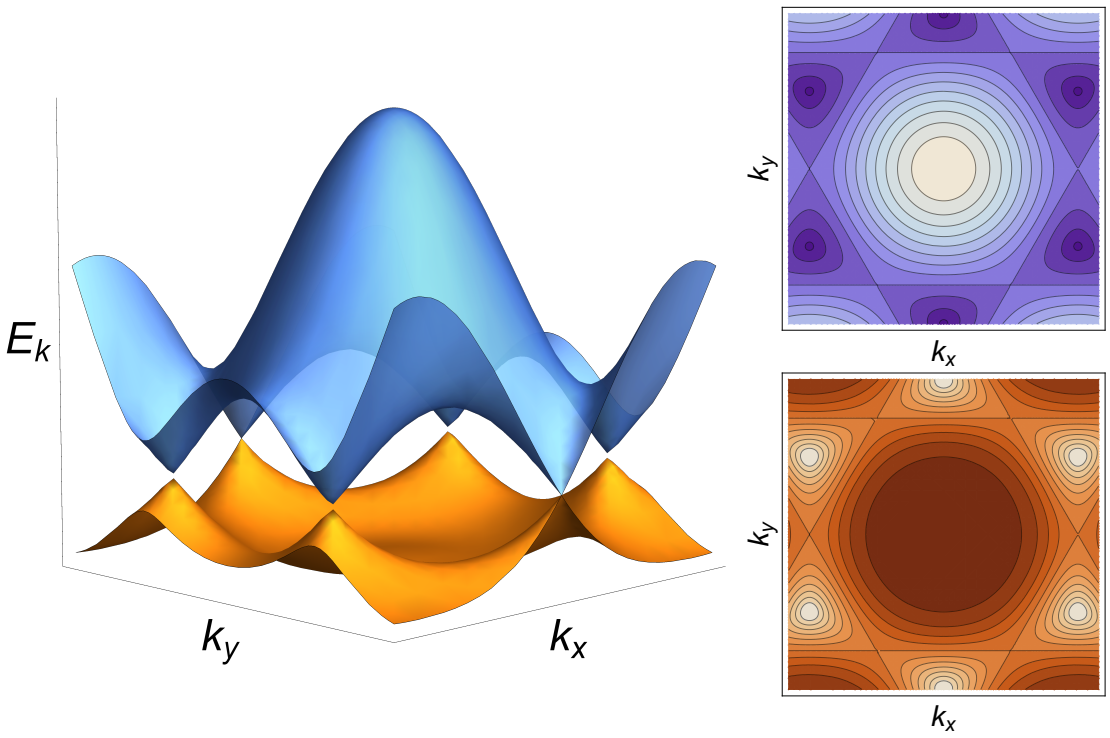

Figure 2.2: 3D plot showing the band structure of graphene over the first Brillouin zone (left). Contour plots showing the energy contours for the conduction band (top right) and valence band (bottom right). Valence band in orange and conduction band in blue.

zone [25, 30]. This makes graphene a zero-gap semiconductor, or semi-metal; its electrons have no effective mass and are scattering-free over distances on the order of micrometers [25]. Further, the conductivity of graphene can be tuned with an external gate potential [6, 25]. Graphene has also been investigated for biological applications, although its inert nature doesn't lend itself easily to ensuring biocompatibility. However, while modification of graphene can enhance its compatibility in biological systems [31], graphene oxide (GO) is a more obvious choice for use in nano–bio research.

GO has received more attention in this sphere due to its excellent surface functionality, amphiphilicity, aqueous dispersibility, fluorescence quenching ability and surface-enhanced Raman scattering property [31]. Unlike graphene, the oxygenated sheets of GO allow for easy functionalisation or loading of biological compounds, leading to improved biocompatibility, solubility and selectivity [32]. However, this benefit also limits its use as a substrate or scaffold, as these functional groups increase

the hydrophilicity compared to graphene, meaning that GO readily disperses in water and cell media [27, 33]. For this reason, reduced graphene oxide (rGO) could offer 'the best of both worlds' — rGO maintains enough functional groups to be easily functionalised [34, 35], while also becoming less soluble [36].

2.1.2 Transition metal dichalcogenides

Transition metal dichalcogenides (TMDs) are compounds described by the chemical formula MX_2, where M is a transition metal (e.g. Mo, W) and X is a chalcogen (e.g. S, Se) [8, 38]. The monolayer, formed of a hexagonal plane of transition metal ions sandwiched between planes of chalcogen atoms [39], typically has a thickness of ~6–7 Å (Figure 2.3) [38]. Similar to graphene, the in-plane covalent bonding is strong and the bulk TMD is formed by the stacking of weakly bonded monolayers; this means that the bulk crystal is similarly easy to exfoliate [8]. While not strictly 2D materials, as the monolayer is formed of three planes of atoms, TMDs are often classed as such due to their extremely thin monolayers [38–40].

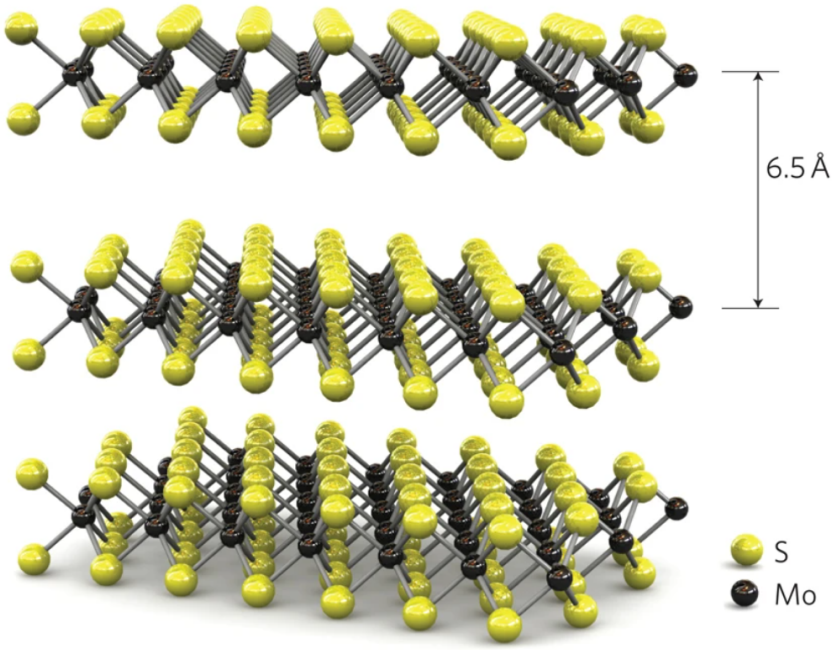

Figure 2.3: Crystal structure of MoS_2. Image from [37].

Some TMDs occur naturally as crystalline minerals such as molybdenite (MoS_2) or the rarer tungstenite (WS_2) [8]. TMDs are also produced synthetically by chemical vapour deposition (CVD), hydrothermal, and solid phase pyrolysis processes [39, 40]. Chemical exfoliation by intercalation was the predominant method of few-layered TMD production for study in the decades before graphene was first isolated [41–48]. However, the work in this thesis uses liquid-phase exfoliated (LPE) materials; this technique is discussed further in 2.2.1.

Naturally occurring MoS_2 commonly has the 2H-MoS_2 crystal phase, while synthetic MoS_2 often has the 3R-MoS_2 phase [8]. Both of these polytypes, with respective hexagonal and rhomboedral symmetries, have a trigonal prismatic geometry and are semiconducting [8, 49, 50]. MoS_2 is probably the most well studied TMD. It has been investigated for several decades; few-layer MoS_2 has been reported since the 1960s [51], and the monolayer was first reported 20 years later [45]. In this thesis few- or monolayered MoS_2, WS_2, and $MoSe_2$ are studied, although these three materials are only some of the about 40 TMDs known to have a layered structure [8].

Bulk MoS_2 is an indirect band gap semiconductor with a band gap of 1.29 eV [53]. As the layer number decreases towards the monolayer, the indirect band gap increases to over 1.90 eV [53]. This shifts the lowest energy transition to the direct band gap (Figure 2.4), resulting in a strong photoluminescence in monolayer MoS_2 [52, 53].

MoS_2 has been used for applications such as lubrication (its weak interplanar bonding gives it a low coefficient of friction) [54–56] and catalysis [57–61] for the best part of a century. More recent research has focussed on the potential of few-layered MoS_2 for new applications, ranging from microelectronics [62–68] to superconductivity [69–76] to photovoltaics [77–84]. Of particular relevance to this thesis are possible biological applications. MoS_2 has been considered for bioimaging because of the photoluminescence of the monolayer form [85–88]. Due to its high fluorescence quenching, recent years have also seen increasing interest in the use of MoS_2 for biosensors [89–96]. Additionally, MoS_2 has high absorbance of near infrared light, leading to its investigation for potential photothermal therapies (PTTs) [97–102].

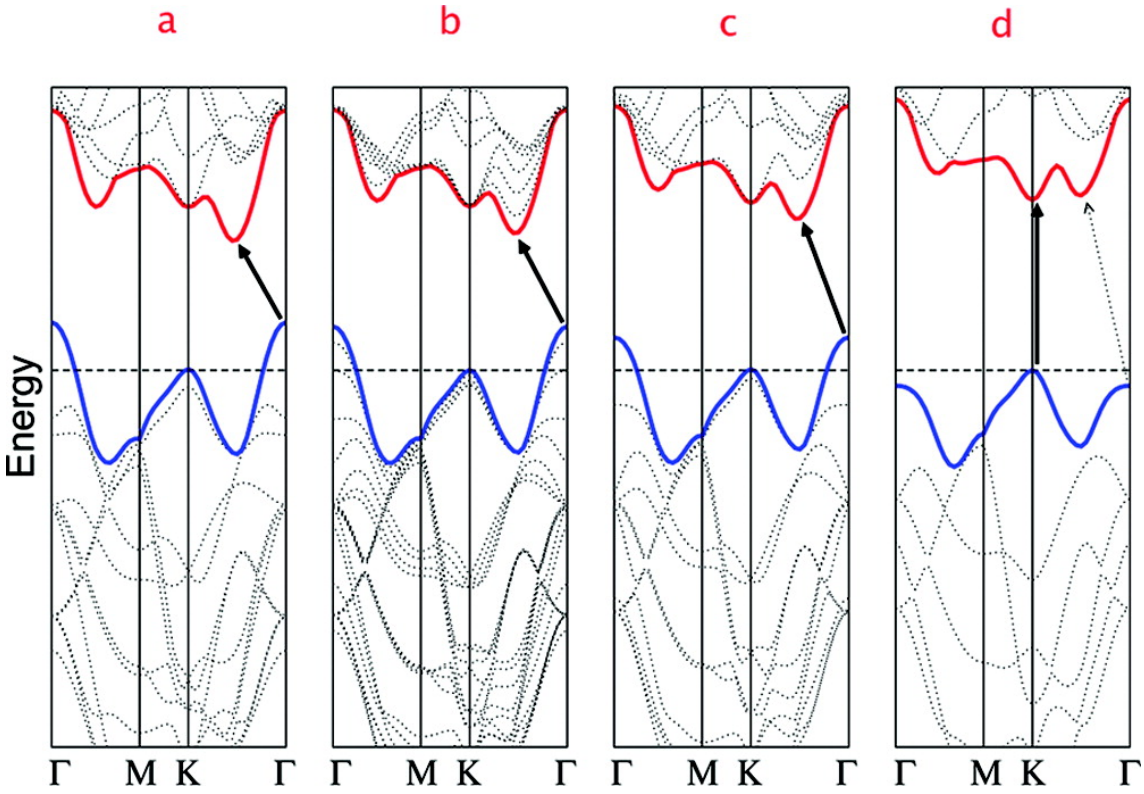

Figure 2.4: Calculated band structures of (a) bulk MoS_2, (b) quadrilayer MoS_2, (c) bilayer MoS_2, and (d) monolayer MoS_2. The solid arrows indicate the lowest energy transitions. Image from [52].

Drug delivery vehicles based on MoS_2 have been described in the literature [103–106], as well as combination PTT/drug delivery applications [107–110]. A new potential theranostic application for MoS_2, utilising its inherent photoluminescence and local heating, is described in detail in Chapter 4.

2.1.3 Other nanomaterials

Like the TMDs, **hexagonal boron nitride (BN)** is another graphene analogue. Its crystal structure is shown in Figure 2.5; the in-plane covalent bonding is very strong, and the layered structure of the bulk is formed by van der Waals bonding between these planes [111]. This differs slightly from graphene because of the two elements involved — when stacked, the boron atoms lie above and below the nitrogen atoms [111]. Although BN also exists in other forms (e.g. cubic, wurtzite, rhombohedral), the hexagonal form is the most common as it is the most stable [112].

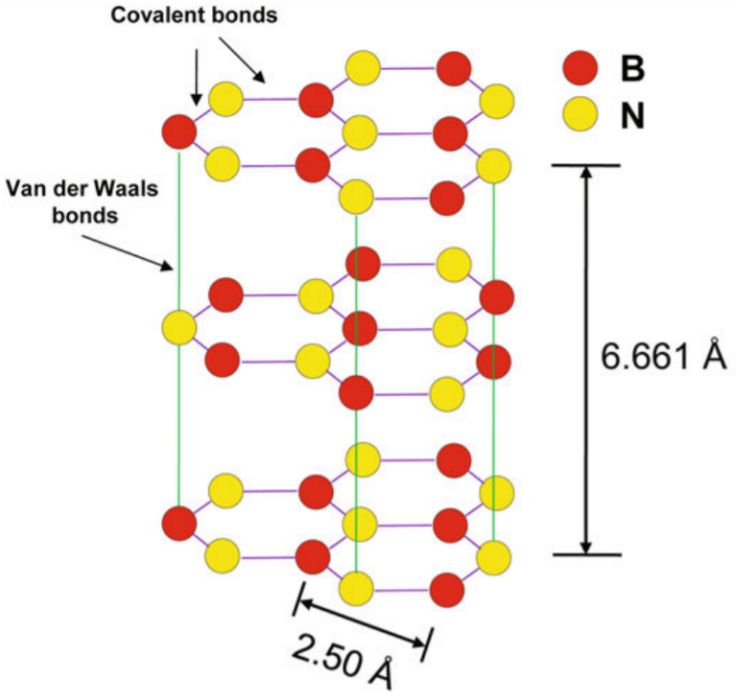

Figure 2.5: Crystal structure of BN. Image from [111].

Despite the similarity in structure, BN exhibits different electronic properties to those of graphene. This change is caused by the narrowing of the sp^2 π bands (due to the difference in electronegativity) compared to graphene [113]. As a result there is a loss of conductivity, yielding an insulator (or a wide-band semiconductor) [113]. A range of wide band gaps (5.5–5.9 eV) have been reported recently [114, 115], though depending on the method used, this range increases to 3.6–7.1 eV [116].

Because it acts as an insulator, BN is a promising material for use as a dielectric in electronic devices [117]. However, to scale up, this requires the production of large areas of flat BN. Dean et al. used a mechanical transfer process to produce graphene-on-BN devices [117]. Another method which could produce thin films of BN suitable for such devices is Langmuir deposition (technique described in more detail in 2.2.3). Recent work has produced the first demonstrations of Langmuir–Schaefer [118] (discussed in Chapter 3) and Langmuir–Blodgett [119] films of BN. Although this research is in its infancy, utilising such processing techniques could give new approaches to transparent and flexible devices [119], or to controllable substrates for biological studies [118].

Potential applications of other nanomaterials including

- **metal nanoparticles (NPs)**

  (e.g. AuNPs, CuNPs, metallofullerenes, etc.),

- **transition metal oxides and hydroxides**

  (e.g. TiO_2, ZnO NPs, layered $Zn(OH)_2$), and

- **silica NPs**

are discussed in the review of low-dimensional nanomaterials with intercellular function for diagnostics, therapeutics and theranostics in 2.4.

2.2 Synthesis of layered materials and substrate production

To achieve the properties associated with few-layered nanomaterials, the initial material needs to be well exfoliated. The reasons that exfoliated materials are desirable are numerous. As discussed at the beginning of this chapter, it is as the 2D landscape is approached that the unique and special properties of nanomaterials are enabled. Moreover, delaminating the bulk material increases the accessible surface area of the material, leading to enhanced reactivity in catalytic applications [120].

Synthesis of few- or monolayered nanomaterials can be separated into two broad categories: top-down, where bulk material is exfoliated to produce thin sheets; and bottom-up, where the material is created from scratch from the relevant building blocks. Liquid-phase exfoliation by sonication (LPE) is one example of a top-down approach. The work presented in this thesis uses nanomaterials produced by this method, and LPE is discussed in more detail in 2.2.1. Some other synthesis techniques are discussed briefly in 2.2.2.

Once a nanomaterial is produced, the resultant dispersion is available for processing. Nanomaterial dispersions provide a convenient basis for the creation of a number of useful substrates for further experimentation. The work in this thesis

focuses on 2D thin films produced by Langmuir film deposition, and this method is described further in 2.2.3. Additionally, the experimental details of the synthesis and processing techniques used for work in this thesis are provided in 2.2.4.

2.2.1 Liquid-phase exfoliation by sonication

Liquid-phase exfoliation by sonication (LPE) to produce monolayer graphene was first described by Hernandez et al. in 2008 [121]. This paper describes the production of graphene, though the same sonication process was quickly shown to debundle CNTs [122, 123], and thereafter shown to exfoliate a wide range of layered materials including TMDs [49, 124], BN [124, 125], and black phosphorus [126, 127].

LPE is easily scaleable compared to other methods such as mechanical exfoliation. This scalability means that it is possible to achieve higher production rates, important if nanomaterials are to become key materials in industry [120]. LPE also produces defect-free nanosheets [128], which could be important in applications where the material quality is paramount. However, it is important to note that this method isn't without problems. Although defect-free, the size of the nanosheets produced are often small compared to those produced by mechanical exfoliation [129]. Despite this drawback, nanosheets produced by LPE can still be harnessed for their enhanced properties [129].

The LPE process begins with a mixture of the bulk material in the chosen dispersant. This is introduced to either bath or probe sonication, which produces ultrasonic waves [120]. These waves cause cavitation bubbles to form in the dispersant;

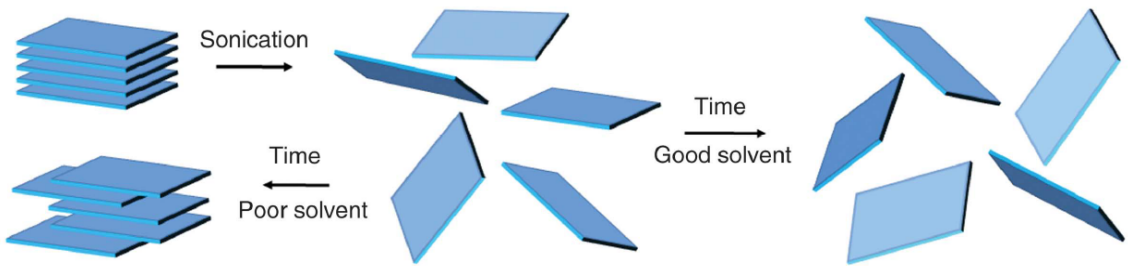

Figure 2.6: Schematic description of sonication-assisted liquid-phase exfoliation (LPE). Image adapted from [120].

when these bubbles burst, high-energy jets are released [120]. This energy is enough to break the inter-layer bonding of the bulk material, producing exfoliated few-layer nanosheets [120]. This is shown in Figure 2.6. The success of the sonication depends in no small part on the dispersant used. Solvents [130–132], surfactants [133–137], polymers [138, 139], and biomolecules [140–142] have all been demonstrated as dispersants. Du et al. have reviewed many different dispersants used for LPE of various layered materials [143]. Water is available in abundance and is nontoxic, so would make an ideal dispersant for nanomaterials. However, nanomaterials are not soluble in water, so the addition of surfactants or polymers is necessary. The work in this thesis uses nanomaterial dispersions in organic solvents, as surfactants are toxic to biological systems. As such, only solvent dispersants are discussed in detail.

The success in producing a stable nanomaterial dispersion, i.e. a dispersion which doesn't reaggregate and precipitate quickly, has been shown to depend on surface energy matching between material and solvent [121]. Solvents with surface energies close to that of the layered material produce a more stable dispersion; reaggregation is less likely because the energy difference between the exfoliated and reaggregated states is small [120, 128]. Good solvents for the exfoliation of graphene therefore require surface tensions of ~40–50 mJ/m^2 [121]; this explains the inability of pure water to satisfactarily exfoliate graphite, as it has a surface tension of 72 mJ/m^2 [120].

Which solvents make 'good' dispersions is a subject which has received much investigation. As discussed above, the energy cost of exfoliation is a key factor. Hernandez et al. identified the use of Hansen solubility parameters to estimate the energy cost of nanomaterial exfoliation [144]. Originally developed to explain the solubility of polymers, this framework is also able to describe the dispersibility of nanomaterials satisfactorily. The intermolecular interactions between solvent and solute can be broadly classified into dispersive (D), polar (P), and hydrogen-bonding (H) components [144]. The distance in Hansen parameter space from solvent (B) to solute (A) can be used as a simple parameter to represent the similarity of the

materials' suface energies. This is given as

$$R = \sqrt{4(\delta_{\mathrm{D},A} - \delta_{\mathrm{D},B})^2 + (\delta_{\mathrm{P},A} - \delta_{\mathrm{P},B})^2 + (\delta_{\mathrm{H},A} - \delta_{\mathrm{H},B})^2} \tag{2.1}$$

where $\delta_{\mathrm{D},B}$, $\delta_{\mathrm{P},B}$, $\delta_{\mathrm{H},B}$ are the solvent Hansen parameters and $\delta_{\mathrm{D},A}$, $\delta_{\mathrm{P},A}$, $\delta_{\mathrm{H},A}$ are the solute Hansen parameters [145, p. 29]. The constant "4" is included in front of the first term having been found empirically to ensure that R is spherical in Hansen parameter space [145, p. 29]. When R is minimised, so is the energy cost of graphene exfoliation. Although shown to work for graphene, this framework has also successfully described other materials [124, 146].

Hernandez et al. showed that dispersion concentration increases as R decreases [144], and dispersions of MoS_2 have been produced with concentrations as high as 40 mg/mL [147]. Graphene dispersions have been shown to reach concentrations of at least 63 mg/mL, though this method included a centrifugation step before redispersion of the material in fresh solvent [148].

Centrifugation is therefore an important step in obtaining high quality nanomaterial dispersions. This method is well established, having been used in laboratory practice for well over 100 years [149]. In short, the dispersion is rotated at a high number of revolutions per minute (RPM); this artificially increases the gravitational force felt by nanosheets in the dispersion. The largest sheets feel the largest gravitational force, so separate quickest from the rest of the dispersion. Hence, separation occurs at different rates depending on sheet size, allowing the isolation of few-layered nanosheets in minutes, rather than days.

Not only does centrifugation remove unexfoliated bulk material and increase the concentration of the final dispersion, but it can also be used to obtain specific sizes of nanosheets. LPE produces nanomaterials with a broad range of sheet sizes and thicknesses [150]. If nanosheets within a specific, narrow range are required then additional processing is needed. One size selection technique is known as **liquid cascade centrifugation (LCC)** [151]. This process covers a series of successively stronger centrifugation steps. Each step has a gradually increased RPM, such that

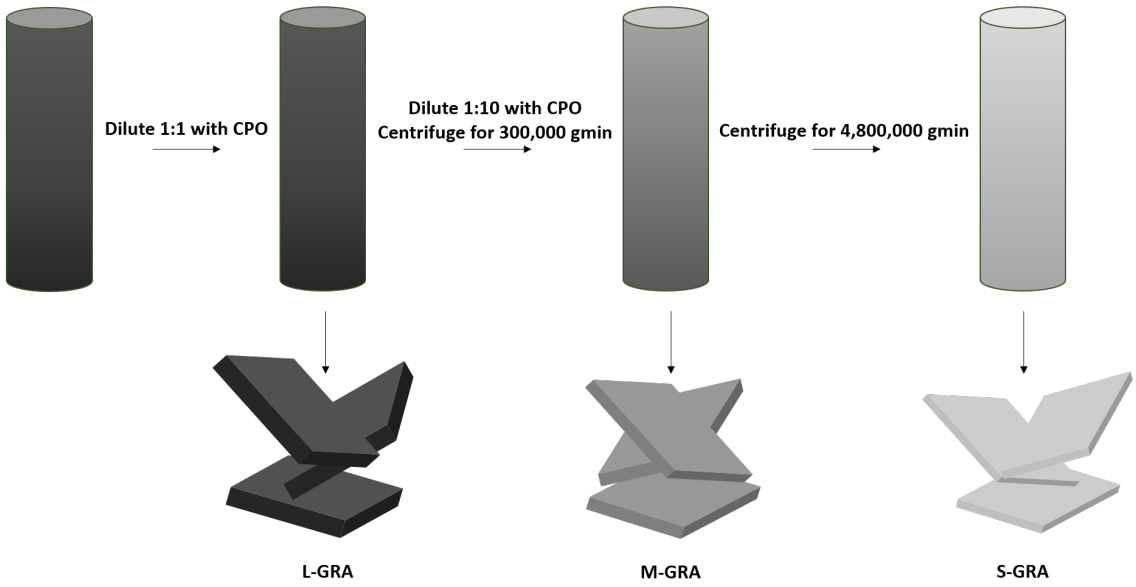

Figure 2.7: Diagram illustrating the liquid cascade centrifugation (LCC) process, beginning with a graphene dispersion in cyclohexanone. Details in figure relate to 2.2.4.1.

the dispersion is subjected to steadily increasing gravitational forces. These fractions, each with smaller and thinner nanosheets, can be redispersed to produce samples. The LCC technique is shown in Figure 2.7.

2.2.1.1 High-pressure homogenisation

While sonication-assisted LPE materials are mainly used in this thesis, some material was produced by high-pressure homogenisation. The shear forces required to exfoliate the material are provided by forcing the dispersion through a narrow nozzle at high pressure [152]. The specific system used in this thesis is described by Large et al. and is shown in Figure 2.8 [137]. The initial dispersion is poured into the inlet reservoir, and from here it is drawn into the intensifier pump. The system can generate pressures of up to 3000 atm, and the compressed dispersion is decompressed through a diamond nozzle within the process cell [137]. The resultant high-speed jet of dispersion collides with fluid flowing in the opposite direction, generating the shear forces which exfoliate the bulk material. From here the dispersion is passed into a heat exchanger; the turbulent forces necessary for exfoliation produce a lot of

heat, so the dispersion is cooled to a specified temperature controlled by an external chiller. At the end of the cycle, the dispersion can either be collected or recirculated, depending on the system configuration [137].

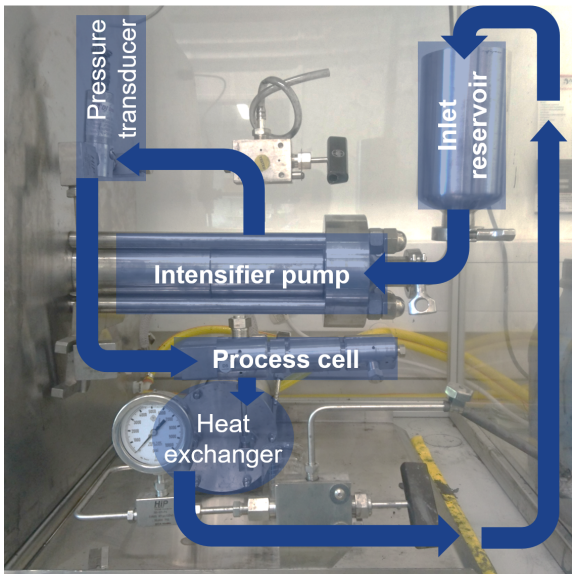

Figure 2.8: Schematic of the high-pressure homogenisation equipment used, overlayed on a photograph of the system. Image from [137].

2.2.2 Other synthesis techniques

While liquid-phase exfoliation by sonication and high-pressure homogenisation were the only synthesis techniques used in this thesis, other methods are commonly used in the literature. Some other techniques are discussed briefly in this section.

One method mentioned in passing in 2.1.2 is **ion intercalation**. Whereas LPE utilises sonication to break the weak bonding between the layers in layered nanomaterials, ion intercalation involves the introduction of ion guests between these layers [153]. The ions increase the size of the gaps between layers [154], leading to exfoliation if enough energy is supplied [120]. In 2.1.2 the long history of TMD exfoliation by ion intercalation was mentioned, but it is important here to note that graphite has also been subject to ion intercalation studies for the past several decades [155].

No discussion of nanomaterial exfoliation would be complete without mentioning **mechanical exfoliation**. This method is well known as the technique first used to isolate monolayer graphene by Novoselov and Geim in 2004 [6]. This simple yet powerful technique works by physically peeling individual layers from the bulk crystal using scotch tape, allowing each layer to be deposited on a substrate of choice. This synthesis technique has also been used to obtain other few-layered materials, including but not limited to TMDs [156] and group IV metal chalcogenides [157].

Possibly the most common bottom-up synthesis method is **chemical vapour deposition (CVD)**. The process involves the introduction of the precursor material as a vapour to a vacuum chamber which contains the substrate; the vapour then reacts with the substrate to produce a monolayer of the desired material [158]. This can create monolayers with large areas, but is an expensive process that currently lends itself mainly to high-performance applications [159]. Moreover, the nanosheets produced can be quite defective, and cannot be transferred from the initial substrate used. Regardless, CVD is the one of the most common bottom-up synthesis techniques in industry, used for microelectronics (mobile phones, laptops, etc.), data storage, and medical equipment applications [160].

2.2.3 Langmuir deposition

The Langmuir deposition technique functions by utilising the air–liquid interface as a 2D plane for the assembly of exfoliated nanosheets. Nanomaterial dispersion is dropped onto the liquid subphase (frequently deionised water is used, though some materials may require a modified subphase); the droplets spread on the subphase surface until the solvent evaporates and a thin, monolayer film is left at the air–liquid interface.

Therefore, solvent choice is an important aspect of the process. The chosen solvent must fulfil three main requirements. It must:

- have a high vapour pressure, so that it evaporates and leaves a film of particulates at the interface [161];

- spread on the water surface, to maximize the area over which nanoparticles are spread to minimize reaggregation during solvent evaporation [162]; and
- be water-immiscible, to avoid mixing with the subphase.

The density of the nanomaterial monolayer can be modified before deposition by controlling the film area with barriers. This was first described by Agnes Pockels in 1891 [163]; she had created a trough with moveable barriers from a tin pan and inserts. The trough was further developed by Irving Langmuir and Katherine Blodgett [164].

Control over the film density is important, as this is related to the surface pressure of the film and can affect its behaviour. When trough area is large and the film density is low, the material is sparsely distributed in the trough; these 'films' are not continuous, and may consist of islands of material across the trough area. As the trough area decreases, the film density increases until nanosheets come into contact with each other. If this continues, the film will eventually cease to be monolayer as the density reaches a maximum and the nanosheets begin to overlap. This process describes the change of surface pressure from low to high, and can be described as the 'phase transitions' [165] of the monolayer film (Figure 2.9).

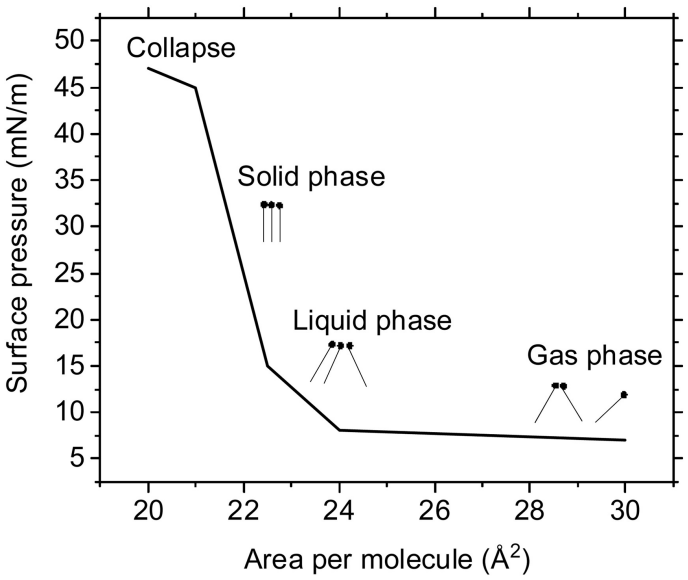

Figure 2.9: Typical pressure–area isotherm indicating the different phases in a Langmuir monolayer. As the trough area, and hence area per molecule, decreases, the surface pressure increases, causing the monolayer to undergo 'phase transitions'. The molecular arrangement in the different phases is indicated. Image from [166].

Once the nanomaterial film is at the desired density it is deposited onto a suitable substrate. The thin films studied throughout this thesis are deposited onto glass cover slips as these are standard substrates in the biological sciences, so compatibility with cell study methods was ensured. There are two main techniques to deposit the nanomaterial film from the air–water interface onto a substrate: Langmuir–Blodgett deposition, which involves the vertical dipping of a substrate through the monolayer [164], and Langmuir–Schaefer (L–S) deposition, which involves the horizontal dipping of a substrate [167].

The Langmuir deposition technique was developed with amphiphilic molecules, as the polar nature of these molecules meant that they would align in the same orientation on the subphase and transfer easily to the substrate [168]. The technique has since been shown to work for a range of nanoparticles [166] including but not limited to pure and functionalised fullerenes [169–171]; capped metallic NPs [172–174]; functionalised CNTs [175–177]; silver nanowires [178]; graphene [179–181]; MoS_2 [182–184]; and phosphorene [185].

2.2.4 Synthesis and processing of materials for Chapters 3–5

This section contains experimental details of the material synthesis and substrate production for the work presented in Chapters 3–5.

2.2.4.1 Synthesis and processing of materials for Chapter 3

Synthesis of materials

BN powder (0.5 g, Aldrich Chemistry) was added to 20 mL of cyclohexanone (VWR Chemicals) and probe sonicated using a Sonics Vibracell VCX750 and ½-inch (13 mm) tip at 60% amplitude for 3 hours. The resulting dispersion was centrifuged for 25,000 g min using a Thermo Scientific Sorvall Legend X1. The supernatant was collected for further characterisation.

MoS_2 powder (0.4 g, Aldrich Chemistry) was added to 20 mL of cyclopentanone (VWR Chemicals) and probe sonicated using a Sonics Vibracell VCX750 and ½-inch (13 mm) tip at 60% amplitude for 1 hour. The resulting dispersion was centrifuged for 150,000 g min using a Thermo Scientific Sorvall Legend X1. The supernatant was discarded, and 20 mL of fresh cyclopentanone added. This was probe sonicated using a Sonics Vibracell VCX750 and ½-inch (13 mm) tip at 60% amplitude for 3 hours. The resulting dispersion was centrifuged for 25,000 g min using a Thermo Scientific Sorvall Legend X1. The supernatant was collected for further characterisation.

WS_2 powder (0.75 g, Aldrich Chemistry) was added to 30 mL of acetone (VWR Chemicals) and probe sonicated using a Sonics Vibracell VCX750 and ½-inch (13 mm) tip at 60% amplitude for 1 hour. The resulting dispersion was centrifuged for 150,000 g min using a Thermo Scientific Sorvall Legend X1. The supernatant was discarded, and 20 mL of fresh cyclopentanone added. This was probe sonicated using a Sonics Vibracell VCX750 and ½-inch (13 mm) tip at 60% amplitude for 3 hours. The resulting dispersion was centrifuged for 25,000 g min using a Thermo Scientific Sorvall Legend X1. The resultant WS_2/acetone dispersion was centrifuged for 5,400,000 g min using a Thermo Scientific Sorvall Legend X1. The supernatant was discarded, and the solute redispersed in 5 mL of fresh cyclohexanone added to each centrifuge tube.

Graphene dispersions in cyclohexanone were processed as described in Large et al. [137]. Size-selected graphene dispersions were required. The dispersion was diluted 1:1 with cyclopentanone (Aldrich Chemistry) for the largest flake size (referred to as L-gra). LCC [151] was used to obtain fractions of the original dispersion with different nanosheet size by extraction and re-centrifugation of the supernatant after each centrifugation step (Figure 2.7). Each time, this process leaves behind a solute that has an increasingly smaller average flake size. The dispersion to be size-selected for small flake size (referred to as S-gra) was further diluted 1:10 in cyclopentanone before centrifugation for 4,800,000 g min using a Thermo Scientific Sorvall Legend X1. The supernatant was collected for further characterisation.

Langmuir–Schaefer deposition of films

A NIMA 102A Langmuir trough and NIMA surface pressure sensor (type PS4, serial no. 045) equipped with platinum Wilhelmy plate was used. Material dispersions were used to create thin films with varying surface coverages. The dispersion concentrations used ranged between 0.018–2.558 g/L (i.e. within the range typically produced by LPE), and the amounts deposited ranged between 100–900 µL. For film fabrication calibration, a range of surface pressures has been used (ranging from approximately 0.5–40 mN/m). To investigate quantitatively, a series of thin films of various materials were deposited by L–S technique at varying pressures.

2.2.4.2 Synthesis and processing of materials for Chapter 4

Synthesis of materials

MoS_2 powder (0.4 g, Aldrich Chemistry) was added to cyclopentanone (20 mL, VWR Chemicals) and probe sonicated using a Sonics Vibracell VCX750 and ½-inch (13 mm) tip at 60% amplitude for 1 hour. The resulting dispersion was centrifuged for 150,000 g min using a Thermo Scientific Sorvall Legend X1. The supernatant was discarded, and fresh cyclopentanone (20 mL) added. This was probe sonicated using a Sonics Vibracell VCX750 and ½-inch (13 mm) tip at 60% amplitude for 3 hours. The resulting dispersion was centrifuged for 25,000 g min using a Thermo Scientific Sorvall Legend X1 to remove unexfoliated nanosheets. The supernatant was collected for further characterisation.

Langmuir–Schaefer deposition of films

A MoS_2 dispersion was used to create thin films by the Langmuir deposition technique. Films were created using both a NIMA 102A Langmuir trough and NIMA surface pressure sensor (type PS4, serial no. 045) equipped with platinum Wilhelmy plate, and by using a Petri dish without a surface pressure sensor. Material was deposited onto pristine glass cover slips once the films appeared dense to the naked eye.

2.2.4.3 Synthesis and processing of materials for Chapter 5

Synthesis of materials

WS_2 powder (0.75 g, Aldrich Chemistry) was added to 30 mL of acetone (VWR Chemicals) and probe sonicated using a Sonics Vibracell VCX750 and ½-inch (13 mm) tip at 60% amplitude for 1 hour. The resulting dispersion was centrifuged for 150,000 g min using a Thermo Scientific Sorvall Legend X1. The supernatant was discarded, and 20 mL of fresh cyclopentanone added. This was probe sonicated using a Sonics Vibracell VCX750 and ½-inch (13 mm) tip at 60% amplitude for 3 hours. The resulting dispersion was centrifuged for 25,000 g min using a Thermo Scientific Sorvall Legend X1. The supernatant was collected for further characterisation.

The WS_2/acetone dispersion was centrifuged for 5,400,000 g min using a Thermo Scientific Sorvall Legend X1. The supernatant was discarded, and the solute redispersed in 5 mL of fresh cyclohexanone added to each centrifuge tube.

$MoSe_2$ powder (0.5 g, Aldrich Chemistry) was added to 20 mL of cyclopentanone (VWR Chemicals; Sigma-Aldrich) and probe sonicated using a Sonics Vibracell VCX750 and ½-inch (13 mm) tip at 60% amplitude for 1 hour. The resulting dispersion was centrifuged for 150,000 g min using a Thermo Scientific Sorvall Legend X1. The supernatant was discarded, and 20 mL of fresh cyclopentanone added. This was probe sonicated using a Sonics Vibracell VCX750 and ½-inch (13 mm) tip at 60% amplitude for 3 hours. The resulting dispersion was centrifuged for 25,000 g min using a Thermo Scientific Sorvall Legend X1. The supernatant was collected for further characterisation.

Langmuir–Schaefer deposition of films

WS_2 and $MoSe_2$ dispersions were used to create thin films by the Langmuir deposition technique. Films were created using both a NIMA 102A Langmuir trough and NIMA surface pressure sensor (type PS4, serial no. 045) equipped with platinum

Wilhelmy plate, and by using a Petri dish without a surface pressure sensor. Pristine glass cover slips were masked with scotch tape approximately halfway; material was deposited onto these substrates once the films appeared dense to the naked eye.

2.3 Characterisation techniques

This section describes the physics behind the characterisation techniques used in this thesis. Broadly, these encompass microscopy (2.3.1, 2.3.4) and spectroscopy (2.3.2, 2.3.3).

2.3.1 Optical microscopy

While this technique is well known, it is worth mentioning here as it is used extensively throughout the work in this thesis. Light microscopes use visible light to produce a magnified image of an object that is projected onto a sensor (e.g. the retina of the eye or the photosensitive surface of an imaging device) [186]. Compound light microscopes use two lenses together to produce the final image magnification [187].

The optical components of a typical upright optical microscope are shown in Figure 2.10a. Light is provided to the microscope stage by a mirror or an integrated light source. The light passes through the condenser, which focuses the light onto a small area of the specimen, before illuminating it [186]. From the specimen, the light next reaches the objective, which collects the light diffracted by the specimen and forms a magnified real image near the eyepieces (depicted in Figure 2.10b) [186]. The eyepiece together with the detector (eye, camera, etc.) forms a final real image which is interpreted as having been magnified [186].

Bright-field microscopy occurs when light is transmitted through the sample to the objective; the image contrast is generated by the absorption of light in dense areas of the sample [188]. Until the late 1980s, other imaging modes were laborious to implement because most microscopes had a fixed tube length (i.e. the distance between the objective and the eyepiece is specified) [186]. This 'finite' design,

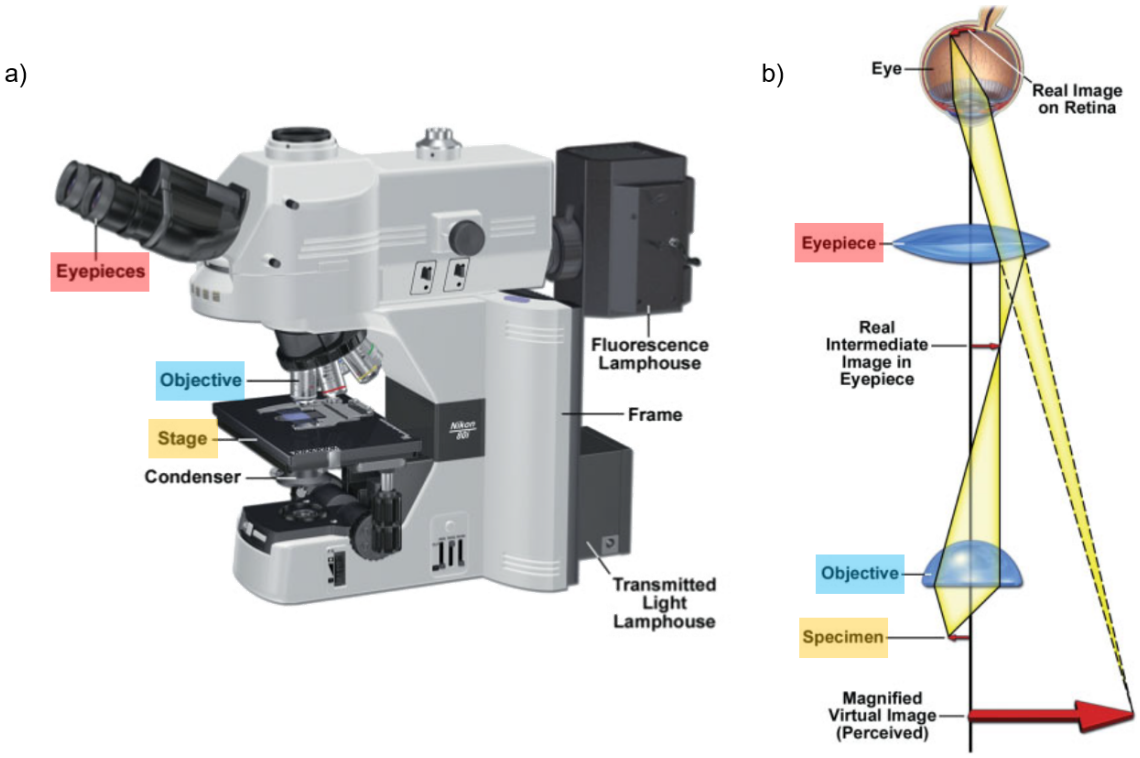

Figure 2.10: (a) Diagram showing optical components of an upright optical microscope. (b) Perception of a magnified virtual image of a specimen in the microscope. The objective forms a magnified real image of the specimen (called the real intermediate image) in the eyepiece. The intermediate image is examined by both the eyepiece and eye, which together form a real image on the retina. Because of the perspective, the retina and brain interpret the scene as a magnified virtual image about 25 cm in front of the eye. Image and caption adapted from [186].

shown in Figure 2.11a, doesn't easily allow for additional optical accessories such as polarisers to be added to the light path [186]. These additions increase the effective tube length, resulting either in image artefacts or in the placement of additional optical elements to counteract the effect of the accessories [186].

To combat the problems associated with fixed tube length microscopes, an alternative approach dubbed 'infinity optics' was developed (shown in Figure 2.11b) [186]. Instead of focusing light rays from the objective at the intermediate image plane, the design is modified such that the objective produces parallel light rays that image at infinity [186]. These rays are brought into focus by an additional component, the tube lens [186]. The area between the objective and the tube lens is designated the 'infinity space', and it is possible to introduce additional optical accessories into the light path here without producing artefacts [186].

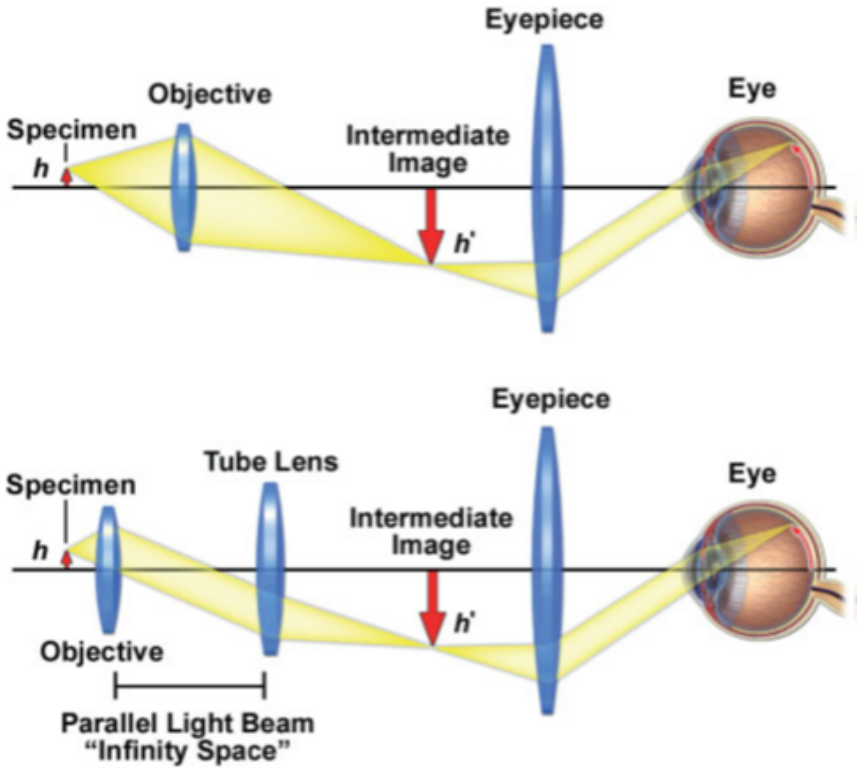

Figure 2.11: Finite and infinity-corrected optical configurations. (a) Finite optical configuration; light rays are focused from the objective at the intermediate image plane. (b) Infinity-corrected optical configuration; light rays between the objective and tube lens are parallel, providing the 'infinity space' region where optical accessories may be placed without causing image artefats. Image from [186].

Although bright-field microscopy can be used to image living cells, many biological samples appear with low contrast. In particular, specimens which are colourless and transparent, such as many types of cells, are not easily seen. To improve visibility of these samples, other imaging modes must also be utilised.

Dark-field microscopy excludes the unscattered light ray from the final image, which appears as a very dark background with a bright sample on it [189]. The technique is simple, and requires only the addition of a dark-field condensor lens. Artefacts which are common in phase-contrast microscopy, such as halos or shadows, do not usually appear in dark-field images. However, due to the low light in the final image the sample must be strongly illuminated [189], which can damage biological samples.

Another method that improves the contrast in transparent samples is differential interference contrast (DIC) microscopy. As its name suggests, DIC microscopy uses principles of interferometry to resolve features that would otherwise be invisible. This is because most detectors are sensitive only to the intensity of light, only showing contrast based on how much light is absorbed; DIC microscopy instead utilises the phase changes caused by transparent specimens to produce an image of the specimen [190].

In microscopes adapted for this technique, the initial light is polarised first by a polariser and then by the first Nomarski-modified Wollarston prism [190]. This produces two laterally-separated light rays which are orthogonally polarised and coherent [191]. These rays are focused by the condenser such that they pass through the sample a small (sub-resolution) distance apart from each other [190]. Because the adjacent areas of the sample will have different thicknesses or refractive indices, the light rays will experience different optical path lengths (OPLs), causing a relative change in phase between the rays. The light rays travel through the objective and are focused onto the second Nomarski-modified Wollarston prism, which recombines the light rays into one polarised beam and gives rise to interference of the rays [188].

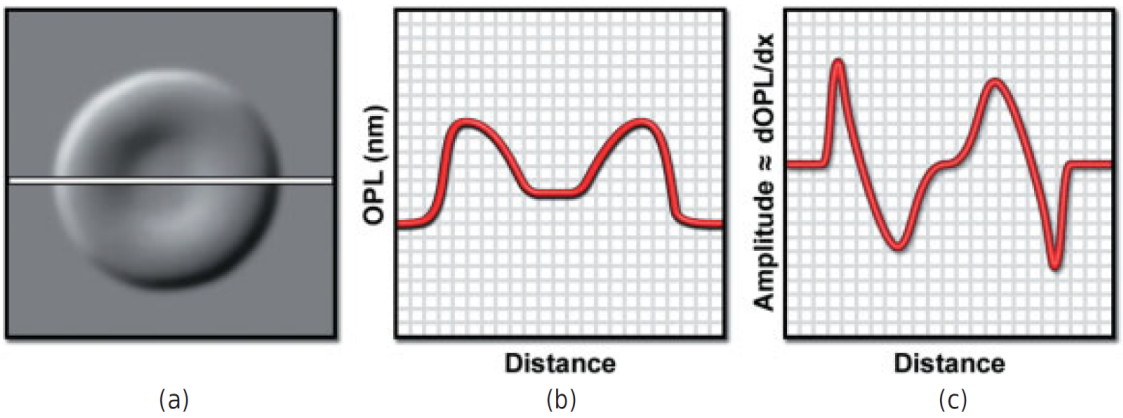

Figure 2.12: Gradients in optical path length (OPL) yield differences in amplitude. (a) DIC image of a mammalian erythrocyte (its diameter indicated by the white line). (b) Plot and (c) first derivative of the OPL across the diameter of the cell. Positive and negative slopes in panel (a) correspond to regions of higher and lower amplitude in panel (c). Regions of the object exhibiting no change in slope (e.g. centre of the cell) have the same amplitude as the background. This gives DIC images their misleading "3D" appearance. Image from [186].

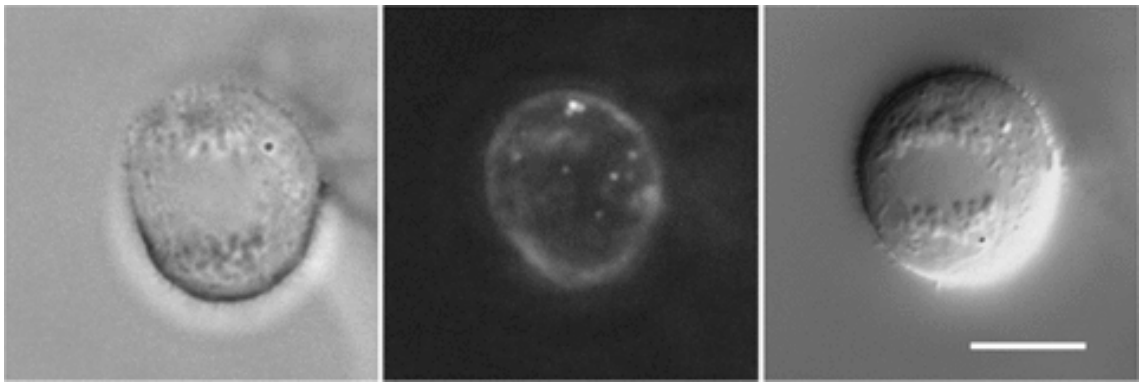

Figure 2.13: Comparison of images of the same Madin Darby canine kidney cell obtained from bright-field (left), dark-field (centre) and DIC (right) microscopy. Scale bar = 10 µm. Image from [192].

The final DIC image depends on the gradient of the OPL (Figure 2.12). The advantage of DIC microscopy is apparent when compared with bright-field and dark-field microscopy; this technique produces images with higher contrast and better z-resolution [192] (Figure 2.13).

Fluorescence microscopy is a technique commonly used for biological imaging. The term 'fluorescence' describes the process where specimens absorb light of one wavelength and re-emit it at a longer wavelength [187]. It is an example of the wave–particle duality of light. When a photon of light is incident upon fluorescent material an electron is excited from the ground state to a higher energy state. As the electron relaxes within the excited state, energy is dissipated to the surroundings until the electron reaches the lowest level of the excited state [187]. At this point it returns to the ground state, and a photon of corresponding energy is emitted. Because some of the initial energy has dissipated, the emitted photon has less energy than the incident photon; this is why light emitted by fluorescence always has a longer wavelength than the incident light (Figure 2.14) [187].

The fluorescence microscopy technique has the ability to localise enzymes, substrates, and genes, and to characterise physicochemical properties of the cell, including membrane potentials, viscosity, and pH with high resolution and contrast [187]. Usually nonfluorescent molecules or antibodies are tagged with a fluorescent dye or material to make these structures visible [186]. However, recent research increas-

ingly utilises fluorescent nanoparticles for imaging purposes; unlike more traditional fluorescence microscopy, these materials don't suffer from photobleaching, and don't require tagging. Some nanomaterials used for fluorescence imaging are discussed in 2.4.

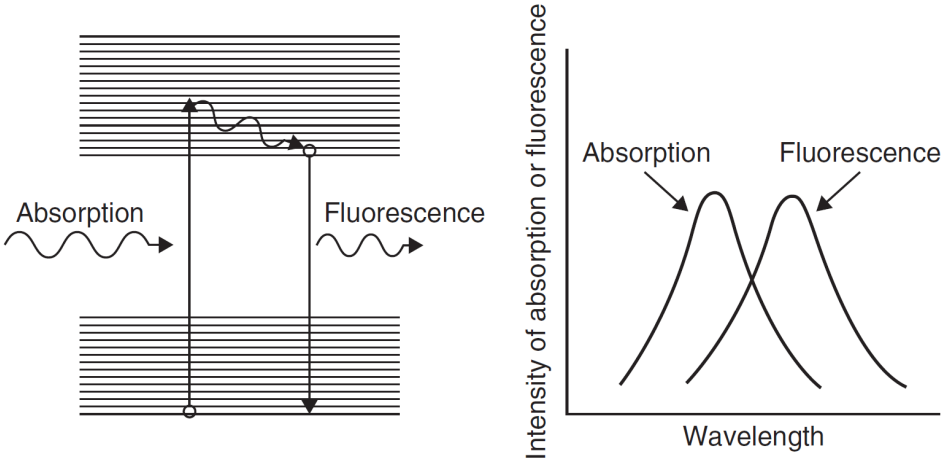

Figure 2.14: Energy diagram of a fluorescent molecule. The absorption and fluorescence emission spectra of the molecule are shown on the right. Image from [187].

2.3.2 Raman spectroscopy

Light is not only absorbed and emitted by atoms and molecules; photons can also be scattered by a sample. Scattering is either *elastic*, where molecules are left in the same state, or *inelastic*, where molecules are left in a different state. These two types of scattering are known as Rayleigh scattering and Raman scattering, respectively.

Rayleigh scattering is much more common than Raman scattering, the latter comprising only $\sim 10^{-5}$ of the incident beam [193, p. 15]. It is responsible for the blueness of the sky due to its strong ($I \propto \lambda^{-4}$) wavelength dependence [194, 195]. Rayleigh scattering is shown in Figure 2.15.

Raman scattering causes the wavelength (and hence energy) of the scattered light to change compared to the incident light. This can be split into two categories depending on whether the scattered light has an increased or decreased wavelength compared to the incident light. Stokes scattering occurs when the emitted light has a longer wavelength; this is caused by the excitation of a ground state molecule to

a virtual state, before relaxation back down to a higher energy vibrational state. Anti-Stokes scattering occurs when the emitted light has a shorter wavelength; this is caused by the excitation of a molecule in a vibrational state to a virtual state, before relaxation back down to the ground state. Stokes scattering is more common than anti-Stokes scattering because it is more likely for the molecule to be in the ground state when light is incident upon it. However, the ratio of anti-Stokes to Stokes scattering increases with temperature following the Boltzmann distribution, $N \propto \exp\left(-\frac{E}{k_B T}\right)$, because more molecules will be in the first vibrationally excited state under these circumstances. Both of these are shown in Figure 2.15.

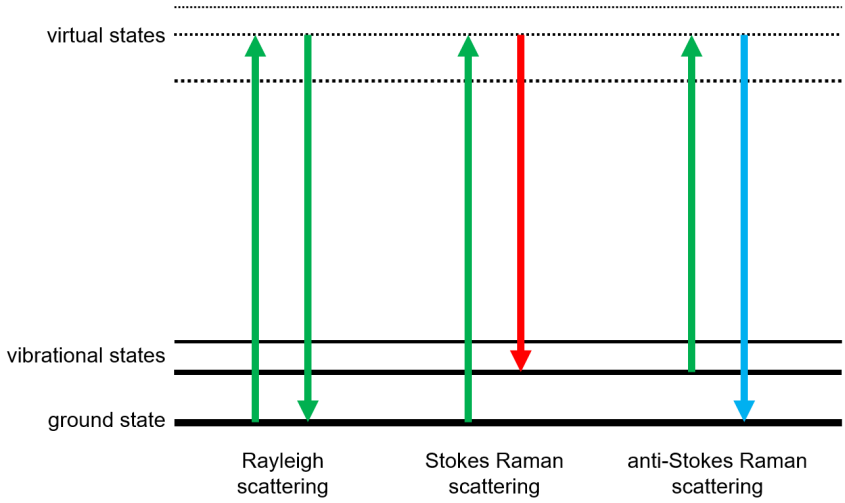

Figure 2.15: Energy diagram of Rayleigh, Stokes Raman, and anti-Stokes Raman scattering.

A Raman spectrometer is used to measure the Raman scattering of a material (a basic schematic is shown in Figure 2.16). In simple terms, this comprises a laser to illuminate the sample, followed by filters to collect either Stokes or anti-Stokes Raman scattered light (filters out other light components) and diffraction gratings to diffract the scattered light into a spectrum, before finally being detected by a CCD detector. This gives a Raman spectrum at a single point of the sample. Some Raman spectrometers have the ability to obtain a 2D map by scanning in x and y directions across a specified area, giving a picture of the material across a wider

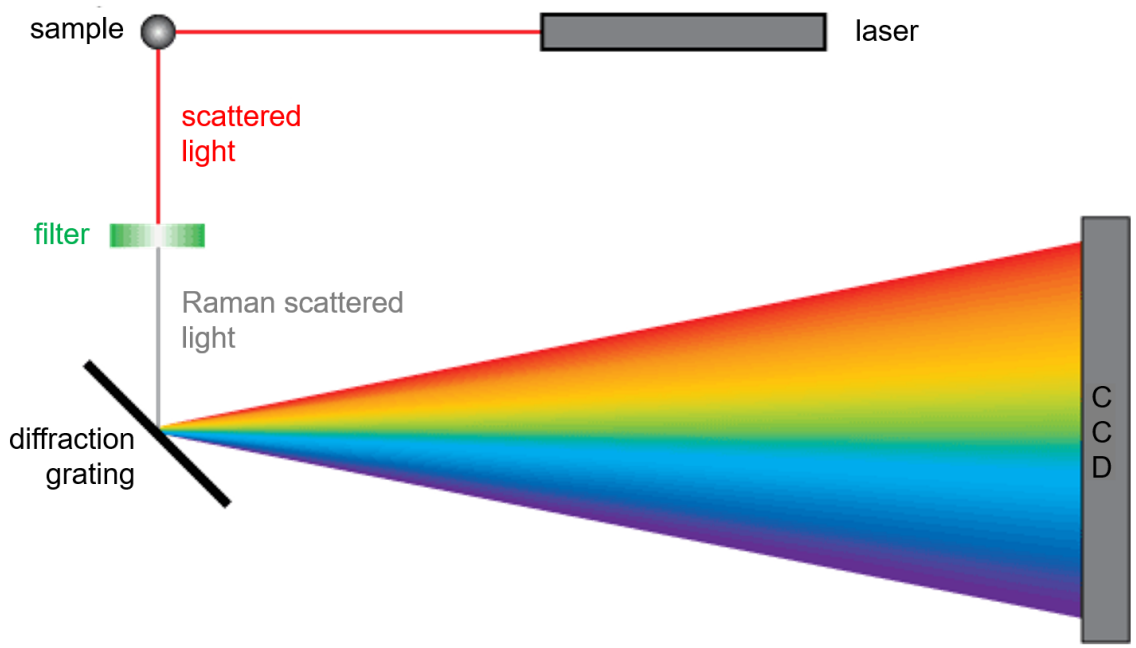

Figure 2.16: Basic schematic of a Raman spectrometer. Image from [196].

area. With a confocal system, which is additionally capable of incrementing in the z direction automatically, this process can be extended into three dimensions to create a 3D volumetric map.

For a material to be Raman-active, a molecular rotation or vibration must cause a change in the molecular polarisability, α [197, p. 63]. If Raman-active, then Raman spectroscopy measures the intensity of the scattered light as a function of Raman shift (the difference in wavenumber between the excitation and scattering). These spectra exhibit bands at various frequencies that correspond to vibrations of specific bonds in the material; these are known as Raman modes. The vibrational frequencies of the Raman modes depend on the masses of the atoms involved and the strength of the bonds between them; low vibrational frequency indicates heavy atoms and weak bonds, while high vibrational frequency indicates light atoms and strong bonds [193, p. 18]. An overall idea of the composition of the material is gained by observing which modes are present, and their ratios to one another.

It is well established that the ratio between Raman mode intensities, e.g. between the I_D and I_G modes for graphene, changes with nanosheet size [198–201]. Metrics based on this concept were developed for LPE graphene samples by Backes et al. [202].

Recently, improved Raman metrics utilising pixel-wise metricised Raman mapping have been developed by Amorim Graf et al., and are shown to apply to both graphene and MoS_2 [203]. Furthermore, a new metric for MoS_2 layer number was developed based on an intensity ratio, I_{465}/I_{453}, of resonant Raman modes [203].

Raman spectroscopy is a non-destructive, non-invasive technique, which lends itself well to the study of sensitive samples, such as biological cells or tissues. Spectra are aquired rapidly, without need for sample preparation. However, the Raman signal can be swamped by fluorescence from some materials; this characterisation technique can be used in combination with other techniques that may be less affected by, or that actively utilise, fluorescence signals.

2.3.3 UV–visible spectroscopy

UV–visible spectroscopy is a technique used to measure the optical extinction (comprising absorbance and scattering components) or transmittance of a solid or liquid sample as a function of wavelength.

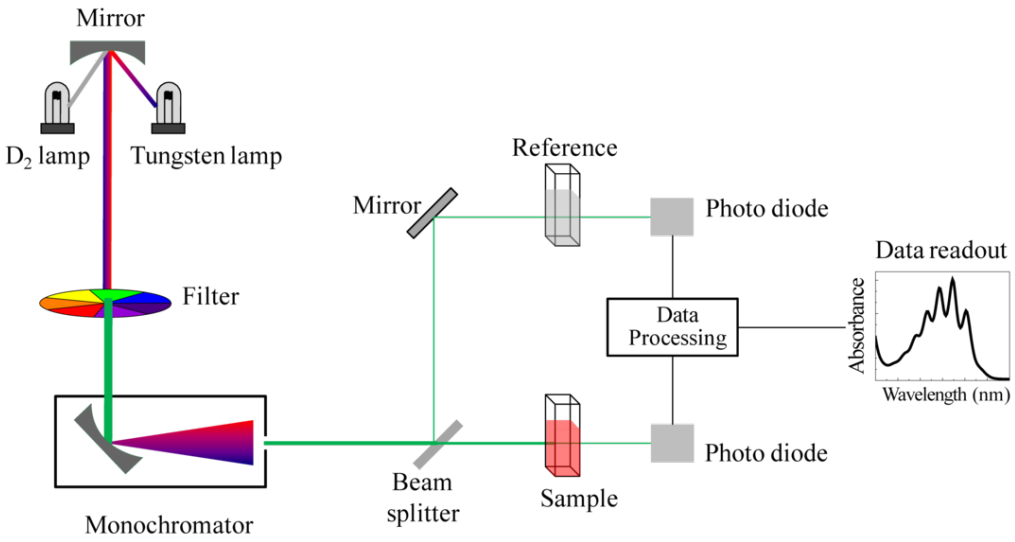

Figure 2.17: Schematic of a UV–visible spectrometer. Image from [204].

The internal components of a UV–visible spectrometer are shown in Figure 2.17. Briefly, a broadband light source is filtered and monochromated such that only light of a single wavelength is used for illumination. This light is passed through a beam splitter, forming two paths so that both the sample and reference can be measured simultaneously. Some of this light is absorbed by the sample, some is scattered, and some is transmitted; the transmitted light is measured by photodiodes. Any difference between the sample and reference transmittance measurements is assumed to be caused by the material in the sample.

Often, knowing the extinction (Ext) may be more useful than knowing the transmittance (T) of a sample. The two are related by the equation

$$\text{Ext} = -\log_{10}(T). \tag{2.2}$$

For many samples, extinction can be directly related to concentration (c) by the Beer–Lambert law. This can be written as

$$\text{Ext} = \varepsilon \ell c, \tag{2.3}$$

where ε is the extinction coefficient and ℓ is the OPL through the sample.

UV–visible spectroscopy can reveal exciton peaks in the spectra which are caused by electronic transitions in the material. Electronic structure is affected by the exfoliation of the material (as shown for MoS_2 in Figure 2.4), so there is a correlation between the measured exciton peaks and the thickness of the material. This has led to the development of spectroscopic metrics based on UV–visible spectroscopy measurements, which can provide information about the lateral size and the layer number of the material in question [202, 205–208].

2.3.4 Atomic force microscopy

Scanning probe microscopy encompasses several techniques that obtain images of sample surfaces by using a physical probe to scan the sample. Atomic force microscopy (AFM) is one of these techniques. Compared to the traditional optical microscope it has a very high resolution. AFM can overcome the optical diffraction limit, so has a resolution on the nanometer scale [209]; however, a slow imaging speed is required to achieve the best resolution. Additionally, it provides a 3D image of the sample surface [209]; to use reading a book as an analogy, AFM is to optical microscopy what Braille is to standard print on a page.

A diagram of a typical atomic force microscope (AFM) setup is shown in Figure 2.18. The force sensor is based on a cantilever with a sharp tip (tip radius of a few nanometers). As the cantilever rasters across the sample surface, the tip interacts with the sample, sensing attractive or repulsive forces between the molecules of the tip and sample [209]. Even small changes in the forces cause the cantilever to deflect, altering the reflection angle of the laser light incident upon the cantilever. This shifts the position of the reflected light on the photodiode array, and hence influences the photocurrent produced. Combining feedback from the photodiode array with the piezoelectric sensor controlling the motion of the cantilever allows precise measurements of the surface structure to be obtained.

There are three main scanning modes used for AFM measurements: contact mode, noncontact mode, and tapping mode [209]. Contact mode can be used to achieve high resolution images in both air and fluid environments; however, it can only be used to image samples with hard surfaces which cannot be deformed, because more fragile surfaces can be damaged. In noncontact mode the tip never makes contact with the sample surface. While this avoids issues associated with contact mode, such as damaging soft samples (e.g. some biological tissues), the resolution is lower due to the long-range forces used, and the image can be inaccurate due to the contamination layer present on all samples in ambient conditions.

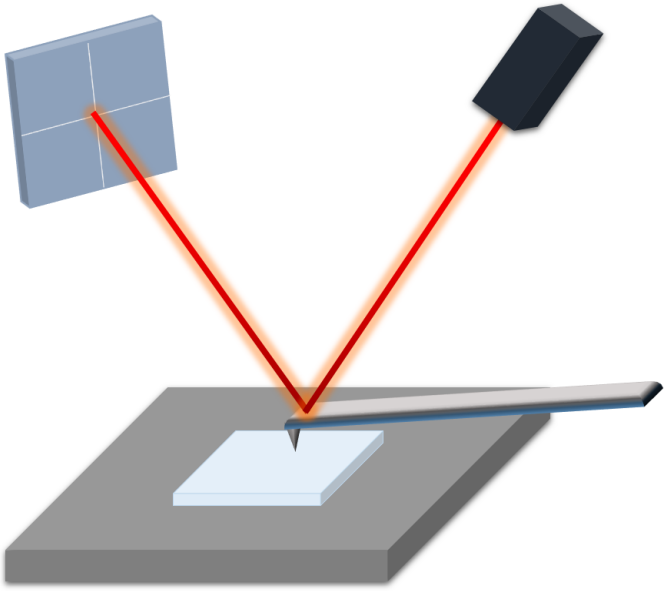

Figure 2.18: Schematic of AFM. The laser path goes from the laser source to the photodiode via reflection on the cantilever. The cantilever is attached to the tip, which interacts with the sample.

Tapping mode is a good alternative, combining features from both contact and noncontact modes. In this mode, the cantilever is oscillated at or near its resonant frequency, and the phase shift between the driving oscillation and the feedback is measured. This mode is suited to most biological samples, as it can provide high resolution images of soft samples which may be damaged easily. Figure 2.19a shows the force response curve of the tip. When close to the surface repulsive forces are dominant; moving further from the surface attractive forces are dominant, until the tip is far enough away that any forces from the surface are negligible [210]. The domains for contact, noncontact, and tapping mode can be mapped onto this graph, and are shown in Figure 2.19b.

Artefacts are features that appear in images but which are not naturally present. They occur as a result of the imaging procedure. Some of the main sources of artefacts when using AFM are the quality of the tip used, vibrations during imaging, and issues arising from image processing. This underlines the importance of ensuring that the tip is undamaged, ensuring that there are as few environmental vibrations as possible (e.g. by mounting the stage on a bed of gas, etc.).

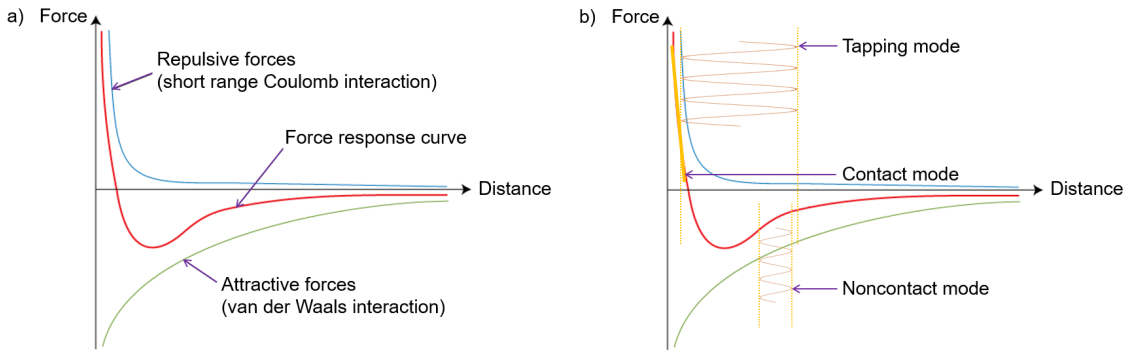

Figure 2.19: Force–distance graph for tip–sample interactions during AFM. (a) Plot shows the force response curve resulting from the repulsive and attractive forces felt by the tip. (b) The domains for contact, noncontact, and tapping mode are overlaid onto this plot. Image adapted from [211].

AFM has been used in this thesis to obtain statistics related to nanosheet lateral size and layer number. The nanosheet layer number can be obtained from the measured AFM thicknesses using established metrics based on step height analysis [151, 205, 206, 212]. It is well established that direct conversion of AFM-measured height to layer number is complicated by adsorbed surfactant or solvent on nanosheets and substrate. Step height analysis accounts for this by considering the heights of several nanosheets simultaneously. By plotting each nanosheet height in ascending order, a series of steps appear in the data; the first step in the data gives the thickness of the monolayer.

2.3.5 Characterisation techniques for Chapters 3–5

This section contains experimental details of the characterisation techniques used for the work presented in Chapters 3–5.

2.3.5.1 Characterisation techniques for Chapter 3

Optical microscopy

Optical microscopy was performed using an Olympus BX53M microscope with a 5× magnification in bright-field mode. The optical micrographs were pre-processed to crop the image down to the area of the cover slip only.

Optical images of the samples were required for calculation of surface coverage. Images were taken of large sample areas (at least half of each 18 mm × 18 mm sample) to allow a more accurate approximation of the film distribution over the whole sample.

Binary threshold method to determine film surface coverage

A simple, two-step post-processing method was used to determine the film surface coverage from the optical micrographs. Firstly, the open-source ImageJ software [213] was used to run a binary threshold on the micrographs to separate the nanomaterial film from the substrate (a small section of a typical optical micrograph and its corresponding threshold is shown in Figure 2.20 as an example). Secondly, a custom Python script was written to automate the calculation for determining the fraction of nanomaterial present.

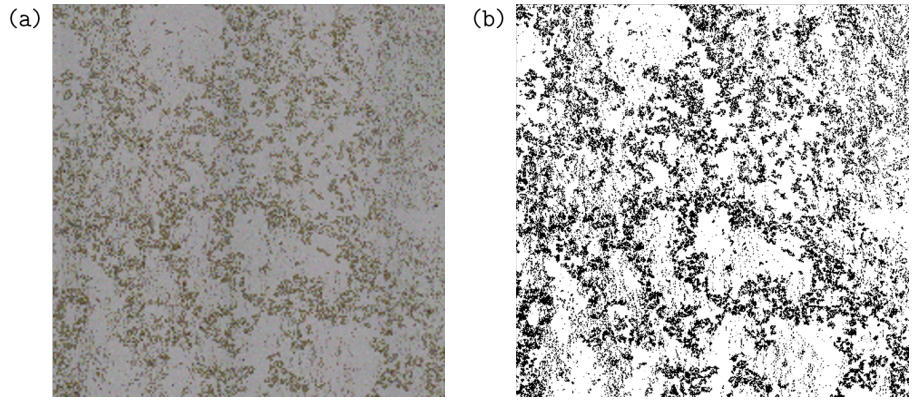

Figure 2.20: (a) Optical micrograph. (b) Binary threshold of the optical micrograph.

UV–visible spectroscopy

UV–visible spectroscopy measurements were performed using a Shimadzu UV-3600 Plus spectrophotometer. Liquid characterisation was performed using quartz cuvettes (Starna Scientific); solid characterisation was performed using a microscope slide holder.

Atomic force microscopy

AFM measurements were performed using a Bruker Dimension Icon AFM system in PeakForce QNM® mode. AFM was performed on sparse Langmuir films of each material to obtain statistics on flake length, width, and layer number using NanoScope Analysis software. This allows flake area to be calculated. At least 100 flakes of each material were used to obtain reliable statistics.

2.3.5.2 Characterisation techniques for Chapter 4

Atomic force microscopy

AFM measurements were performed using a Bruker Dimension Icon AFM system in PeakForce QNM® mode. AFM was performed on sparse Langmuir films to obtain statistics on flake length, width, and layer number using NanoScope Analysis software.

Optical microscopy

Optical microscopy was performed using an Olympus BX53M microscope with a range of objectives (5×–100×) in both bright-field and DIC modes.

Raman spectroscopy

Raman spectra were taken using an upright Renishaw InVia confocal Raman microscope. A 660 nm laser was used for resonant measurements of MoS_2. Volumetric maps were taken using resonant laser (660 nm) and 100× objective and a grating of 1800 l mm^{-1}. The maximum depth uncertainty is ~3 µm, but using small step sizes and overlapped data provides a much greater accuracy (closer to 1 µm). The step size and area were varied depending on the sample size (step size ranged from 0.1 to 0.5 µm). Very low power (0.001 mW) and short exposure times (< 0.5 s) were used.

2.3.5.3 Characterisation techniques for Chapter 5

Optical microscopy

Optical microscopy was performed using an Olympus BX53M microscope with a range of objectives (5×–100×) in both bright-field and dark-field modes.

Raman spectroscopy

Raman spectra were taken using an upright Renishaw InVia confocal Raman microscope. A 532 nm laser was used with a grating of 2400 l mm^{-1}. A power of 5 mW was used for exposure times of 10 s.

2.3.6 Cell experiments for Chapters 3–5

This section contains experimental details of the cell experiments conducted for the work presented in Chapters 3–5.

2.3.6.1 Cell experiment for Chapter 3

The cell line used for the cell study was U87 glioblastoma from the American Type Culture Collection. The study ran for 14 days, with observations made at day 3 and day 13, and images taken at day 4 and day 12 using an EVOS FLC imaging system (Life Technologies) at 20× magnification.

2.3.6.2 Cell experiments for Chapter 4

The cell lines used for the cell studies were U2OS (obtained from the American Type Culture Collection) and 1BR primary fibroblasts (obtained from the Genome Damage and Stability Centre Research Tissue Bank, University of Sussex). Cell lines were grown on MoS_2 thin films (deposited onto pristine glass cover slips as described in 2.2.4.2), and grown on pristine glass cover slips used for the control. The 1BR primary fibroblasts were seeded with 0.4×10^3 #/mL and the U2OS with 0.6×10^4 #/mL cell seeding density. Cells were fixed on cover slips using 3% paraformaldyhyde and 2% sucrose PBS, for 10 minutes at room temperature. Samples

were washed with DI water before imaging. Study lengths ranged from 3 to 14 days. Cells were grown in DMEM and MEM, respectively, supplemented with 15% FCS, L-glutamine, and pen–strep at 370 °C and 5% CO_2. Cell counting was performed using hemocytometry after tryspinisation using trypsin EDTA (0.25%). For the nystatin studies, cells were grown with a 20% nystatin solution in the complete media. Error bars in cell counts are calculated as the standard error in the mean of three repeated experiments (one experiment has two repeats per sample, four counts per sample) for the U2OS cells. Error bars for the fibroblasts come from experimental error in single experiment (two repeats per sample, four counts per sample).

In one experiment, U2OS cells were grown on MoS_2 substrates and pristine glass controls. Once the cells reached confluence after 7 days in culture, they were trypsinised, split, and reseeded with fresh media and onto fresh substrates at the initial (day 0) density to allow room for further proliferation on the new substrates. The new substrates used were either further fresh MoS_2 substrates or pristine glass controls. The cells were reseeded such that cells initially from MoS_2 substrates (M) were grown on further fresh MoS_2 substrates (MM) or glass controls (MC), and cells from control substrates (C) were seeded onto MoS_2 substrates (CM) or further control substrates (CC). Error bars are calculated from standard error in the mean from two repeat experiments (two samples per type in each experiment).

2.3.6.3 Cell experiments for Chapter 5

The cell lines used for the cell studies were U2OS (obtained from the American Type Culture Collection) and 1BR primary fibroblasts (obtained from the Genome Damage and Stability Centre Research Tissue Bank, University of Sussex). Cell lines were grown on WS_2 and $MoSe_2$ thin films (deposited onto pristine glass cover slips as described in 2.2.4.3), and grown on pristine glass cover slips used for the control. The 1BR primary fibroblasts were seeded with 0.4×10^3 #/mL and the U2OS with 0.6×10^4 #/mL cell seeding density. Cells were fixed on cover slips using 3% paraformaldyhyde and 2% sucrose PBS, for 10 minutes at room temperature.

Cells were grown in DMEM and MEM, respectively, supplemented with 15% FCS, L-glutamine, and pen–strep at 370 °C and 5% CO_2. The study ran for 7 days on the original substrates. At this point, cell counting was performed using hemocytometry after trypsinisation using trypsin EDTA (0.25%). The trypsinised cells from control, WS_2, and $MoSe_2$ substrates were all reseeded onto pristine glass cover slips for a further 2 days before fixation. Samples were washed with DI water before imaging.

2.4 Applications of low-dimensional nanomaterials in diagnostics, therapeutics and theranostics in life sciences

The rise of nanobiotechnology research has led to new nano–bio interfaces aiming to achieve controlled manipulation of cellular functions and features. Herein, recent developments in the use of a range of nanomaterials (e.g. carbon-based materials, transition metal dichalcogenides, layered metal hydroxides, etc.) for diagnostic, therapeutic and theranostic applications is reported. Imaging is the area of diagnostics considered, encompassing fluorescence imaging, live cell imaging, and biosensing. Photothermal therapy, drug delivery, and stem cell control are the discussed therapeutic applications. Toxicity studies for various materials are also included. Finally, theranostic applications are considered. The recent COVID-19 pandemic has exposed the necessity of innovation in many of these areas, particularly for improved biosensing systems. The vast array of well characterised nanoparticles now available offers a promising route to develop many of these technologies, with optionality through control of chemistry, structure and optoelectronic properties.

2.4.1 Introduction

Nanobiotechnology is a rapidly developing field of research. The use of nanomaterials in cellular biology is enabling growth of new imaging techniques, drug delivery and therapies. In particular, the more recent acceleration of research into nanomaterials provides a new opportunity to develop nano–bio interfaces that have not been possible previously. Cells and their organelles, transport vesicles, etc. operate on the nanoscale, so interdisciplinary research provides a new way to address these nanoscale features and functions in a controlled way.

Exhibiting properties vastly different to those of bulk material, nanomaterials have become a promising new tool in this field. Their small size allows for nanomaterials to be internalised by the body's own mechanisms, while researchers' high degree of control over shape and functionalisation gives the ability to target these materials to particular areas of the body.

There remains debate over the role of material morphology and the chemistry of the material. While a resolution to this question is not yet apparent, simplifying the parameter space can help address this problem. The use of synthetic analogues is one way to achieve this, as is to focus on lower-dimensional cases as a starting point.

While recent decades have seen the isolation of myriad new two-dimensional (2D) materials with wide-ranging properties and possibilities, carbon remains an obvious first choice for research into diagnostics and therapeutics as it provides a starting point for biocompatibility in carbon-based life.

At the nanoscale, therefore, carbon provides a plethora of potentially useful properties. The strength and chemical stability of carbon nanomaterials lends them well to production of tissue scaffolds and implant production, while the easy manipulation of the material is a recurring theme for intercellular processes such as fluorescent tagging, drug delivery, and photothermal therapy. Carbon-based materials considered in this section include graphene, graphene oxide (GO), and

reduced graphene oxide (rGO); carbon and graphene nanodots and quantum dots (QDs); carbon black; nanodiamonds; carbon nanotubes (CNTs), carbon nanofibers; carbon fullerenes; and other more exotic carbon nanomaterials.

Although carbon-based materials are clearly well researched for biological applications, other low-dimensional materials also receive increasing attention in this sphere. In particular, nanohybrids or nanocomposites combining materials seem to be a popular choice to enable precise control over chemical properties, and hence over nano–bio interactions. Other materials included in this review are transition metal dichalcogenides (TMDs); gold nanoparticles (AuNPs); silica NPs; hexagonal boron nitride (BN); copper nanoclusters; metal oxide NPs; layered zinc hydroxide; TiO_2; metallofullerenes; metallo-QDs; among others.

There are good and bad aspects to each of these materials. Some common aspects are discussed by Anık, Timur, and Dursun [214] and have been summarised in Table 2.1.

Table 2.1: Pros and cons for a range of materials commonly researched for nanobiotechnological applications.

Material	**Pros**	**Cons**
2D graphene-based nanomaterials (inc. GO, rGO)	• Enters the cell membrane easily • Can merge with DNA and protect it from enzymatic degradation • Can be utilised as nanocarriers in *in vivo* structures • Higher drug loading because of their large surface areas	• Aggregation of graphene-based nanomaterials in lungs and liver • Cause oxidative stress • Damage to cell membranes • Bonding or adhesion with cell receptors can activate stress and apoptotic mechanisms • Toxicity depends on time, concentration, aspect, and surface chemistry
Carbon nanotubes (CNTs)	• Functionalised, water-soluble CNTs can enter into cells easily (depending on size and surface chemistry) • Drugs can be loaded within CNTs' hollow inner channel, or on the wall surface with the help of hydrophobic interaction	• Some MWCNTs and SWCNTs can accumulate in the lungs causing pulmonary toxicity and inflammation (based on CNT size and uniformity) • Large MWCNTs, and SWCNTs injected intraperitoneally, can cause inflammation and granuloma formation • Raw CNTs show worse *in vivo* toxicity than functionalised CNTs

Table 2.1: Pros and cons for a range of materials commonly researched for nanobiotechnological applications (continued).

Material	**Pros**	**Cons**
Fullerenes	• Fullerene C_{60} has a spherical structure and is apolar, allowing it to pass the cell membranes • Can easily be modified • Convenient structure leads to use as drug delivery vehicles and sometimes as nano drugs	• Fullerene exposition resulted in lipid peroxidation and glucose depletion in the brain • Fullerenes that reach the brain through circulation or axonal translocation dissolve into the lipid-rich brain tissue, and because of their direct redox activity, brain damage might occur
Quantum dots (QDs)	• Fluorescent properties in broad-spectrum • High quantum yield • Low photobleaching • Can be used in photodynamic therapy, *in vivo* imaging, and drug biodistribution	• Based on the usage of heavy metals in their composition, and also their discharge from the body, *in vitro* studies have shown that QDs may be toxic • Degree of toxicity sometimes depends on the surface coating • Plain QDs can be cytotoxic by induction of reactive oxygen species which leads to damage to plasma membranes, mitochondria, and nucleus
Gold nanoparticles (AuNPs)	• Biocompatible nature • Controllable size distribution • Possible to vary NP shape • Easily conjugated • Ease of preparation	• The stabiliser CTAB which has been used in the production of gold nanorods causes considerable cytotoxicity • Conformational change in protein structure, e.g. serum albumin, has also been reported upon exposure of the protein to AuNPs • Surface interaction of proteins at the nanoscale affects protein fibrillation, which could lead to neurodegenerative diseases such as Parkinson's and Alzheimer's
Iron oxide nanoparticles (IONPs)	• Less cytotoxic • Magnetic properties • Controlled size and surface modification	• Superparamagnetic IONPs tend to accumulate in the liver without showing any significant biological degradation

This review will consider three overarching themes: diagnostic (with a particular focus on imaging), therapeutic, and theranostic applications of low-dimensional materials. Within these themes, narrower topics will be considered. Discussion of

imaging applications includes fluorescence imaging, live cell imaging, and cell sensing, while discussion of therapeutic applications will include photothermal therapy, drug delivery, stem cell control, and toxicity studies.

2.4.2 Imaging

The ability to diagnose illnesses quickly, correctly, and efficiently is an important first step to combating diseases. Without an accurate understanding of the disease in question, treatment may be ineffective, or worse, actively detrimental to the patient. However, diagnosis is important not only at the macro scale, but also at the cellular level. Some of the most promising nanoscale approaches to this small-scale diagnosis include fluorescence probes, live cell imaging, and cell sensing. Other imaging techniques are also being investigated. In particular, non-fluorescence Raman imaging could provide a new avenue of exploration, as a non-invasive technique that has the potential to be used with live cells [215, 216]. However, studies dedicated to these other techniques are still relatively few in number, so the focus of the following sections will be on the three methods mentioned above.

2.4.2.1 Fluorescence imaging

Fluorescence imaging allows for certain molecular processes or structures to be observed. This is achieved by utilising fluorescent probes that are able to target specific locations within the cell. Targeting is traditionally best achieved with carbon materials that are easily functionalised to attach to particular probes, often fluorescent dyes or proteins, however these carbon materials are not innately fluorescent. Advances in recent years have given rise to studies using different targeting materials that are inherently fluorescent and so do not necessarily require functionalisation with a separate fluorescent probe.

Of particular interest in this area are nanodots. Carbon nanodots, or carbon QDs, have properties that make them well suited for use as fluorescence probes. Not only does their small size (< 10 nm) and low cytotoxicity make them an obvious choice

for such biological applications, carbon nanodots also show low or no photobleaching, a common problem associated with the fluorescent dyes and proteins which have been in use for some time [217].

There is a good range of analyte specification across the various available NPs in serum and blood, but for cell imaging the fluorescent NPs are mostly limited to the cytoplasm, indicating that work on improving localisation and perhaps adding targeting functional groups would develop these materials further.

Although carbon or graphene nanodots in various forms constitute a large proportion of the materials included, others are also referenced. Research is grouped by material in Table A.1, beginning with carbon and graphene nanodots/QDs before moving on to various other materials investigated for use in fluorescence imaging. Where known, the table gives the proposed material, probe (if different to material), specific target, and cell lines and/or animal models tested.

2.4.2.2 Live cell imaging

Live cell imaging expands further on fluorescence imaging by tracking molecular processes or structures in real time. This is predominantly mediated through fluorescence imaging, and so similar fluorescent nanoparticles are used for this specific case in addition to the more general case discussed in 2.4.2.1. However, some other detection methods have been considered, including photoluminescence, stimulated emission depletion (STED) nanoscopy, and amperometric experiments (these are all included in Table A.2).

Perhaps unsurprisingly given the strong link between fluorescence imaging and live cell imaging, carbon nanodots and QDs are also popularly investigated for this application. These are discussed by Kim et al. [218] in addition to a host of other graphene or graphene-based nanomaterials used for live cell biosensing platforms.

Again, we see that the current targets are somewhat limited in this field. Only ions are so far reported, with no organelle staining for example, so there is scope to further improve the localisation and specificity of these NPs. Interestingly, a combination of imaging techniques may be relevant here; combining Raman with fluorescence could improve live cell imaging.

As in 2.4.2.1, although carbon or graphene nanodots in various forms constitute a large proportion of the materials included in Table A.2, other materials are also referenced. Research is grouped by material, beginning with carbon and graphene nanodots/QDs before moving on to other carbon and non-carbon nanomaterials and composites. Where known, the table includes the proposed material, probe (if different to material), detection method, specific target, and cell lines and/or animal models tested.

2.4.2.3 Biosensing

Biosensing refers to the detection of biomolecules using an analytical device (i.e., biosensor) that combines a biological component with a physicochemical detector [219, 220]. Conventionally, a biosensor consists of a bioreceptor (often a biological component such as cells, enzymes, antibodies, peptides, oligonucleotides, etc.) which interacts with the target and yields a physical or chemical change that is amplified into a readable signal with the help of a transducer (detector) component [221]. More recent developments have led to the aptasensor, a type of biosensor that uses DNA or RNA aptamers as the biological recognition element [222]. In aptasensors, the recognition reaction is independent of the transducer used [222].

The past ~15–20 years have seen a rapid increase in the influence of nanomaterials on biosensor development [223]. Moreover, the COVID-19 pandemic (currently ongoing) has emphasised the need for "easy-to-use, quick, cheap, sensitive and selective detection of virus pathogens" [224]. Comprehensive reviews focusing on biosensors for COVID-19 detection can be found at [225, 226].

Graphene is commonly investigated for biosensors and aptasensors, helped by the fact that it is abundant, chemically stable, and conductive [224]. Vermisoglou et al. summarise state-of-the-art graphene-based sensing systems for a variety of viruses [224]. However, the biosensing field is broadly open for a huge variety of NPs. The range of possible analytes is enormous, and with such a wide palette of nanomaterials to choose from, it should be possible to select for end application. There is likely to be huge growth in the area of nanomaterial biosensors over the coming years as affinities and targets are identified for the various NPs and the technology to incorporate them into sensing platforms becomes more standardised.

Research reviewed here is grouped by material in Table A.3, beginning with graphene-based systems, then covering other carbon-based systems and systems based on other materials. The proposed material, probe (if different to material), detection method, target, and cell lines and/or animal models tested are listed in the table.

2.4.3 Therapeutics

Once disease has been successfully diagnosed, the aim is to treat it as efficiently as possible. Without effective therapy, a diagnosis is useful only to curb curiosity. Some of the most cutting edge nanoscale approaches include photothermal therapy, drug delivery, and stem cell control. In addition, nanomaterials are not native to the human body, so a wide range of toxicity studies have been conducted on various materials considered for these and other treatments. These areas of research are discussed further in this review.

2.4.3.1 Photothermal therapy

One of the most developed technologies discussed in this review, photothermal therapy (PTT) is a minimally invasive technique which uses laser light to heat contrast agents or nanomaterials presented to the tissue. This causes thermal damage in this region.

Lower laser wavelengths are desirable for PTT, as they are less energetic and so are less likely to cause damage to surrounding healthy tissues. Recent developments focus on nanomaterials tailored to target specific tissues.

Nanostructures based on gold are heavily researched due to its good biocompatibility and localised plasmon surface resonance (meaning that AuNPs can absorb light at specific wavelengths) [227]. In fact, AuNPs are used in clinical settings already. Gold-based therapies feature several times in Table A.4, and the use of AuNPs for photothermal cancer therapies is reviewed by Vines et al. in [227]. However, many of the new layered and carbon-based NPs are also being investigated as the use of infrared excitation is appealing in biological applications.

Research is grouped by material in Table A.4, beginning with carbon-based materials before moving on to other materials investigated for use in PTT. The table gives the proposed material, probe (if different to material), irradiation method, specific target, and cell lines and/or animal models tested.

2.4.3.2 Drug delivery

Drug delivery is a broad term that encompasses several aspects important for the therapeutic delivery of drugs, including development of new materials or carrier systems, research into the administration route to the disease, etc. [228]. In 2004, nanomedicine was defined by the European Science Foundation (ESF) [229] as

> The science and technology of diagnosing, treating and preventing disease and traumatic injury, of relieving pain, and of preserving and improving human health, using molecular tools and molecular knowledge of the human body.

'Novel therapeutics and drug delivery systems' was chosen by the ESF as one of five key areas of focus [229]. Drug delivery systems could offer site-specific, time-controlled, noninvasive delivery of different molecular weight drugs and other bioactive molecules for the treatment of medical infections and diseases [230].

Drug delivery is perhaps the area which is most suited to the new nanomaterials available. The vast array of chemistries and morphologies now available in NPs should make drug attachment and targeting more specific, providing a whole host of new vector systems. Research is ongoing to identify the suitable NP–drug partnerships to optimise these systems. Perhaps unsurprisingly given the emphasis placed on developing new drug delivery systems, there are several reviews concerning suitability of a range of materials for this purpose. Plachá and Jampilek [231] review graphene-based nanomaterial drug delivery systems research in 2017–2019; Guo et al. [232] review research into *in vitro* and *in vivo* CNTs-based drug delivery to cancer and the brain (as of 2017); and Wang et al. [233] provide a review of nanocarriers based on 2D materials beyond graphene, such as TMDs, MXenes, BN and others (as of 2019).

The materials included in Table A.5 are mostly carbon-based, with several small 0D materials such as carbon dots, nanodiamonds, and C_{60} fullerenes, possibly because these smaller particles can follow internalisation pathways more easily or be used as cages. Research is grouped by material in Table A.5, beginning with carbon-based materials before moving on to various other materials proposed. Where known, the table gives the proposed material, probe (if different to material), drug, specific target, and cell lines and/or animal models tested.

2.4.3.3 Stem cell control

In this review, stem cell control is used as a term to describe the effect of various materials on stem cell behaviour (e.g. differentiation, proliferation, etc.). Stem cells exist at the origin of a cell lineage, can differentiate into various types of cells, and proliferate indefinitely to produce more of the same stem cell [234]. The ability to stimulate stem cell differentiation is a topic of interest, because this control could allow for better medical implant biocompatibility, improved wound healing, and tailored tissue engineering scaffolds, among other possible applications for a range of diseases.

Stem cell control is one of the newest research areas. Since our understanding of how much cell function is dependent upon nanoscale cues has increased, the possibility to use nanomaterials to manipulate and stimulate at the nanoscale has become apparent. Stem cell fate is however a hugely complex process and isolation of individual components or response is difficult. Akin to drugs requiring delivery to specific areas in the body, discussed in 2.4.3.2, often various molecules (e.g. proteins) need to be transported to the stem cells to induce specific behaviours. GO has been investigated for various stem cell control studies because it can be easily functionalised with such molecules. Various metals have also been researched, possibly due to their common use in medical implants; as mentioned above, better stem cell control could lead to medical implants that adapt to the body more quickly and that take longer to be rejected by the body. Research is grouped by material in Table A.6, beginning with graphene and GO materials before moving on to other carbon-based materials and then metal nanomaterials. In general, complexes involving GO seem to result in enhanced stem cell differentiation and proliferation, those involving nanodiamonds seem to show improved stem cell adhesion, and Ti surfaces with a rougher topography seem to improve stem cell differentiation and proliferation. Key conclusions for each paper are included in the table, along with the proposed material, probe (if different to material), and cell lines and/or animal models tested.

2.4.3.4 Toxicity studies

For any of the applications discussed throughout this review to be put into practice, it is vital that the proposed materials themselves, alone or in composites, are not toxic to humans. Toxicity studies aim to address this by systematically testing different materials with standard tests (e.g. cytotoxicity, effect of dosage or repeat dosage, duration of treatment, etc.). Testing can be categorised into three main sections [235]:

- acute toxicity studies (adverse effects occurring within a short time, up to 14 days, after administration of a single dose or after multiple doses administered in a short time period [236]);
- sub-acute toxicity studies (adverse effects occurring after administration for 14–28 days of a single dose or after multiple doses administered in a short time period [237]); and
- chronic toxicity studies (adverse effects occurring after repeated or continuous long-term exposure [238]).

However, as new materials begin to be used in biological applications, their toxicity is also becoming assessed. It is clear that much more plays into toxicity than just the chemistry of the material, with size and shape also a key factor. This makes understanding of NP toxicity particularly challenging, as a blanket recommendation for a material will not catch such nuances. As shown in Tables A.1–A.6, carbon-based nanomaterials are commonly explored for new nanodiagnostics and nanotherapies. As such, the toxicity of these materials is particularly important to study, and carbon-based nanomaterials feature heavily in Table A.7. Research is grouped by material in Table A.7, beginning with carbon-based materials before moving on to various other materials proposed. Where known, the table gives the proposed material, tests, cell lines and/or animal models tested, and key conclusions for each paper.

2.4.4 Theranostics

Theranostics, a term coined by combining the words therapeutics and diagnostics, is exactly that — NPs or nanocomposites that provide simultaneous diagnostic and therapeutic effects [239]. Materials capable of theranostic applications could be the key to unlock the door to exciting new avenues of research into areas such

as personalised medicine. This combination therapy could improve early disease detection and optimise treatment for individuals [240]. Other benefits could include enhanced drug efficiency, better disease management, and improved healthcare [240].

That theranostics is a subject of burgeoning interest is therefore unsurprising, and this is highlighted by the range of reviews on different aspects of theranostics. Panwar et al. [241] review a range of nanocarbons for theranostic applications including sensing, imaging, and drug delivery, and also provide an outlook on current challenges (as of 2019). Also considering carbon materials, Hassan et al. [242] review specifically carbon QDs for photomediated theranostics, with emphasis on the importance of the integration of light with nanotechnology (as of 2017). Hu et al. [243] discuss QDs, NPs, and 2D materials decorated with various biomolecules for targeted diagnosis and treatment (as of 2020). Gong et al. [244] provide a review of photothermal combination cancer therapy based on 2D TMDs, and consider future prospects and challenges of using 2D TMD-based nanomaterials for theranostics (as of 2017). Yang et al. [245], Raja et al. [246], and Mohammandpour and Majidzadeh-A [247] all present reviews on 2D nanomaterials for cancer theranostics.

The present work also considers a range of materials, mostly carbon- and metal-based. Research is grouped by material in Table A.8, beginning with carbon-based materials before moving on to various other materials. The proposed material, probe (if different to material), detection method, therapy, specific target, and cell lines and/or animal models tested are given in the table.

2.4.5 Conclusions

While some technologies are already well developed, such as fluorescence imaging and PTT, there remains more scope for development in areas such as biosensing and drug delivery. This has been shown especially by the push for improved sensing systems spurred by the COVID-19 pandemic. Carbon-based nanomaterials still

hold much promise in all these areas, and are shown here to be the focus of much research. However, the new layered NPs are beginning to shine through, especially for biosensing and imaging applications with their tuneable optoelectronic properties.

Chapter 3

Langmuir films of layered nanomaterials: edge interactions and cell culture applications

The application of nanomaterials in technology is limited by challenges in their processing into macroscopic structures with reliable and scaleable methods. Herein, it is demonstrated that using scaleable fabrication methods such as liquid-phase exfoliation by sonication (LPE) it is possible to produce dispersions of a wide variety of layered nanomaterials with controllable and standardised size and thickness scaling. These can be used as-produced for Langmuir deposition, to create single layer films with tuneable density, including the first demonstration of hexagonal boron nitride (BN). Of particular importance, we show that the difference in edge chemistry of these materials dictates the film formation process, and therefore can be used to provide a generic fabrication methodology that is demonstrated for various layered nanomaterials, including graphene, BN and transition metal dichalcogenides (TMDs). We show that this leads to controllable cancer cell growth on graphene substrates with different edge densities but comparable surface coverage, which can be produced

on a statistically relevant cell study amount. This opens up pathways for the generic fabrication of a range of layered nanomaterial films for various applications, towards a commercially viable film fabrication technology.

3.1 Introduction

LPE is a process which has been shown to be the most effective way to produce large-scale yields of various layered nanomaterials, making it the most practical production technique available [120, 248]. Layered nanomaterials incorporate a range of two-dimensional (2D) materials with a variety of different properties associated with them. Graphene is possibly the most well known of these, having received much attention both in the academic sphere and also in public discourse. Since it was first isolated [6], its interesting mechanical, electronic, optical and thermal properties have been studied extensively [25, 26, 249, 250]. Further research has looked into these properties in other layered nanomaterials such as TMDs [49, 251, 252], BN [112, 253], and other exotic layered crystals [254–256].

These new materials could lead to many innovations. 2D materials can be utilised for such wide-ranging applications as electronics and optoelectronics [117, 249, 252], biomarker detection [257, 258], and energy-related areas [259]. Liquid processing of 2D layered nanomaterials is necessary to obtain dispersions suitable for Langmuir deposition; this is a well known method of creating thin films, whereby a nanomaterial dispersion is spread on a liquid subphase [163, 260].

The thin films produced by this method are 2D, in the sense that they comprise a single layer of particles, i.e. they are only as thick as the thickness of the exfoliated layered nanomaterial used, and depending upon the parameters used varying from monolayer to multilayer. By use of a moveable barrier it is possible to vary the surface area of a Langmuir trough, and hence to compress a nanomaterial film. This technique gives simple control of film creation, with small quantities (mg m^{-2}) of material resulting in high material efficiency. This allows production of single layer particulate films with high surface coverages.

Control over thin film creation is therefore crucial as different applications may require different finely-tuned film properties [183]. Control over Langmuir film assembly would allow for generic scaleable procedures for a range of materials dependent upon application requirements. By providing a framework for normalising for material interactions, it is possible to understand film densities for different layered nanomaterials, including BN (the first time its Langmuir behaviour and deposition has been shown), graphene, MoS_2, and WS_2. This will be useful for various applications, including in biomaterials, where edge interactions play a critical role in cellular growth and adhesion as well as the optimisation of the nanomaterial surface for functionalisation or surface interaction [182]. Moreover, sample substrates for biological studies must be able to be produced repeatably to allow for statistically significant trials. We demonstrate that the growth of glioblastoma cancer cells is significantly modified by the presence of graphene edges by comparing growth on films made from two different size graphene nanosheets (larger sheets, L-gra, and smaller sheets, S-gra). This is critical not only for the understanding of cancer growth, but also for developing novel, stable, synthetic substrate systems for cellular studies.

The synthesis and processing of the materials used in this work is described in 2.2.4.1, the characterisation techniques used are described in 2.3.5.1, and details of the cell experiment are included in 2.3.6.1.

3.2 Substrate production

Dispersions of various nanomaterials were prepared in-house using LPE. These dispersions were used to perform Langmuir–Schaefer (L–S) deposition. Langmuir films are created by dropping nanomaterial dispersion onto a water subphase; as the solvent evaporates, a thin, monolayer film is left at the air–water interface. Schaefer deposition is the horizontal lowering of a substrate to transfer this film [261], as shown in Figure 3.1a.

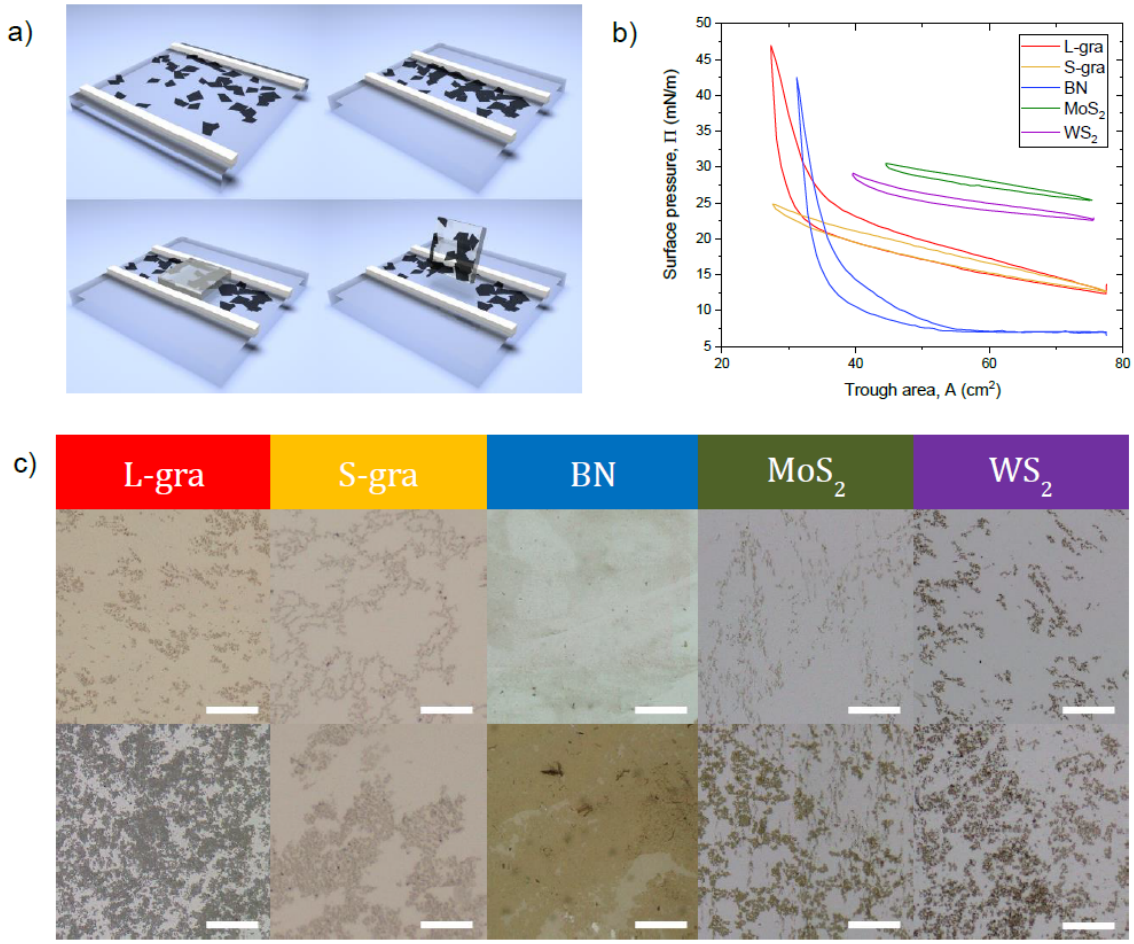

Figure 3.1: (a) Diagram showing the L–S deposition process. The deposited nanomaterial film is compressed with the trough barriers, then the substrate is brought into contact with the film before being lifted directly upwards (substrate parallel to air–water interface). (b) Representative pressure–area isotherms for each material used. (c) Optical micrographs for each material; the top row is of films deposited at a lower pressure (~10 mN/m), while the bottom row is of films deposited at a higher pressure (~25–30 mN/m). Images shown are small areas representative of the whole film. All scale bars = 100 µm.

There are a few main requirements for solvents used for the L–S process. These include that the solvent has a high vapour pressure, so that it evaporates and leaves a film of particulates at the interface [161]; that the solvent spreads on the water surface, to maximize the area over which nanoparticles are spread to minimize reaggregation during solvent evaporation [162]; and that ideally, the dispersion should be water-immiscible.

Cycloketones such as cyclopentanone and cyclohexanone have been shown to be good solvents that satisfy all of these criteria [162]. Additionally, they have been shown to be good solvents for the exfoliation of layered nanomaterials [144, 262]. This removes the need to exfoliate into a different solvent than that used for spreading, avoiding the extra step of redispersion of the material into a suitable spreading solvent. Moreover, redispersion is not always possible because generally good spreading solvents are not good for dispersion of 2D layered nanomaterials, even if transferred [162]. By making use of these solvents, it is possible to process the nanomaterials from powder to completed Langmuir film in a single solvent, greatly simplifying the procedure, and providing the opportunity for bulk processing.

Typical pressure–area isotherms for all material monolayers with aqueous subphases used are given in Figure 3.1b. These isotherms show the 'phase transitions' [165] of the monolayer film. At low pressure (the gas phase) the material is sparsely distributed in the trough, creating 'films' which appear to be mostly blank substrate with islands of monolayer material. As the pressure increases and flakes of the material come into contact with each other (the liquid phase), the films become denser. This is more apparent in the isotherms for BN and L-gra, where the pressure increases rapidly at smaller trough areas. The variance in behaviour for the different materials is discussed in more detail later. Once the nanomaterial film is at a given surface pressure, measured by use of a Wilhelmy plate, it is deposited onto a glass cover slip. Choosing a range of surface pressures allowed films to range from those which were visibly dense and homogeneous to those which were visibly sparse.

Optical micrographs of typical films for each material after deposition at high and low pressures are shown in Figure 3.1c. It is clear that L-gra and BN differ from the other materials, as they have denser films. Although small sample areas are shown in Figure 3.1c, large film areas (of at least half of each 18 mm $\times$ 18 mm sample) were measured and used for the analysis. A simple, two-step post-processing method was used to determine the film surface coverage from the optical micrographs (shown in Figure 2.20).

3.3 Nanosheet characterisation

The aim of this study is to develop a standardised method of creating films with known parameters using a scaleable, commercially viable approach. To this end, the dispersions used were created using standard processes. These dispersions were characterised and shown to demonstrate universal (and expected) size scaling [150].

UV–visible spectroscopy measurements were performed on all dispersions, and representative spectra shown in Figure 3.2a. Metrics that make use of the absorbance feature ratios associated with each different material have been described in detail by Backes et al., and indicate the presence of exfoliated nanosheets [151, 202, 205, 206]. This confirms the successful exfoliation to few-layer nanosheets. Lateral dimensions (length L, width W) of material nanosheets were measured by atomic force microscope

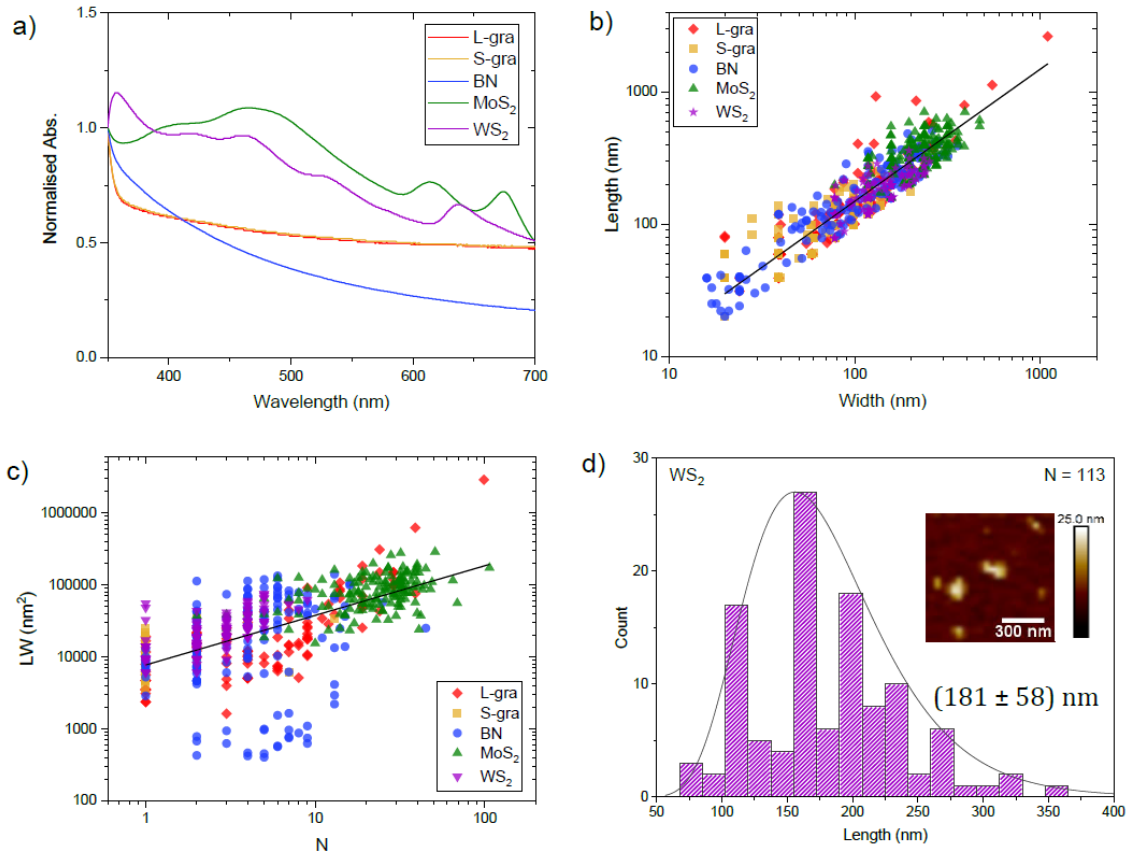

Figure 3.2: (a) UV–visible spectroscopy of nanomaterial dispersions used; absorbance normalised at 350 nm. (b) Nanosheet length vs width AFM statistics. (c) Sheet-wise LW (length × width) vs layer number AFM statistics. (d) Plotted histogram for WS_2 length data, used to determine an average value $\langle L \rangle = (181 \pm 58)$ nm. Inset shows AFM image of the material.

(AFM). Sheet thicknesses were measured from AFM profiles, and converted into layer number N using values for monolayer thicknesses from the literature for graphene [248], MoS_2 [205], WS_2 [151], and BN [206].

The L vs W scaling is given in Figure 3.2b and shows that while all nanosheets follow a power law scaling of the aspect ratio, length scales near linearly with width, i.e. constant aspect ratio. The fit in Figure 3.2b is provided as a guide to the eyes and demonstrates a common aspect ratio. Each material is additionally fitted individually, assuming a linear scaling, to obtain an aspect ratio for each material. Results for all cases are given in Table 3.1. As the plot is on a $\log_{10}$ scale, the aspect ratio is calculated by 10^c, where c is the intercept of the fit. These aspect ratios imply that the shape is independent of the material, and suggests we can approximate the sheets as rectangles.

Table 3.1: Fit results for L vs W plot for each material to obtain values of aspect ratio.

Material	**Intercept, c**	**Intercept std err, σ_c**	**Adj. R^2 values**	**Aspect ratio**
L-gra	0.173	0.014	0.79	1.49
S-gra	0.153	0.014	0.59	1.42
BN	0.184	0.010	0.88	1.53
MoS_2	0.204	0.010	0.16	1.60
WS_2	0.116	0.009	0.46	1.31

The product of length and width, LW, gives an approximation of nanosheet area. Plotting LW against N therefore shows how nanosheet area varies with number of layers. For liquid-exfoliated materials, the lateral size decreases as the thickness decreases; this is due to an increased sonication time leading to the creation of new edges [263, 264]. Figure 3.2c shows that the materials used behave as expected. Moreover, all materials generally fall on a universal scaling, although BN shows some scatter. This is broadly consistent with other research into the effect of LPE on the size–thickness relationship [150]. The fit in Figure 3.2c, on all materials, is provided as a guide to the eyes. There are some small differences between materials; results of fitting each material independently are shown in Table 3.2.

Table 3.2: Fit results for LW vs N plot for each material.

	Material	**Intercept, c**	**Intercept std err, σ_c**	**Gradient, m**	**Gradient std err, σ_m**	**Adj. R^2 values**
Fitted independently	L-gra	3.577	0.062	0.958	0.072	0.65
	S-gra	4.030	0.043	0.301	0.163	0.06
	BN	3.882	0.121	0.424	0.172	0.03
	MoS_2	4.348	0.088	0.406	0.065	0.21
	WS_2	4.033	0.039	0.758	0.081	0.44
Fitted together	all	3.887	0.034	0.689	0.037	0.39

From Figures 3.2b and 3.2c it is ascertained that all materials have a lateral size of less than 1 µm, and are all less than 30 layers thick on average (spread between 1 and 100 layers). Plotting histograms for each sample allows average values to be obtained by analysis of the distributions. Figure 3.2d shows a representative histogram and inset micrograph; additional histograms are available in Appendix B. All histograms are broadly log-normal, as expected [265, 266]. The average values are consistent with the positions of clusters in the sheet-wise plots shown in Figures 3.2b and 3.2c and are shown in Table 3.3. The average length and average number of layers, as obtained from fitting the histograms in Appendix B (Figures B.1–B.5), are plotted for each material in Figure 3.3.

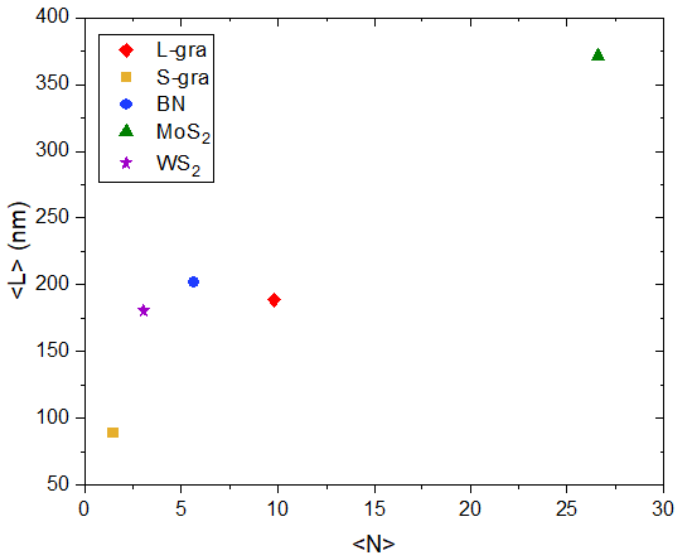

Figure 3.3: Average length plotted against average number of layers for each material.

Table 3.3: Average values for nanomaterial length, width, layer number, and approximate area, given with standard errors.

	$\langle L \rangle$ (nm)	$\sigma_{\langle L \rangle}$ (nm)	$\langle W \rangle$ (nm)	$\sigma_{\langle W \rangle}$ (nm)	$\langle N \rangle$	$\sigma_{\langle N \rangle}$	$\langle LW \rangle$ (nm^2)	$\sigma_{\langle LW \rangle}$ (nm^2)
L-gra	190	170	119	91	10	15	36000	89000
S-gra	89	49	63	36	2	1	7000	9000
BN	200	190	130	130	6	5	50000	160000
MoS_2	370	120	232	75	27	19	91000	56000
WS_2	181	58	139	47	3	2	27000	18000

3.4 Surface pressure–surface coverage relation

The surface pressure of a film can change either through addition of more nanomaterial or by decreasing the trough area. For all materials, and a range of deposition pressures, surface pressure (Π) was plotted against surface coverage (Φ). Intuitively, the relation can be fitted logarithmically, as $\Pi \propto \log \Phi$. This implies that the denser the film, the slower the rate of change of pressure with respect to the surface coverage. This is represented mathematically by $\frac{d\Pi}{d\Phi} \propto \frac{1}{\Phi}$; i.e., once a film becomes dense, ever-greater increases in pressure are required to produce any further increases in surface coverage. This fit is shown in Figure 3.4a, and R^2 values are included in Table 3.4. Figure 3.4a shows that the materials behave as expected for a Langmuir process and can still be fitted effectively, despite the system being noisy due to factors such as transfer efficiency causing a scatter in data.

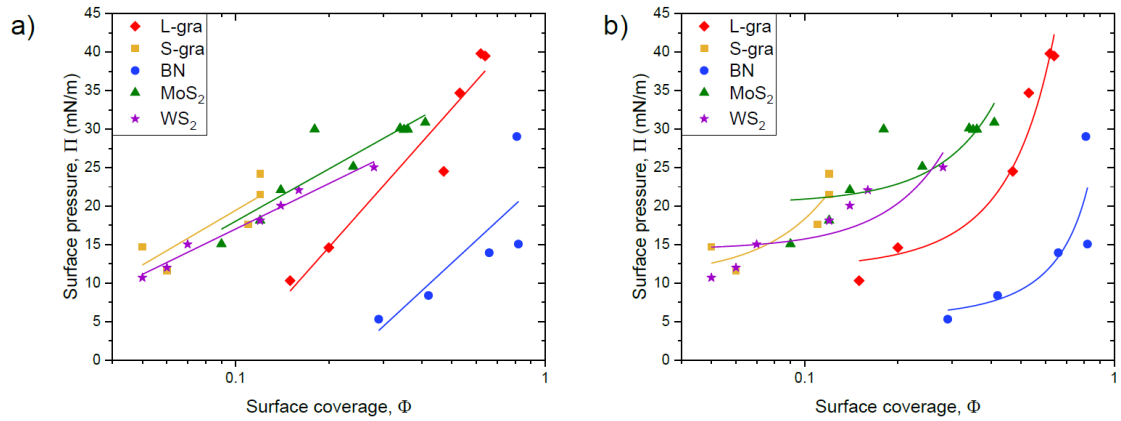

Figure 3.4: (a) Surface pressure versus surface coverage plot, fitted with a simple logarithm. (b) Surface pressure–surface coverage plot, fitted with Equation 3.1 [267].

Although this basic relation works well, Fainerman et al. [267] describe a thermodynamic model for the interpretation of pressure-area isotherms of material monolayers. This also accounts for the size difference between material monolayers and solvent molecules. Their equation is

$$\Pi = -\frac{kT}{\omega_0}\left[\ln\left(1-\frac{\omega}{A}\right)+\left(\frac{\omega}{A}\right)\right]-\Pi_{\text{coh}}, \tag{3.1}$$

where in the first term k is the Boltzmann constant, T is the temperature, ω_0 is the molecular area of a solvent molecule, ω is the molecular area of a nanoparticle, and A is the available surface area per nanoparticle.

The first term describes the increase in surface pressure with surface coverage due to entropy terms associated with subphase–nanosheet interactions. The offset term is the cohesion pressure, a term related to enthalpy, which describes long-range interactions between components [267]. In this study it is anticipated that these interactions will be dominated by attraction or repulsion between nanosheets when separated on the water surface, and based on the charge of edge states or van der Waals forces [268]. This information could suggest some phenomenon in the long-range interactions that is associated with the chemistry of materials used, leading to controlled film surface coverage.

The same surface pressure and surface coverage data are plotted in Figure 3.4b, but fitted with the model described in Equation 3.1. Although the model is designed for amphiphilic particles and only in the liquid expanded (low pressure) phase, the fit provides some insight for the layered nanomaterials and the intercept value at minimum pressure should hold true, with deviation expected for the higher pressure phases. The R^2 values are included in Table 3.4. As for the fitting in Figure 3.4a, although the fit is not ideal, presumably not capturing all of the complex edge interactions, it is an interesting start to capturing the dominant physics in what is a noisy and complex system that has not been previously described.

Table 3.4: R^2 values for simple logarithm and Equation 3.1 fitting of surface pressure vs surface coverage plots.

Material	**Adj. R^2 values**	
	Simple log	**Fainerman (Eq. 3.1)**
L-gra	0.90	0.94
S-gra	0.63	0.75
BN	0.18	0.55
MoS_2	0.80	0.56
WS_2	0.97	0.61

Values of Π_{coh} for each material are given in Table 3.5. Negative values of Π_{coh} indicate repulsive forces between the particles. This will be dominated by the edges rather than the surface, due to the unique geometry of the L–S process. Higher interparticle forces lead to greater stability of films on the surface, because this creates a higher surface tension and therefore the films remain assembled without reorganisation or loss to the other phases [268]. Higher interparticle forces also lead to higher 2D film moduli, but will reduce the spreading efficiency of the nanomaterial at low density, and hence the optimisation of the surface coverage efficiency [269].

It is seen from Table 3.5 that BN has the least negative cohesion force and hence forms a film with the least pressure. This might correlate with the micrographs in Figure 3.1c, which show the BN films as being the densest and most uniform. Interestingly, it is still a slightly repulsive interparticle force, counter to bulk dispersion of BN which is usually described as attractive compared to other layered nanomaterials (although $\Pi_{coh} = 0$ mN/m is within error) [270]. However, as the edge effects dominate, the ionic nature of the BN bond leads to charged edges and potential for functionalised edge sites leading to dominant repulsive edges [270, 271].

Table 3.5: Cohesion pressure values (Π_{coh}) and uncertainties ($\sigma_{\Pi_{coh}}$) for each material, as obtained from the fit in Figure 3.4b.

Material	$\mathbf{\Pi_{coh}}$ **(mN/m)**	$\boldsymbol{\sigma_{\Pi_{coh}}}$ **(mN/m)**
L-gra	-11.9	2.1
S-gra	-10.8	2.3
BN	-2.0	4.3
MoS_2	-20.3	2.1
WS_2	-14.3	1.6

For the exfoliation and size selection processes used in this experiment a broad range of size values were used, implying that pressure–area behaviour is not solely determined by either nanosheet size or material class. If only nanosheet size had any effect then Figures 3.4a, 3.4b would show L-gra, BN, and WS_2 grouped together, with MoS_2 to one side of this cluster, and S-gra to the other. If material class alone affected the pressure–area behaviour, then in Figures 3.4a, 3.4b clear distinctions between the graphene, TMD, and BN samples are expected. In practice, S-gra and the two TMD samples are clustered together, with L-gra and BN separated, and the idea that behaviour might rely on a combination of nanosheet size and material class seems logical. Different material classes have different edge functionalities, which will influence film formation in different ways; however, size differences within material classes result in differing numbers of edges per unit area, and hence varying edge–edge interactions. If edge interactions between nanosheets play a significant role, as expected for L–S films, then this emphasises the need to account for nanosheet size before comparing the pressure–surface coverage data of the different samples. This would allow a fair comparison of how the intrinsic chemistry affects the edge–edge interaction between nanosheets.

3.5 Surface coverage normalisation

As discussed previously, the influence of material edge interactions on the film surface pressure can be ascertained more easily by normalising the surface coverage, Φ, to nanosheet size, approximated by $\langle LW \rangle$. In particular, the need for a parameter that scales with the number of nanosheet edges per unit area is apparent. For this purpose, the centre-to-centre interparticle distance, s, is used. This is derived in Appendix C, and has the form

$$s = \sqrt{\frac{\langle LW \rangle}{\Phi}}. \tag{3.2}$$

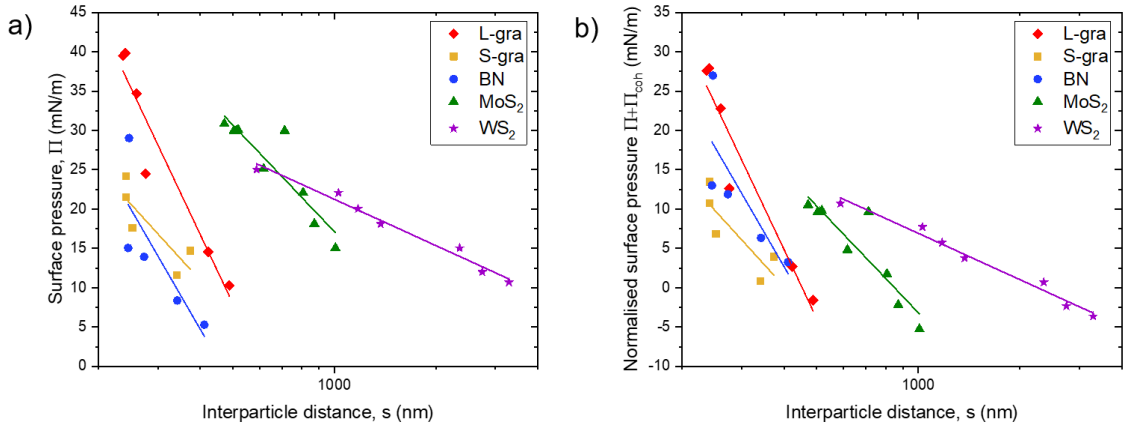

Figure 3.5: (a) Plot of surface pressure vs interparticle distance. (b) Plot of normalised surface pressure vs interparticle distance (y-axis normalised for cohesion pressure).

This new variable represents a normalisation of the surface coverage to account for the influence of the nanosheet size. Plotting surface pressure against this variable therefore represents a normalisation of the surface pressure–surface coverage plot. This is shown in Figure 3.5a, where it can be seen that this reduces the materials to two generic curves. BN shows the closest particle approach, and densest film, as expected due to the stronger cohesion forces between the BN particles (Table 3.5).

If one normalises for the cohesion pressure determined from the fitting in Figure 3.4b, then in principle the long range interaction differences between the different materials is removed. Indeed, it is seen in Figure 3.5b that the BN and graphene converge onto a single curve, but interestingly, the TMDs remain at a distance and with slightly lower slopes. The TMD films have the largest repulsion from the cohesion pressure (Table 3.5); this is expected because the sulfur-terminated edge sites are stable and so the charge distribution at the edge is uneven due the electronegativity difference between the sulfur and the metal [38, 272]. This leads to highly polarised edges and therefore strong dipole interactions [38, 272]. This effect is noted to be particularly strong for small particles as the edges become proportionally more dominant compared to the particle volume [273]. The WS_2 particles in this study are highly exfoliated and of small lateral dimensions, meaning they are likely to have a high degree of edge charge. This explains the strong repulsive cohesion pressure, but also the variation in the interparticle force compared to the other

materials as seen in Figure 3.5. In addition to the long-range edge interactions, the MoS_2 in this experiment is particularly large, and multi-layered, so it is likely that there are large enough capillary forces acting on these particles compared to the WS_2 particles to start to affect the interactions [268]. The TMD films remain at a further interparticle separation compared to the other layered nanomaterials, due to their more polarised edge states and the comparatively stable nature of the edges. In this way, the class of material can be used to separate out the expected behaviour for monolayer film formation.

In nanomaterial films, rigidity percolation is reached when the particles form a connected bridge from one side of the Langmuir trough barrier to the other. For particles with the least repulsive edge interactions (such as BN) this bridge can form quickly, without total surface coverage, as even small numbers of particles agglomerate together forming branched networks. Conversely, a repulsive film will need to reach almost complete surface coverage to reach rigidity percolation ($\Phi = 0.7$) [274]. This is because the particles will continually rearrange on the subphase surface to minimise their interaction, and therefore will spread out across the entire area until forced by density to form a rigid film. The 2D bulk modulus, β, is one way of quantifying this behaviour. This is described by

$$\beta = -A\left(\frac{\partial \Pi}{\partial A}\right)_T, \tag{3.3}$$

where A is the trough area, Π is the surface pressure, and T represents that the temperature is kept constant [274]. This is plotted for each material in Figure 3.6a. Although different materials clearly have different maximum bulk moduli, the rigidity onset occurs at varying surface pressures.

However, when normalised to the cohesion pressure, the 2D bulk modulus follows a similar onset and maximisation (Figure 3.6b). This fits well with the concept of rigidity percolation. As expected, the BN has the largest 2D bulk modulus as it has the strongest interparticle interactions and the densest films. The TMDs show very weak modulus behaviours, as the repulsive edge states allow for particle slippage in

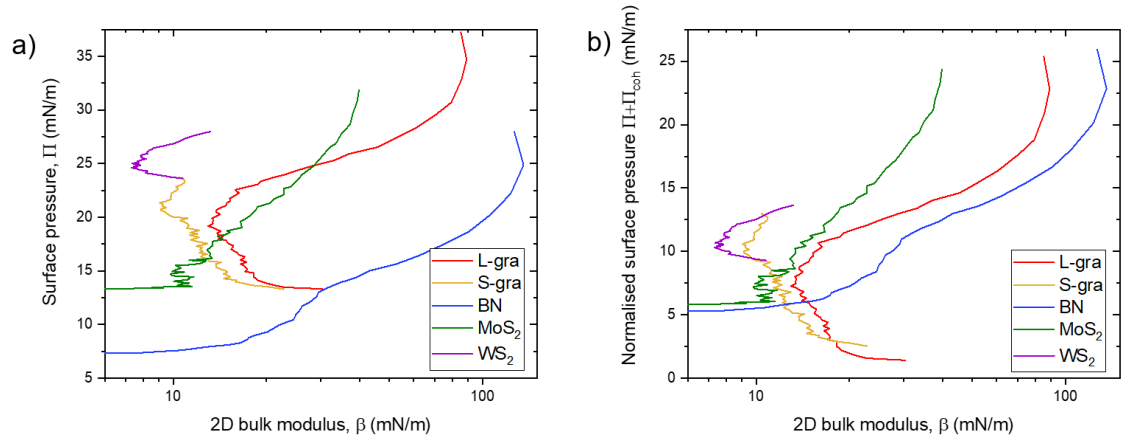

Figure 3.6: (a) Plot of surface pressure vs 2D bulk modulus. (b) Plot of normalised surface pressure vs 2D bulk modulus (y-axis normalised for cohesion pressure).

the film system, maintaining a 'liquid-like' state for far longer, until geometrically 'jammed'. Therefore, the larger MoS_2 particles are locked into place more rapidly than the smaller WS_2 particles, or even the exceptionally small S-gra flakes.

This confirms that it is possible to extract interesting information about edge interactions from the cohesion pressure Π_{coh} only. This is a useful value beyond just Langmuir, providing insight into films more generally, including hybrid films, printing, heterostructure stitching, etc [275, 276].

The process from Figure 3.2 to Figure 3.6 describes how variable pressure–surface coverage data can be normalised to nanosheet size to account for edge effects. This results in data clustered by material group that Equation 3.1 suggests is related to the area coverage when accounting for the area density of edges. Outstanding differences remaining in Figures 3.5 and 3.6 are due to the chemical nature of the edge functionalities and therefore merit study in further detail. Examining the edge chemistries in more detail should confirm the relative interaction strengths described above. However, even without knowing the detail of the chemistry it is possible to account for nanomaterial class and size across a broad range of materials to determine film density from standard dispersion properties.

3.6 Cell study

To demonstrate the importance of controlled film properties, a cell study comparing different edge densities was conducted. Two sets of films were produced from the same graphene dispersion size-selected to have larger and smaller sized nanosheets. As these films were deposited at similar surface coverages, the L-gra films had a lower area density of edges than the S-gra films.

It is observed that the edge density strongly determines the growth of glioblastoma cells (Figure 3.7). The films with greater edge density have greatly increased (~1.5 times greater) cell proliferation at 12 days compared to those with lower edge density, with increased cell cluster formation and improved cell spreading both at 4 and 12 days. This increased proliferation is likely due to the increased surface roughness

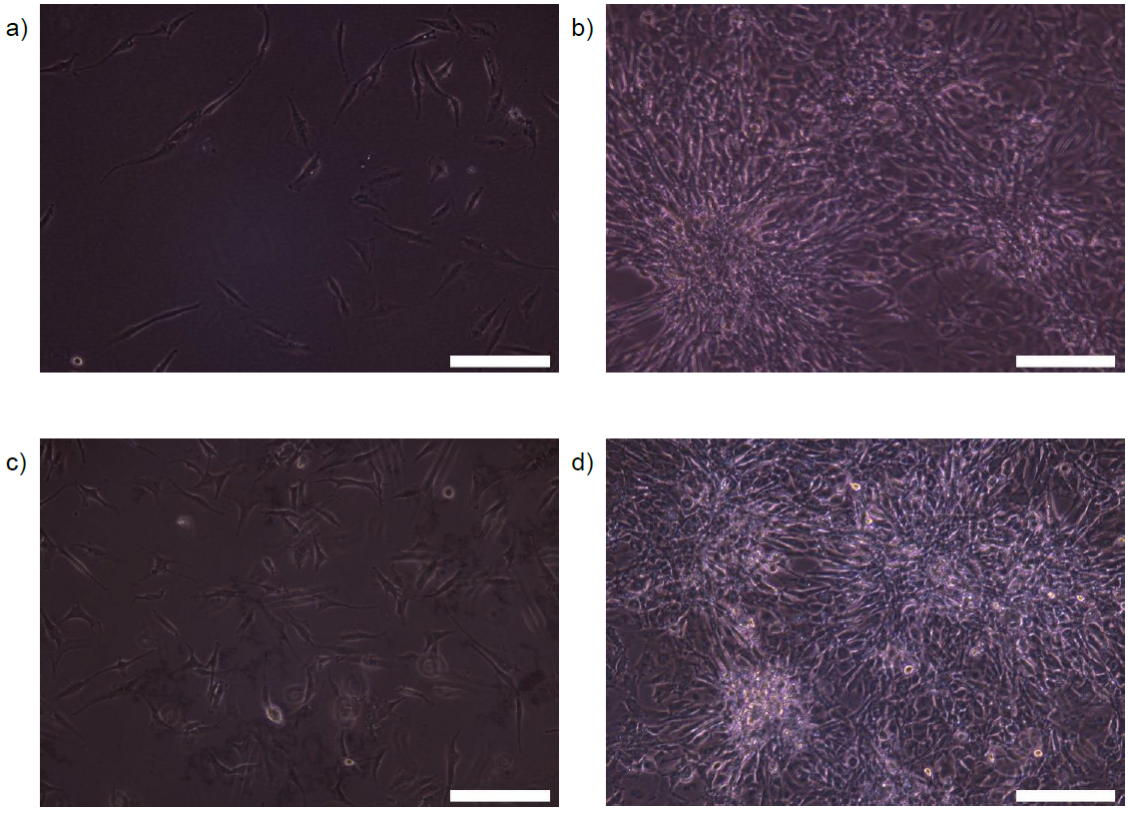

Figure 3.7: Optical micrographs showing U87 glioblastoma cell growth (a) at 4 days on L-gra substrate, few cells present and not inclined to growth; (b) at 12 days on L-gra substrate, still few proper cell clusters but those present were less confluent compared to other substrates; (c) at 4 days on S-gra substrate, cells had good size extensions; (d) at 12 days on S-gra substrate, many cell clusters observed and overconfluency apparent. All figures have scale bar = 200 µm.

that the cells experience with the greater edge density (as the graphene should itself be relatively inert), allowing them to form more adhesion sites. The cell stability is therefore increased, allowing more effective mobilisation and proliferation. Such a large impact on cell growth is critical when setting up controlled cell studies, and importantly this Langmuir substrate technique allows for the production of large quantities of identical substrates, which are important for the statistical requirements of biological studies [277].

3.7 Conclusions

Liquid-phase exfoliated (LPE) dispersions of BN, MoS_2, WS_2, and two sizes of graphene were prepared and used to deposit L–S films at a range of different surface pressures. This is the first demonstration of the production of single layer BN films using this method. These dispersions were made by generic processes to facilitate a standardised film creation method. UV–visible spectroscopy measurements showed the dispersions to be exfoliated, while AFM measurements were used to obtain average lateral dimensions and thicknesses for each material. Running a binary threshold on optical micrographs of the films gave quantitative values for the surface coverage of the material films, allowing the surface pressure–surface area relation to be plotted. To gain further insight from these plots, the data were normalised to account for differing sizes of nanosheets between materials. Plotting surface pressure against the interparticle distance begins to account for edge density effects and results in near parallel data. Additionally, the 2D bulk modulus was plotted, and, once normalised to the cohesion pressure, showed a similar rigidity onset and maximum for each material. Increased edge density on a graphene cell substrate increased colony formation and proliferation, demonstrating the importance, and tissue engineering potential, of control over film properties.

These results allow for an improved understanding of the physical and chemical influences on film formation, surface pressure, and surface coverage behaviour in Langmuir films of 2D layered nanomaterials. This straightforward process has been

demonstrated for a range of layered nanomaterials, including BN, which has not yet been used extensively for Langmuir deposition. An approach for analysis has been developed where size effects can be discarded, leaving only the effects due to the inherent chemistry of the material type. This combination of variable surface coverage and edge functionalities makes Langmuir films of layered nanomaterials interesting as substrate modifications for studies of cell growth and proliferation. These results will have uses beyond even cell studies, as this technique can be used to create films for a wide range of applications, such as transparent electrodes, supercapacitors, etc. as well as providing a framework for processing new layered materials into single layer films, with maximised surface area.

Chapter 4

Cell–substrate interactions lead to internalisation and localisation of layered MoS_2 nanosheets

Using an ultrathin film substrate, the first internalisation of MoS_2 nanosheets through mechanotransduction is demonstrated. The usual method of dispersing nanomaterials in the media limits interactions to random, serendipitous surface contact, and the nanoparticles must be dispersible in media. A substrate approach means that cells directly engage with the nanomaterial, sensing and adhering through sustained interaction and actively internalising the nanomaterial. This activates previously unobserved cell–substrate mechanotransduction mechanisms and receptor-mediated uptake pathways. Moreover, a wide variety of nonsoluble nanomaterials can be used, improving control over the amount of material exposed to a cell through tuneable deposition density. Volumetric Raman mapping demonstrates localisation of material to the endoplasmic reticulum (ER), a historically hard-to-target region. The nanosheets do not cause cytotoxicity, are transferred to daughter cells, and have applicability across multiple cell lines. The innate fluorescence or Raman signal of the nanosheet can be utilised for live cell imaging, and targeted accumulation within specific cellular organelles offers potential for photothermal treatments or

drug delivery vectors. This substrate-mediated approach provides a step change to studying nanomaterial–cellular interactions, taking advantage of the broad palette of available two-dimensional (2D) materials and making use of mechanosensing to stimulate tuneable responses, with potential for therapies and diagnostics.

4.1 Introduction

The properties of nanomaterials are of increasing interest for biological applications. The transition metal dichalcogenides (TMDs), such as molybdenum disulfide (MoS_2) and tungsten disulfide (WS_2), are of particular interest. These tend to have direct band gaps in the monolayer form, making them key to optoelectronic devices [278–280]. This also means that they are inherently fluorescent [251], which is a useful attribute in cell studies as a probe, if an appropriate target can be identified. TMDs also have accessible chemistries [281] and can be easily functionalised [282–284], which can improve the biological interaction [285,286] or allow the material to be used as a drug vector [107,108,287]. MoS_2 has fluorescence in the red [288] in the monolayer form, strong Raman-active phonon modes that are correlated to its geometry [289], and sulfur edge chemistry that is particularly useful for protein binding [290]. In addition, molybdenum and tungsten enzymes are known to be essential to life [291,292], yet how cells access these metals is not well understood, which makes TMDs important materials for investigation.

Previous work on MoS_2 in cell studies has always made use of a media dispersion and then measured the uptake and localisation from this system [293–296]. Issues with dispersed nanomaterial studies include the general lack of nanomaterial solubility [295, 296], degradation of the material within the cell [297], and toxicity [298–300]. How cells sense and physically engage with their substrate is critical to a multitude of cellular processes, including mobility, motility, proliferation, nutrient uptake, and stem cell differentiation [301,302]. Development of ultrathin film substrates provides a unique way to present 2D nanosheets to a cell [118], allowing cells to be seeded directly onto the material of interest. This physical interaction between cell and

material leads to different mechanotransduction responses [303,304]. These substrate-mediated responses provide an opportunity, through the use of nanomaterials, to access different mechanisms and organelles and stimulate various cellular responses, which has not been possible before [305]. Although there is little research into active mechanotransduction of nanomaterials currently, Yeh et al. have shown that when cells are grown on chemical vapour deposition (CVD) WS_2, the cells are able to internalise portions of the single crystal and also present fluorescence in daughter cells [306]. However, they did not speculate as to the mechanisms for this uptake or the internal localisation of the materials.

The synthesis and processing of the materials used in this work is described in 2.2.4.2, the characterisation techniques used are described in 2.3.5.2, and the details of the cell experiments are included in 2.3.6.2. The cell lines used are described in more detail in 5.3.

4.2 Substrate production

Liquid-phase exfoliation by sonication (LPE) is the most scaleable way to produce large quantities of various layered nanomaterials in dispersion [120, 248]. By controlling exfoliation and centrifugation parameters and solvent choice, it is possible to tune the morphology and chemistry of the nanosheets produced. Common parameters that have been used in this work yield MoS_2 nanosheets that are ~200 nm in length and 8 layers thick, confirmed by atomic force microscopy (AFM) (Figures 4.1a–c)

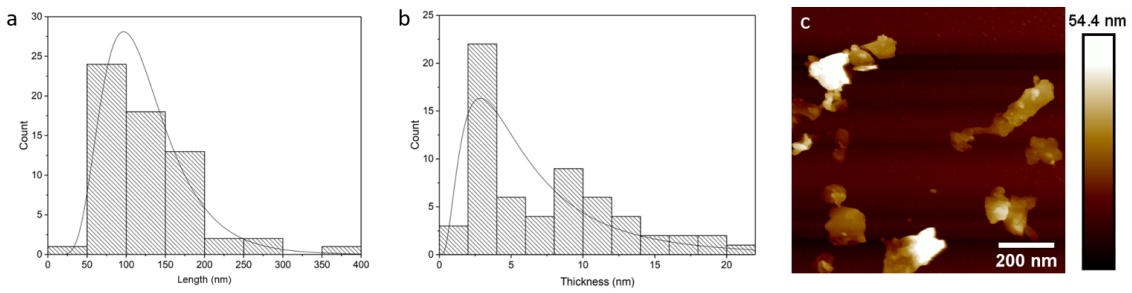

Figure 4.1: MoS_2 nanosheet characterisation. (a & b) AFM statistics histograms for MoS_2 nanosheets showing length and thickness data. (c) AFM image of as-produced MoS_2 nanosheets.

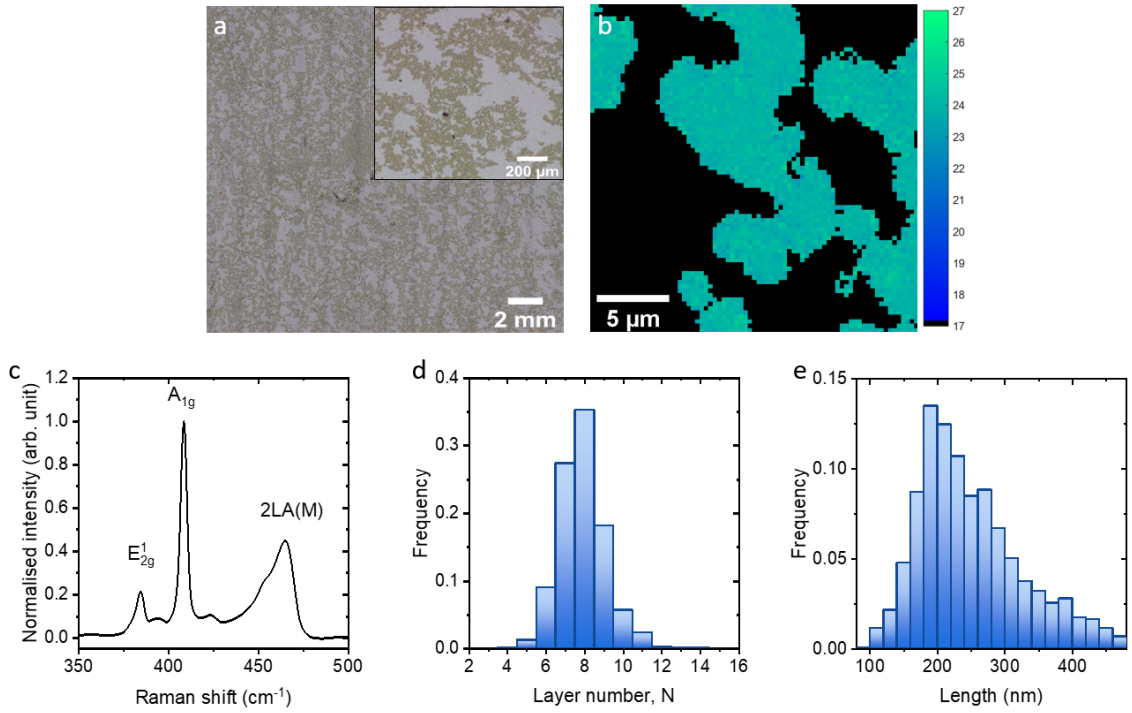

Figure 4.2: MoS_2 thin film substrate characterisation. (a) Optical micrograph of a typical thin film substrate on glass, a close-up shown in the inset. (b) Map of the layer number, N, for a typical MoS_2 thin film substrate on glass. (c) Typical resonant Raman spectra (660 nm) taken from the 2D Raman map (b) of the thin film substrate; metrics [203] indicate that (d) the average thickness is 8 layers and that (e) the average length is ~200 nm.

and Raman metrics (Figures 4.2b–e) [203, 212]. MoS_2 has Raman-active modes that can be correlated to the thickness and defect densities, and also has strong resonance with a 660 nm laser [203]. Figure 4.2c, in particular, illustrates this as the 2LA(M) mode is not present at other wavelengths [203]. These properties mean that a significant signal can be gathered from a very small sample volume [203]. This provides an excellent way to characterise the MoS_2, to track its location throughout a cellular interaction, and also to determine any modifications it undergoes [203, 297].

The Langmuir–Schaefer (L–S) deposition technique works by dropping nanomaterial dispersion onto a trough of water, such that the dispersion solvent evaporates, leaving a thin film of material at the air–water interface. It has proven to be highly effective for the production of ultrathin films of a variety of nanomaterials and has been shown to be possible to tune the thin film density, as discussed in Chapter 3 [118, 162]. With careful solvent selection for the LPE process, it is also

possible to deposit films directly without any solvent transfer steps. These thin films can be deposited onto various substrates, but for this work, glass slides have been used to provide compatibility with standard cell culture techniques and equipment, and still enable characterisation by Raman spectroscopy before and after cell growth. The film density is controlled via barriers on the Langmuir trough to provide full or partial surface coverage (Figure 4.2a). Combining LPE and L–S deposition means that these thin film substrates can be produced with various 2D layered nanosheets, in large quantities, repeatably, and therefore can be used for multiple cell growth studies. Figure 4.3 is a scheme that shows the process from bulk MoS_2 powder via LPE to the final L–S film.

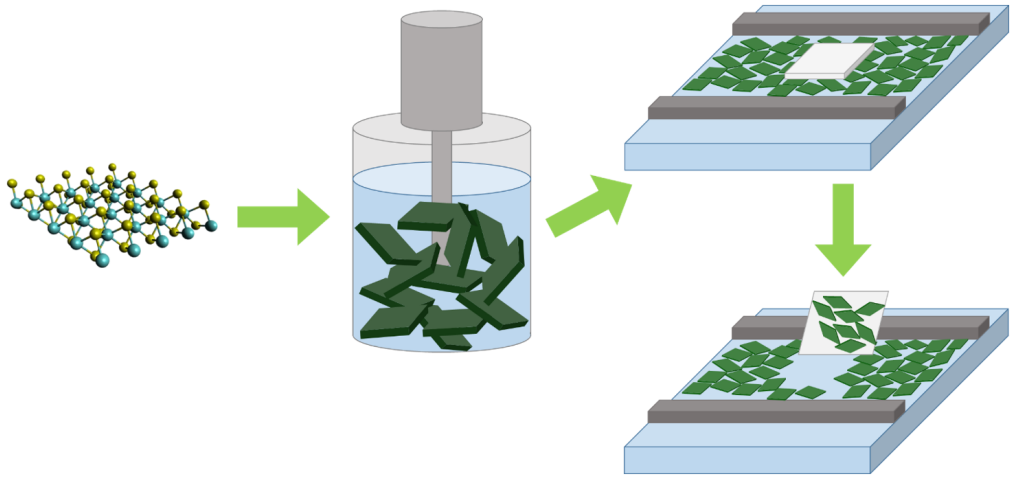

Figure 4.3: Bulk MoS_2 (structure shown, left) is added to a suitable solvent, in this work cyclopentanone, and exfoliated by ultrasonication (shown centre). After exfoliation is complete, the resulting dispersion is used to create an L–S film (shown right).

4.3 Cell studies

When cancer cells (U2OS) are seeded onto the L–S thin film substrates, the cells grow and proliferate with no cytotoxicity evident even after 14 days. In fact, there is a nonsignificant increase in the cell count after growth on the MoS_2 substrates compared to that on pristine glass cover slips (Figure 4.4a). Potentially, this is due to the increased surface roughness providing improved adhesion. Of great interest is that after ~3 days of incubation on the substrate, the cells begin to modify

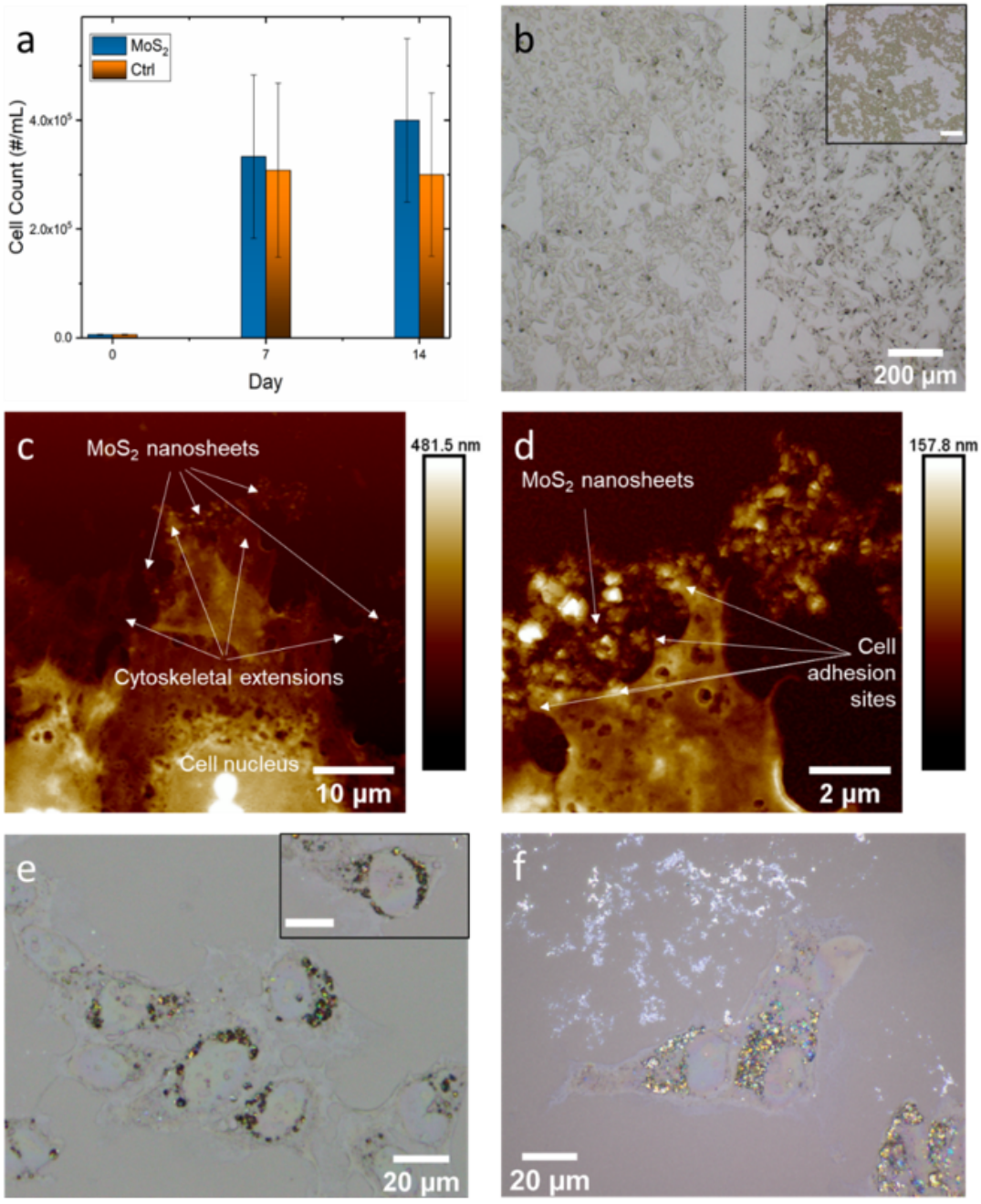

Figure 4.4: Cell–substrate interactions and uptake. (a) Cell count data for U2OS cells grown on MoS_2 substrates (blue) and pristine glass controls (orange); error bars calculated as standard error in the mean from three repeat experiments (two samples per type for each experiment). (b) Optical micrograph of U2OS cells (7 days of growth) on a split substrate (left half of the substrate pristine glass and the right half coated in a MoS_2 Langmuir thin film of typical density shown in the inset); MoS_2 nanosheets have been accreted by the cells (dark regions). The inset scale bar is also 200 µm. (c & d) AFM height images of U2OS cells (3 days of growth) on MoS_2 nanosheets, with cytoskeletal extensions and adhesion sites directed toward the MoS_2 nanosheets on the substrate. (e & f) Optical micrographs showing the internalisation of the MoS_2 nanosheets and the localisation around the nucleus in the ER (taken of the same sample as shown in Figure 4.4b). The inset scale bar is also 20 µm.

the film and internalise the MoS_2 nanosheets. After 7 days, the majority of the MoS_2 has been accreted under the cells and large proportions of it are internalised (Figures 4.4b, e & f).

Using substrates that are only half-coated in the MoS_2 allows this physical interaction to be seen clearly. What was once a complete thin film on the right half of the substrate (typical density shown in Figure 4.4b inset) now forms the dark regions of MoS_2 that have been accumulated under and internalised within the cells (Figures 4.4b, e & f). This is due to the action of the cells adhering to, and mobilising on, the substrate. As the nanosheet forms part of the cell substrate, the material is internalised through a mechanotransduction response; the cell senses the substrate and then actively internalises the material. This response is of enormous interest and is little understood; it is an entirely different approach to the internalisation of nanomaterials, which are usually dispersed in the cell media. It can be seen that the majority of the MoS_2 nanosheets are internalised in the region around the nucleus (Figures 4.4e & f). Some recent work has shown that the stiffness of the cell substrate influences how much uptake of dispersed nutrients the cell engages in [307, 308]. For the stiffer materials, the cells can be seen to have formed far larger cytoskeletons, with extensions and adhesion sites that spread throughout the substrate. The cells must mechanically interact with their substrate to be able to engage in material uptake. In this work, the cells are actively interacting with the MoS_2 nanosheets, adhering to them, and applying forces to remove and move them across the substrate. The cells can be clearly seen to have large spreading areas, lots of cytoskeletal extensions, and adhesion sites associated with migration and motility (Figures 4.4c–f). The atomic force microscope (AFM) images illustrate extensions and adhesion sites specifically grown toward dense regions of MoS_2 nanosheets; when grown on sparse film substrates (Figures 4.4c & d), the cells are seeking out the nanosheet material. This in turn means that the cells tend to congregate around denser MoS_2 regions, improving their ability to conduct cell-to-cell communication, which is vital for proliferation and viability.

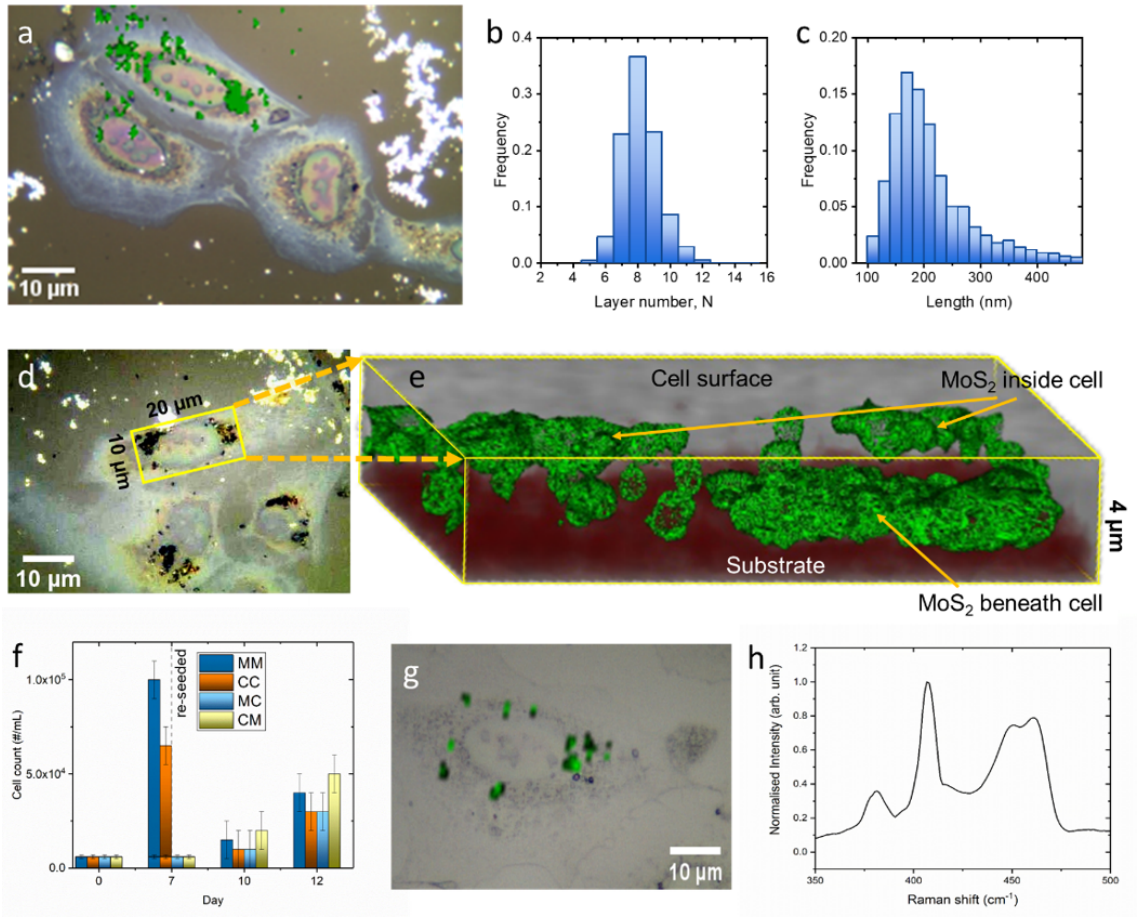

Figure 4.5: Localisation and lifetime of MoS_2 nanosheets. (a) 2D Raman map of the intensity of the ~405 cm^{-1} A_{1g} peak of MoS_2 (green) overlaid on the optical microscope image of cells; (b & c) metrics [203] indicate the same layer number (8 layers) but reduced length (<200 nm). (d) Top-down optical view of the location of (e) volumetric Raman mapping of the intensity of the A_{1g} peak (green), with some nanosheets inside the cell and some still on the substrate. (f) Cell count data for U2OS cells grown on MoS_2 substrates and glass controls for 7 days and then removed from the substrate, split, and reseeded as described in 2.3.6.2; the error bars are calculated from standard error in the mean from two repeat experiments (two samples per type in each experiment). (g) Raman mapping of cells taken from MoS_2 substrates and reseeded onto pristine glass controls, indicating that MoS_2 nanosheets are still localised within the ER and present in daughter cells, with (h) minimal modification of innate Raman spectra indicating limited degradation.

Raman volumetric mapping is a powerful technique for determining the localisation of MoS_2 nanosheets within the cell. Mapping the peak intensity of the ~405 cm^{-1} A_{1g} mode yields detailed spatial information for the nanosheet within the cell. Combining multiple overlapping steps gives a z-resolution of < 1 µm, and therefore, it is possible to confirm the difference between the material internalised within the cell and that above or below the cell. Volumetric (Figures 4.5d, e & D.1)

and 2D (Figures 4.5a, g & D.2) Raman mapping confirms our observations from the optical microscopy (Figures 4.4e & f). The MoS_2 nanosheets were presented as a thin film substrate only; no MoS_2 was added directly to the cell media, so there is no possibility of the material being on top of the cells, as can be the case for media-dispersed nanomaterials. This volumetric map shows nanosheets that are clearly raised above the substrate, indicating that they are largely internalised in the region around the nucleus (the endoplasmic reticulum, ER), with some material identified in the cytoplasm (most likely in lysosomes) and some still lying at the base of the cell and therefore still on the substrate (Figure 4.5e).

If the cells are harvesting transition metals or sulfur components for internal processes, then it would be interesting to note if the cells are able to break down the MoS_2 to access the elemental components. Raman spectroscopy (Figure D.3) indicates that there is little change to the layer number for the MoS_2 nanosheets after its internalisation — still 8 layers (Figure 4.5b) — but the average length has decreased (Figure 4.5c). This suggests either that the cells are able to begin to decompose the edge sites (spectra taken from cells after 7 days of growth), as the metrics do not indicate an increase in defect sites, such as holes, in the basal plane; or that cells are selectively internalising any smaller-sized sheets on the substrate, due to a possible limit on the size of the sheets able to be internalised via the caveolin pathway.

Excitingly, the MoS_2 is also transferred to daughter cells (Figure 4.5g), as was also seen by Yeh et al. with the CVD WS_2 [306]. In an experiment, after 7 days of growth on MoS_2 and pristine glass control substrates, the cells reached confluence and were trypsinised, split, and reseeded onto new substrates (Figure 4.5f). The cells were reseeded at the initial (day 0) density to allow room for further proliferation on the new substrates (indicated by the sudden decrease in cell count in Figure 4.5f). The new substrates used were either further fresh MoS_2 substrates or pristine glass cover slips (control). In this way, cells that had been initially grown on MoS_2 are seeded onto both further MoS_2 and clean controls, and cells from the clean controls

are seeded onto further clean controls and onto MoS_2. As before, it is seen that this does not affect the proliferation of the cells (Figure 4.5f); if anything (although it is not significant), the MoS_2 actually increases the cell proliferation both before and after the substrate change. Importantly, MoS_2 is still observed to be internalised within the ER of cells seeded onto the clean substrates (Figure 4.5g), so the MoS_2 is retained within the cell and passed on to daughter cells (U2OS doubling time is ~29 hours). Although we have not performed extensive studies to quantitatively determine for how many generations the MoS_2 is retained in the cells, we can make some speculation based on the U2OS doubling time. The cell study continued for 7 days after cells initially seeded on MoS_2 were reseeded onto pristine glass substrates. As the U2OS doubling time is ~29 hours, and this part of the cell study ran for 7 days, we estimate that the MoS_2 remains present in daughter cells for at least five to six generations.

Raman spectroscopy of the MoS_2 internalised in the daughter cells again shows similar layer numbers and no further significant decrease in length compared to that of the continuous growth for the same length of time (Figure 4.5h). This has implications for theranostics, as the vector remains within the cell line. As the tumour grows, for example, all cells may contain the vector, which could be used as a therapeutic centre or tag. The nanosheet perseverance is further confirmation of their potential to act as new probes, as the nanosheets can be tracked throughout long live cell imaging experiments, over multiple generations, and also tracked within a co-culture. This paves the way for the next generation of diagnostics and imaging that can investigate the microenvironment and complex tissue development.

4.4 Internalisation mechanisms

The receptor-mediated endocytosis pathways transport material to the ER and Golgi apparatus, whereas more passive processes silo unwanted or unknown material into lysosomes and usually eject it [309]. The ER, in particular, is associated with molybdenum enzymes and sulfur bridges for protein building [291]. Several transition

metals, including molybdenum, are vital for cell function. The molybdenum cofactor is found in all kingdoms of life; five molybdenum cofactor enzymes are known to exist in eukaryotes and four of these are found in humans [310]. A lack of molybdenum in the environment can lead to a deficiency in molybdenum cofactor, a rare disease first identified in 1978; this can lead to neurological damage, seizures, and feeding difficulties [310]. Despite their importance, little is known about how cells access and internalise these materials. The active interaction and accumulation of the MoS_2 nanosheets, shown here, may provide a new means to study the cellular uptake of essential transition metals.

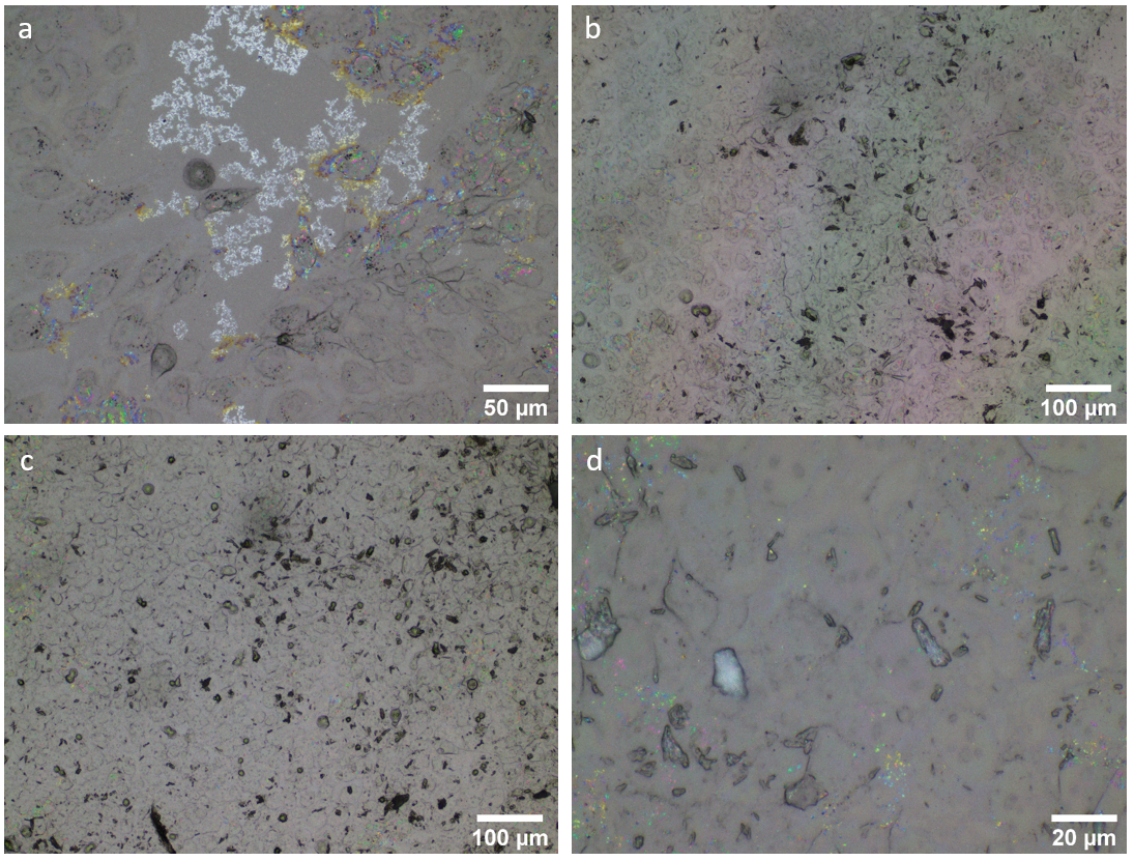

Figure 4.6: (a) U2OS cells grown on MoS_2 substrates, no nystatin solution (control). (b–d) U2OS cells grown on MoS_2 substrates with 20% nystatin solution to limit caveolin uptake.

Other works using MoS_2 nanosheets in dispersion have identified the predominance of the caveolin pathway in the internalisation process. This pathway is poorly understood, but recent insights have identified its important role in substrate sensing [311–313], mechanoprotection [314], and cancer growth [311, 314]. Nystatin

is used as an inhibitor for the caveolin pathway. In the present study, the use of nystatin did not alter the U2OS cell accretion of the MoS_2, but significantly reduced internalisation was observed, implying that this uptake pathway is dominant for MoS_2. There was some evidence of MoS_2 within the cytoplasm, most likely in lysosomes through passive diffusion or alternate endocytic pathways. Typical optical micrographs of the U2OS cells grown in 20% nystatin solution are shown in Figure 4.6. This fits with the expected uptake mechanism for transition metals in a mechanotransduction substrate response. Additionally, this uptake pathway is a direct route to the ER, explaining the accumulation within that organelle [314, 315]. This all adds strong weight to the argument that the cells identify the transition metal and sulfur chemistry within the substrate through sensing mechanisms, and harvest the materials through this directed route for protein and enzyme building. The caveolin pathway is little studied, and so this nanomaterial substrate technique provides a route to probe and understand these fundamental cell processes further.

The unfolded protein response (UPR) is a cellular response to errors in protein folding in the ER; the cell enlarges the ER to accommodate the unfolded material [316]. This response aims to restore normal function to the cell, but, if unsuccessful and ER stress is prolonged, leads to apoptosis. One of the mechanisms of cancer is that it is able to maintain the unfolded protein response (UPR) far longer than a normal cell, thus evading apoptosis. In the present study, a clear increase is seen in the size of the ER in the sarcoma cells grown on the MoS_2 (Figure 4.7a), compared to those grown on the control (Figure 4.7b), indicating stress in the ER. Not only does this confirm the localisation of the MoS_2 within this organelle, but also this indicates that the exposed sulfur edges and/or molybdenum metal sites of the MoS_2 are being identified by the cell as protein or enzyme components, thus activating the UPR. It is interesting to note that this large accumulation of nanosheets within the ER of a cancerous cell could provide novel cancer theranostics, targeting a specific cancer mechanism. The overactive UPR of cancer cells could be utilised to accumulate a critical mass of material in only the cancerous cells, which either drives them to

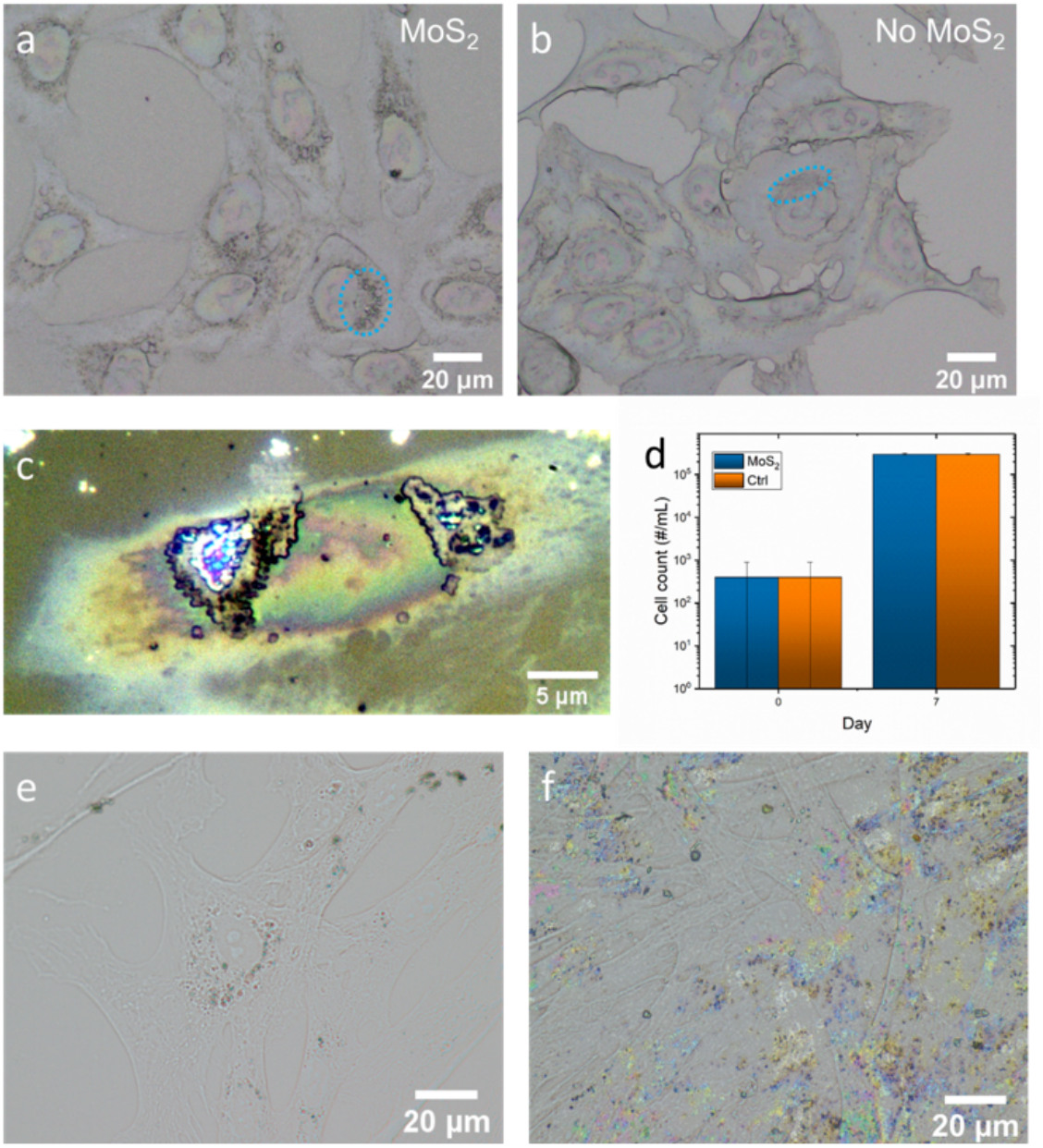

Figure 4.7: Generalisation of the methodology and applications. (a & b) Optical images of U2OS cells grown on (a) MoS_2 and (b) control substrates; a substantial increase in the size of the ER is observed for the cells grown on MoS_2 nanosheets. One ER from each image is highlighted with blue dotted circles to give a guide to its size and location within the cell. (c) A cell with internalised MoS_2 after irradiation with a 100 mW 660 nm laser showing severe local damage. (d) Cell count data for primary fibroblast cells, showing no toxicity after 7 days; error bars calculated from the experimental error of single experiment. (e & f) Optical micrographs of fibroblast cells grown on MoS_2 substrates with nanosheets localised in the ER, but less accretion under the cells compared to U2OS.

apoptosis (although cell death was not seen even after 14 days of incubation) or can be used as a photothermal site. High exposure of the internalised MoS_2 with a resonant laser causes significant localised damage to a cell — the ER is destroyed through local heating of the excited MoS_2 (Figure 4.7c), confirming the possible use of the internalised MoS_2 for photothermal therapy (PTT). Alternatively, drugs that target this organelle could be attached to the material. All the while, the condition and location of the nanomaterial could be tracked by Raman volumetric mapping or indeed by the material's inherent fluorescence in the case of monolayer TMDs (as demonstrated by Yeh et al. [306]).

A noncancerous cell line (fibroblasts) also shows localisation of MoS_2 within the ER, although the amount is not as significant as for the cancerous cell line (U2OS), and there is more material distributed in the cytoplasm (Figures 4.7e & f). The cells do not seem to actively accrete the nanosheets as the cancer cells do, the multicoloured contrast indicating the presence of MoS_2 still distributed across the substrate in Figure 4.7f. In this work, the fibroblasts proliferated faster than U2OS cells and also have larger spreading areas, so they reached confluence more quickly, limiting the time spent mobilising on the substrate before intercellular interactions started to dominate. Regardless, there is no indication of cytotoxicity up to 7 days of growing on the substrate (Figure 4.7d), however, the slight nonsignificant increase in proliferation as for the U2OS cells was not observed, probably due to the lower mechanical substrate interaction of fibroblasts compared to that of bone-derived cells. This shows that the mechanotransduction-mediated uptake of nanosheets is a potential pathway to internalisation for many different cell types. A new mechanotransduction internalisation route could be used for developing new fluorescent and Raman probes for previously unattained targets. However, there may be more specific implications for cancer cells due to the exaggerated cancer cell–substrate interactions, the 'hungry' nature of cancer cells to scavenge materials from the environment, and the overactive UPR. These phenomena could all be exploited through mechanotransduction-mediated uptake of nanosheets to internalise

imageable drug delivery vectors or localise photothermal sites to cancer-specific targets, for example. Therefore, this approach may have exciting potential for cancer theranostics.

4.5 Conclusions

The need for the cell to form adhesions, and deform its environment, is critical to its functioning. In this work, the substrate is stimulating the cellular membrane proteins for sensing and recognition, triggering uptake pathways, as well as spreading and proliferation. These mechanotransduction responses provide new insights into the full interaction of a cell with its environment and offer novel approaches to studying cellular mechanisms.

This work presents a completely new internalisation methodology for synthetic nanoparticles. A new technique for targeting receptor-mediated uptake has been demonstrated, and its links to internal structures such as the ER have been shown, which is important in many different diseases [317]. It is well known that accurate internal mapping is difficult; this work aims to improve this by using Raman spectroscopy. While it is possible that the determination of the localisation within the cell could be improved, significant localisation of the nanosheets in specific organelles has been seen, all identified and mapped through volumetric Raman spectroscopy, a non-invasive process that has the potential to be used with live cells. Additionally, novel insights into mechanotransduction responses to substrate-derived nanomaterials have been made and shown to be generic to different types of cells with no toxicity, but of particular interest to cancer cells due to their overactive mechanical substrate interactions and modified UPR. Following this initial study, presented here to introduce the broad scope of this method of looking at cell–substrate interactions, further biological characterisation experiments are needed to further understand this system, including detailed cytotoxicity assays, comparisons of other nanomaterials, and further investigations of the UPR effects.

The sulfur chemistry of the TMDs can be exploited for biological attachment and for drug delivery or more specific targeting [182]. By utilising MoS_2 as a cell substrate, there is real potential to use the material's inherent fluorescence or unique Raman features for tracking, live cell imaging, and potential therapies with photothermal treatment or drug delivery of a mechanotransduction-internalised nanovector. This new approach to nanomaterial–cell interfacing offers an exciting opportunity to develop the next generation of theranostics.

Chapter 5

Internalisation and localisation of transition metal dichalcogenide nanosheets

5.1 Introduction

A clear way to extend the work in Chapter 4 was to consider other transition metal dichalcogenides (TMDs). While MoS_2 was shown to be internalised in that work, it had not been ascertained whether the same would be true of WS_2, or $MoSe_2$. Yeh et al. [306] had previously shown that cells internalised chemical vapour deposition (CVD) WS_2, so it seemed likely that this research would yield positive results. However, this had not yet been studied for liquid-phase exfoliation by sonication (LPE)-produced TMDs other than the work on MoS_2 [318].

As discussed in Section 2.1.2, TMDs are compounds described by the chemical formula MX_2, where M is a transition metal (e.g. Mo, W) and X is a chalcogen (e.g. S, Se) [8, 38]. The monolayer, formed of a hexagonal plane of transition metal ions sandwiched between planes of chalcogen atoms [39], is not strictly two-dimensional (2D). However, TMDs are often classed as such due to their extremely thin monolayers [38–40]. This standard structure makes different TMDs structural

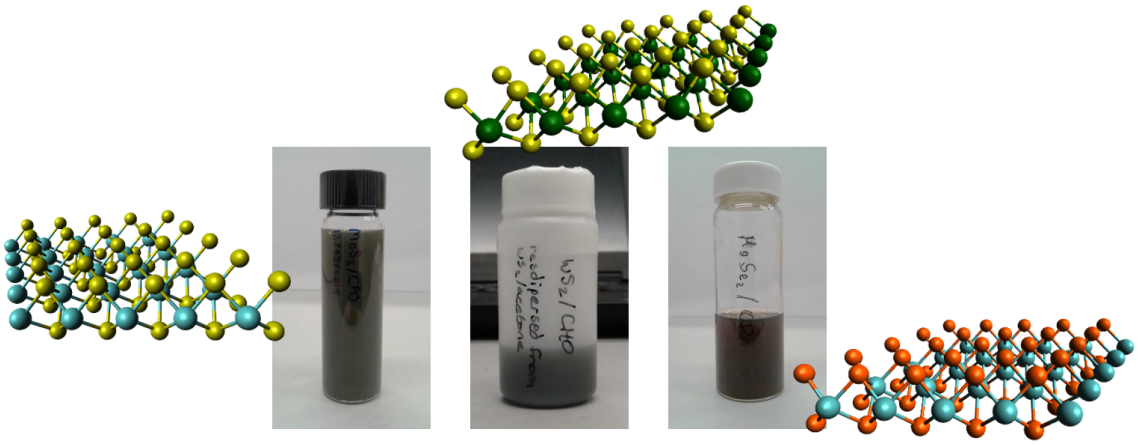

Figure 5.1: Structure and dispersion of MoS_2 (left), WS_2 (centre), and $MoSe_2$ (right). The materials are structural analogues of each other.

analogues of each other (Figure 5.1). Dispersions of these materials are made in the same way and have similar solvent compatibilities, but have different band gap structures due to their different components.

The synthesis and processing of the materials used in this work is described in 2.2.4.3, the characterisation techniques used are described in 2.3.5.3, and the details of the cell experiments are included in 2.3.6.3.

5.2 Nanosheet characterisation

Briefly, the WS_2 and $MoSe_2$ dispersions used in this study were produced by LPE, and these dispersions were used to create dense Langmuir–Schaefer (L–S) thin films. Raman spectra of the substrates were taken to confirm the presence of the expected material and to show the level of material exfoliation. These spectra can be seen in Figure 5.2, with labelled phonon modes [319–321]. The WS_2 Raman spectrum shows a sharp peak assigned to the 2LA(M) mode at 349 cm^{-1}, and another peak assigned to the A_{1g} mode at 419 cm^{-1} [319]. The high intensity of the second-order 2LA(M) mode compared to the A_{1g} mode implies the presence of mono- or few-layer (~2–3 layer) WS_2 [319]. The $MoSe_2$ Raman spectrum shows a sharp peak assigned to the A_{1g} mode at 242 cm^{-1}, and another peak assigned to the E^1_{2g} mode at 292 cm^{-1} [321]. The peak spacing of approximately 50 cm^{-1} indicates the presence of

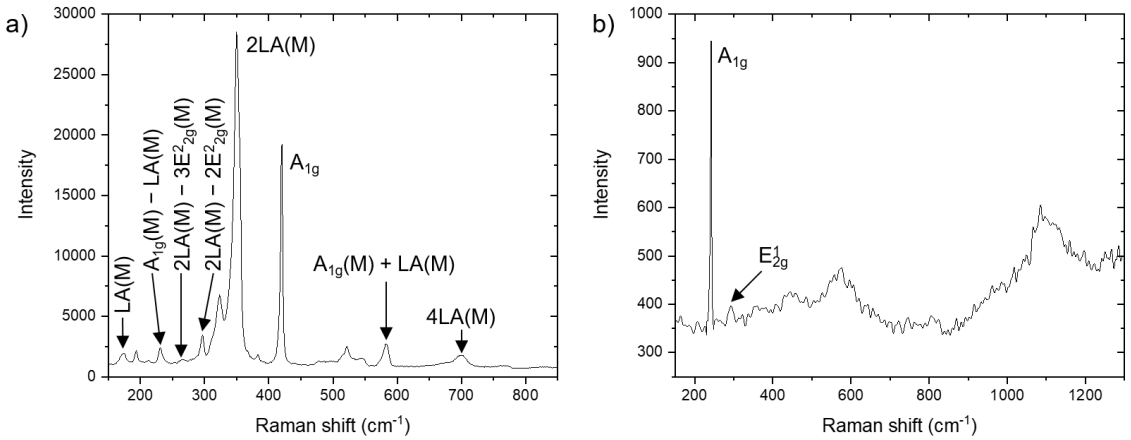

Figure 5.2: Raman spectra of (a) WS_2 and (c) $MoSe_2$ substrates used for cell studies. Labelled with WS_2 [319] and $MoSe_2$ [321] literature values for comparison.

$MoSe_2$ monolayers [321]. The high degree of exfoliation shows that the methodology is good for optimising the nanoscale properties, and Raman spectroscopy is a simple and effective way to characterise the material. The exfoliation compares well to that of the MoS_2 used in Chapters 3 and 4.

5.3 Cell lines

The same cell lines were used for this study as for the MoS_2 study in Chapter 4, namely 1BR primary fibroblasts and U2OS bone carcinoma. Here, these are described in more detail. Fibroblasts are mesenchymal cells with an elongated, spindle shape [322]. Their branched cytoplasm projections surround a nucleus with two or more nucleoli, and contains an abundance of rough endoplasmic reticulum and a large Golgi apparatus [323]. Fibroblasts are one of the most common cell types in connective tissue [323], and are responsible for maintaining the structural integrity of connective tissues by synthesising extracellular matrix components throughout the body [322]. Additionally, fibroblasts are involved in the wound healing process [322]; when tissue is injured, nearby fibroblasts proliferate, migrate into the wound, and produce large amounts of collagenous matrix [324]. However, it is important to note that there is

variation between fibroblasts from different anatomic sites [322], and that a number of different functions can be displayed even within one system [323]. Figure 5.3a shows control 1BR primary fibroblasts from this study.

U2OS cells are human osteosarcoma cells derived in 1964 from a moderately differentiated sarcoma of the tibia of a 15 year old girl [325]. They have an epithelial morphology. The chromosomes present in this cell line are significantly abnormal [325]. Furthermore, the cells show typical signs of malignancy, including an increased nucleocytoplasmic ratio, pleomorphism and enlarged nucleoli [325]. Figure 5.3b shows control U2OS osteosarcoma cells from this study.

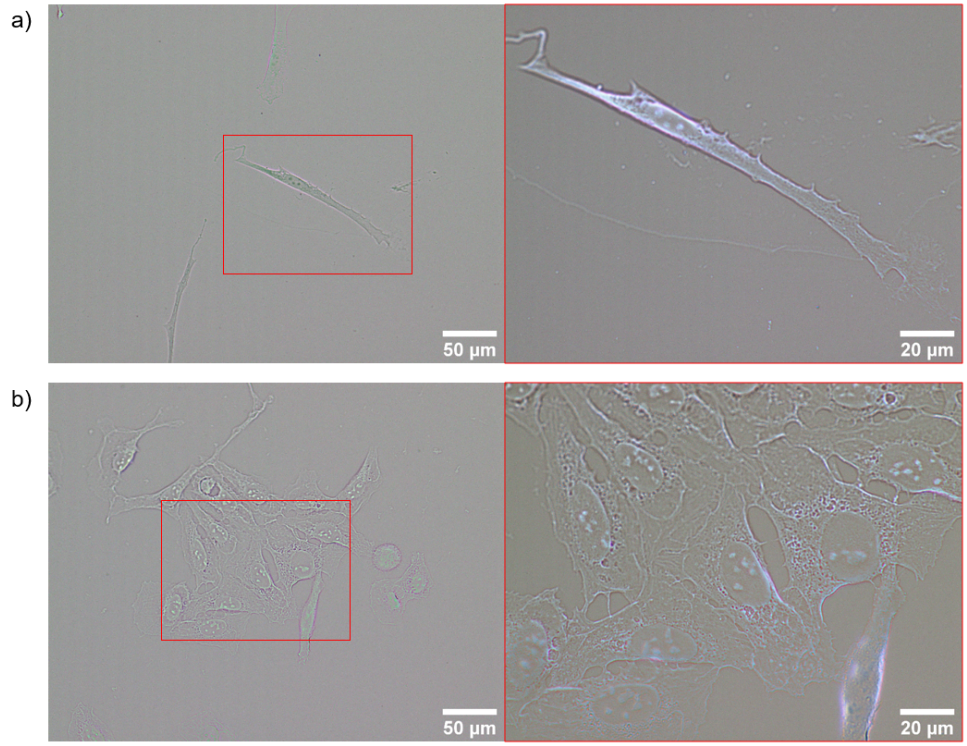

Figure 5.3: Optical micrographs of control (a) 1BR primary fibroblasts and (b) U2OS osteosarcoma cells. Red boxes indicate magnified areas.

5.4 WS_2 Substrates

First considering the 1BR primary fibroblasts, the WS_2 is visibly internalised within the cells (Figure 5.4b–e). This is confirmed by Raman spectroscopy of one of these dark areas within a cell. Figure 5.4a shows the characteristic Raman modes associated

with WS_2 (cf. Figure 5.2a). Because the cells were trypsinised and reseeded onto pristine glass cover slips for 2 days before fixation, any material present must be either within the cells, or loose having been ejected by the cell after reseeding.

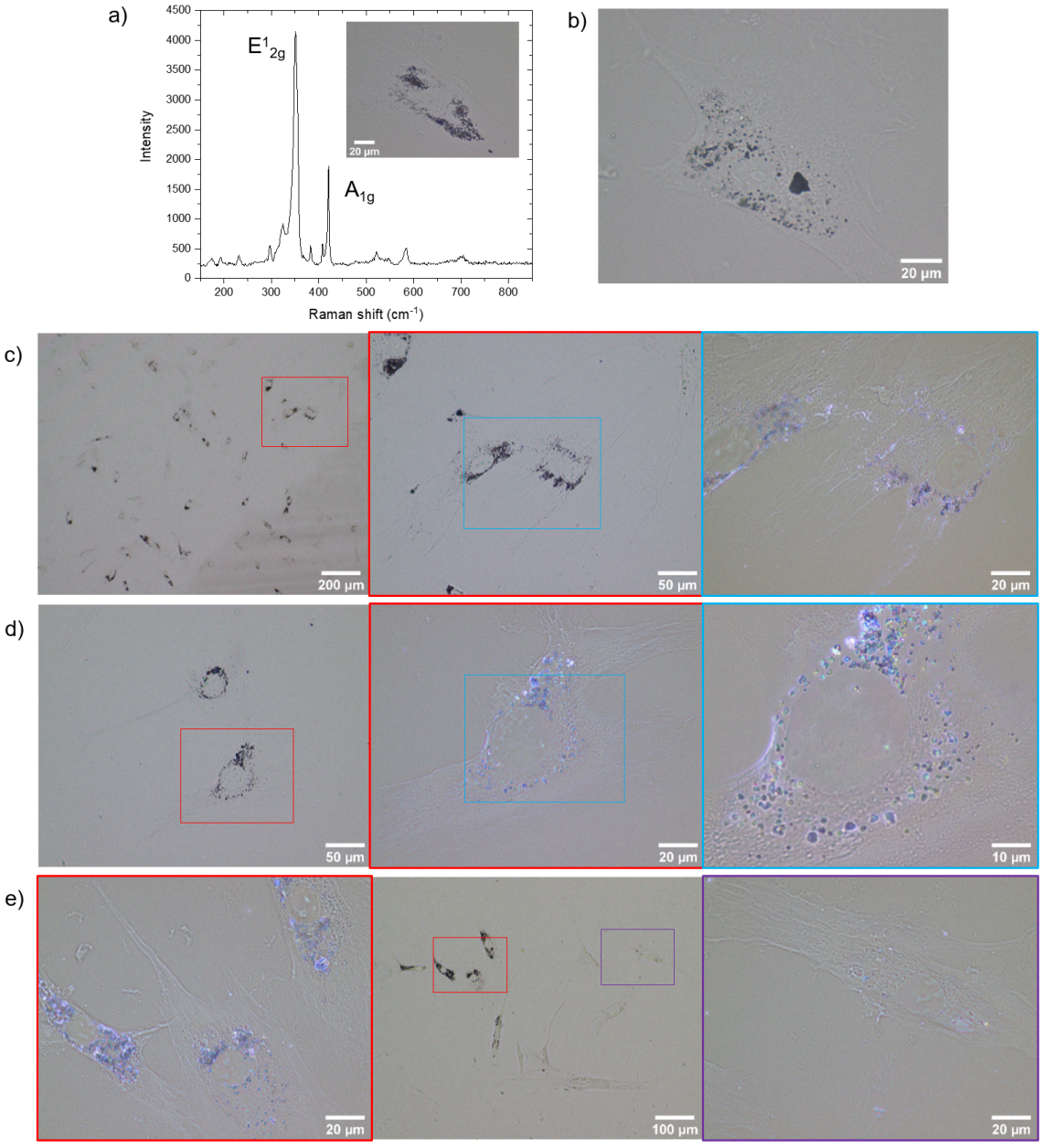

Figure 5.4: (a) Raman spectrum taken of a visibly dark area in a 1BR cell which grew on a WS_2 substrate for 7 days before trypsinisation and reseeding onto a pristine glass control. WS_2 features are still present, indicating the presence of WS_2 within the cell. Inset shows a typical 1BR cell with visibly internalised WS_2. (b–e) Optical micrographs of 1BR primary fibroblasts grown on WS_2 substrates. Red then blue boxes indicate areas undergoing increasing magnification. Red and purple boxes indicate different areas of an image undergoing the same magnification.

There are clear similarities between the amount of internalised WS_2 in this work and the amount of internalised MoS_2 in Chapter 4. However, while the WS_2 is still localised to the cell body, it is not as obviously localised to the endoplasmic reticulum (ER) as MoS_2 was previously. Further, the material appears to be occupying spherical vesicles, suggesting that it is likely that the material may be contained within lysosomes.

The work presented by Yeh et al. [306] also shows strong uptake of WS_2. However, they use CVD WS_2 rather than liquid-phase exfoliated (LPE) WS_2, so the size and quality of the material may differ. Further, Yeh et al. use the LMH hepatocellular carcinoma cell line whereas this work considers 1BR primary fibroblasts and U2OS osteosarcoma cells, meaning that direct comparison between cell lines is not possible.

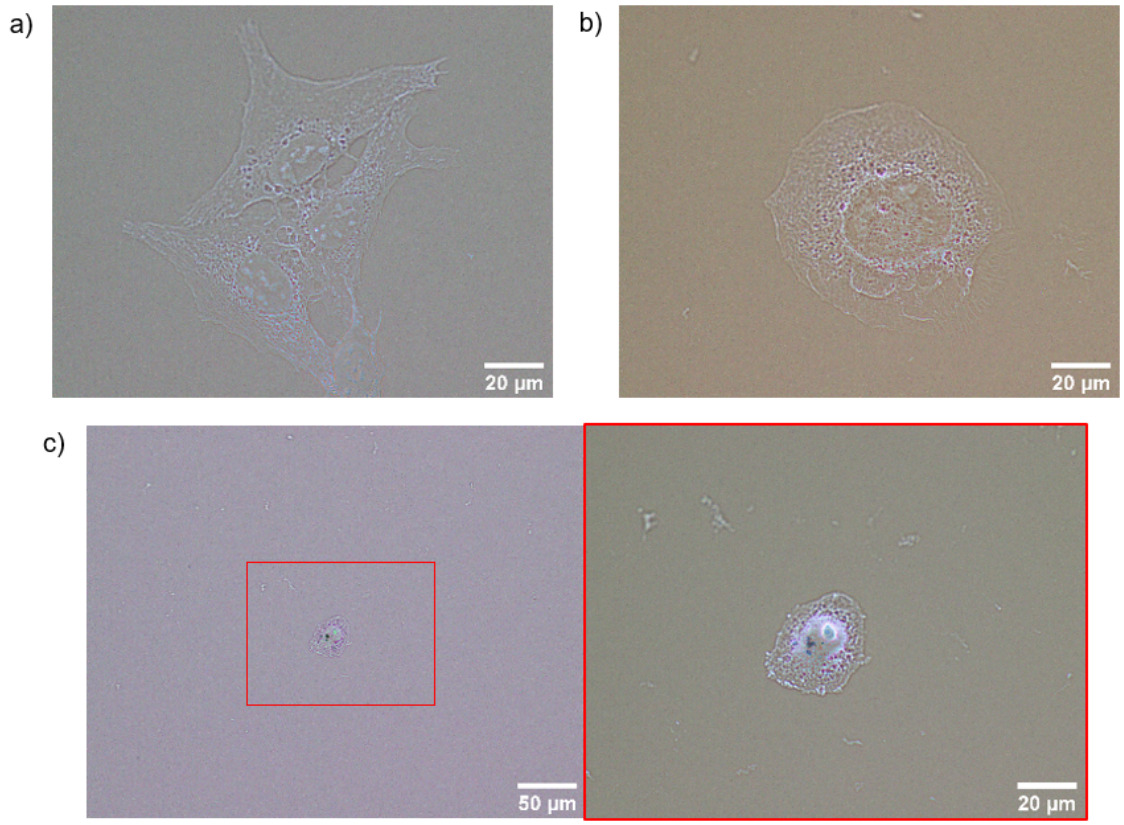

Figure 5.5: Optical micrographs of U2OS osteosarcoma cells grown on WS_2 substrates. (a & b) Many cells show no obvious internalisation of WS_2, typical examples given here. (c) Some cells did show internalisation, but not to the extent as for the 1BR primary fibroblasts. Red box indicates areas undergoing increasing magnification.

When looking at the U2OS cells, the contrast with 1BR cells is stark; although some cells show WS_2 uptake (Figure 5.5c), not as much material is seen within these cells, and several cells do not show any evidence of internalisation (Figure 5.5a & b). The amount of internalisation is also less than that seen for MoS_2.

This suggests that the presence of sulfur groups may cause the generic uptake by 1BR primary fibroblasts, as these cells show large amounts of internalisation of both MoS_2 and WS_2. Because there is not as much internalisation of WS_2 in the U2OS cells, it is not so clear that the sulfur groups are the main cause of uptake by these cells.

Therefore, it is possible that the transition metal has more influence on the material internalisation for U2OS cells. While Mo and W are both key elements to cells, only Mo is used in eukaryotic cells; this might explain why less WS_2 is internalised by U2OS cells compared to the amount of MoS_2 that was internalised in Chapter 4. W may also be internalised by the same process due to the similar chemistries of the two materials [291], but perhaps this would not be as efficient as the uptake of MoS_2. However, this is speculative, and more experimentation is required to investigate this aspect.

If these hypotheses are correct, namely that 1BR fibroblasts favour the sulfur groups of the material, and that U2OS favours the Mo transition metal, then it is possible to suggest potential outcomes for the cell study on $MoSe_2$ substrates. The 1BR fibroblasts grown on $MoSe_2$ would not necessarily show much material internalisation because the sulfur groups are not present. U2OS cells may show more internalisation of $MoSe_2$ than WS_2 if the Mo transition metal is preferred. However, selenium is known to be toxic to cells, so the selenium groups of $MoSe_2$ may mean that neither cell line shows much internalisation.

5.5 $MoSe_2$ Substrates

Both cell lines grown on $MoSe_2$ substrates showed very little internalisation and limited growth, including no growth on one run of U2OS cells (Figure 5.6, 5.7). However, the cell counts can't be compared directly with those on WS_2 or MoS_2 because the cell density wasn't controlled at reseeding for this initial experiment, designed to look at internalisation rather than toxicity. Cell extensions are visible, particularly for several of the U2OS cells grown on $MoSe_2$ (Figure 5.6). Although extensions are seen for U2OS cell growth on WS_2 (e.g. Figure 5.5b), they are far less common than those seen for U2OS cell growth on $MoSe_2$. This implies a different substrate interaction for the $MoSe_2$ substrates, perhaps trying to find adhesion sites not associated with $MoSe_2$ nanosheets (i.e. avoiding the material). This agrees with the earlier suggestion that the sulfur chemistry could be critical to the biocompatibility of the TMDs, with coincidental internalisation of the transition

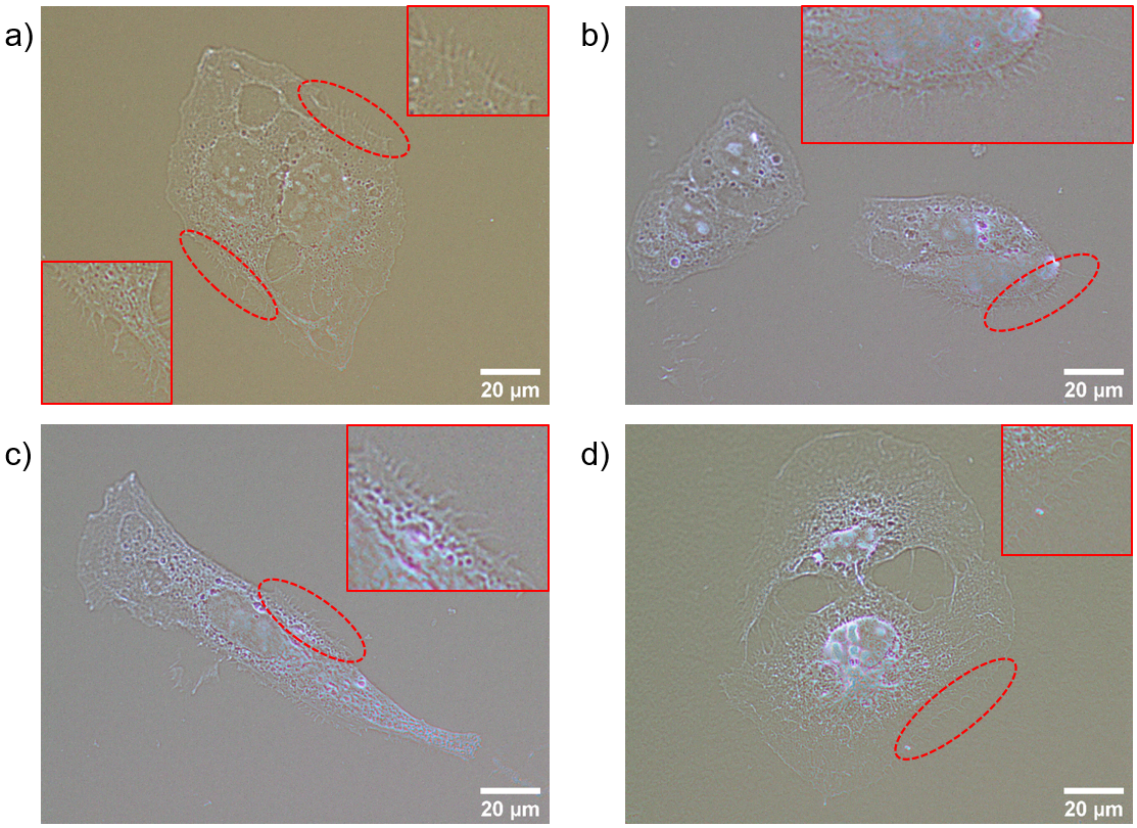

Figure 5.6: Optical micrographs of U2OS osteosarcoma cells grown on $MoSe_2$ Langmuir thin film substrates. Red circles indicate cell extensions; these are enlarged in the insets.

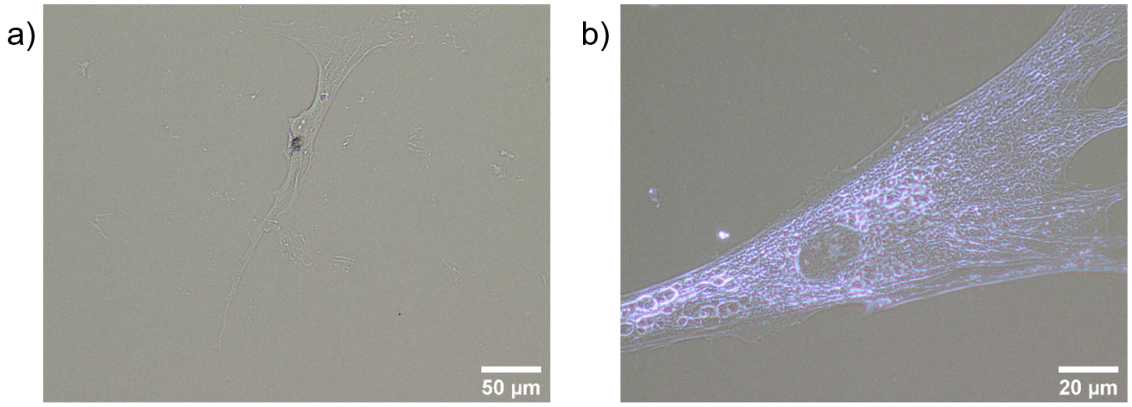

Figure 5.7: Optical micrographs of 1BR primary fibroblasts grown on $MoSe_2$ Langmuir thin film substrates.

metal. However, this experiment uses reseeded cells; it is possible that the cell lines grown on $MoSe_2$ may have internalised and then expelled the unwanted material within the initial 7 day growth period before trypsinisation and reseeding onto controls.

5.6 Conclusions

This work builds on the foundations laid by the initial MoS_2 internalisation study presented in Chapter 4 (from [318]). It is shown that the internalisation methodology — utilising cell–substrate interactions instead of passive material uptake from the cell media — is not unique to MoS_2, but is also shown for WS_2. As in the MoS_2 study, the sulfur chemistry is suggested to play an important role in the internalisation process. While $MoSe_2$ is not seen internalised within either cell line, it is still undetermined whether this is due to the material never having been internalised, or due to rapid internalisation and excretion of the material in the 7 day growth window before trypsinisation and reseeding for imaging. This requires further investigation by repeating these experiments at a range of growth windows. U2OS cells on $MoSe_2$ substrates are imaged with cell extensions, showing the active sensing processes at work. This approach has been shown to be generic to other TMDs in addition to MoS_2, opening the door to further potential theranostic applications utilising the various TMD materials.

Chapter 6

Conclusions and future work

Nanobiotechnology is a flourishing field in which nanotechnological advances are used to explore biological applications. Still, interactions between nanomaterials and cells or tissues are not well understood. To investigate cell–substrate interactions, it is therefore crucial to use well-characterised substrates. Presently, it is hard to ensure that substrates have the same properties from sample to sample because substrate synthesis is not standardised. This observation prompted the first aim of this thesis:

> Is it possible to define a methodology to ensure a controlled and tuneable production of two-dimensional (2D) thin film substrates?

The ability to control thin film production would allow properties of the thin film to be known from initial parameters set during synthesis. To become widely adopted, not only would any such method need to be easily applied, but production of the materials required would also need to be simple, scaleable, and standardised.

Work in Chapter 3 tackles this by utilising sonication-assisted liquid-phase exfoliated (LPE) nanomaterial dispersions. As discussed in 2.2.1, liquid-phase exfoliation by sonication (LPE) is known to be an easily scaleable method of nanomaterial production [120] with several standard characterisation metrics, making it a good choice for the development of a standardised film creation methodology. Several LPE materials (hexagonal boron nitride (BN), MoS_2, WS_2, and two sizes of graphene) were

used for Langmuir–Schaefer (L–S) deposition at a range of surface pressures, with the idea that it might be possible to predict the film surface area from measurements of the surface pressure and the material dimensions alone. Surface pressure–surface area plots were obtained after surface area was quantitatively measured by analysis of binary thresholds of optical micrographs of the films, but because film surface area depends on edge-edge interactions, normalisation for nanosheet size was necessary to assess the effect of intrinsic chemistry on the edge-edge interactions between nanosheets. These edge density effects start to be accounted for by plotting surface pressure against centre-to-centre interparticle distance. The 2D bulk modulus, which can quantify rigidity percolation, showed a similar rigidity onset and maximum for each material after normalisation for cohesion pressure (a term which describes long-range interactions between nanosheets). This straightforward process allows for an improved understanding of the physical and chemical influences on film formation, surface pressure, and surface coverage behaviour in Langmuir films of 2D layered nanomaterials.

The combination of variable surface coverage and edge functionalisation made Langmuir films of layered nanomaterials an interesting candidate for studies of cell growth and proliferation. Cell colonies were shown to form and to proliferate on thin film substrates; furthermore, the cells showed preference for the substrates with increased edge density. This emphasises the importance of control over thin film substrate production. The cell study served as an initial proof of concept for the second aim of this thesis:

> Most nano–bio studies introduce the nanomaterial to the cell by dispersion in the cell medium — can nanomaterials be introduced to the cell from the substrate alone? Does this change the effect on the cell?

Langmuir thin films for cell studies needed further exploration to fully address this question. Chapter 4 investigates this further, with focus on MoS_2 rather than graphene substrates due to the material's interesting chemistry. Cells were found

to exhibit mechanotransduction responses to the thin film substrate; stimulation of the cellular membrane proteins for sensing and recognition triggered uptake pathways. This method of introducing the cell to the nanomaterial leads to uptake to cell organelles such as the endoplasmic reticulum (ER); noninvasive 2D and three-dimensional (3D) Raman spectroscopy mapping showed internalisation to this structure. Moreover, different cell lines were tested and these cell–substrate interactions were shown to be generic to different types of cells with no toxicity. This is of particular interest for research into cancer cells due to their overactive mechanical substrate interactions and modified unfolded protein response (UPR).

It is unclear whether it is the molybdenum or sulfur components which are the main target of the uptake mechanism. Certainly, the internalisation of monolayer transition metal dichalcogenides (TMDs) holds particular benefits. The monolayers are inherently fluorescent and have unique wavelength-dependent Raman modes which opens up potential applications such as tracking or live cell imaging. The differing band gaps of the TMDs could provide a way to co-stain samples if the materials localise to different cellular regions. Photothermal or drug delivery therapies could also potentially be made possible due to material localisation, so this new approach to nanomaterial–cell interfacing could provide an exciting opportunity to develop the next generation of theranostics.

One way to test which of the molybdenum or sulfur components had the biggest effect on the internalisation of MoS_2 was to conduct further experiments on other TMDs. This is discussed in Chapter 5. Two new materials, WS_2 and $MoSe_2$, were used to create similar Langmuir thin film substrates. The same cell lines were tested for these materials as for MoS_2, namely, 1BR primary fibroblasts and U2OS osteosarcoma cells. While a reasonable amount of WS_2 was seen to be internalised by the 1BR fibroblasts, less appeared to be internalised in the U2OS cells, and very little $MoSe_2$ appeared to be internalised into either cell line.

The results from these initial experiments show that this internalisation methodology, where material uptake is mediated by cell mechanotransduction, is not unique to MoS_2, but is also shown in WS_2. The fact that little to no $MoSe_2$ internalisation is seen may bolster the hypothesis that the sulfur chemistry is what plays a particularly important role in the internalisation process, rather than the molybdenum. Although there is little $MoSe_2$ uptake, the reasons for this are still unclear and require further exploration. To ensure that any material present is within the cells, the cells were trypsinised at 7 days and reseeded onto pristine glass cover slips. This leaves open the question of whether the $MoSe_2$ was never internalised at all, or whether it was rapidly internalised and excreted within the first 7 days. Moreover, several cells which had grown on $MoSe_2$ substrates were imaged with noticeable cell extensions (although there was some evidence of this in the cells from the WS_2 substrates, far fewer cells were observed with this behaviour). This indicates some strong substrate interactions; whether this behaviour is due to cells trying to locate areas without $MoSe_2$, avoiding a toxic material, or due to a rapid attachment process to the nanomaterial is still unclear.

This places emphasis on the need of further study into the mechanotransduction processes. Despite the limitations on this preliminary research, it has suggested that the sulfur chemistry may play the starring role in the uptake pathways associated with this internalisation methodology. Among other tests needed to complete the work presented here, full biological characterisation experiments are required to understand the system; this includes detailed cytotoxicity assays and investigation of the UPR effects for cells grown on MoS_2, WS_2, and $MoSe_2$ substrates. Additionally, repeat tests at a range of growth windows with WS_2 and $MoSe_2$ are required, and comparisons with other nanomaterials may also give insight into the processes at work.

Better understanding of these processes will be key to realising cell imaging and drug delivery possibilities. With uptake and localisation of monolayer TMDs, fluorescent or Raman imaging is possible. Furthermore, this material internalisation

occurs without fixation or permeabilisation of the cells, so there is no reason that live cell imaging would not be possible. For TMDs which show localisation, such as MoS_2, the creation of drug delivery vectors is promising. With the known chemistries of these materials, then for example, adding drug groups via simple sulfur chemistry should be straightforward. Some specificity of the drug delivery may even be possible, because uptake seems to differ slightly between cancerous and healthy cells.

Looking ahead, one avenue to explore could be the extension of these initial experiments into the realm of biosensors. TMDs have previously been shown to be capable of sensing bovine serum albumin by surface plasmon resonance [326, 327] and of detecting dengue by electrochemical impedance spectroscopy [182]. This dengue biosensor is of particular interest as it also utilises the Langmuir deposition technique (although Solanki et al. use the Langmuir–Blodgett technique as opposed to the L–S technique used throughout this thesis). As mentioned in 2.4.2.3, the need to develop simple, cheap and sensitive biosensors has been brought into sharp relief over the past year since the advent of the ongoing COVID-19 pandemic. It seems possible that biosensors based on MoS_2, similar to that for dengue described by Solanki et al., could be developed towards the SARS-CoV-2 virus (or other viruses). This would be an interesting angle to explore in future work.

Bibliography

[1] N. Taniguchi, *On the basic concept of "nano-technology"*. In: *Proceedings of International Conference on Production Engineering*, vol. Part II, (Tokyo), Japan Society of Precision Engineering, 1974. Cited on 1.

[2] G. Binnig, H. Rohrer, Ch. Gerber and E. Weibel, *Tunneling through a controllable vacuum gap*. Applied Physics Letters, 1982, **40** (2) pp. 178–180. Cited on 1.

[3] G. Binnig, H. Rohrer, Ch. Gerber and E. Weibel, *Surface Studies by Scanning Tunneling Microscopy*. Physical Review Letters, 1982, **49** (1) pp. 57–61. Cited on 1.

[4] G. Binnig, C. F. Quate and Ch. Gerber, *Atomic Force Microscope*. Physical Review Letters, 1986, **56** (9) pp. 930–933. Cited on 1.

[5] E. Gazit and A. Mitraki, *Plenty of room for biology at the bottom: an introduction to bionanotechnology*, 2nd ed. Imperial College Press, London, 2013. Cited on 1, 2.

[6] K. S. Novoselov, A. K. Geim, S. V. Morozov, D. Jiang, Y. Zhang, S. V. Dubonos et al., *Electric Field Effect in Atomically Thin Carbon Films*. Science, 2004, **306** (5696) pp. 666–669. Cited on 2, 7, 9, 20, 58.

[7] P. S. Nnamchi and C. S. Obayi, *Chapter 4 - Electrochemical Characterization of Nanomaterials.* In: *Characterization of Nanomaterials*, S. Mohan Bhagyaraj, O. S. Oluwafemi, N. Kalarikkal and S. Thomas, eds., Micro and Nano Technologies, Woodhead Publishing, 2018, pp. 103–127. Cited on 3.

[8] A. V. Kolobov and J. Tominaga, *Two-Dimensional Transition-Metal Dichalcogenides*, Springer Series in Materials Science. Springer International Publishing, 2016. Cited on 7, 10, 11, 91.

[9] E. Osawa, *Superaromaticity*. Kagaku, 1970, **25** pp. 854–863. Cited on 7.

[10] H. W. Kroto, J. R. Heath, S. C. O'Brien, R. F. Curl and R. E. Smalley, *C_{60}: Buckminsterfullerene*. Nature, 1985, **318** (6042) pp. 162–163. Cited on 7.

[11] S. Iijima and T. Ichihashi, *Single-shell carbon nanotubes of 1-nm diameter*. Nature, 1993, **363** (6430) pp. 603–605. Cited on 7.

[12] D. S. Bethune, C. H. Kiang, M. S. de Vries, G. Gorman, R. Savoy, J. Vazquez et al., *Cobalt-catalysed growth of carbon nanotubes with single-atomic-layer walls*. Nature, 1993, **363** (6430) pp. 605–607. Cited on 7.

[13] S. Iijima, *Helical microtubules of graphitic carbon*. Nature, 1991, **354** (6348) pp. 56–58. Cited on 7.

[14] L. V. Radushkevich and V. Á. Lukyanovich, *O strukture ugleroda, obrazujucegosja pri termiceskom razlozenii okisi ugleroda na zeleznom kontakte*. Zhurnal Fizicheskoi Khimii, 1952, **26** (1) pp. 88–95. Cited on 7.

[15] M. Monthioux and V. L. Kuznetsov, *Who should be given the credit for the discovery of carbon nanotubes?*. Carbon, 2006, **44** (9) pp. 1621–1623. Cited on 7.

[16] X. Xu, R. Ray, Y. Gu, H. J. Ploehn, L. Gearheart, K. Raker et al., *Electrophoretic Analysis and Purification of Fluorescent Single-Walled Carbon Nanotube Fragments*. Journal of the American Chemical Society, 2004, **126** (40) pp. 12736–12737. Cited on 7.

[17] S. Anwar, H. Ding, M. Xu, X. Hu, Z. Li, J. Wang et al., *Recent Advances in Synthesis, Optical Properties, and Biomedical Applications of Carbon Dots*. ACS Applied Bio Materials, 2019, **2** (6) pp. 2317–2338. Cited on 7.

[18] H. P. Boehm, *Some aspects of the surface chemistry of carbon blacks and other carbons*. Carbon, 1994, **32** (5) pp. 759–769. Cited on 7.

[19] A. Oberlin, M. Endo and T. Koyama, *Filamentous growth of carbon through benzene decomposition*. Journal of Crystal Growth, 1976, **32** (3) pp. 335–349. Cited on 7.

[20] X. Zhou, Y. Wang, C. Gong, B. Liu and G. Wei, *Production, structural design, functional control, and broad applications of carbon nanofiber-based nanomaterials: A comprehensive review*. Chemical Engineering Journal, 2020, **402** p. 126189. Cited on 7.

[21] S. Iijima, M. Yudasaka, R. Yamada, S. Bandow, K. Suenaga, F. Kokai et al., *Nano-aggregates of single-walled graphitic carbon nano-horns*. Chemical Physics Letters, 1999, **309** (3) pp. 165–170. Cited on 7.

[22] P. J. F. Harris, S. C. Tsang, J. B. Claridge and M. L. H. Green, *High-resolution electron microscopy studies of a microporous carbon produced by arc-evaporation*. Journal of the Chemical Society, Faraday Transactions, 1994, **90** (18) pp. 2799–2802. Cited on 7.

[23] D. Ugarte, *Curling and closure of graphitic networks under electron-beam irradiation*. Nature, 1992, **359** (6397) pp. 707–709. Cited on 7.

[24] M. E. Plonska-Brzezinska, *Carbon Nano-Onions: A Review of Recent Progress in Synthesis and Applications*. ChemNanoMat, 2019, **5** (5) pp. 568–580. Cited on 7.

[25] A. H. Castro Neto, F. Guinea, N. M. R. Peres, K. S. Novoselov and A. K. Geim, *The electronic properties of graphene*. Reviews of Modern Physics, 2009, **81** (1) pp. 109–162. Cited on 7, 8, 9, 58.

[26] A. K. Geim and K. S. Novoselov, *The rise of graphene*. Nature Materials, 2007, **6** (3) pp. 183–191. Cited on 8, 58.

[27] F. Schäffel, *Chapter 2 - The Atomic Structure of Graphene and Its Few-layer Counterparts*. In: *Graphene: Fundamentals and emergent applications*, J. H. Warner, F. Schäffel, A. Bachmatiuk and M. H. Rümmeli, eds., Elsevier, 2013, pp. 5–59. Cited on 7, 8, 10.

[28] C. Lee, X. Wei, J. W. Kysar and J. Hone, *Measurement of the Elastic Properties and Intrinsic Strength of Monolayer Graphene*. Science, 2008, **321** (5887) pp. 385–388. Cited on 8.

[29] D. R. Cooper, B. D'Anjou, N. Ghattamaneni, B. Harack, M. Hilke, A. Horth et al., *Experimental Review of Graphene*. ISRN Condensed Matter Physics, 2012, **2012** pp. 1–56. Cited on 8.

[30] P. R. Wallace, *The Band Theory of Graphite*. Physical Review, 1947, **71** (9) pp. 622–634. Cited on 8, 9.

[31] S. Priyadarsini, S. Mohanty, S. Mukherjee, S. Basu and M. Mishra, *Graphene and graphene oxide as nanomaterials for medicine and biology application*. Journal of Nanostructure in Chemistry, 2018, **8** (2) pp. 123–137. Cited on 9.

[32] Y. Wang, Z. Li, J. Wang, J. Li and Y. Lin, *Graphene and graphene oxide: biofunctionalization and applications in biotechnology*. Trends in Biotechnology, 2011, **29** (5) pp. 205–212. Cited on 9.

[33] T. Kuila, S. Bose, A. K. Mishra, P. Khanra, N. H. Kim and J. H. Lee, *Chemical functionalization of graphene and its applications*. Progress in Materials Science, 2012, **57** (7) pp. 1061–1105. Cited on 10.

[34] S. S. Abbas, N. L. Kelly, G. Patias, J. V. Hanna and T. McNally, *Cysteamine functionalised reduced graphene oxide modification of maleated poly(propylene)*. Polymer, 2020, **203** p. 122750. Cited on 10.

[35] A. Midya, S. Mukherjee, S. Roy, S. Santra, N. Manna and S. K. Ray, *Selective chloroform sensor using thiol functionalized reduced graphene oxide at room temperature*. Materials Research Express, 2018, **5** (2) p. 025604. Cited on 10.

[36] Z. D. Seibers, E. Brim, S. Lee Pittelli, E. Beltran, M. L. Shofner and J. R. Reynolds, *Readily Dispersible Chemically Functionalized Reduced Graphene Oxide Nanosheets for Solution-Processable Electrodes and Conductive Coatings*. ACS Applied Nano Materials, 2020, **3** (11) pp. 11455–11464. Cited on 10.

[37] B. Radisavljevic, A. Radenovic, J. Brivio, V. Giacometti and A. Kis, *Single-layer MoS_2 transistors*. Nature Nanotechnology, 2011, **6** (3) pp. 147–150. Cited on 10.

[38] M. Chhowalla, H. S. Shin, G. Eda, L.-J. Li, K. P. Loh and H. Zhang, *The chemistry of two-dimensional layered transition metal dichalcogenide nanosheets*. Nature Chemistry, 2013, **5** (4) pp. 263–275. Cited on 10, 69, 91.

[39] J. Huo, R. Ge, Y. Liu, J. Guo, L. Lu, W. Chen et al., *Recent advances of two–dimensional molybdenum disulfide based materials: Synthesis, modification and applications in energy conversion and storage*. Sustainable Materials and Technologies, 2020, **24** p. e00161. Cited on 10, 11, 91.

[40] X. Zhu, R. Ding, Z. Wang, Y. Wang, X. Guo, Z. Song et al., *Recent advances in synthesis and biosensors of two-dimensional MoS2*. Nanotechnology, 2019, **30** (50) p. 502004. Cited on 10, 11, 91.

[41] J. V. Acrivos, W. Y. Liang, J. A. Wilson and A. D. Yoffe, *Optical studies of metal-semiconductor transmutations produced by intercalation*. Journal of Physics C: Solid State Physics, 1971, **4** (1) pp. L18–L20. Cited on 11.

[42] R. B. Somoano, V. Hadek and A. Rembaum, *Alkali metal intercalates of molybdenum disulfide*. The Journal of Chemical Physics, 1973, **58** (2) pp. 697–701. Cited on 11.

[43] M. Stanley Whittingham and F. R. Gamble, *The lithium intercalates of the transition metal dichalcogenides*. Materials Research Bulletin, 1975, **10** (5) pp. 363–371. Cited on 11.

[44] J. A. Woollam and R. B. Somoano, *Physics and chemistry of* $_{mos2}$ *intercalation compounds*. Materials Science and Engineering, 1977, **31** pp. 289–295. Cited on 11.

[45] P. Joensen, R. F. Frindt and S. R. Morrison, *Single-layer* MoS_2. Materials Research Bulletin, 1986, **21** (4) pp. 457–461. Cited on 11.

[46] M. Kamaratos and C. Papageorgopoulos, *Intercalation of* $MoS_2(0001)$ *with Fe, Ni and Pd*. Solid State Communications, 1987, **61** (9) pp. 567–569. Cited on 11.

[47] B. K. Miremadi and S. R. Morrison, *The intercalation and exfoliation of tungsten disulfide*. Journal of Applied Physics, 1988, **63** (10) pp. 4970–4974. Cited on 11.

[48] K. Chrissafis, M. Zamani, K. Kambas, J. Stoemenos, N. A. Economou, I. Samaras et al., *Structural studies of* MoS_2 *intercalated by lithium*. Materials Science and Engineering: B, 1989, **3** (1-2) pp. 145–151. Cited on 11.

[49] K. Lee, H.-Y. Kim, M. Lotya, J. N. Coleman, G.-T. Kim and G. S. Duesberg, *Electrical Characteristics of Molybdenum Disulfide Flakes Produced by Liquid Exfoliation*. Advanced Materials, 2011, **23** (36) pp. 4178–4182. Cited on 11, 15, 58.

[50] V. Podzorov, M. E. Gershenson, Ch. Kloc, R. Zeis and E. Bucher, *High-mobility field-effect transistors based on transition metal dichalcogenides*. Applied Physics Letters, 2004, **84** (17) pp. 3301–3303. Cited on 11.

[51] R. F. Frindt, *Single Crystals of MoS_2 Several Molecular Layers Thick*. Journal of Applied Physics, 1966, **37** (4) pp. 1928–1929. Cited on 11.

[52] A. Splendiani, L. Sun, Y. Zhang, T. Li, J. Kim, C.-Y. Chim et al., *Emerging Photoluminescence in Monolayer MoS_2*. Nano Letters, 2010, **10** (4) pp. 1271–1275. Cited on 11, 12.

[53] K. F. Mak, C. Lee, J. Hone, J. Shan and T. F. Heinz, *Atomically Thin MoS_2: A New Direct-Gap Semiconductor*. Physical Review Letters, 2010, **105** (13) p. 136805. Cited on 11.

[54] E. E. Smith, *Molybdenum disulfide as a lubricant additive*. ACS Division of Petroleum Chemistry, Inc. Preprints, 1956, **1** (3) pp. 85–97. Cited on 11.

[55] R. S. Barnett, *Review of recent U.S.A. publications on lubricating grease*. Wear, 1970, **16** (1-2) pp. 87–142. Cited on 11.

[56] J. P. G. Farr, *Molybdenum disulphide in lubrication. A review*. Wear, 1975, **35** (1) pp. 1–22. Cited on 11.

[57] M. H. Gwynn, *Catalysts for hydrogenation*. Oil & Soap, 1939, **16** (2) pp. 25–28. Cited on 11.

[58] A. A. Tolstopyatova, A. A. Balandin, V. Kh. Matyushenko and Yu. I. Petrov, *Kinetics of dehydrogenation and dehydration of alcohols and dehydrogenation of hydrocarbons on WS_2 and MoS_2 catalysts*. Bulletin of the Academy of Sciences of the USSR, Division of chemical science, 1961, **10** (4) pp. 537–544. Cited on 11.

[59] R. L. Wilson and C. Kemball, *Catalytic reactions of methyl mercaptan on disulfides of molybdenum and tungsten*. Journal of Catalysis, 1964, **3** (5) pp. 426–437. Cited on 11.

[60] P. Grange and B. Delmon, *The role of cobalt and molybdenum sulphides in hydrodesulphurisation catalysts: A review*. Journal of the Less Common Metals, 1974, **36** (1-2) pp. 353–360. Cited on 11.

[61] G. C. Stevens and T. Edmonds, *Catalytic activity of the basal and edge planes of molybdenum disulphide*. Journal of the Less Common Metals, 1977, **54** (2) pp. 321–330. Cited on 11.

[62] R. Tenne, *Inorganic nanotubes and fullerene-like nanoparticles*. Journal of Materials Research, 2006, **21** (11) pp. 2726–2743. Cited on 11.

[63] R. V. Kashid, D. J. Late, S. S. Chou, Y.-K. Huang, M. De, D. S. Joag et al., *Enhanced Field-Emission Behavior of Layered MoS_2 Sheets*. Small, 2013, **9** (16) pp. 2730–2734. Cited on 11.

[64] M. C. Lemme, L.-J. Li, T. Palacios and F. Schwierz, *Two-dimensional materials for electronic applications*. MRS Bulletin, 2014, **39** (8) pp. 711–718. Cited on 11.

[65] H. Xu, F. Liao, Z. Guo, X. Guo, P. Zhou, W. Bao et al., *Recent progress in two-dimensional transition metal dichalcogenides: Material synthesis for microelectronics*. Chinese Science Bulletin, 2017, **62** (36) pp. 4237–4255. Cited on 11.

[66] S. Letourneau, M. J. Young, N. M. Bedford, Y. Ren, A. Yanguas-Gil, A. U. Mane et al., *Structural Evolution of Molybdenum Disulfide Prepared by Atomic Layer Deposition for Realization of Large Scale Films in Microelectronic Applications*. ACS Applied Nano Materials, 2018, **1** (8) pp. 4028–4037. Cited on 11.

[67] Z. Gu, T. Zhang, J. Luo, Y. Wang, H. Liu, L. Chen et al., *MoS_2-on-AlN Enables High-Performance MoS_2 Field-Effect Transistors through Strain Engineering*. ACS Applied Materials & Interfaces, 2020, **12** (49) pp. 54972–54979. Cited on 11.

[68] X. Jing, Y. Illarionov, E. Yalon, P. Zhou, T. Grasser, Y. Shi et al., *Engineering Field Effect Transistors with 2D Semiconducting Channels: Status and Prospects*. Advanced Functional Materials, 2020, **30** (18) p. 1901971. Cited on 11.

[69] R. B. Somoano and A. Rembaum, *Superconductivity in Intercalated Molybdenum Disulfide*. Physical Review Letters, 1971, **27** (7) pp. 402–404. Cited on 11.

[70] V. P. Gupta, *Band structural properties of MoS_2 (molybdenite)*. Journal of Physics and Chemistry of Solids, 1980, **41** (7) pp. 757–760. Cited on 11.

[71] J. T. Ye, Y. J. Zhang, R. Akashi, M. S. Bahramy, R. Arita and Y. Iwasa, *Superconducting Dome in a Gate-Tuned Band Insulator*. Science, 2012, **338** (6111) pp. 1193–1196. Cited on 11.

[72] J. Biscaras, Z. Chen, A. Paradisi and A. Shukla, *Onset of two-dimensional superconductivity in space charge doped few-layer molybdenum disulfide*. Nature Communications, 2015, **6** (1) p. 8826. Cited on 11.

[73] J. M. Lu, O. Zheliuk, I. Leermakers, N. F. Q. Yuan, U. Zeitler, K. T. Law et al., *Evidence for two-dimensional Ising superconductivity in gated MoS_2*. Science, 2015, **350** (6266) pp. 1353–1357. Cited on 11.

[74] D. Costanzo, S. Jo, H. Berger and A. F. Morpurgo, *Gate-induced superconductivity in atomically thin MoS_2 crystals*. Nature Nanotechnology, 2016, **11** (4) pp. 339–344. Cited on 11.

[75] Y. Fang, J. Pan, J. He, R. Luo, D. Wang, X. Che et al., *Structure Re-determination and Superconductivity Observation of Bulk 1T MoS_2*. Angewandte Chemie International Edition, 2018, **57** (5) pp. 1232–1235. Cited on 11.

[76] D. J. Trainer, B. Wang, F. Bobba, N. Samuelson, X. Xi, J. Zasadzinski et al., *Proximity-Induced Superconductivity in Monolayer MoS_2*. ACS Nano, 2020, **14** (3) pp. 2718–2728. Cited on 11.

[77] E. Fortin and W. M. Sears, *Photovoltaic effect and optical absorption in MoS_2*. Journal of Physics and Chemistry of Solids, 1982, **43** (9) pp. 881–884. Cited on 11.

[78] J. C. Bernède, J. Pouzet, E. Gourmelon and H. Hadouda, *Recent studies on photoconductive thin films of binary compounds*. Synthetic Metals, 1999, **99** (1) pp. 45–52. Cited on 11.

[79] M. Bernardi, M. Palummo and J. C. Grossman, *Extraordinary Sunlight Absorption and One Nanometer Thick Photovoltaics Using Two-Dimensional Monolayer Materials*. Nano Letters, 2013, **13** (8) pp. 3664–3670. Cited on 11.

[80] G. Eda and S. A. Maier, *Two-Dimensional Crystals: Managing Light for Optoelectronics*. ACS Nano, 2013, **7** (7) pp. 5660–5665. Cited on 11.

[81] X. Hong, J. Kim, S.-F. Shi, Y. Zhang, C. Jin, Y. Sun et al., *Ultrafast charge transfer in atomically thin MoS_2/WS_2 heterostructures*. Nature Nanotechnology, 2014, **9** (9) pp. 682–686. Cited on 11.

[82] M. Long, E. Liu, P. Wang, A. Gao, H. Xia, W. Luo et al., *Broadband Photovoltaic Detectors Based on an Atomically Thin Heterostructure*. Nano Letters, 2016, **16** (4) pp. 2254–2259. Cited on 11.

[83] Y. Lin, B. Adilbekova, Y. Firdaus, E. Yengel, H. Faber, M. Sajjad et al., *17% Efficient Organic Solar Cells Based on Liquid Exfoliated WS_2 as a Replacement for PEDOT:PSS*. Advanced Materials, 2019, **31** (46) p. 1902965. Cited on 11.

[84] M. Bhatnagar, M. C. Giordano, C. Mennucci, D. Chowdhury, A. Mazzanti, G. D. Valle et al., *Ultra-broadband photon harvesting in large-area few-layer MoS_2 nanostripe gratings*. Nanoscale, 2020, **12** (48) pp. 24385–24393. Cited on 11.

[85] H. Lin, C. Wang, J. Wu, Z. Xu, Y. Huang and C. Zhang, *Colloidal synthesis of MoS_2 quantum dots: size-dependent tunable photoluminescence and bioimaging*. New Journal of Chemistry, 2015, **39** (11) pp. 8492–8497. Cited on 11.

[86] S. Xu, D. Li and P. Wu, *One-Pot, Facile, and Versatile Synthesis of Monolayer MoS_2/WS_2Quantum Dots as Bioimaging Probes and Efficient Electrocatalysts for Hydrogen Evolution Reaction*. Advanced Functional Materials, 2015, **25** (7) pp. 1127–1136. Cited on 11.

[87] W. Dai, H. Dong, B. Fugetsu, Y. Cao, H. Lu, X. Ma et al., *Tunable Fabrication of Molybdenum Disulfide Quantum Dots for Intracellular MicroRNA Detection and Multiphoton Bioimaging*. Small, 2015, **11** (33) pp. 4158–4164. Cited on 11.

[88] S. Tezuka, T. Seki, T. Ohnishi, H. Noguchi, M. Tanaka, M. Okochi et al., *In situ bioimaging of Lactobacillus by photoluminescence of MoS_2*. 2D Materials, 2020, **7** (2) p. 024002. Cited on 11.

[89] C. Zhu, Z. Zeng, H. Li, F. Li, C. Fan and H. Zhang, *Single-Layer MoS_2-Based Nanoprobes for Homogeneous Detection of Biomolecules*. Journal of the American Chemical Society, 2013, **135** (16) pp. 5998–6001. Cited on 11.

[90] J. Lee, P. Dak, Y. Lee, H. Park, W. Choi, M. A. Alam et al., *Two-dimensional Layered MoS_2 Biosensors Enable Highly Sensitive Detection of Biomolecules.* Scientific Reports, 2014, **4** (1) p. 7352. Cited on 11.

[91] D. Sarkar, W. Liu, X. Xie, A. C. Anselmo, S. Mitragotri and K. Banerjee, *MoS_2 Field-Effect Transistor for Next-Generation Label-Free Biosensors.* ACS Nano, 2014, **8** (4) pp. 3992–4003. Cited on 11.

[92] R.-M. Kong, L. Ding, Z. Wang, J. You and F. Qu, *A novel aptamer-functionalized MoS_2 nanosheet fluorescent biosensor for sensitive detection of prostate specific antigen.* Analytical and Bioanalytical Chemistry, 2015, **407** (2) pp. 369–377. Cited on 11.

[93] X. Gan, H. Zhao and X. Quan, *Two-dimensional MoS_2: A promising building block for biosensors.* Biosensors and Bioelectronics, 2017, **89** pp. 56–71. Cited on 11.

[94] Y.-H. Wang, K.-J. Huang and X. Wu, *Recent advances in transition-metal dichalcogenides based electrochemical biosensors: A review.* Biosensors and Bioelectronics, 2017, **97** pp. 305–316. Cited on 11.

[95] S. Barua, H. S. Dutta, S. Gogoi, R. Devi and R. Khan, *Nanostructured MoS_2-Based Advanced Biosensors: A Review.* ACS Applied Nano Materials, 2018, **1** (1) pp. 2–25. Cited on 11.

[96] P. Zhang, S. Yang, R. Pineda-Gómez, B. Ibarlucea, J. Ma, M. R. Lohe et al., *Electrochemically Exfoliated High-Quality 2H-MoS_2 for Multiflake Thin Film Flexible Biosensors.* Small, 2019, **15** (23) p. 1901265. Cited on 11.

[97] S. S. Chou, B. Kaehr, J. Kim, B. M. Foley, M. De, P. E. Hopkins et al., *Chemically Exfoliated MoS_2 as Near-Infrared Photothermal Agents.* Angewandte Chemie International Edition, 2013, **52** (15) pp. 4160–4164. Cited on 11.

[98] T. Liu, C. Wang, W. Cui, H. Gong, C. Liang, X. Shi et al., *Combined photothermal and photodynamic therapy delivered by PEGylated MoS_2 nanosheets*. Nanoscale, 2014, **6** (19) pp. 11219–11225. Cited on 11.

[99] S. Wang, K. Li, Y. Chen, H. Chen, M. Ma, J. Feng et al., *Biocompatible PEGylated MoS_2 nanosheets: Controllable bottom-up synthesis and highly efficient photothermal regression of tumor*. Biomaterials, 2015, **39** pp. 206–217. Cited on 11.

[100] J. Han, H. Xia, Y. Wu, S. N. Kong, A. Deivasigamani, R. Xu et al., *Single-layer MoS_2 nanosheet grafted upconversion nanoparticles for near-infrared fluorescence imaging-guided deep tissue cancer phototherapy*. Nanoscale, 2016, **8** (15) pp. 7861–7865. Cited on 11.

[101] L. Chen, Y. Feng, X. Zhou, Q. Zhang, W. Nie, W. Wang et al., *One-Pot Synthesis of MoS_2 Nanoflakes with Desirable Degradability for Photothermal Cancer Therapy*. ACS Applied Materials & Interfaces, 2017, **9** (20) pp. 17347–17358. Cited on 11.

[102] J. Shi, J. Li, Y. Wang, J. Cheng and C. Y. Zhang, *Recent advances in MoS_2-based photothermal therapy for cancer and infectious disease treatment*. Journal of Materials Chemistry B, 2020, **8** (27) pp. 5793–5807. Cited on 11.

[103] L. Joly-Pottuz, J. M. Martin, F. Dassenoy, C. Schuffenhauer, R. Tenne and N. Fleischer, *Inorganic Fullerene-Like Nanoparticles as New Lubricant Additives: A Drug Delivery Mechanism*. In: *World Tribology Congress III, Volume 1*, (Washington, D.C., USA), ASMEDC, 2005, pp. 613–614. Cited on 12.

[104] A. R. Adini, M. Redlich and R. Tenne, *Medical applications of inorganic fullerene-like nanoparticles*. Journal of Materials Chemistry, 2011, **21** (39) pp. 15121–15131. Cited on 12.

[105] B. L. Li, M. I. Setyawati, L. Chen, J. Xie, K. Ariga, C.-T. Lim et al., *Directing Assembly and Disassembly of 2D MoS_2 Nanosheets with DNA for Drug Delivery*. ACS Applied Materials & Interfaces, 2017, **9** (18) pp. 15286–15296. Cited on 12.

[106] L. Chen, J. Xu, Y. Wang and R. Huang, *Ultra-small MoS_2 nanodots-incorporated mesoporous silica nanospheres for pH-sensitive drug delivery and CT imaging*. Journal of Materials Science & Technology, 2021, **63** pp. 91–96. Cited on 12.

[107] T. Liu, C. Wang, X. Gu, H. Gong, L. Cheng, X. Shi et al., *Drug Delivery with PEGylated MoS_2 Nano-sheets for Combined Photothermal and Chemotherapy of Cancer*. Advanced Materials, 2014, **26** (21) pp. 3433–3440. Cited on 12, 76, 200.

[108] W. Yin, L. Yan, J. Yu, G. Tian, L. Zhou, X. Zheng et al., *High-Throughput Synthesis of Single-Layer MoS_2 Nanosheets as a Near-Infrared Photothermal-Triggered Drug Delivery for Effective Cancer Therapy*. ACS Nano, 2014, **8** (7) pp. 6922–6933. Cited on 12, 76, 200.

[109] X. Zhang, J. Wu, G. R. Williams, S. Niu, Q. Qian and L.-M. Zhu, *Functionalized MoS_2-nanosheets for targeted drug delivery and chemo-photothermal therapy*. Colloids and Surfaces B: Biointerfaces, 2019, **173** pp. 101–108. Cited on 12.

[110] Y. Yang, J. Wu, D. H. Bremner, S. Niu, Y. Li, X. Zhang et al., *A multifunctional nanoplatform based on MoS_2-nanosheets for targeted drug delivery and chemo-photothermal therapy*. Colloids and Surfaces B: Biointerfaces, 2020, **185** p. 110585. Cited on 12.

[111] K. K. Kim, S. M. Kim and Y. H. Lee, *A new horizon for hexagonal boron nitride film*. Journal of the Korean Physical Society, 2014, **64** (10) pp. 1605–1616. Cited on 12, 13.

[112] L. Liu, Y. P. Feng and Z. X. Shen, *Structural and electronic properties of h-BN*. Physical Review B, 2003, **68** (10) p. 104102. Cited on 12, 58.

[113] P. Miró, M. Audiffred and T. Heine, *An atlas of two-dimensional materials*. Chemical Society Reviews, 2014, **43** (18) pp. 6537–6554. Cited on 13.

[114] L. Song, L. Ci, H. Lu, P. B. Sorokin, C. Jin, J. Ni et al., *Large Scale Growth and Characterization of Atomic Hexagonal Boron Nitride Layers*. Nano Letters, 2010, **10** (8) pp. 3209–3215. Cited on 13.

[115] R. Arenal and A. Lopez-Bezanilla, *Boron nitride materials: an overview from 0D to 3D (nano)structures*. WIREs Computational Molecular Science, 2015, **5** (4) pp. 299–309. Cited on 13.

[116] V. L. Solozhenko, A. G. Lazarenko, J.-P. Petitet and A. V. Kanaev, *Bandgap energy of graphite-like hexagonal boron nitride*. Journal of Physics and Chemistry of Solids, 2001, **62** (7) pp. 1331–1334. Cited on 13.

[117] C. R. Dean, A. F. Young, I. Meric, C. Lee, L. Wang, S. Sorgenfrei et al., *Boron nitride substrates for high-quality graphene electronics*. Nature Nanotechnology, 2010, **5** (10) pp. 722–726. Cited on 13, 58.

[118] R. W. Harries, C. J. Brown, S. P. Ogilvie, M. J. Large, A. Amorim Graf, K. Clifford et al., *Langmuir Films of Layered Nanomaterials: Edge Interactions and Cell Culture Applications*. The Journal of Physical Chemistry B, 2020, **124** (33) pp. 7184–7193. Cited on 13, 76, 78.

[119] A. N. Esfahani, A. J. Malcolm, L. Xu, H. Yang, T. Storwick, N. Y. Kim et al., *Ultra-thin films of solution-exfoliated hexagonal boron nitride by Langmuir deposition*. Journal of Materials Chemistry C, 2020, **8** (39) pp. 13695–13704. Cited on 13.

[120] V. Nicolosi, M. Chhowalla, M. G. Kanatzidis, M. S. Strano and J. N. Coleman, *Liquid Exfoliation of Layered Materials*. Science, 2013, **340** (6139) p. 1226419. Cited on 14, 15, 16, 19, 58, 77, 100.

[121] Y. Hernandez, V. Nicolosi, M. Lotya, F. M. Blighe, Z. Sun, S. De et al., *High-yield production of graphene by liquid-phase exfoliation of graphite*. Nature Nanotechnology, 2008, **3** (9) pp. 563–568. Cited on 15, 16.

[122] J. N. Coleman, *Liquid-Phase Exfoliation of Nanotubes and Graphene*. Advanced Functional Materials, 2009, **19** (23) pp. 3680–3695. Cited on 15.

[123] G. P. Moriarty, S. De, P. J. King, U. Khan, M. Via, J. A. King et al., *Thermoelectric behavior of organic thin film nanocomposites*. Journal of Polymer Science Part B: Polymer Physics, 2013, **51** (2) pp. 119–123. Cited on 15.

[124] J. N. Coleman, M. Lotya, A. O'Neill, S. D. Bergin, P. J. King, U. Khan et al., *Two-Dimensional Nanosheets Produced by Liquid Exfoliation of Layered Materials*. Science, 2011, **331** (6017) pp. 568–571. Cited on 15, 17.

[125] G. Gao, W. Gao, E. Cannuccia, J. Taha-Tijerina, L. Balicas, A. Mathkar et al., *Artificially Stacked Atomic Layers: Toward New van der Waals Solids*. Nano Letters, 2012, **12** (7) pp. 3518–3525. Cited on 15.

[126] D. Hanlon, C. Backes, E. Doherty, C. S. Cucinotta, N. C. Berner, C. Boland et al., *Liquid exfoliation of solvent-stabilized few-layer black phosphorus for applications beyond electronics*. Nature Communications, 2015, **6** (1) p. 8563. Cited on 15.

[127] P. Yasaei, B. Kumar, T. Foroozan, C. Wang, M. Asadi, D. Tuschel et al., *High-Quality Black Phosphorus Atomic Layers by Liquid-Phase Exfoliation*. Advanced Materials, 2015, **27** (11) pp. 1887–1892. Cited on 15.

[128] J. N. Coleman, *Liquid Exfoliation of Defect-Free Graphene*. Accounts of Chemical Research, 2013, **46** (1) pp. 14–22. Cited on 15, 16.

[129] A. V. Tyurnina, I. Tzanakis, J. Morton, J. Mi, K. Porfyrakis, B. M. Maciejewska et al., *Ultrasonic exfoliation of graphene in water: A key parameter study*. Carbon, 2020, **168** pp. 737–747. Cited on 15.

[130] A. B. Bourlinos, V. Georgakilas, R. Zboril, T. A. Steriotis and A. K. Stubos, *Liquid-Phase Exfoliation of Graphite Towards Solubilized Graphenes*. Small, 2009, **5** (16) pp. 1841–1845. Cited on 16.

[131] G. P. Keeley, A. O'Neill, N. McEvoy, N. Peltekis, J. N. Coleman and G. S. Duesberg, *Electrochemical ascorbic acid sensor based on DMF-exfoliated graphene*. Journal of Materials Chemistry, 2010, **20** (36) pp. 7864–7869. Cited on 16.

[132] W. W. Liu and J. N. Wang, *Direct exfoliation of graphene in organic solvents with addition of NaOH*. Chemical Communications, 2011, **47** (24) pp. 6888–6890. Cited on 16.

[133] L. Guardia, J. I. Paredes, R. Rozada, S. Villar-Rodil, A. Martínez-Alonso and J. M. D. Tascón, *Production of aqueous dispersions of inorganic graphene analogues by exfoliation and stabilization with non-ionic surfactants*. RSC Advances, 2014, **4** (27) pp. 14115–14127. Cited on 16.

[134] A. Y. W. Sham and S. M. Notley, *Layer-by-Layer Assembly of Thin Films Containing Exfoliated Pristine Graphene Nanosheets and Polyethyleneimine*. Langmuir, 2014, **30** (9) pp. 2410–2418. Cited on 16.

[135] S. Mutyala and J. Mathiyarasu, *Preparation of graphene nanoflakes and its application for detection of hydrazine*. Sensors and Actuators B: Chemical, 2015, **210** pp. 692–699. Cited on 16.

[136] M. Zhang, R. C. T. Howe, R. I. Woodward, E. J. R. Kelleher, F. Torrisi, G. Hu et al., *Solution processed MoS_2-PVA composite for sub-bandgap mode-locking of a wideband tunable ultrafast Er:fiber laser*. Nano Research, 2015, **8** (5) pp. 1522–1534. Cited on 16.

[137] M. J. Large, S. P. Ogilvie, A. A. Graf, P. J. Lynch, M. A. O'Mara, T. Waters et al., *Large-Scale Surfactant Exfoliation of Graphene and Conductivity-Optimized Graphite Enabling Wireless Connectivity*. Advanced Materials Technologies, 2020, **5** (7) p. 2000284. Cited on 16, 18, 19, 23.

[138] V. Vega-Mayoral, C. Backes, D. Hanlon, U. Khan, Z. Gholamvand, M. O'Brien et al., *Photoluminescence from Liquid-Exfoliated WS_2 Monomers in Poly(Vinyl Alcohol) Polymer Composites*. Advanced Functional Materials, 2016, **26** (7) pp. 1028–1039. Cited on 16.

[139] W.-B. Tseng, C.-H. Lee and W.-L. Tseng, *Poly(diallydimethylammonium chloride)-Induced Dispersion and Exfoliation of Tungsten Disulfide for the Sensing of Glutathione and Catalytic Hydrogenation of p-Nitrophenol*. ACS Applied Nano Materials, 2018, **1** (12) pp. 6808–6817. Cited on 16.

[140] M. Pykal, K. Šafářová, K. Machalová Šišková, P. Jurečka, A. B. Bourlinos, R. Zbořil et al., *Lipid Enhanced Exfoliation for Production of Graphene Nanosheets*. The Journal of Physical Chemistry C, 2013, **117** (22) pp. 11800–11803. Cited on 16.

[141] H. Sim, J. Lee, B. Park, S. J. Kim, S. Kang, W. Ryu et al., *High-concentration dispersions of exfoliated MoS_2 sheets stabilized by freeze-dried silk fibroin powder*. Nano Research, 2016, **9** (6) pp. 1709–1722. Cited on 16.

[142] J. I. Paredes and S. Villar-Rodil, *Biomolecule-assisted exfoliation and dispersion of graphene and other two-dimensional materials: a review of recent progress and applications*. Nanoscale, 2016, **8** (34) pp. 15389–15413. Cited on 16.

[143] W. Du, X. Jiang and L. Zhu, *From graphite to graphene: direct liquid-phase exfoliation of graphite to produce single- and few-layered pristine graphene*. Journal of Materials Chemistry A, 2013, **1** (36) pp. 10592–10606. Cited on 16.

[144] Y. Hernandez, M. Lotya, D. Rickard, S. D. Bergin and J. N. Coleman, *Measurement of Multicomponent Solubility Parameters for Graphene Facilitates Solvent Discovery*. Langmuir, 2010, **26** (5) pp. 3208–3213. Cited on 16, 17, 61.

[145] C. M. Hansen, *Hansen Solubility Parameters: A User's Handbook*, 2nd ed. CRC Press, Boca Raton, Fla., 2007. Cited on 17.

[146] S. P. Ogilvie, M. J. Large, M. A. O'Mara, P. J. Lynch, C. L. Lee, A. A. K. King et al., *Size selection of liquid-exfoliated 2D nanosheets*. 2D Materials, 2019, **6** (3) p. 031002. Cited on 17.

[147] A. O'Neill, U. Khan and J. N. Coleman, *Preparation of High Concentration Dispersions of Exfoliated MoS_2 with Increased Flake Size*. Chemistry of Materials, 2012, **24** (12) pp. 2414–2421. Cited on 17.

[148] U. Khan, H. Porwal, A. O'Neill, K. Nawaz, P. May and J. N. Coleman, *Solvent-Exfoliated Graphene at Extremely High Concentration*. Langmuir, 2011, **27** (15) pp. 9077–9082. Cited on 17.

[149] T. W. Richards, *The Use of the Centrifuge.*. Journal of the American Chemical Society, 1908, **30** (2) pp. 285–286. Cited on 17.

[150] C. Backes, D. Campi, B. M. Szydłowska, K. Synnatschke, E. Ojala, F. Rashvand et al., *Equipartition of Energy Defines the Size–Thickness Relationship in Liquid-Exfoliated Nanosheets*. ACS Nano, 2019, **13** (6) pp. 7050–7061. Cited on 17, 62, 63.

[151] C. Backes, B. M. Szydłowska, A. Harvey, S. Yuan, V. Vega-Mayoral, B. R. Davies et al., *Production of Highly Monolayer Enriched Dispersions of Liquid-Exfoliated Nanosheets by Liquid Cascade Centrifugation*. ACS Nano, 2016, **10** (1) pp. 1589–1601. Cited on 17, 23, 38, 62, 63.

[152] R. Lødeng and H. Bergem, *7 - Stabilisation of pyrolysis oils.* In: *Direct Thermochemical Liquefaction for Energy Applications*, L. Rosendahl, ed., Woodhead Publishing, 2018, pp. 193–247. Cited on 18.

[153] W. Müller-Warmuth and R. Schöllhorn, *Progress in Intercalation Research*, Physics and Chemistry of Materials with Low-Dimensional Structures. Springer, Dordrecht, 1994. Cited on 19.

[154] E. Wiberg, A. F. Holleman and N. Wiberg, *Inorganic Chemistry*. Academic Press, 2001. Cited on 19.

[155] Y. Li, Y. Lu, P. Adelhelm, M.-M. Titirici and Y.-S. Hu, *Intercalation chemistry of graphite: alkali metal ions and beyond*. Chemical Society Reviews, 2019, **48** (17) pp. 4655–4687. Cited on 19.

[156] L. M. Xie, *Two-dimensional transition metal dichalcogenide alloys: preparation, characterization and applications*. Nanoscale, 2015, **7** (44) pp. 18392–18401. Cited on 20.

[157] X. Zhou, Q. Zhang, L. Gan, H. Li, J. Xiong and T. Zhai, *Booming Development of Group IV–VI Semiconductors: Fresh Blood of 2D Family*. Advanced Science, 2016, **3** (12) p. 1600177. Cited on 20.

[158] P. M. Martin, *Handbook of Deposition Technologies for Films and Coatings: Science, Applications and Technology*, 3rd ed. William Andrew Publishing, Oxford, 2009. Cited on 20.

[159] C. Soldano, A. Mahmood and E. Dujardin, *Production, properties and potential of graphene*. Carbon, 2010, **48** (8) pp. 2127–2150. Cited on 20.

[160] Grand View Research, *Chemical Vapor Deposition Market Size, Share & Trends Analysis Report By Category, By Applications (Microelectronics, Data Storage, Solar Products, Cutting Tools, Medical Equipment), By Region, And Segment Forecasts, 2018 - 2025.* (report) 2017. Cited on 20.

[161] A. Fahimi, I. Jurewicz, R. J. Smith, C. S. Sharrock, D. A. Bradley, S. J. Henley et al., *Density controlled conductivity of pristine graphene films*. Carbon, 2013, **64** pp. 435–443. Cited on 20, 60.

[162] M. J. Large, S. P. Ogilvie, A. A. K. King and A. B. Dalton, *Understanding Solvent Spreading for Langmuir Deposition of Nanomaterial Films: A Hansen Solubility Parameter Approach*. Langmuir, 2017, **33** (51) pp. 14766–14771. Cited on 21, 60, 61, 78.

[163] A. Pockels, *On the Spreading of Oil upon Water*. Nature, 1894, **50** (1288) pp. 223–224. Cited on 21, 58.

[164] K. B. Blodgett, *Films Built by Depositing Successive Monomolecular Layers on a Solid Surface*. Journal of the American Chemical Society, 1935, **57** (6) pp. 1007–1022. Cited on 21, 22.

[165] D. K. Schwartz, *Langmuir-Blodgett film structure*. Surface Science Reports, 1997, **27** (7-8) pp. 245–334. Cited on 21, 61.

[166] M. Bodik, M. Jergel, E. Majkova and P. Siffalovic, *Langmuir films of low-dimensional nanomaterials*. Advances in Colloid and Interface Science, 2020, **283** p. 102239. Cited on 21, 22.

[167] I. Langmuir, V. J. Schaefer and D. M. Wrinch, *Built-up Films of Proteins and Their Properties*. Science, 1937, **85** (2194) pp. 76–80. Cited on 22.

[168] J. J. Ramsden, *Chapter 6 - Nanomaterials and their Production*. In: *Nanotechnology: An Introduction*, J. J. Ramsden, ed., Micro and Nano Technologies, (Oxford), William Andrew Publishing, 2011, pp. 101–124. Cited on 22.

[169] R. Castillo, S. Ramos and J. Ruiz-Garcia, *Direct Observation of Langmuir Films of C_{60} and C_{70} Using Brewster Angle Microscopy*. The Journal of Physical Chemistry, 1996, **100** (37) pp. 15235–15241. Cited on 22.

[170] F. Lu, E. A. Neal and T. Nakanishi, *Self-Assembled and Nonassembled Alkylated-Fullerene Materials*. Accounts of Chemical Research, 2019, **52** (7) pp. 1834–1843. Cited on 22.

[171] Y. Wu, H. Fan, C. Yang and L. Zhang, *Pyrene-based amphiphile regulated C_{60} aggregation in monolayers and Langmuir–Blodgett films*. Colloids and Surfaces A: Physicochemical and Engineering Aspects, 2020, **585** p. 124111. Cited on 22.

[172] S. Capone, M. G. Manera, A. Taurino, P. Siciliano, R. Rella, S. Luby et al., *Fe_3O_4/γ-Fe_2O_3 Nanoparticle Multilayers Deposited by the Langmuir–Blodgett Technique for Gas Sensors Application*. Langmuir, 2014, **30** (4) pp. 1190–1197. Cited on 22.

[173] M. Tahghighi, I. Mannelli, D. Janner and J. Ignés-Mullol, *Tailoring plasmonic response by Langmuir–Blodgett gold nanoparticle templating for the fabrication of SERS substrates*. Applied Surface Science, 2018, **447** pp. 416–422. Cited on 22.

[174] M. E. Villanueva, A. E. Lanterna and R. V. Vico, *Hydrophobic silver nanoparticles interacting with phospholipids and stratum corneum mimic membranes in Langmuir monolayers*. Journal of Colloid and Interface Science, 2019, **543** pp. 247–255. Cited on 22.

[175] X. Li, L. Zhang, X. Wang, I. Shimoyama, X. Sun, W.-S. Seo et al., *Langmuir−Blodgett Assembly of Densely Aligned Single-Walled Carbon Nanotubes from Bulk Materials*. Journal of the American Chemical Society, 2007, **129** (16) pp. 4890–4891. Cited on 22.

[176] G. Giancane, A. Ruland, V. Sgobba, D. Manno, A. Serra, G. M. Farinola et al., *Aligning Single-Walled Carbon Nanotubes By Means Of Langmuir–Blodgett Film Deposition: Optical, Morphological, and Photo-electrochemical Studies*. Advanced Functional Materials, 2010, **20** (15) pp. 2481–2488. Cited on 22.

[177] Q. Cao, S.-j. Han, G. S. Tulevski, Y. Zhu, D. D. Lu and W. Haensch, *Arrays of single-walled carbon nanotubes with full surface coverage for high-performance electronics*. Nature Nanotechnology, 2013, **8** (3) pp. 180–186. Cited on 22.

[178] A. Tao, F. Kim, C. Hess, J. Goldberger, R. He, Y. Sun et al., *Langmuir−Blodgett Silver Nanowire Monolayers for Molecular Sensing Using Surface-Enhanced Raman Spectroscopy*. Nano Letters, 2003, **3** (9) pp. 1229–1233. Cited on 22.

[179] K. H. Park, B. H. Kim, S. H. Song, J. Kwon, B. S. Kong, K. Kang et al., *Exfoliation of Non-Oxidized Graphene Flakes for Scalable Conductive Film*. Nano Letters, 2012, **12** (6) pp. 2871–2876. Cited on 22.

[180] H. Kim, C. Mattevi, H. J. Kim, A. Mittal, K. A. Mkhoyan, R. E. Riman et al., *Optoelectronic properties of graphene thin films deposited by a Langmuir–Blodgett assembly*. Nanoscale, 2013, **5** (24) pp. 12365–12374. Cited on 22.

[181] A. Matković, I. Milošević, M. Milićević, T. Tomašević-Ilić, J. Pešić, M. Musić et al., *Enhanced sheet conductivity of Langmuir–Blodgett assembled graphene thin films by chemical doping*. 2D Materials, 2016, **3** (1) p. 015002. Cited on 22.

[182] S. Solanki, A. Soni, M. K. Pandey, A. Biradar and G. Sumana, *Langmuir–Blodgett Nanoassemblies of the MoS_2–Au Composite at the Air–Water Interface for Dengue Detection*. ACS Applied Materials & Interfaces, 2018, **10** (3) pp. 3020–3028. Cited on 22, 59, 90, 104.

[183] A. Kalosi, M. Demydenko, M. Bodik, J. Hagara, M. Kotlar, D. Kostiuk et al., *Tailored Langmuir–Schaefer Deposition of Few-Layer MoS_2 Nanosheet Films for Electronic Applications*. Langmuir, 2019, **35** (30) pp. 9802–9808. Cited on 22, 59.

[184] M. Bodik, M. Demydenko, T. Shabelnyk, Y. Halahovets, M. Kotlar, D. Kostiuk et al., *Collapse Mechanism in Few-Layer MoS_2 Langmuir Films*. The Journal of Physical Chemistry C, 2020, **124** (29) pp. 15856–15861. Cited on 22.

[185] H. Kaur, S. Yadav, A. K. Srivastava, N. Singh, J. J. Schneider, Om. P. Sinha et al., *Large Area Fabrication of Semiconducting Phosphorene by Langmuir-Blodgett Assembly*. Scientific Reports, 2016, **6** (1) p. 34095. Cited on 22.

[186] D. B. Murphy and M. W. Davidson, *Fundamentals of Light Microscopy and Electronic Imaging*, 2nd ed. John Wiley & Sons, Inc., Hoboken, NJ, USA, 2013. Cited on 26, 27, 28, 29, 30.

[187] R. Wayne, *Light and Video Microscopy*. Academic Press, Amsterdam, Boston, 2009. Cited on 26, 30, 31.

[188] G. Wang and N. Fang, *Detecting and Tracking Nonfluorescent Nanoparticle Probes in Live Cells*. In: *Methods in Enzymology*, vol. 504, Elsevier, 2012, pp. 83–108. Cited on 26, 29.

[189] S. H. Gage, *Modern Dark-Field Microscopy and the History of Its Development*. Transactions of the American Microscopical Society, 1920, **39** (2) pp. 95–141. Cited on 28.

[190] S. B. Mehta and C. J. R. Sheppard, *Partially coherent image formation in differential interference contrast (DIC) microscope*. Optics Express, 2008, **16** (24) pp. 19462–19479. Cited on 29.

[191] R. D. Allen, G. B. David and G. Nomarski, *The Zeiss-Nomarski differential interference equipment for transmitted-light microscopy*. Zeitschrift für wissenschaftliche Mikroskopie und mikroskopische Technik, 1969, **69** (4) pp. 193–221. Cited on 29.

[192] M. Tsunoda, D. Isailovic and E. S. Yeung, *Real-time three-dimensional imaging of cell division by differential interference contrast microscopy*. Journal of Microscopy, 2008, **232** (2) pp. 207–211. Cited on 30.

[193] J. R. Ferraro, K. Nakamoto and C. W. Brown, *Introductory Raman Spectroscopy*, 2nd ed. Academic Press, 2003. Cited on 31, 33.

[194] J. Tyndall, *IV. On the blue colour of the sky, the polarization of skylight, and on the polarization of light by cloudy matter generally*. Proceedings of the Royal Society of London, 1869, **17** pp. 223–233. Cited on 31.

[195] Lord Rayleigh, *XXXIV. On the transmission of light through an atmosphere containing small particles in suspension, and on the origin of the blue of the sky*. The London, Edinburgh, and Dublin Philosophical Magazine and Journal of Science, 1899, **47** (287) pp. 375–384. Cited on 31.

[196] Dissemination of IT for the Promotion of Materials Science (DoITPoMS), *Teaching & Learning Packages Library - Raman Spectroscopy - Method (dispersive Raman spectroscopy)*. [Accessed 2021-02-22]. Cited on 33.

[197] N. Colthup, L. Daly and S. Wiberley, *Introduction to Infrared and Raman Spectroscopy*, 3rd ed. Academic Press, 1990. Cited on 33.

[198] F. Tuinstra and J. L. Koenig, *Raman Spectrum of Graphite*. The Journal of Chemical Physics, 1970, **53** (3) pp. 1126–1130. Cited on 33.

[199] A. C. Ferrari, J. C. Meyer, V. Scardaci, C. Casiraghi, M. Lazzeri, F. Mauri et al., *Raman Spectrum of Graphene and Graphene Layers*. Physical Review Letters, 2006, **97** (18) p. 187401. Cited on 33.

[200] A. C. Ferrari, *Raman spectroscopy of graphene and graphite: Disorder, electron–phonon coupling, doping and nonadiabatic effects*. Solid State Communications, 2007, **143** (1) pp. 47–57. Cited on 33.

[201] A. C. Ferrari and D. M. Basko, *Raman spectroscopy as a versatile tool for studying the properties of graphene*. Nature Nanotechnology, 2013, **8** (4) pp. 235–246. Cited on 33.

[202] C. Backes, K. R. Paton, D. Hanlon, S. Yuan, M. I. Katsnelson, J. Houston et al., *Spectroscopic metrics allow in situ measurement of mean size and thickness of liquid-exfoliated few-layer graphene nanosheets*. Nanoscale, 2016, **8** (7) pp. 4311–4323. Cited on 33, 35, 62.

[203] A. Amorim Graf, S. P. Ogilvie, H. J. Wood, C. J. Brown, M. Tripathi, A. A. K. King et al., *Raman metrics for molybdenum disulfide and graphene enable statistical mapping of nanosheet populations*. Chemistry of Materials, 2020, **32** (14) pp. 6213–6221. Cited on 34, 78, 82.

[204] Sobarwiki, *Schematic of UV-visible spectrophotometer*. 2013. [Accessed 2021-02-19]. Cited on 34.

[205] C. Backes, R. J. Smith, N. McEvoy, N. C. Berner, D. McCloskey, H. C. Nerl et al., *Edge and confinement effects allow in situ measurement of size and thickness of liquid-exfoliated nanosheets*. Nature Communications, 2014, **5** (1) p. 4576. Cited on 35, 38, 62, 63.

[206] A. Griffin, A. Harvey, B. Cunningham, D. Scullion, T. Tian, C.-J. Shih et al., *Spectroscopic Size and Thickness Metrics for Liquid-Exfoliated h-BN*. Chemistry of Materials, 2018, **30** (6) pp. 1998–2005. Cited on 35, 38, 62, 63.

[207] K. Synnatschke, P. A. Cieslik, A. Harvey, A. Castellanos-Gomez, T. Tian, C.-J. Shih et al., *Length- and Thickness-Dependent Optical Response of Liquid-Exfoliated Transition Metal Dichalcogenides*. Chemistry of Materials, 2019, **31** (24) pp. 10049–10062. Cited on 35.

[208] B. M. Szydłowska, O. Hartwig, B. Tywoniuk, T. Hartman, T. Stimpel-Lindner, Z. Sofer et al., *Spectroscopic thickness and quality metrics for $PtSe_2$ layers produced by top-down and bottom-up techniques*. 2D Materials, 2020, **7** (4) p. 045027. Cited on 35.

[209] G. Haugstad, *Atomic Force Microscopy: Understanding Basic Modes and Advanced Applications*. John Wiley & Sons, Inc., Hoboken, NJ, USA, 2012. Cited on 36.

[210] B. Voigtländer, *Scanning Probe Microscopy: Atomic Force Microscopy and Scanning Tunneling Microscopy*, NanoScience and Technology. Springer Berlin Heidelberg, Berlin, Heidelberg, 2015. Cited on 37.

[211] Dissemination of IT for the Promotion of Materials Science (DoITPoMS), *Teaching & Learning Packages Library - Atomic Force Microscopy - Tip Surface Interaction*. [Accessed 2021-02-16]. Cited on 38.

[212] C. Backes, T. M. Higgins, A. Kelly, C. Boland, A. Harvey, D. Hanlon et al., *Guidelines for Exfoliation, Characterization and Processing of Layered Materials Produced by Liquid Exfoliation*. Chemistry of Materials, 2017, **29** (1) pp. 243–255. Cited on 38, 78.

[213] C. A. Schneider, W. S. Rasband and K. W. Eliceiri, *NIH Image to ImageJ: 25 years of image analysis*. Nature Methods, 2012, **9** (7) pp. 671–675. Cited on 39.

[214] Ü. Anık, S. Timur and Z. Dursun, *Recent pros and cons of nanomaterials in drug delivery systems*. International Journal of Polymeric Materials and Polymeric Biomaterials, 2020, **69** (17) pp. 1090–1100. Cited on 45.

[215] A. F. Palonpon, J. Ando, H. Yamakoshi, K. Dodo, M. Sodeoka, S. Kawata et al., *Raman and SERS microscopy for molecular imaging of live cells*. Nature Protocols, 2013, **8** (4) pp. 677–692. Cited on 47.

[216] S. Hong, T. Chen, Y. Zhu, A. Li, Y. Huang and X. Chen, *Live-Cell Stimulated Raman Scattering Imaging of Alkyne-Tagged Biomolecules*. Angewandte Chemie International Edition, 2014, **53** (23) pp. 5827–5831. Cited on 47.

[217] A. Kasouni, T. Chatzimitakos and C. Stalikas, *Bioimaging Applications of Carbon Nanodots: A Review*. C, 2019, **5** (2) p. 19. Cited on 48.

[218] T.-H. Kim, D. Lee and J.-W. Choi, *Live cell biosensing platforms using graphene-based hybrid nanomaterials*. Biosensors and Bioelectronics, 2017, **94** (Supplement C) pp. 485–499. Cited on 48.

[219] A. A. Ibn Sina, K. M. Koo, M. Ahmed, L. G. Carrascosa and M. Trau, *Interfacial Biosensing: Direct Biosensing of Biomolecules at the Bare Metal Interface*. In: *Encyclopedia of Interfacial Chemistry*, K. Wandelt, ed., (Oxford, UK), Elsevier, 2018, pp. 269–277. Cited on 49.

[220] A. P. F. Turner, I. Karube and G. S. Wilson, *Biosensors: Fundamentals and Applications*. Oxford University Press, Oxford, UK, 1987. Cited on 49.

[221] H. Kaur and M. Shorie, *Nanomaterial based aptasensors for clinical and environmental diagnostic applications*. Nanoscale Advances, 2019, **1** (6) pp. 2123–2138. Cited on 49.

[222] M. Moreno, *Sensors | Aptasensors*. In: *Encyclopedia of Analytical Science*, P. Worsfold, C. Poole, A. Townshend and M. Miró, eds., (Oxford, UK), Academic Press, 2019, pp. 150–153. Cited on 49.

[223] A. P. F. Turner, *Biosensors: sense and sensibility*. Chemical Society Reviews, 2013, **42** (8) pp. 3184–3196. Cited on 49.

[224] E. Vermisoglou, D. Panáček, K. Jayaramulu, M. Pykal, I. Frébort, M. Kolář et al., *Human virus detection with graphene-based materials*. Biosensors and Bioelectronics, 2020, **166** p. 112436. Cited on 49, 50.

[225] D. S. Chauhan, R. Prasad, R. Srivastava, M. Jaggi, S. C. Chauhan and M. M. Yallapu, *Comprehensive Review on Current Interventions, Diagnostics, and Nanotechnology Perspectives against SARS-CoV-2*. Bioconjugate Chemistry, 2020, **31** (9) pp. 2021–2045. Cited on 49.

[226] M. Soler, M. C. Estevez, M. Cardenosa-Rubio, A. Astua and L. M. Lechuga, *How Nanophotonic Label-Free Biosensors Can Contribute to Rapid and Massive Diagnostics of Respiratory Virus Infections: COVID-19 Case*. ACS Sensors, 2020, **5** (9) pp. 2663–2678. Cited on 49.

[227] J. B. Vines, J.-H. Yoon, N.-E. Ryu, D.-J. Lim and H. Park, *Gold Nanoparticles for Photothermal Cancer Therapy*. Frontiers in Chemistry, 2019, **7** . Cited on 51.

[228] A. K. Nayak, S. A. Ahmad, S. Beg, T. J. Ara and M. S. Hasnain, *12 - Drug delivery: Present, past, and future of medicine*. In: *Applications of Nanocomposite Materials in Drug Delivery*, Inamuddin, A. M. Asiri and A. Mohammad, eds., Woodhead Publishing Series in Biomaterials, Woodhead Publishing, 2018, pp. 255–282. Cited on 51.

[229] European Science Foundation (ESF), *Nanomedicine: An ESF–European Medical Research Councils (EMRC) Forward Look Report*. (report) 2005. Cited on 51.

[230] E. Andronescu and A. M. Grumezescu, eds., *Nanostructures for Drug Delivery*, Nanostructures in Therapeutic Medicine Series. Elsevier, Amsterdam, Netherlands, 2017. Cited on 51.

[231] D. Plachá and J. Jampilek, *Graphenic Materials for Biomedical Applications*. Nanomaterials, 2019, **9** (12) p. 1758. Cited on 52.

[232] Q. Guo, X.-t. Shen, Y.-y. Li and S.-q. Xu, *Carbon nanotubes-based drug delivery to cancer and brain*. Journal of Huazhong University of Science and Technology [Medical Sciences], 2017, **37** (5) pp. 635–641. Cited on 52.

[233] Y. Wang, M. Qiu, M. Won, E. Jung, T. Fan, N. Xie et al., *Emerging 2D material-based nanocarrier for cancer therapy beyond graphene*. Coordination Chemistry Reviews, 2019, **400** p. 213041. Cited on 52.

[234] C. S. Potten and J. W. Wilson, *Chapter 39 - The Development of Epithelial Stem Cell Concepts*. In: *Handbook of Stem Cells*, R. Lanza and A. Atala, eds., (San Diego, Calif.), Academic Press, 2013, pp. 451–461. Cited on 52.

[235] A. David and E. Chinedu, *The importance of toxicity testing*. Journal of Pharmaceutical and BioSciences, 2013, **1** (4) p. 3. Cited on 53.

[236] International Union of Pure and Applied Chemistry (IUPAC), *"acute toxicity"*. In: *Compendium of Chemical Terminology (The "Gold Book") Online version*, S. J. Chalk, A. D. McNaught and A. Wilkinson, eds., 2019. Cited on 54.

[237] J. M. Anderson, *4.402 - Biocompatibility and the Relationship to Standards: Meaning and Scope of Biomaterials Testing*. In: *Comprehensive Biomaterials*, P. Ducheyne, ed., (Oxford), Elsevier, 2011, pp. 7–26. Cited on 54.

[238] W. H. De Jong, J. W. Carraway and R. E. Geertsma, *7 - In vivo and in vitro testing for the biological safety evaluation of biomaterials and medical devices*. In: *Biocompatibility and Performance of Medical Devices*, J.-P. Boutrand, ed., Woodhead Publishing Series in Biomaterials, Woodhead Publishing, 2012, pp. 120–158. Cited on 54.

[239] C. K. Sudhakar, N. Upadhyay, A. Verma, A. Jain, R. Narayana Charyulu and S. Jain, *Chapter 1 - Nanomedicine and Tissue Engineering*. In: *Nanotechnology Applications for Tissue Engineering*, S. Thomas, Y. Grohens and N. Ninan, eds., (Oxford), William Andrew Publishing, 2015, pp. 1–19. Cited on 54.

[240] R. G. Bai, K. Muthoosamy and S. Manickam, *Chapter 12 - Nanomedicine in Theranostics*. In: *Nanotechnology Applications for Tissue Engineering*, S. Thomas, Y. Grohens and N. Ninan, eds., (Oxford), William Andrew Publishing, 2015, pp. 195–213. Cited on 55.

[241] N. Panwar, A. M. Soehartono, K. K. Chan, S. Zeng, G. Xu, J. Qu et al., *Nanocarbons for Biology and Medicine: Sensing, Imaging, and Drug Delivery*. Chemical Reviews, 2019, **119** (16) pp. 9559–9656. Cited on 55.

[242] M. Hassan, V. G. Gomes, A. Dehghani and S. M. Ardekani, *Engineering carbon quantum dots for photomediated theranostics*. Nano Research, 2018, **11** (1) pp. 1–41. Cited on 55.

[243] X.-L. Hu, N. Kwon, K.-C. Yan, A. C. Sedgwick, G.-R. Chen, X.-P. He et al., *Bio-Conjugated Advanced Materials for Targeted Disease Theranostics*. Advanced Functional Materials, 2020, **30** (13) p. 1907906. Cited on 55.

[244] L. Gong, L. Yan, R. Zhou, J. Xie, W. Wu and Z. Gu, *Two-dimensional transition metal dichalcogenide nanomaterials for combination cancer therapy*. Journal of Materials Chemistry B, 2017, **5** (10) pp. 1873–1895. Cited on 55.

[245] B. Yang, Y. Chen and J. Shi, *Material Chemistry of Two-Dimensional Inorganic Nanosheets in Cancer Theranostics*. Chem, 2018, **4** (6) pp. 1284–1313. Cited on 55.

[246] I. S. Raja, M. S. Kang, K. S. Kim, Y. J. Jung and D.-W. Han, *Two-Dimensional Theranostic Nanomaterials in Cancer Treatment: State of the Art and Perspectives*. Cancers, 2020, **12** (6) p. 1657. Cited on 55.

[247] Z. Mohammadpour and K. Majidzadeh-A, *Applications of Two-Dimensional Nanomaterials in Breast Cancer Theranostics*. ACS Biomaterials Science & Engineering, 2020, **6** (4) pp. 1852–1873. Cited on 55.

[248] K. R. Paton, E. Varrla, C. Backes, R. J. Smith, U. Khan, A. O'Neill et al., *Scalable production of large quantities of defect-free few-layer graphene by shear exfoliation in liquids*. Nature Materials, 2014, **13** (6) pp. 624–630. Cited on 58, 63, 77.

[249] F. Bonaccorso, Z. Sun, T. Hasan and A. C. Ferrari, *Graphene photonics and optoelectronics*. Nature Photonics, 2010, **4** (9) pp. 611–622. Cited on 58.

[250] A. A. Balandin, *Thermal properties of graphene and nanostructured carbon materials*. Nature Materials, 2011, **10** (8) pp. 569–581. Cited on 58.

[251] G. Eda, H. Yamaguchi, D. Voiry, T. Fujita, M. Chen and M. Chhowalla, *Photoluminescence from Chemically Exfoliated MoS_2*. Nano Letters, 2011, **11** (12) pp. 5111–5116. Cited on 58, 76.

[252] Q. H. Wang, K. Kalantar-Zadeh, A. Kis, J. N. Coleman and M. S. Strano, *Electronics and optoelectronics of two-dimensional transition metal dichalcogenides*. Nature Nanotechnology, 2012, **7** (11) pp. 699–712. Cited on 58.

[253] M. Xu, T. Liang, M. Shi and H. Chen, *Graphene-Like Two-Dimensional Materials*. Chemical Reviews, 2013, **113** (5) pp. 3766–3798. Cited on 58.

[254] X.-H. Zha, J. Yin, Y. Zhou, Q. Huang, K. Luo, J. Lang et al., *Intrinsic Structural, Electrical, Thermal, and Mechanical Properties of the Promising Conductor Mo_2C MXene*. The Journal of Physical Chemistry C, 2016, **120** (28) pp. 15082–15088. Cited on 58.

[255] K. Hantanasirisakul and Y. Gogotsi, *Electronic and Optical Properties of 2D Transition Metal Carbides and Nitrides (MXenes)*. Advanced Materials, 2018, **30** (52) p. 1804779. Cited on 58.

[256] X.-H. Zha, J. Zhou, Y. Zhou, Q. Huang, J. He, J. S. Francisco et al., *Promising electron mobility and high thermal conductivity in Sc_2CT_2 (T = F, OH) MXenes*. Nanoscale, 2016, **8** (11) pp. 6110–6117. Cited on 58.

[257] H. J. Yoon, T. H. Kim, Z. Zhang, E. Azizi, T. M. Pham, C. Paoletti et al., *Sensitive capture of circulating tumour cells by functionalized graphene oxide nanosheets*. Nature Nanotechnology, 2013, **8** (10) pp. 735–741. Cited on 58.

[258] S. Singh, A. A. S. Gill, M. Nlooto and R. Karpoormath, *Prostate cancer biomarkers detection using nanoparticles based electrochemical biosensors*. Biosensors and Bioelectronics, 2019, **137** pp. 213–221. Cited on 58.

[259] B. Luo, S. Liu and L. Zhi, *Chemical Approaches toward Graphene-Based Nanomaterials and their Applications in Energy-Related Areas*. Small, 2012, **8** (5) pp. 630–646. Cited on 58.

[260] I. Langmuir, *The Constitution and Fundamental Properties of Solids and Liquids. II. Liquids.*. Journal of the American Chemical Society, 1917, **39** (9) pp. 1848–1906. Cited on 58.

[261] I. Langmuir and V. J. Schaefer, *Activities of Urease and Pepsin Monolayers*. Journal of the American Chemical Society, 1938, **60** (6) pp. 1351–1360. Cited on 59.

[262] Y. Gao, W. Shi, W. Wang, Y. Leng and Y. Zhao, *Inkjet Printing Patterns of Highly Conductive Pristine Graphene on Flexible Substrates*. Industrial & Engineering Chemistry Research, 2014, **53** (43) pp. 16777–16784. Cited on 61.

[263] U. Khan, A. O'Neill, M. Lotya, S. De and J. N. Coleman, *High-Concentration Solvent Exfoliation of Graphene*. Small, 2010, **6** (7) pp. 864–871. Cited on 63.

[264] Y. Xu, H. Cao, Y. Xue, B. Li and W. Cai, *Liquid-Phase Exfoliation of Graphene: An Overview on Exfoliation Media, Techniques, and Challenges*. Nanomaterials, 2018, **8** (11) p. 942. Cited on 63.

[265] A. V. Alaferdov, A. Gholamipour-Shirazi, M. A. Canesqui, Y. A. Danilov and S. A. Moshkalev, *Size-controlled synthesis of graphite nanoflakes and multi-layer graphene by liquid phase exfoliation of natural graphite*. Carbon, 2014, **69** pp. 525–535. Cited on 64.

[266] K. Kouroupis-Agalou, A. Liscio, E. Treossi, L. Ortolani, V. Morandi, N. M. Pugno et al., *Fragmentation and exfoliation of 2-dimensional materials: a statistical approach*. Nanoscale, 2014, **6** (11) pp. 5926–5933. Cited on 64.

[267] V. B. Fainerman, V. I. Kovalchuk, E. H. Lucassen-Reynders, D. O. Grigoriev, J. K. Ferri, M. E. Leser et al., *Surface-Pressure Isotherms of Monolayers Formed by Microsize and Nanosize Particles*. Langmuir, 2006, **22** (4) pp. 1701–1705. Cited on 65, 66.

[268] F. Bresme and M. Oettel, *Nanoparticles at fluid interfaces*. Journal of Physics: Condensed Matter, 2007, **19** (41) p. 413101. Cited on 66, 67, 70.

[269] L. J. Cote, F. Kim and J. Huang, *Langmuir−Blodgett Assembly of Graphite Oxide Single Layers*. Journal of the American Chemical Society, 2009, **131** (3) pp. 1043–1049. Cited on 67.

[270] T. M. Mohona, A. Gupta, A. Masud, S.-C. Chien, L.-C. Lin, P. C. Nalam et al., *Aggregation Behavior of Inorganic 2D Nanomaterials Beyond Graphene: Insights from Molecular Modeling and Modified DLVO Theory*. Environmental Science & Technology, 2019, **53** (8) pp. 4161–4172. Cited on 67.

[271] Y. Liu, S. Bhowmick and B. I. Yakobson, *BN White Graphene with "Colorful" Edges: The Energies and Morphology*. Nano Letters, 2011, **11** (8) pp. 3113–3116. Cited on 67.

[272] Z. Lin, A. McCreary, N. Briggs, S. Subramanian, K. Zhang, Y. Sun et al., *2D materials advances: from large scale synthesis and controlled heterostructures to improved characterization techniques, defects and applications*. 2D Materials, 2016, **3** (4) p. 042001. Cited on 69.

[273] A. C. H. Da Silva, N. A. M. S. Caturello, R. Besse, M. P. Lima and J. L. F. Da Silva, *Edge, size, and shape effects on WS_2, WSe_2, and WTe_2 nanoflake stability: design principles from an ab initio investigation*. Physical Chemistry Chemical Physics, 2019, **21** (41) pp. 23076–23084. Cited on 69.

[274] A. Gopal and K. Y. C. Lee, *Headgroup Percolation and Collapse of Condensed Langmuir Monolayers*. The Journal of Physical Chemistry B, 2006, **110** (44) pp. 22079–22087. Cited on 70.

[275] H. Li, P. Li, J.-K. Huang, M.-Y. Li, C.-W. Yang, Y. Shi et al., *Laterally Stitched Heterostructures of Transition Metal Dichalcogenide: Chemical Vapor Deposition Growth on Lithographically Patterned Area*. ACS Nano, 2016, **10** (11) pp. 10516–10523. Cited on 71.

[276] A. Winter, A. George, C. Neumann, Z. Tang, M. J. Mohn, J. Biskupek et al., *Lateral heterostructures of two-dimensional materials by electron-beam induced stitching*. Carbon, 2018, **128** pp. 106–116. Cited on 71.

[277] C. Hirsch and S. Schildknecht, *In Vitro Research Reproducibility: Keeping Up High Standards*. Frontiers in Pharmacology, 2019, **10** p. 1484. Cited on 73.

[278] G. L. Frey, R. Tenne, M. J. Matthews, M. S. Dresselhaus and G. Dresselhaus, *Raman and resonance Raman investigation of MoS_2 nanoparticles*. Physical Review B, 1999, **60** (4) pp. 2883–2892. Cited on 76.

[279] P. Johari and V. B. Shenoy, *Tuning the Electronic Properties of Semiconducting Transition Metal Dichalcogenides by Applying Mechanical Strains*. ACS Nano, 2012, **6** (6) pp. 5449–5456. Cited on 76.

[280] M. M. Ugeda, A. J. Bradley, S.-F. Shi, F. H. da Jornada, Y. Zhang, D. Y. Qiu et al., *Giant bandgap renormalization and excitonic effects in a monolayer transition metal dichalcogenide semiconductor*. Nature Materials, 2014, **13** (12) pp. 1091–1095. Cited on 76.

[281] S. Najmaei, X. Zou, D. Er, J. Li, Z. Jin, W. Gao et al., *Tailoring the Physical Properties of Molybdenum Disulfide Monolayers by Control of Interfacial Chemistry*. Nano Letters, 2014, **14** (3) pp. 1354–1361. Cited on 76.

[282] C. Backes, N. C. Berner, X. Chen, P. Lafargue, P. LaPlace, M. Freeley et al., *Functionalization of Liquid-Exfoliated Two-Dimensional 2H-MoS_2.* Angewandte Chemie International Edition, 2015, **54** (9) pp. 2638–2642. Cited on 76.

[283] D. O. Li, M. S. Gilliam, X. S. Chu, A. Yousaf, Y. Guo, A. A. Green et al., *Covalent chemical functionalization of semiconducting layered chalcogenide nanosheets.* Molecular Systems Design & Engineering, 2019, **4** (4) pp. 962–973. Cited on 76.

[284] A. Amorim Graf, M. J. Large, S. P. Ogilvie, Y. Rong, P. J. Lynch, G. Fratta et al., *Sonochemical edge functionalisation of molybdenum disulfide.* Nanoscale, 2019, **11** (33) pp. 15550–15560. Cited on 76.

[285] J. Kaur, M. Singh, C. Dell'Aversana, R. Benedetti, P. Giardina, M. Rossi et al., *Biological interactions of biocompatible and water-dispersed MoS_2 nanosheets with bacteria and human cells.* Scientific Reports, 2018, **8** (1) p. 16386. Cited on 76.

[286] J.-K. Yang, H.-R. Lee, I.-J. Hwang, H.-I. Kim, D. Yim and J.-H. Kim, *Fluorescent 2D WS_2 Nanosheets Bearing Chemical Affinity Elements for the Recognition of Glycated Hemoglobin.* Advanced Healthcare Materials, 2018, **7** (14) p. 1701496. Cited on 76.

[287] Y. Liu and J. Liu, *Hybrid nanomaterials of WS_2 or MoS_2 nanosheets with liposomes: biointerfaces and multiplexed drug delivery.* Nanoscale, 2017, **9** (35) pp. 13187–13194. Cited on 76, 200.

[288] N. Wang, F. Wei, Y. Qi, H. Li, X. Lu, G. Zhao et al., *Synthesis of Strongly Fluorescent Molybdenum Disulfide Nanosheets for Cell-Targeted Labeling.* ACS Applied Materials & Interfaces, 2014, **6** (22) pp. 19888–19894. Cited on 76.

[289] H. Li, Q. Zhang, C. C. R. Yap, B. K. Tay, T. H. T. Edwin, A. Olivier et al., *From Bulk to Monolayer MoS_2: Evolution of Raman Scattering*. Advanced Functional Materials, 2012, **22** (7) pp. 1385–1390. Cited on 76.

[290] T. R. Walsh and M. R. Knecht, *Biomolecular Material Recognition in Two Dimensions: Peptide Binding to Graphene, h-BN, and MoS_2 Nanosheets as Unique Bioconjugates*. Bioconjugate Chemistry, 2019, **30** (11) pp. 2727–2750. Cited on 76.

[291] R. Hille, T. Nishino and F. Bittner, *Molybdenum enzymes in higher organisms*. Coordination Chemistry Reviews, 2011, **255** (9-10) pp. 1179–1205. Cited on 76, 84, 97.

[292] C. M. Cordas and J. J. G. Moura, *Molybdenum and tungsten enzymes redox properties – A brief overview*. Coordination Chemistry Reviews, 2019, **394** pp. 53–64. Cited on 76.

[293] S. Behzadi, V. Serpooshan, W. Tao, M. A. Hamaly, M. Y. Alkawareek, E. C. Dreaden et al., *Cellular uptake of nanoparticles: journey inside the cell*. Chemical Society Reviews, 2017, **46** (14) pp. 4218–4244. Cited on 76.

[294] X. Zhu, X. Ji, N. Kong, Y. Chen, M. Mahmoudi, X. Xu et al., *Intracellular Mechanistic Understanding of 2D MoS_2 Nanosheets for Anti-Exocytosis-Enhanced Synergistic Cancer Therapy*. ACS Nano, 2018, **12** (3) pp. 2922–2938. Cited on 76.

[295] S. Liu, X. Pan and H. Liu, *Two-Dimensional Nanomaterials for Photothermal Therapy*. Angewandte Chemie International Edition, 2020, **59** (15) pp. 5890–5900. Cited on 76.

[296] L. Cheng, X. Wang, F. Gong, T. Liu and Z. Liu, *2D Nanomaterials for Cancer Theranostic Applications*. Advanced Materials, 2020, **32** (13) p. 1902333. Cited on 76.

[297] C. Moore, A. Harvey, J. N. Coleman, H. J. Byrne and J. McIntyre, *In vitro localisation and degradation of few-layer MoS_2 submicrometric plates in human macrophage-like cells: a label free Raman micro-spectroscopic study*. 2D Materials, 2020, **7** (2) p. 025003. Cited on 76, 78.

[298] C. Moore, D. Movia, R. J. Smith, D. Hanlon, F. Lebre, E. C. Lavelle et al., *Industrial grade 2D molybdenum disulphide (MoS_2): an in vitro exploration of the impact on cellular uptake, cytotoxicity, and inflammation*. 2D Materials, 2017, **4** (2) p. 025065. Cited on 76.

[299] Y. Yu, N. Wu, Y. Yi, Y. Li, L. Zhang, Q. Yang et al., *Dispersible MoS_2 Nanosheets Activated TGF-β/Smad Pathway and Perturbed the Metabolome of Human Dermal Fibroblasts*. ACS Biomaterials Science & Engineering, 2017, **3** (12) pp. 3261–3272. Cited on 76.

[300] P. Ganguly, A. Breen and S. C. Pillai, *Toxicity of Nanomaterials: Exposure, Pathways, Assessment, and Recent Advances*. ACS Biomaterials Science & Engineering, 2018, **4** (7) pp. 2237–2275. Cited on 76.

[301] W. L. Murphy, T. C. McDevitt and A. J. Engler, *Materials as stem cell regulators*. Nature Materials, 2014, **13** (6) pp. 547–557. Cited on 76.

[302] N. J. Walters and E. Gentleman, *Evolving insights in cell–matrix interactions: Elucidating how non-soluble properties of the extracellular niche direct stem cell fate*. Acta Biomaterialia, 2015, **11** pp. 3–16. Cited on 76.

[303] J. M. Stukel and R. K. Willits, *Mechanotransduction of Neural Cells Through Cell–Substrate Interactions*. Tissue Engineering Part B: Reviews, 2016, **22** (3) pp. 173–182. Cited on 77.

[304] V. Panzetta, S. Fusco and P. A. Netti, *Cell mechanosensing is regulated by substrate strain energy rather than stiffness*. Proceedings of the National Academy of Sciences, 2019, **116** (44) pp. 22004–22013. Cited on 77.

[305] L. Li, J. Eyckmans and C. S. Chen, *Designer biomaterials for mechanobiology.* Nature Materials, 2017, **16** (12) pp. 1164–1168. Cited on 77.

[306] Y.-T. Yeh, Y. Tang, Z. Lin, K. Fujisawa, Y. Lei, Y. Zhou et al., *Light-Emitting Transition Metal Dichalcogenide Monolayers under Cellular Digestion.* Advanced Materials, 2018, **30** (8) p. 1703321. Cited on 77, 83, 88, 91, 96.

[307] C. Huang, P. J. Butler, S. Tong, H. S. Muddana, G. Bao and S. Zhang, *Substrate Stiffness Regulates Cellular Uptake of Nanoparticles.* Nano Letters, 2013, **13** (4) pp. 1611–1615. Cited on 81.

[308] Y. Wang, T. Gong, Z.-R. Zhang and Y. Fu, *Matrix Stiffness Differentially Regulates Cellular Uptake Behavior of Nanoparticles in Two Breast Cancer Cell Lines.* ACS Applied Materials & Interfaces, 2017, **9** (31) pp. 25915–25928. Cited on 81.

[309] L. Treuel, X. Jiang and G. U. Nienhaus, *New views on cellular uptake and trafficking of manufactured nanoparticles.* Journal of The Royal Society Interface, 2013, **10** (82) p. 20120939. Cited on 84.

[310] S. J. Mayr, R.-R. Mendel and G. Schwarz, *Molybdenum cofactor biology, evolution and deficiency.* Biochimica et Biophysica Acta (BBA) - Molecular Cell Research, 2021, **1868** (1) p. 118883. Cited on 85.

[311] S. D. Conner and S. L. Schmid, *Regulated portals of entry into the cell.* Nature, 2003, **422** (6927) pp. 37–44. Cited on 85.

[312] A. Echarri and M. A. del Pozo, *Caveolae — mechanosensitive membrane invaginations linked to actin filaments.* Journal of Cell Science, 2015, **128** (15) pp. 2747–2758. Cited on 85.

[313] R. Moreno-Vicente, D. M. Pavón, I. Martín-Padura, M. Català-Montoro, A. Díez-Sánchez, A. Quílez-Álvarez et al., *Caveolin-1 Modulates Mechanotransduction Responses to Substrate Stiffness through Actin-Dependent Control of YAP*. Cell Reports, 2018, **25** (6) pp. 1622–1635.e6. Cited on 85.

[314] R. G. Parton, *Caveolae: Structure, Function, and Relationship to Disease*. Annual Review of Cell and Developmental Biology, 2018, **34** (1) pp. 111–136. Cited on 85, 86.

[315] S. Zhang, H. Gao and G. Bao, *Physical Principles of Nanoparticle Cellular Endocytosis*. ACS Nano, 2015, **9** (9) pp. 8655–8671. Cited on 86.

[316] K. Mori, *Tripartite Management of Unfolded Proteins in the Endoplasmic Reticulum*. Cell, 2000, **101** (5) pp. 451–454. Cited on 86.

[317] C. Hetz and S. Saxena, *ER stress and the unfolded protein response in neurodegeneration*. Nature Reviews Neurology, 2017, **13** (8) pp. 477–491. Cited on 89.

[318] R. W. Harries, C. J. Brown, L. Woodbine, A. Amorim Graf, M. J. Large, K. Clifford et al., *Cell–Substrate Interactions Lead to Internalization and Localization of Layered MoS_2 Nanosheets*. ACS Applied Nano Materials, 2021, **4** (2) pp. 2002–2010. Cited on 91, 99.

[319] A. Berkdemir, H. R. Gutiérrez, A. R. Botello-Méndez, N. Perea-López, A. L. Elías, C.-I. Chia et al., *Identification of individual and few layers of WS_2 using Raman Spectroscopy*. Scientific Reports, 2013, **3** (1) p. 1755. Cited on 92, 93.

[320] H. Zeng, G.-B. Liu, J. Dai, Y. Yan, B. Zhu, R. He et al., *Optical signature of symmetry variations and spin-valley coupling in atomically thin tungsten dichalcogenides*. Scientific Reports, 2013, **3** (1) p. 1608. Cited on 92.

[321] J. Xia, X. Huang, L.-Z. Liu, M. Wang, L. Wang, B. Huang et al., *CVD synthesis of large-area, highly crystalline MoSe2 atomic layers on diverse substrates and application to photodetectors*. Nanoscale, 2014, **6** (15) pp. 8949–8955. Cited on 92, 93.

[322] J. L. Rinn, C. Bondre, H. B. Gladstone, P. O. Brown and H. Y. Chang, *Anatomic Demarcation by Positional Variation in Fibroblast Gene Expression Programs*. PLoS Genetics, 2006, **2** (7) . Cited on 93, 94.

[323] M. K. Dick, J. H. Miao and F. Limaiem, *Histology, Fibroblast.* In: *StatPearls*, (Treasure Island (FL)), StatPearls Publishing, 2021. Cited on 93, 94.

[324] B. Alberts, A. Johnson, J. Lewis, M. Raff, K. Roberts and P. Walter, *Fibroblasts and Their Transformations: The Connective-Tissue Cell Family.* In: *Molecular Biology of the Cell*, (New York), Garland Science, 2002. Cited on 93.

[325] J. Ponten and E. Saksela, *Two established in vitro cell lines from human mesenchymal tumours*. International Journal of Cancer, 1967, **2** (5) pp. 434–447. Cited on 94.

[326] S. Kaushik, U. K. Tiwari, A. Deep and R. K. Sinha, *Two-dimensional transition metal dichalcogenides assisted biofunctionalized optical fiber SPR biosensor for efficient and rapid detection of bovine serum albumin*. Scientific Reports, 2019, **9** (1) p. 6987. Cited on 104, 194.

[327] C. M. Das, L. Kang, M. W. Chen, P. Coquet and K.-T. Yong, *Heterolayered Films of Monolayer WS_2 Nanosheets on Monolayer Graphene Embedded in Poly(methyl methacrylate) for Plasmonic Biosensing*. ACS Applied Nano Materials, 2020, **3** (10) pp. 10446–10453. Cited on 104, 192.

[328] H. M. Kashani, T. Madrakian, A. Afkhami, F. Mahjoubi and M. A. Moosavi, *Bottom-up and green-synthesis route of amino functionalized graphene quantum dot as a novel biocompatible and label-free fluorescence probe for in vitro cellular imaging of human ACHN cell lines*. Materials Science and Engineering: B, 2019, **251** p. 114452. Cited on 185.

[329] T. Gao, X. Wang, J. Zhao, P. Jiang, F.-L. Jiang and Y. Liu, *Bridge between Temperature and Light: Bottom-Up Synthetic Route to Structure-Defined Graphene Quantum Dots as a Temperature Probe In Vitro and in Cells*. ACS Applied Materials & Interfaces, 2020, **12** (19) pp. 22002–22011. Cited on 185.

[330] W. Li, S. Wu, X. Xu, J. Zhuang, H. Zhang, X. Zhang et al., *Carbon Dot-Silica Nanoparticle Composites for Ultralong Lifetime Phosphorescence Imaging in Tissue and Cells at Room Temperature*. Chemistry of Materials, 2019, **31** (23) pp. 9887–9894. Cited on 185.

[331] G. Kalaiyarasan and J. Joseph, *Cholesterol derived carbon quantum dots as fluorescence probe for the specific detection of hemoglobin in diluted human blood samples*. Materials Science and Engineering: C, 2019, **94** pp. 580–586. Cited on 185.

[332] X. Lu, Z. Zhang, Q. Xia, M. Hou, C. Yan, Z. Chen et al., *Glucose functionalized carbon quantum dot containing organic radical for optical/MR dual-modality bioimaging*. Materials Science and Engineering: C, 2018, **82** (Supplement C) pp. 190–196. Cited on 185.

[333] J. S. Sidhu, A. Singh, N. Garg, N. Kaur and N. Singh, *Gold conjugated carbon dots nano assembly: FRET paired fluorescence probe for cysteine recognition*. Sensors and Actuators B: Chemical, 2019, **282** pp. 515–522. Cited on 185.

[334] C. Zhao, Y. Jiao, F. Hu and Y. Yang, *Green synthesis of carbon dots from pork and application as nanosensors for uric acid detection*. Spectrochimica Acta Part A: Molecular and Biomolecular Spectroscopy, 2018, **190** (Supplement C) pp. 360–367. Cited on 185.

[335] N. Pourreza and M. Ghomi, *Green synthesized carbon quantum dots from Prosopis juliflora leaves as a dual off-on fluorescence probe for sensing mercury (II) and chemet drug*. Materials Science and Engineering: C, 2019, **98** pp. 887–896. Cited on 185.

[336] Y. Yang, X. Wang, G. Liao, X. Liu, Q. Chen, H. Li et al., *iRGD-decorated red shift emissive carbon nanodots for tumor targeting fluorescence imaging*. Journal of Colloid and Interface Science, 2018, **509** (Supplement C) pp. 515–521. Cited on 185.

[337] S. Konar, B. N. P. Kumar, M. K. Mahto, D. Samanta, M. A. S. Shaik, M. Shaw et al., *N-doped carbon dot as fluorescent probe for detection of cysteamine and multicolor cell imaging*. Sensors and Actuators B: Chemical, 2019, **286** pp. 77–85. Cited on 185.

[338] R. Zhang and Z. Fan, *Nitrogen-doped carbon quantum dots as a "turn off-on" fluorescence sensor based on the redox reaction mechanism for the sensitive detection of dopamine and alpha lipoic acid*. Journal of Photochemistry and Photobiology A: Chemistry, 2020, **392** p. 112438. Cited on 185.

[339] H. Lin, J. Huang and L. Ding, *Preparation of Carbon Dots with High-Fluorescence Quantum Yield and Their Application in Dopamine Fluorescence Probe and Cellular Imaging*. Journal of Nanomaterials, 2019, **2019** p. 5037243. Cited on 185.

[340] Y. Chen, C. Wang, Y. Xu, G. Ran and Q. Song, *Red emissive carbon dots obtained from direct calcination of 1,2,4-triaminobenzene for dual-mode pH sensing in living cells*. New Journal of Chemistry, 2020, **44** (17) pp. 7210–7217. Cited on 185.

[341] X. Shi, Y. Hu, H.-M. Meng, J. Yang, L. Qu, X.-B. Zhang et al., *Red emissive carbon dots with dual targetability for imaging polarity in living cells*. Sensors and Actuators B: Chemical, 2020, **306** p. 127582. Cited on 186.

[342] B. K. Poudel, J. H. Park, J. Lim and J. H. Byeon, *Direct fluorescent labeling for efficient biological assessment of inhalable particles*. Nanotoxicology, 2017, **11** (8) pp. 953–963. Cited on 186.

[343] X. Duan, Q. Liu, G. Wang and X. Su, *WS_2 quantum dots as a sensitive fluorescence probe for the detection of glucose*. Journal of Luminescence, 2019, **207** pp. 491–496. Cited on 186.

[344] Y. S. Borghei, M. Hosseini, M. R. Ganjali and S. Hosseinkhani, *A novel dual-mode and label-free aptasensor based methodology for breast cancer tissue marker targeting*. Sensors and Actuators B: Chemical, 2020, **315** p. 128084. Cited on 186.

[345] Y. Z. Yang, N. Xiao, Y. Y. Cen, J. R. Chen, S. G. Liu, Y. Shi et al., *Dual-emission ratiometric nanoprobe for visual detection of Cu(II) and intracellular fluorescence imaging*. Spectrochimica Acta Part A: Molecular and Biomolecular Spectroscopy, 2019, **223** p. 117300. Cited on 186.

[346] J. Peng, Y. Su, F.-Q. Huang, Q. Zuo, L. Yang, J. Li et al., *A simple and rapid fluorescent approach for flavonoids sensor based on gold nanoclusters*. Journal of Colloid and Interface Science, 2019, **539** pp. 175–183. Cited on 186.

[347] H.-H. Deng, Q. Deng, K.-L. Li, Q.-Q. Zhuang, Y.-B. Zhuang, H.-P. Peng et al., *Fluorescent gold nanocluster-based sensor for detection of alkaline phosphatase in human osteosarcoma cells*. Spectrochimica Acta Part A: Molecular and Biomolecular Spectroscopy, 2020, **229** p. 117875. Cited on 186.

[348] M. Ding, K. Wang, M. Fang, W. Zhu, L. Du and C. Li, *MPA-CdTe quantum dots as "on-off-on" sensitive fluorescence probe to detect ascorbic acid via redox reaction*. Spectrochimica Acta Part A: Molecular and Biomolecular Spectroscopy, 2020, **234** p. 118249. Cited on 186.

[349] Z. He, R. Jiang, W. Long, H. Huang, M. Liu, Y. Feng et al., *Red aggregation-induced emission luminogen and Gd^{3+} codoped mesoporous silica nanoparticles as dual-mode probes for fluorescent and magnetic resonance imaging*. Journal of Colloid and Interface Science, 2020, **567** pp. 136–144. Cited on 186.

[350] S. Zhou, C. Ding, C. Wang and J. Fu, *UV-light cross-linked and pH de-cross-linked coumarin-decorated cationic copolymer grafted mesoporous silica nanoparticles for drug and gene co-delivery in vitro*. Materials Science and Engineering: C, 2020, **108** p. 110469. Cited on 187.

[351] Z. Guo, Q. Zhao, Y. Zhang, B. Li, L. Li, L. Feng et al., *A novel "turn-on" fluorescent sensor for hydrogen peroxide based on oxidized porous g-C_3N_4 nanosheets*. Journal of Biomedical Materials Research Part B: Applied Biomaterials, 2020, **108** (3) pp. 1077–1084. Cited on 187.

[352] Y. Peng, C. Ye, R. Yan, Y. Lei, D. Ye, H. Hong et al., *Activatable Core–Shell Metallofullerene: An Efficient Nanoplatform for Bimodal Sensing of Glutathione*. ACS Applied Materials & Interfaces, 2019, **11** (50) pp. 46637–46644. Cited on 187.

[353] Y. Lv, F. Wang, N. Li, R. Wu, J. Li, H. Shen et al., *Development of dual quantum dots-based fluorescence-linked immunosorbent assay for simultaneous detection on inflammation biomarkers*. Sensors and Actuators B: Chemical, 2019, **301** p. 127118. Cited on 187.

[354] C. Zhou, H. Wu, M. Wang, C. Huang, D. Yang and N. Jia, *Functionalized graphene oxide/Fe_3O_4 hybrids for cellular magnetic resonance imaging and fluorescence labeling*. Materials Science and Engineering: C, 2017, **78** (Supplement C) pp. 817–825. Cited on 188.

[355] R. Cheng, Y. Peng, C. Ge, Y. Bu, H. Liu, H. Huang et al., *A turn-on fluorescent lysine nanoprobe based on the use of the Alizarin Red aluminum(III) complex conjugated to graphene oxide, and its application to cellular imaging of lysine*. Microchimica Acta, 2017, **184** (9) pp. 3521–3528. Cited on 188.

[356] Y. Wang, Z. Li, M. Liu, J. Xu, D. Hu, Y. Lin et al., *Multiple-targeted graphene-based nanocarrier for intracellular imaging of mRNAs*. Analytica Chimica Acta, 2017, **983** (Supplement C) pp. 1–8. Cited on 188.

[357] N. Kaur, V. Sharma, P. Tiwari, A. K. Saini and S. M. Mobin, *"Vigna radiata" based green C-dots: Photo-triggered theranostics, fluorescent sensor for extracellular and intracellular iron (III) and multicolor live cell imaging probe*. Sensors and Actuators B: Chemical, 2019, **291** pp. 275–286. Cited on 188.

[358] H. Li, S. Ye, J. Guo, H. Wang, W. Yan, J. Song et al., *Biocompatible carbon dots with low-saturation-intensity and high-photobleaching-resistance for STED nanoscopy imaging of the nucleolus and tunneling nanotubes in living cells*. Nano Research, 2019, **12** (12) pp. 3075–3084. Cited on 188.

[359] G. Liu, H. Chai, Y. Tang and P. Miao, *Bright carbon nanodots for miRNA diagnostics coupled with concatenated hybridization chain reaction*. Chemical Communications, 2020, **56** (8) pp. 1175–1178. Cited on 188.

[360] X. He, P. Chen, J. Zhang, T.-Y. Luo, H.-J. Wang, Y.-H. Liu et al., *Cationic polymer-derived carbon dots for enhanced gene delivery and cell imaging*. Biomaterials Science, 2019, **7** (5) pp. 1940–1948. Cited on 188.

[361] B. Wang, J. Li, Z. Tang, B. Yang and S. Lu, *Near-infrared emissive carbon dots with 33.96% emission in aqueous solution for cellular sensing and light-emitting diodes*. Science Bulletin, 2019, **64** (17) pp. 1285–1292. Cited on 188.

[362] R. Atchudan, T. N. J. I. Edison, S. Perumal, N. Muthuchamy and Y. R. Lee, *Eco-friendly synthesis of tunable fluorescent carbon nanodots from Malus floribunda for sensors and multicolor bioimaging*. Journal of Photochemistry and Photobiology A: Chemistry, 2020, **390** p. 112336. Cited on 188.

[363] K. Raji, V. Ramanan and P. Ramamurthy, *Facile and green synthesis of highly fluorescent nitrogen-doped carbon dots from jackfruit seeds and its applications towards the fluorimetric detection of Au^{3+} ions in aqueous medium and in in vitro multicolor cell imaging*. New Journal of Chemistry, 2019, **43** (29) pp. 11710–11719. Cited on 188.

[364] F. Wu, H. Su, K. Wang, W.-K. Wong and X. Zhu, *Facile synthesis of N-rich carbon quantum dots from porphyrins as efficient probes for bioimaging and biosensing in living cells*. International Journal of Nanomedicine, 2017, **12** pp. 7375–7391. Cited on 188.

[365] R. Atchudan, T. N. J. I. Edison, K. R. Aseer, S. Perumal, N. Karthik and Y. R. Lee, *Highly fluorescent nitrogen-doped carbon dots derived from Phyllanthus acidus utilized as a fluorescent probe for label-free selective detection of Fe^{3+} ions, live cell imaging and fluorescent ink*. Biosensors and Bioelectronics, 2018, **99** (Supplement C) pp. 303–311. Cited on 189.

[366] V. K. Singh, V. Singh, P. K. Yadav, S. Chandra, D. Bano, B. Koch et al., *Nitrogen doped fluorescent carbon quantum dots for on-off-on detection of Hg^{2+} and glutathione in aqueous medium: Live cell imaging and IMPLICATION logic gate operation*. Journal of Photochemistry and Photobiology A: Chemistry, 2019, **384** p. 112042. Cited on 189.

[367] A. K. Singh, V. K. Singh, M. Singh, P. Singh, S. R. Khadim, U. Singh et al., *One pot hydrothermal synthesis of fluorescent NP-carbon dots derived from Dunaliella salina biomass and its application in on-off sensing of Hg (II), Cr (VI) and live cell imaging*. Journal of Photochemistry and Photobiology A: Chemistry, 2019, **376** pp. 63–72. Cited on 189.

[368] L. Xu, X. Yang, H. Ding, S. Li, M. Li, D. Wang et al., *Synthesis of green fluorescent carbon materials using byproducts of the sulfite-pulping procedure residue for live cell imaging and Ag^{+} ion determination*. Materials Science and Engineering: C, 2019, **102** pp. 917–922. Cited on 189.

[369] F.-J. Hsieh, S. Sotoma, H.-H. Lin, C.-Y. Cheng, T.-Y. Yu, C.-L. Hsieh et al., *Bioorthogonal Fluorescent Nanodiamonds for Continuous Long-Term Imaging and Tracking of Membrane Proteins*. ACS Applied Materials & Interfaces, 2019, **11** (22) pp. 19774–19781. Cited on 189.

[370] M. Gravely, M. M. Safaee and D. Roxbury, *Biomolecular Functionalization of a Nanomaterial To Control Stability and Retention within Live Cells*. Nano Letters, 2019, **19** (9) pp. 6203–6212. Cited on 189.

[371] T. S. T. Balamurugan, V. Mani, C.-C. Hsieh, S.-T. Huang, T.-K. Peng and H.-Y. Lin, *Real-time tracking and quantification of endogenous hydrogen peroxide production in living cells using graphenated carbon nanotubes supported Prussian blue cubes*. Sensors and Actuators B: Chemical, 2018, **257** (Supplement C) pp. 220–227. Cited on 190.

[372] D. Xu, M. Liu, Q. Huang, J. Chen, H. Huang, F. Deng et al., *A Novel method for the preparation of fluorescent C_{60} poly(amino acid) composites and their biological imaging*. Journal of Colloid and Interface Science, 2018, **516** pp. 392–397. Cited on 190.

[373] H. Xiao, H. Fan, L. Xu, Z. Pei, S. Lei, J. Xu et al., *A gold-nanodot-decorated hollow carbon nanosphere based nanoplatform for intracellular miRNA imaging in colorectal cancer cells*. Chemical Communications, 2019, **55** (82) pp. 12352–12355. Cited on 190.

[374] K. Zhang, Z. Fan, Y. Huang, M. Xie, J. Zhao and J. Wang, *A well-designed Gold nanoparticle based fluorescence probe for assay Argonaute2 and Let-7a interaction in living cells*. Sensors and Actuators B: Chemical, 2020, **312** p. 128000. Cited on 190.

[375] Y. Li, M. Yuan, A. J. Khan, L. Wang and F. Zhang, *Peptide-gold nanocluster synthesis and intracellular Hg^{2+} sensing*. Colloids and Surfaces A: Physicochemical and Engineering Aspects, 2019, **579** p. 123666. Cited on 190.

[376] B. A. Lakshmi and S. Kim, *Quercetin mediated gold nanoclusters explored as a dual functional nanomaterial in anticancer and bio-imaging disciplines*. Colloids and Surfaces B: Biointerfaces, 2019, **178** pp. 230–237. Cited on 190.

[377] X. Gao, X. Zhuang, C. Tian, H. Liu, W.-F. Lai, Z. Wang et al., *A copper nanocluster incorporated nanogel: Confinement-assisted emission enhancement for zinc ion detection in living cells*. Sensors and Actuators B: Chemical, 2020, **307** p. 127626. Cited on 190.

[378] N. Chandran, P. Janardhanan, M. Bayal, U. Unniyampurath, R. Pilankatta and S. S. Nair, *Label Free, Nontoxic Cu-GSH NCs as a Nanoplatform for Cancer Cell Imaging and Subcellular pH Monitoring Modulated by a Specific Inhibitor: Bafilomycin A1*. ACS Applied Bio Materials, 2020, **3** (2) pp. 1245–1257. Cited on 191.

[379] S. Mallick, P. Kumar and A. L. Koner, *Freeze-Resistant Cadmium-Free Quantum Dots for Live-Cell Imaging*. ACS Applied Nano Materials, 2019, **2** (2) pp. 661–666. Cited on 191.

[380] L. Sang, H. Shi, N. Niu, Y. Zhang, H. Zhou, X. Huang et al., *Benzoperylene probe/ZnS quantum dots nanocomposite for the ratiometric detection and intracellular imaging of highly reactive oxygen species*. Sensors and Actuators B: Chemical, 2019, **281** pp. 795–800. Cited on 191.

[381] J. Selvaraj, A. Mahesh, V. Baskaralingam, A. Dhayalan and T. Paramasivam, *Organic-to-water dispersible Mn:ZnS–ZnS doped core–shell quantum dots: synthesis, characterization and their application towards optical bioimaging and a turn-off fluorosensor*. New Journal of Chemistry, 2019, **43** (30) pp. 11912–11925. Cited on 191.

[382] J. E. Eixenberger, C. B. Anders, K. Wada, K. M. Reddy, R. J. Brown, J. Moreno-Ramirez et al., *Defect Engineering of ZnO Nanoparticles for Bioimaging Applications*. ACS Applied Materials & Interfaces, 2019, **11** (28) pp. 24933–24944. Cited on 191.

[383] R. Wang, X. Xu, X. Li, N. Zhang and W. Jiang, *pH-responsive ZnO nanoprobe mediated DNAzyme signal amplification strategy for sensitive detection and live cell imaging of multiple microRNAs*. Sensors and Actuators B: Chemical, 2019, **293** pp. 93–99. Cited on 191.

[384] L. Xiao, T. Li, M. Ding, J. Yang, J. Rodríguez-Corrales, S. M. LaConte et al., *Detecting Chronic Post-Traumatic Osteomyelitis of Mouse Tibia via an IL-13Ra2 Targeted Metallofullerene Magnetic Resonance Imaging Probe*. Bioconjugate Chemistry, 2017, **28** (2) pp. 649–658. Cited on 191.

[385] S. Wu, J. Yin, H. Qu, A. Li, L. Liu and Y. Shao, *Photoluminescence properties of gadolinium phosphate nanoprisms doped with lanthanide ions for multicolor live cell imaging*. Journal of Materials Science: Materials in Electronics, 2019, **30** (12) pp. 11336–11345. Cited on 191.

[386] L. Wu, H. Ji, Y. Guan, X. Ran, J. Ren and X. Qu, *A graphene-based chemical nose/tongue approach for the identification of normal, cancerous and circulating tumor cells*. NPG Asia Materials, 2017, **9** (3) pp. e356–e356. Cited on 192.

[387] A. Roberts, N. Chauhan, S. Islam, S. Mahari, B. Ghawri, R. K. Gandham et al., *Graphene functionalized field-effect transistors for ultrasensitive detection of Japanese encephalitis and Avian influenza virus*. Scientific Reports, 2020, **10** (1) p. 14546. Cited on 192.

[388] Z. Rafiee, A. Mosahebfard and M. H. Sheikhi, *High-performance ZnO nanowires-based glucose biosensor modified by graphene nanoplates*. Materials Science in Semiconductor Processing, 2020, **115** p. 105116. Cited on 192.

[389] T.-W. Chen, U. Rajaji, S.-M. Chen, J.-Y. Wang, Z. Abdullah Alothman, M. Ajmal Ali et al., *Sonochemical preparation of carbon nanosheets supporting cuprous oxide architecture for high-performance and non-enzymatic electrochemical sensor in biological samples*. Ultrasonics Sonochemistry, 2020, **66** p. 105072. Cited on 192.

[390] D. Maity, M. C.r. and R. K. R.t., *Glucose oxidase immobilized amine terminated multiwall carbon nanotubes/reduced graphene oxide/polyaniline/gold nanoparticles modified screen-printed carbon electrode for highly sensitive amperometric glucose detection*. Materials Science and Engineering: C, 2019, **105** p. 110075. Cited on 192.

[391] P. V. Jena, D. Roxbury, T. V. Galassi, L. Akkari, C. P. Horoszko, D. B. Iaea et al., *A Carbon Nanotube Optical Reporter Maps Endolysosomal Lipid Flux*. ACS Nano, 2017, **11** (11) pp. 10689–10703. Cited on 193.

[392] M. Keerthi, G. Boopathy, S.-M. Chen, T.-W. Chen and B.-S. Lou, *A core-shell molybdenum nanoparticles entrapped f-MWCNTs hybrid nanostructured material based non-enzymatic biosensor for electrochemical detection of dopamine neurotransmitter in biological samples*. Scientific Reports, 2019, **9** (1) p. 13075. Cited on 193.

[393] F. J. Rawson, M. T. Cole, J. M. Hicks, J. W. Aylott, W. I. Milne, C. M. Collins et al., *Electrochemical communication with the inside of cells using micro-patterned vertical carbon nanofibre electrodes*. Scientific Reports, 2016, **6** p. srep37672. Cited on 193.

[394] Y. Huang, Y. Wen, K. Baryeh, S. Takalkar, M. Lund, X. Zhang et al., *Magnetized carbon nanotubes for visual detection of proteins directly in whole blood*. Analytica Chimica Acta, 2017, **993** (Supplement C) pp. 79–86. Cited on 193.

[395] M. P. Lake and L.-S. Bouchard, *Targeted nanodiamonds for identification of subcellular protein assemblies in mammalian cells*. PLOS ONE, 2017, **12** (6) p. e0179295. Cited on 193.

[396] Y. Zhang, H. Lu, F. Yang, Y. Cheng, W. Dai, X. Meng et al., *Uniform palladium nanosheets for fluorimetric detection of circulating tumor DNA*. Analytica Chimica Acta, 2020, **1139** pp. 164–168. Cited on 193.

[397] Y. Xia, Y. Chen, Y. Tang, G. Cheng, X. Yu, H. He et al., *Smartphone-Based Point-of-Care Microfluidic Platform Fabricated with a ZnO Nanorod Template for Colorimetric Virus Detection*. ACS Sensors, 2019, **4** (12) pp. 3298–3307. Cited on 193.

[398] Q. Wu, N. Li, Y. Wang, Y. liu, Y. Xu, S. Wei et al., *A 2D transition metal carbide MXene-based SPR biosensor for ultrasensitive carcinoembryonic antigen detection*. Biosensors and Bioelectronics, 2019, **144** p. 111697. Cited on 194.

[399] D. Zhao, Q. Zhang, Y. Zhang, Y. Liu, Z. Pei, Z. Yuan et al., *Sandwich-type Surface Stress Biosensor Based on Self-Assembled Gold Nanoparticles in PDMS Film for BSA Detection*. ACS Biomaterials Science & Engineering, 2019, **5** (11) pp. 6274–6280. Cited on 194.

[400] B. Du, J. Liu, G. Ding, X. Han, D. Li, E. Wang et al., *Positively charged graphene/Fe_3O_4/polyethylenimine with enhanced drug loading and cellular uptake for magnetic resonance imaging and magnet-responsive cancer therapy*. Nano Research, 2017, **10** (7) pp. 2280–2295. Cited on 195.

[401] R. Hosseinzadeh, K. Khorsandi and G. Hosseinzadeh, *Graphene oxide-methylene blue nanocomposite in photodynamic therapy of human breast cancer*. Journal of Biomolecular Structure and Dynamics, 2017, **0** (0) pp. 1–8. Cited on 195.

[402] M. M. Leitão, C. G. Alves, D. de Melo-Diogo, R. Lima-Sousa, A. F. Moreira and I. J. Correia, *Sulfobetaine methacrylate-functionalized graphene oxide-IR780 nanohybrids aimed at improving breast cancer phototherapy*. RSC Advances, 2020, **10** (63) pp. 38621–38630. Cited on 195.

[403] S. G. Mun, H. W. Choi, J. M. Lee, J. H. Lim, J. H. Ha, M.-J. Kang et al., *rGO nanomaterial-mediated cancer targeting and photothermal therapy in a microfluidic co-culture platform*. Nano Convergence, 2020, **7** (1) p. 10. Cited on 195.

[404] P. Das, S. V. Mudigunda, G. Darabdhara, P. K. Boruah, S. Ghar, A. K. Rengan et al., *Biocompatible functionalized AuPd bimetallic nanoparticles decorated on reduced graphene oxide sheets for photothermal therapy of targeted cancer cells*. Journal of Photochemistry and Photobiology B: Biology, 2020, **212** p. 112028. Cited on 195.

[405] C. Wang, X. Wang, Y. Chen and Z. Fang, *In-vitro photothermal therapy using plant extract polyphenols functionalized graphene sheets for treatment of lung cancer*. Journal of Photochemistry and Photobiology B: Biology, 2020, **204** p. 111587. Cited on 195.

[406] G.-H. Lu, W.-T. Shang, H. Deng, Z.-Y. Han, M. Hu, X.-Y. Liang et al., *Targeting carbon nanotubes based on IGF-1R for photothermal therapy of orthotopic pancreatic cancer guided by optical imaging*. Biomaterials, 2019, **195** pp. 13–22. Cited on 195.

[407] X. Dong, Z. Sun, X. Wang and X. Leng, *An innovative MWCNTs/DOX/TC nanosystem for chemo-photothermal combination therapy of cancer*. Nanomedicine: Nanotechnology, Biology and Medicine, 2017, **13** (7) pp. 2271–2280. Cited on 195.

[408] D. Franskevych, K. Palyvoda, D. Petukhov, S. Prylutska, I. Grynyuk, C. Schuetze et al., *Fullerene C_{60} Penetration into Leukemic Cells and Its Photoinduced Cytotoxic Effects*. Nanoscale Research Letters, 2017, **12** (1) p. 40. Cited on 195.

[409] Y. Mackeyev, C. Mark, N. Kumar and R. E. Serda, *The influence of cell and nanoparticle properties on heating and cell death in a radiofrequency field*. Acta Biomaterialia, 2017, **53** pp. 619–630. Cited on 196.

[410] L. Hou, Y. Yuan, J. Ren, Y. Zhang, Y. Wang, X. Shan et al., *In vitro and in vivo comparative study of the phototherapy anticancer activity of hyaluronic acid-modified single-walled carbon nanotubes, graphene oxide, and fullerene.* Journal of Nanoparticle Research, 2017, **19** (8) p. 286. Cited on 196.

[411] W. Zhou, M. Chen, X. Liu, W. Zhang, F. Cai, F. Li et al., *Selective photothermal ablation of cancer cells by patterned gold nanocages using surface acoustic waves.* Lab on a Chip, 2019, **19** (20) pp. 3387–3396. Cited on 196.

[412] J. Wang, Y. Gao, P. Liu, S. Xu and X. Luo, *Core–Shell Multifunctional Nanomaterial-Based All-in-One Nanoplatform for Simultaneous Multilayer Imaging of Dual Types of Tumor Biomarkers and Photothermal Therapy.* Analytical Chemistry, 2020, **92** (22) pp. 15169–15178. Cited on 196.

[413] J. Byun, D. Kim, J. Choi, G. Shim and Y.-K. Oh, *Photosensitizer-Trapped Gold Nanocluster for Dual Light-Responsive Phototherapy.* Biomedicines, 2020, **8** (11) p. 521. Cited on 196.

[414] L. Zheng, B. Zhang, H. Chu, P. Cheng, H. Li, K. Huang et al., *Assembly and in vitro assessment of a powerful combination: aptamer-modified exosomes combined with gold nanorods for effective photothermal therapy.* Nanotechnology, 2020, **31** (48) p. 485101. Cited on 196.

[415] F. Rahimi-Moghaddam, N. Sattarahmady and N. Azarpira, *Gold-Curcumin Nanostructure in Photo-thermal Therapy on Breast Cancer Cell Line: 650 and 808 nm Diode Lasers as Light Sources.* Journal of Biomedical Physics and Engineering, 2019, **9** (4) pp. 473–482. Cited on 196.

[416] E. Soratijahromi, S. Mohammadi, R. Dehdari Vais, N. Azarpira and N. Sattarahmady, *Photothermal/sonodynamic therapy of melanoma tumor by a gold/manganese dioxide nanocomposite: In vitro and in vivo studies.* Photodiagnosis and Photodynamic Therapy, 2020, **31** p. 101846. Cited on 197.

[417] T. Liu, S. Shi, C. Liang, S. Shen, L. Cheng, C. Wang et al., *Iron Oxide Decorated MoS_2 Nanosheets with Double PEGylation for Chelator-Free Radiolabeling and Multimodal Imaging Guided Photothermal Therapy*. ACS Nano, 2015, **9** (1) pp. 950–960. Cited on 197.

[418] Z. Zhou, B. Li, C. Shen, D. Wu, H. Fan, J. Zhao et al., *Metallic 1T Phase Enabling MoS_2 Nanodots as an Efficient Agent for Photoacoustic Imaging Guided Photothermal Therapy in the Near-Infrared-II Window*. Small, 2020, **16** (43) p. 2004173. Cited on 197.

[419] S. Rajasekar, E. M. Martin, S. Kuppusamy and C. Vetrivel, *Chitosan coated molybdenum sulphide nanosheet incorporated with tantalum oxide nanomaterials for improving cancer photothermal therapy*. Arabian Journal of Chemistry, 2020, **13** (3) pp. 4741–4750. Cited on 197.

[420] Q. Wang, H. Wang, Y. Yang, L. Jin, Y. Liu, Y. Wang et al., *Plasmonic Pt Superstructures with Boosted Near-Infrared Absorption and Photothermal Conversion Efficiency in the Second Biowindow for Cancer Therapy*. Advanced Materials, 2019, **31** (46) p. 1904836. Cited on 197.

[421] S. Wang, J. Liu, S. Qiu and J. Yu, *Facile fabrication of Cu_9-S_5 loaded core-shell nanoparticles for near infrared radiation mediated tumor therapeutic strategy in human esophageal squamous carcinoma cells nursing care of esophageal cancer patients*. Journal of Photochemistry and Photobiology B: Biology, 2019, **199** p. 111583. Cited on 197.

[422] Y. Cheng, Y. Chang, Y. Feng, H. Jian, X. Wu, R. Zheng et al., *Bismuth Sulfide Nanorods with Retractable Zinc Protoporphyrin Molecules for Suppressing Innate Antioxidant Defense System and Strengthening Phototherapeutic Effects*. Advanced Materials, 2019, **31** (10) p. 1806808. Cited on 197.

[423] M. Mugnano, G. C. Lama, R. Castaldo, V. Marchesano, F. Merola, D. del Giudice et al., *Cellular Uptake of Mildly Oxidized Nanographene for Drug-Delivery Applications*. ACS Applied Nano Materials, 2020, **3** (1) pp. 428–439. Cited on 198.

[424] G. Consiglio, P. Di Pietro, L. D'Urso, G. Forte, G. Grasso, C. Sgarlata et al., *Surface tailoring of polyacrylate-grafted graphene oxide for controlled interactions at the biointerface*. Journal of Colloid and Interface Science, 2017, **506** (Supplement C) pp. 532–542. Cited on 198.

[425] H. Zhu, J. Deng, Z. Yang, Y. Deng, W. Yang, X.-L. Shi et al., *Facile synthesis and characterization of multifunctional cobalt-based nanocomposites for targeted chemo-photothermal synergistic cancer therapy*. Composites Part B: Engineering, 2019, **178** p. 107521. Cited on 198.

[426] Y.-G. Yuan and S. Gurunathan, *Combination of graphene oxide–silver nanoparticle nanocomposites and cisplatin enhances apoptosis and autophagy in human cervical cancer cells*. International Journal of Nanomedicine, 2017, **12** pp. 6537–6558. Cited on 198.

[427] S. M. Ardekani, A. Dehghani, P. Ye, K.-A. Nguyen and V. G. Gomes, *Conjugated carbon quantum dots: Potent nano-antibiotic for intracellular pathogens*. Journal of Colloid and Interface Science, 2019, **552** pp. 378–387. Cited on 198.

[428] J. Yue, L. He, Y. Tang, L. Yang, B. Wu and J. Ni, *Facile design and development of photoluminescent graphene quantum dots grafted dextran/glycol-polymeric hydrogel for thermoresponsive triggered delivery of buprenorphine on pain management in tissue implantation*. Journal of Photochemistry and Photobiology B: Biology, 2019, **197** p. 111530. Cited on 198.

[429] J. Ju, S. Regmi, A. Fu, S. Lim and Q. Liu, *Graphene quantum dot based charge-reversal nanomaterial for nucleus-targeted drug delivery and efficiency controllable photodynamic therapy*. Journal of Biophotonics, 2019, **12** (6) p. e201800367. Cited on 198.

[430] X. Wen, Z. Zhao, S. Zhai, X. Wang and Y. Li, *Stable nitrogen and sulfur co-doped carbon dots for selective folate sensing, in vivo imaging and drug delivery*. Diamond and Related Materials, 2020, **105** p. 107791. Cited on 198.

[431] W. Long, H. Ouyang, W. Wan, W. Yan, C. Zhou, H. Huang et al., *"Two in one": Simultaneous functionalization and DOX loading for fabrication of nanodiamond-based pH responsive drug delivery system*. Materials Science and Engineering: C, 2020, **108** p. 110413. Cited on 198.

[432] Z. Chen, C. Wang, T.-F. Li, K. Li, Y. Yue, X. Liu et al., *Doxorubicin conjugated with nanodiamonds and in free form commit glioblastoma cells to heterodromous fates*. Nanomedicine, 2019, **14** (3) pp. 335–351. Cited on 198.

[433] K. Erdmann, J. Ringel, S. Hampel, C. Rieger, D. Huebner, M. P. Wirth et al., *Chemosensitizing effects of carbon-based nanomaterials in cancer cells: enhanced apoptosis and inhibition of proliferation as underlying mechanisms*. Nanotechnology, 2014, **25** (40) p. 405102. Cited on 198.

[434] A. Mezni, N. B. Saber, A. A. Alhadhrami, A. Gobouri, A. Aldalbahi, S. Hay et al., *Highly biocompatible carbon nanocapsules derived from plastic waste for advanced cancer therapy*. Journal of Drug Delivery Science and Technology, 2017, **41** (Supplement C) pp. 351–358. Cited on 198.

[435] S.-W. Kim, Y. K. Lee, J. Y. Lee, J. H. Hong and D. Khang, *PEGylated anticancer-carbon nanotubes complex targeting mitochondria of lung cancer cells*. Nanotechnology, 2017, **28** (46) p. 465102. Cited on 199.

[436] S. Prylutska, R. Panchuk, G. Gołuński, L. Skivka, Yu. Prylutskyy, V. Hurmach et al., *C_{60} fullerene enhances cisplatin anticancer activity and overcomes tumor cell drug resistance*. Nano Research, 2017, **10** (2) pp. 652–671. Cited on 199.

[437] S. Prylutska, I. Grynyuk, A. Grebinyk, V. Hurmach, Iu. Shatrava, T. Sliva et al., *Cytotoxic Effects of Dimorfolido-N-Trichloroacetylphosphorylamide and Dimorfolido-N-Benzoylphosphorylamide in Combination with C_{60} Fullerene on Leukemic Cells and Docking Study of Their Interaction with DNA*. Nanoscale Research Letters, 2017, **12** (1) p. 124. Cited on 199.

[438] C. Misra, M. Kumar, G. Sharma, R. Kumar, B. Singh, O. P. Katare et al., *Glycinated fullerenes for tamoxifen intracellular delivery with improved anticancer activity and pharmacokinetics*. Nanomedicine, 2017, **12** (9) pp. 1011–1023. Cited on 199.

[439] L. A. Bulavin, Yu. Prylutskyy, O. Kyzyma, M. Evstigneev, U. Ritter and P. Scharff, *Self-organization of pristine C_{60} fullerene and its complexes with chemotherapy drugs in aqueous solution as promising anticancer agents*. In: *Modern Problems of Molecular Physics: Selected Reviews from the 7th International Conference "Physics of Liquid Matter: Modern Problems", Kyiv, Ukraine, May 27-31, 2016*, vol. 197 of *Springer Proceedings in Physics*, (Kyiv, Ukraine), Springer, Cham, 2018, pp. 3–22. Cited on 199.

[440] Q. Zhao, X. Wang, M. Yang, X. Li, Y. Mao, X. Guan et al., *Multi-stimuli responsive mesoporous carbon nano-platform gated by human serum albumin for cancer thermo-chemotherapy*. Colloids and Surfaces B: Biointerfaces, 2019, **184** p. 110532. Cited on 199.

[441] A. Sengupta, M. D. Gray, S. C. Kelly, S. Y. Holguin, N. N. Thadhani and M. R. Prausnitz, *Energy Transfer Mechanisms during Molecular Delivery to Cells by Laser-Activated Carbon Nanoparticles*. Biophysical Journal, 2017, **112** (6) pp. 1258–1269. Cited on 199.

[442] S. J. Devereux, M. Massaro, A. Barker, D. T. Hinds, B. Hifni, J. C. Simpson et al., *Spectroscopic study of the loading of cationic porphyrins by carbon nanohorns as high capacity carriers of photoactive molecules to cells*. Journal of Materials Chemistry B, 2019, **7** (23) pp. 3670–3678. Cited on 199.

[443] Y. Maeda, E. Hirata, Y. Takano, N. Sakaguchi, N. Ushijima, A. Saeki et al., *Stable aqueous dispersions of carbon nanohorns loaded with minocycline and exhibiting antibacterial activity*. Carbon, 2020, **166** pp. 36–45. Cited on 200.

[444] M. d'Amora, A. Camisasca, A. Boarino, S. Arpicco and S. Giordani, *Supramolecular functionalization of carbon nano-onions with hyaluronic acid-phospholipid conjugates for selective targeting of cancer cells*. Colloids and Surfaces B: Biointerfaces, 2020, **188** p. 110779. Cited on 200.

[445] A. Wójtowicz, P. Krug, P. Głowala, A. B. Hungría, M. Chotkowski, K. Wiktorska et al., *Nano-radiogold-decorated composite bioparticles*. Materials Science and Engineering: C, 2019, **97** pp. 768–775. Cited on 200.

[446] S.-Y. Lee and M.-J. Shieh, *Platinum(II) Drug-Loaded Gold Nanoshells for Chemo-Photothermal Therapy in Colorectal Cancer*. ACS Applied Materials & Interfaces, 2020, **12** (4) pp. 4254–4264. Cited on 200.

[447] S. Yang, Q. You, L. Yang, P. Li, Q. Lu, S. Wang et al., *Rodlike MSN@Au Nanohybrid-Modified Supermolecular Photosensitizer for NIRF/MSOT/CT/MR Quadmodal Imaging-Guided Photothermal/Photodynamic Cancer Therapy*. ACS Applied Materials & Interfaces, 2019, **11** (7) pp. 6777–6788. Cited on 200.

[448] H. Nabipour, *Design and Evaluation of Non-steroidal Anti-inflammatory Drug Intercalated into Layered Zinc Hydroxide as a Drug Delivery System*. Journal of Inorganic and Organometallic Polymers and Materials, 2019, **29** (5) pp. 1807–1817. Cited on 200.

[449] A. A. P. Mansur, A. J. Caires, S. M. Carvalho, N. S. V. Capanema, I. C. Carvalho and H. S. Mansur, *Dual-functional supramolecular nanohybrids of quantum dot/biopolymer/chemotherapeutic drug for bioimaging and killing brain cancer cells in vitro*. Colloids and Surfaces B: Biointerfaces, 2019, **184** p. 110507. Cited on 201.

[450] H. D. M. Follmann, O. N. Oliveira, A. C. Martins, D. Lazarin-Bidóia, C. V. Nakamura, A. F. Rubira et al., *Nanofibrous silica microparticles/polymer hybrid aerogels for sustained delivery of poorly water-soluble camptothecin*. Journal of Colloid and Interface Science, 2020, **567** pp. 92–102. Cited on 201.

[451] Y. Zhang, R. Guo, D. Wang, X. Sun and Z. Xu, *Pd nanoparticle-decorated hydroxy boron nitride nanosheets as a novel drug carrier for chemo-photothermal therapy*. Colloids and Surfaces B: Biointerfaces, 2019, **176** pp. 300–308. Cited on 201.

[452] N. J. Hunt, G. P. Lockwood, F. H. Le Couteur, P. A. G. McCourt, N. Singla, S. W. S. Kang et al., *Rapid Intestinal Uptake and Targeted Delivery to the Liver Endothelium Using Orally Administered Silver Sulfide Quantum Dots*. ACS Nano, 2020, **14** (2) pp. 1492–1507. Cited on 201.

[453] D. Zhu, W.-g. Zhang, X.-d. Nie, S.-w. Ding, D.-t. Zhang and L. Yang, *Rational design of ultra-small photoluminescent copper nano-dots loaded PLGA micro-vessels for targeted co-delivery of natural piperine molecules for the treatment for epilepsy*. Journal of Photochemistry and Photobiology B: Biology, 2020, **205** p. 111805. Cited on 201.

[454] Y.-J. Lee, T. H. Seo, S. Lee, W. Jang, M. J. Kim and J.-S. Sung, *Neuronal differentiation of human mesenchymal stem cells in response to the domain size of graphene substrates*. Journal of Biomedical Materials Research Part A, 2018, **106** (1) pp. 43–51. Cited on 202.

[455] C. Wei, Z. Liu, F. Jiang, B. Zeng, M. Huang and D. Yu, *Cellular behaviours of bone marrow-derived mesenchymal stem cells towards pristine graphene oxide nanosheets*. Cell Proliferation, 2017, **50** (5) pp. n/a–n/a. Cited on 202.

[456] C. Zhong, J. Feng, X. Lin and Q. Bao, *Continuous release of bone morphogenetic protein-2 through nano-graphene oxide-based delivery influences the activation of the NF-κB signal transduction pathway*. International Journal of Nanomedicine, 2017, **12** pp. 1215–1226. Cited on 202.

[457] M.-Y. Chiang, Y.-Z. Lin, S.-J. Chang, W.-C. Shyu, H.-E. Lu and S.-Y. Chen, *Direct Reprogramming of Human Suspension Cells into Mesodermal Cell Lineages via Combined Magnetic Targeting and Photothermal Stimulation by Magnetic Graphene Oxide Complexes*. Small, 2017, **13** (32) pp. n/a–n/a. Cited on 202.

[458] J.-W. Yang, K. Y. Hsieh, P. V. Kumar, S.-J. Cheng, Y.-R. Lin, Y.-C. Shen et al., *Enhanced Osteogenic Differentiation of Stem Cells on Phase-Engineered Graphene Oxide*. ACS Applied Materials & Interfaces, 2018, **10** (15) pp. 12497–12503. Cited on 202.

[459] C. Fu, X. Yang, S. Tan and L. Song, *Enhancing Cell Proliferation and Osteogenic Differentiation of MC3T3-E1 Pre-osteoblasts by BMP-2 Delivery in Graphene Oxide-Incorporated PLGA/HA Biodegradable Microcarriers*. Scientific Reports, 2017, **7** (1) p. 12549. Cited on 202.

[460] V. Palmieri, M. Barba, L. D. Pietro, S. Gentilini, M. C. Braidotti, C. Ciancico et al., *Reduction and shaping of graphene-oxide by laser-printing for controlled bone tissue regeneration and bacterial killing*. 2D Materials, 2017, **5** (1) p. 015027. Cited on 203.

[461] E.-S. Kang, I. Song, D.-S. Kim, U. Lee, J.-K. Kim, H. Son et al., *Size-dependent effects of graphene oxide on the osteogenesis of human adipose-derived mesenchymal stem cells*. Colloids and Surfaces B: Biointerfaces, 2018, **169** pp. 20–29. Cited on 203.

[462] Q. Li and Z. Wang, *Involvement of FAK/P38 Signaling Pathways in Mediating the Enhanced Osteogenesis Induced by Nano-Graphene Oxide Modification on Titanium Implant Surface*. International Journal of Nanomedicine, 2020, **2020:15** pp. 4659–4676. Cited on 203.

[463] A. Marrella, G. Tedeschi, P. Giannoni, A. Lagazzo, F. Sbrana, F. Barberis et al., *"Green-reduced" graphene oxide induces in vitro an enhanced biomimetic mineralization of polycaprolactone electrospun meshes*. Materials Science and Engineering: C, 2018, **93** pp. 1044–1053. Cited on 203.

[464] M. C. Serrano, M. J. Feito, A. González-Mayorga, R. Diez-Orejas, M. C. Matesanz and M. T. Portolés, *Response of macrophages and neural cells in contact with reduced graphene oxide microfibers*. Biomaterials Science, 2018, **6** (11) pp. 2987–2997. Cited on 204.

[465] A. Şelaru, D.-M. Drăguşin, E. Olăreț, A. Serafim, D. Steinmüller-Nethl, E. Vasile et al., *Fabrication and Biocompatibility Evaluation of Nanodiamonds-Gelatin Electrospun Materials Designed for Prospective Tissue Regeneration Applications*. Materials, 2019, **12** (18) p. 2933. Cited on 204.

[466] R. G. Stigler, M. M. Schimke, S. Bigus, D. Steinmüller-Nethl, K. Tillmann and G. Lepperdinger, *Pervasion of beta-tricalcium phosphate with nanodiamond particles yields efficient and safe bone replacement material amenable for biofunctionalization and application in large-size osseous defect healing*. Nanomedicine: Nanotechnology, Biology and Medicine, 2019, **16** pp. 250–257. Cited on 204.

[467] A. C. Taylor, C. H. González, B. S. Miller, R. J. Edgington, P. Ferretti and R. B. Jackman, *Surface functionalisation of nanodiamonds for human neural stem cell adhesion and proliferation*. Scientific Reports, 2017, **7** (1) p. 7307. Cited on 204.

[468] Y. Xia, S. Li, C. Nie, J. Zhang, S. Zhou, H. Yang et al., *A multivalent polyanion-dispersed carbon nanotube toward highly bioactive nanostructured fibrous stem cell scaffolds*. Applied Materials Today, 2019, **16** pp. 518–528. Cited on 204.

[469] H. E. Marei, A. A. Elnegiry, A. Zaghloul, A. Althani, N. Afifi, A. Abd-Elmaksoud et al., *Nanotubes impregnated human olfactory bulb neural stem cells promote neuronal differentiation in Trimethyltin-induced neurodegeneration rat model*. Journal of Cellular Physiology, 2017, **232** (12) pp. 3586–3597. Cited on 205.

[470] Z. Du, X. Feng, G. Cao, Z. She, R. Tan, K. E. Aifantis et al., *The effect of carbon nanotubes on osteogenic functions of adipose-derived mesenchymal stem cells in vitro and bone formation in vivo compared with that of nano-hydroxyapatite and the possible mechanism*. Bioactive Materials, 2021, **6** (2) pp. 333–345. Cited on 205.

[471] S. C. Patel, O. Alam and B. Sitharaman, *Osteogenic differentiation of human adipose derived stem cells on chemically crosslinked carbon nanomaterial coatings*. Journal of Biomedical Materials Research Part A, 2018, **106** (5) pp. 1189–1199. Cited on 205.

[472] B. K. Ekambaram, M. S. Niepel, B. Fuhrmann, G. Schmidt and T. Groth, *Introduction of Laser Interference Lithography to Make Nanopatterned Surfaces for Fundamental Studies on Stem Cell Response*. ACS Biomaterials Science & Engineering, 2018, **4** (5) pp. 1820–1832. Cited on 205.

[473] R. B. Bostancioglu, M. Gurbuz, A. G. Akyurekli, A. Dogan, A. S. Koparal and A. T. Koparal, *Adhesion profile and differentiation capacity of human adipose tissue derived mesenchymal stem cells grown on metal ion (Zn, Ag and Cu) doped hydroxyapatite nano-coated surfaces*. Colloids and Surfaces B: Biointerfaces, 2017, **155** pp. 415–428. Cited on 205.

[474] X. Li, M. Liu, H. Cheng, Q. Wang, C. Miao, S. Ju et al., *Development of ionic liquid assisted-synthesized nano-silver combined with vascular endothelial growth factor as wound healing in the care of femoral fracture in the children after surgery*. Journal of Photochemistry and Photobiology B: Biology, 2018, **183** pp. 385–390. Cited on 205.

[475] W. Zhang, J. Gu, K. Li, J. Zhao, H. Ma, C. Wu et al., *A hydrogenated black TiO_2 coating with excellent effects for photothermal therapy of bone tumor and bone regeneration*. Materials Science and Engineering: C, 2019, **102** pp. 458–470. Cited on 206.

[476] Y. C. Shin, K.-M. Pang, D.-W. Han, K.-H. Lee, Y.-C. Ha, J.-W. Park et al., *Enhanced osteogenic differentiation of human mesenchymal stem cells on Ti surfaces with electrochemical nanopattern formation*. Materials Science and Engineering: C, 2019, **99** pp. 1174–1181. Cited on 206.

[477] N. Jiang, Z. Guo, D. Sun, B. Ay, Y. Li, Y. Yang et al., *Exploring the mechanism behind improved osteointegration of phosphorylated titanium implants with hierarchically structured topography*. Colloids and Surfaces B: Biointerfaces, 2019, **184** p. 110520. Cited on 206.

[478] E. G. Long, M. Buluk, M. B. Gallagher, J. M. Schneider and J. L. Brown, *Human mesenchymal stem cell morphology, migration, and differentiation on micro and nano-textured titanium*. Bioactive Materials, 2019, **4** pp. 249–255. Cited on 206.

[479] M. M. Nejadi Babadaei, M. Feli Moghaddam, S. Solhvand, E. Alizadehmollayaghoob, F. Attar, E. Rajabbeigi et al., *Biophysical, bioinformatical, cellular, and molecular investigations on the effects of graphene oxide nanosheets on the hemoglobin structure and lymphocyte cell cytotoxicity*. International Journal of Nanomedicine, 2018, **Volume 13** pp. 6871–6884. Cited on 207.

[480] N. K. Kadiyala, B. K. Mandal, S. Ranjan and N. Dasgupta, *Bioinspired gold nanoparticles decorated reduced graphene oxide nanocomposite using Syzygium cumini seed extract: Evaluation of its biological applications*. Materials Science and Engineering: C, 2018, **93** pp. 191–205. Cited on 207.

[481] P. Shubha, K. Namratha, H. S. Aparna, N. R. Ashok, M. S. Mustak, J. Chatterjee et al., *Facile green reduction of graphene oxide using Ocimum sanctum hydroalcoholic extract and evaluation of its cellular toxicity*. Materials Chemistry and Physics, 2017, **198** (Supplement C) pp. 66–72. Cited on 207.

[482] C. Kiratipaiboon, T. A. Stueckle, R. Ghosh, L. W. Rojanasakul, Y. C. Chen, C. Z. Dinu et al., *Acquisition of cancer stem cell-like properties in human small airway epithelial cells after a long-term exposure to carbon nanomaterials*. Environmental Science: Nano, 2019, **6** (7) pp. 2152–2170. Cited on 207.

[483] N. Mamidi, H. M. Leija, J. M. Diabb, I. Lopez Romo, D. Hernandez, J. V. Castrejón et al., *Cytotoxicity evaluation of unfunctionalized multiwall carbon nanotubes-ultrahigh molecular weight polyethylene nanocomposites*. Journal of Biomedical Materials Research Part A, 2017, **105** (11) pp. 3042–3049. Cited on 208.

[484] M. A. Siddiqui, R. Wahab, J. Ahmad, N. N. Farshori, J. Musarrat and A. A. Al-Khedhairy, *Evaluation of cytotoxic responses of raw and functionalized multi-walled carbon nanotubes in human breast cancer (MCF-7) cells*. Vacuum, 2017, **146** (Supplement C) pp. 578–585. Cited on 208.

[485] G. Visalli, M. Currò, D. Iannazzo, A. Pistone, M. Pruiti Ciarello, G. Acri et al., *In vitro assessment of neurotoxicity and neuroinflammation of homemade MWCNTs*. Environmental Toxicology and Pharmacology, 2017, **56** (Supplement C) pp. 121–128. Cited on 208.

[486] Z. Aminzadeh, M. Jamalan, L. Chupani, H. Lenjannezhadian, M. A. Ghaffari, M. Aberomand et al., *In vitro reprotoxicity of carboxyl-functionalised single- and multi-walled carbon nanotubes on human spermatozoa*. Andrologia, 2017, **49** (9) pp. n/a–n/a. Cited on 208.

[487] M. Zhang, M. Yang, T. Morimoto, N. Tajima, K. Ichiraku, K. Fujita et al., *Size-dependent cell uptake of carbon nanotubes by macrophages: A comparative and quantitative study*. Carbon, 2018, **127** (Supplement C) pp. 93–101. Cited on 209.

[488] A. J. Raghavendra, K. Fritz, S. Fu, J. M. Brown, R. Podila and J. H. Shannahan, *Variations in biocorona formation related to defects in the structure of single walled carbon nanotubes and the hyperlipidemic disease state*. Scientific Reports, 2017, **7** (1) p. 8382. Cited on 209.

[489] O. V. Lynchak, Yu. I. Prylutskyy, V. K. Rybalchenko, O. A. Kyzyma, D. Soloviov, V. V. Kostjukov et al., *Comparative Analysis of the Antineoplastic Activity of C_{60} Fullerene with 5-Fluorouracil and Pyrrole Derivative In Vivo*. Nanoscale Research Letters, 2017, **12** (1) p. 8. Cited on 209.

[490] Y. Hiraku, Y. Nishikawa, N. Ma, T. Afroz, K. Mizobuchi, R. Ishiyama et al., *Nitrative DNA damage induced by carbon-black nanoparticles in macrophages and lung epithelial cells*. Mutation Research/Genetic Toxicology and Environmental Mutagenesis, 2017, **818** (Supplement C) pp. 7–16. Cited on 209.

[491] N. F. Rosli, N. M. Latiff, Z. Sofer, A. C. Fisher and M. Pumera, *In vitro cytotoxicity of covalently protected layered molybdenum disulfide*. Applied Materials Today, 2018, **11** pp. 200–206. Cited on 210.

[492] J. Augustine, T. Cheung, V. Gies, J. Boughton, M. Chen, Z. J. Jakubek et al., *Assessing size-dependent cytotoxicity of boron nitride nanotubes using a novel cardiomyocyte AFM assay*. Nanoscale Advances, 2019, **1** (5) pp. 1914–1923. Cited on 210.

[493] M. Rosłon, A. Jastrzębska, K. Sitarz, I. Książek, M. Koronkiewicz, E. Anuszewska et al., *The toxicity in vitro of titanium dioxide nanoparticles modified with noble metals on mammalian cells*. International Journal of Applied Ceramic Technology, 2019, **16** (2) pp. 481–493. Cited on 210.

[494] M. Razaghi, A. Ramazani, M. Khoobi, T. Mortezazadeh, E. A. Aksoy and T. T. Küçükkılınç, *Highly fluorinated graphene oxide nanosheets for anticancer linoleic-curcumin conjugate delivery and T_2-Weighted magnetic resonance imaging: In vitro and in vivo studies*. Journal of Drug Delivery Science and Technology, 2020, **60** p. 101967. Cited on 211.

[495] Y.-H. Hsu, H.-L. Hsieh, G. Viswanathan, S. H. Voon, C. S. Kue, W. S. Saw et al., *Multifunctional carbon-coated magnetic sensing graphene oxide-cyclodextrin nanohybrid for potential cancer theranosis*. Journal of Nanoparticle Research, 2017, **19** (11) p. 359. Cited on 211.

[496] X.-W. Hua, Y.-W. Bao, Z. Chen and F.-G. Wu, *Carbon quantum dots with intrinsic mitochondrial targeting ability for mitochondria-based theranostics*. Nanoscale, 2017, **9** (30) pp. 10948–10960. Cited on 211.

[497] Y. Niu, H. Tan, X. Li, L. Zhao, Z. Xie, Y. Zhang et al., *Protein–Carbon Dot Nanohybrid-Based Early Blood–Brain Barrier Damage Theranostics*. ACS Applied Materials & Interfaces, 2020, **12** (3) pp. 3445–3452. Cited on 211.

[498] N. Mauro, M. A. Utzeri, S. E. Drago, G. Buscarino, G. Cavallaro and G. Giammona, *Carbon Nanodots as Functional Excipient to Develop Highly Stable and Smart PLGA Nanoparticles Useful in Cancer Theranostics*. Pharmaceutics, 2020, **12** (11) p. 1012. Cited on 211.

[499] S. P. Jovanović, Z. Syrgiannis, M. D. Budimir, D. D. Milivojević, D. J. Jovanovic, V. B. Pavlović et al., *Graphene quantum dots as singlet oxygen producer or radical quencher - The matter of functionalization with urea/thiourea*. Materials Science and Engineering: C, 2020, **109** p. 110539. Cited on 211.

[500] Z. Lin, B.-P. Jiang, J. Liang, C. Wen and X.-C. Shen, *Phycocyanin functionalized single-walled carbon nanohorns hybrid for near-infrared light-mediated cancer phototheranostics*. Carbon, 2019, **143** pp. 814–827. Cited on 212.

[501] W. Tao, X. Zhu, X. Yu, X. Zeng, Q. Xiao, X. Zhang et al., *Black Phosphorus Nanosheets as a Robust Delivery Platform for Cancer Theranostics*. Advanced Materials, 2017, **29** (1) p. 1603276. Cited on 212.

[502] Y. Weng, S. Guan, L. Wang, X. Qu and S. Zhou, *Hollow carbon nanospheres derived from biomass by-product okara for imaging-guided photothermal therapy of cancers*. Journal of Materials Chemistry B, 2019, **7** (11) pp. 1920–1925. Cited on 212.

[503] Y. Peng, D. Yang, W. Lu, X. Hu, H. Hong and T. Cai, *Positron emission tomography (PET) guided glioblastoma targeting by a fullerene-based nanoplatform with fast renal clearance*. Acta Biomaterialia, 2017, **61** pp. 193–203. Cited on 212.

[504] M. K. Kumawat, M. Thakur, R. Bahadur, T. Kaku, P. R.s., A. Ninawe et al., *Preparation of graphene oxide-graphene quantum dots hybrid and its application in cancer theranostics*. Materials Science and Engineering: C, 2019, **103** p. 109774. Cited on 212.

[505] W. Sun, X. Zhang, H.-R. Jia, Y.-X. Zhu, Y. Guo, G. Gao et al., *Water-Dispersible Candle Soot–Derived Carbon Nano-Onion Clusters for Imaging-Guided Photothermal Cancer Therapy*. Small, 2019, **15** (11) p. 1804575. Cited on 212.

[506] M. Theodosiou, N. Boukos, E. Sakellis, M. Zachariadis and E. K. Efthimiadou, *Gold nanoparticle decorated pH-sensitive polymeric nanocontainers as a potential theranostic agent*. Colloids and Surfaces B: Biointerfaces, 2019, **183** p. 110420. Cited on 212.

[507] R. Zhong, R. Wang, X. Hou, L. Song and Y. Zhang, *Polydopamine-doped virus-like structured nanoparticles for photoacoustic imaging guided synergistic chemo-/photothermal therapy*. RSC Advances, 2020, **10** (31) pp. 18016–18024. Cited on 213.

[508] E. Kozenkova, K. Levada, M. V. Efremova, A. Omelyanchik, Y. A. Nalench, A. S. Garanina et al., *Multifunctional Fe_3O_4-Au Nanoparticles for the MRI Diagnosis and Potential Treatment of Liver Cancer*. Nanomaterials, 2020, **10** (9) p. 1646. Cited on 213.

[509] K. Tao, S. Liu, L. Wang, H. Qiu, B. Li, M. Zhang et al., *Targeted multifunctional nanomaterials with MRI, chemotherapy and photothermal therapy for the diagnosis and treatment of bladder cancer*. Biomaterials Science, 2019, **8** (1) pp. 342–352. Cited on 213.

[510] B. Li, T. Gong, N. Xu, F. Cui, B. Yuan, Q. Yuan et al., *Improved Stability and Photothermal Performance of Polydopamine-Modified Fe_3O_4 Nanocomposites for Highly Efficient Magnetic Resonance Imaging-Guided Photothermal Therapy*. Small, 2020, **16** (45) p. 2003969. Cited on 213.

[511] K. Luo, J. Zhao, C. Jia, Y. Chen, Z. Zhang, J. Zhang et al., *Integration of Fe_3O_4 with Bi_2S_3 for Multi-Modality Tumor Theranostics*. ACS Applied Materials & Interfaces, 2020, **12** (20) pp. 22650–22660. Cited on 213.

[512] F. Wu, B. Sun, X. Chu, Q. Zhang, Z. She, S. Song et al., *Hyaluronic Acid-Modified Porous Carbon-Coated Fe_3O_4 Nanoparticles for Magnetic Resonance Imaging-Guided Photothermal/Chemotherapy of Tumors*. Langmuir, 2019, **35** (40) pp. 13135–13144. Cited on 213.

[513] G. Shim, S. Ko, J. Y. Park, J. H. Suh, Q.-V. Le, D. Kim et al., *Tannic acid-functionalized boron nitride nanosheets for theranostics*. Journal of Controlled Release, 2020, **327** pp. 616–626. Cited on 214.

[514] W. Tao, X. Ji, X. Zhu, L. Li, J. Wang, Y. Zhang et al., *Two-Dimensional Antimonene-Based Photonic Nanomedicine for Cancer Theranostics*. Advanced Materials, 2018, **30** (38) p. 1802061. Cited on 214.

[515] L. Peng, X. Mei, J. He, J. Xu, W. Zhang, R. Liang et al., *Monolayer Nanosheets with an Extremely High Drug Loading toward Controlled Delivery and Cancer Theranostics*. Advanced Materials, 2018, **30** (16) p. 1707389. Cited on 214.

[516] J. Wu, S. Zhang, X. Mei, N. Liu, T. Hu, R. Liang et al., *Ultrathin Transition Metal Chalcogenide Nanosheets Synthesized via Topotactic Transformation for Effective Cancer Theranostics*. ACS Applied Materials & Interfaces, 2020, **12** (43) pp. 48310–48320. Cited on 214.

[517] J. Huang, B. He, Z. Zhang, Y. Li, M. Kang, Y. Wang et al., *Aggregation-Induced Emission Luminogens Married to 2D Black Phosphorus Nanosheets for Highly Efficient Multimodal Theranostics*. Advanced Materials, 2020, **32** (37) p. 2003382. Cited on 214.

[518] T. He, H. Xu, Y. Zhang, S. Yi, R. Cui, S. Xing et al., *Glucose Oxidase-Instructed Traceable Self-Oxygenation/Hyperthermia Dually Enhanced Cancer Starvation Therapy*. Theranostics, 2020, **10** (4) pp. 1544–1554. Cited on 214.

Appendices

A Tables for Chapter 2

In Chapter 2, a review of low-dimensional materials in diagnostics and therapeutics for life sciences applications is presented. The background, relevant review papers and discussion of common materials is included in 2.4. Here are included tables of the papers reviewed by the author; relevant information is summarised for each application. A list of abbreviations is included for convenience.

List of applications being reviewed:

List of Abbreviations used in Appendix A:

| **A** | **B** | **C** | **D** | **E** | **F** | **G** | **H** | **I** | **J** | **L** | **M** | **N** | **O** | **P** | **Q** | **R** | **S** | **T** | **U** | **V** | **W**

# #

1D one-dimensional. 197

2D two-dimensional. 197, 212, 214

3D three-dimensional. 197

5-FU 5-fluorouracil. 187, 209

A

AA acrylic acid. 212

Ab antibody. 189, 192, 193, 194, 195

AFM atomic force microscope. 210

AgNP silver nanoparticle. 194, 198, 205

AI activity index. 207

AIV avian influenza virus. 192, 193

AMSC adipose-derived mesenchymal stem cell. 203, 204, 205

APTES (3-aminopropyl)triethoxysilane. 198

AuNC gold nanocluster. 186, 190, 196

AuNP gold nanoparticle. 185, 190, 192, 193, 194, 207, 212

B

BMP-2 bone morphogenetic protein 2. 202

BMSC bone marrow-derived mesenchymal stem cell. 202, 203, 204, 206

BP black phosphorus. 212, 214

BSA bovine serum albumin. 186, 192, 194, 213

C

calcein AM calcein acetoxymethyl. 208

CB carbon black. 186, 199, 207, 209

CCK-8 cell counting kit assay 8. 207

CD carbon dot. 185, 186, 188, 189, 198, 211

CD44 cluster of differentiation 44. 190, 196, 200, 213

CD63 cluster of differentiation 63. 196

CEA carcinoembryonic antigen. 194

CNT carbon nanotube. 190, 193, 198, 199, 200, 204, 205, 208, 209

CQD carbon quantum dot. 185, 188, 189, 198, 211

cRGD cyclo Arg-Gly-Asp (RGD) peptide. 212

CT computed tomography. 213

CuNC copper nanocluster. 190, 191

Cy7 cyanine 7. 195, 212

Cys cysteine. 185

D

DA dopamine. 185, 190, 193

DACHPt dichloro(1,2-diaminocyclohexane)platinum(II). 200

DCF dichlorofluorescein. 207

DCF-DA 2',7'-dichlorofluorescein diacetate. 208

DCFH-DA 2',7'-dichlorodihydrofluorescein diacetate. 208

DeK death kinetics. 207

DIZ diameter of inhibition zone. 207

DMEM Dulbecco's modified Eagle's medium. 209

DMSA meso-2,3-dimercaptosuccinic acid. 197

DNA deoxyribonucleic acid. 188, 189, 191, 193, 207, 208

DOX doxorubicin; doxorubicin hydrochloride. 195, 198, 199, 200, 201, 211, 212, 213, 214

DPPH 2,2-diphenyl-1-picrylhydrazyl. 207

E

ELISA enzyme-linked immunosorbent assay. 208

F

FeTMPyP Fe(III) tetrakis (1-methyl-4-pyridyl) porphyrin pentachlorideporphyrin pentachloride. 187

FITC fluorescein isothiocyanate. 186, 188

G

GO graphene oxide. 188, 192, 195, 196, 198, 202, 203, 207, 211, 212

GQD graphene quantum dot. 185, 189, 198, 211, 212

GrK growth kinetics. 207

GSH glutathione. 187, 189, 191

H

HA hyaluronic acid. 190, 196, 200, 201, 202, 213

HAP hydroxyapatite. 205, 206

Hb haemoglobin. 185, 207

HER2 human epidermal growth receptor 2. 186

HFW human fibroblast. 189, 208

HMVEC human microvascular endothelial cells. 196

hROS highly reactive oxygen species. 191

HSA human serum albumin. 199

hTERT human telomerase reverse transcriptase. 207

HUVEC human umbilical vein endothelial cell. 185, 195, 196, 213

I

IGF-1R insulin-like growth factor 1 receptor. 195

IgG immunoglobulin G. 193

iRGD a 9-amino acid cyclic peptide (sequence: CRGDKGPDC). 185

J

JEV Japanese encephalitis. 192

L

LDH lactate dehydrogenase. 209

LED light-emitting diode. 195

Lys lysine. 188

M

MAA methacrylic acid. 212

MB methylene blue. 193, 195, 196, 198

MBA methylenebisacrylamide. 212

MBC minimum bactericidal concentration. 207

MDCK Madin-Darby Canine Kidney cells. 195

MI-1 1-(4-Cl-benzyl)-3-Cl-4-(CF3-fenylamino)-1H-pyrrol-2,5-dione. 209

MIC minimum inhibition concentration. 207

miRNA micro RNA (ribonucleic acid). 188, 190, 191, 196

MMP mitochondrial membrane potential. 208

MPA mercaptopropionic acid. 186

MRI magnetic resonance imaging. 191, 211, 213, 214

mRNA messenger RNA (ribonucleic acid). 188

MRSA methicillin-resistant *Staphylococcus aureus*. 203

MSC mesenchymal stem cell. 202, 203, 204, 205, 206

MTS 3-(4,5-dimethylthiazol-2-yl)-5-(3-carboxymethoxyphenyl)-2-(4-sulfophenyl)-2H-tetrazolium. 210

MTT 3-(4,5-dimethylthiazol-2-yl)-2,5-diphenyltetrazolium bromide. 207, 208, 210

MWCNT multi-walled carbon nanotube. 192, 193, 194, 195, 205, 207, 208

MXene transition metal carbide, nitride, or carbonitride. 194

N

ND nanodiamond. 189, 193, 198, 204

NHDF normal human dermal fibroblasts. 195

NIR near-infrared. 188, 189, 193, 195, 196, 197, 206, 212, 213, 214

NO nitric oxide. 208, 209

NP nanoparticle. 185, 187, 191, 192, 193, 195, 196, 198, 199, 202, 208, 210, 211, 213

NRP-1 neuropilin-1. 185

NRU neutral red uptake. 208

NSC neural stem cell. 204

O

OBNSC olfactory bulb neural stem cell. 205

P

PAI photoacoustic imaging. 212, 213, 214

PBMC peripheral blood mononuclear cell. 202

PCL polycaprolactone. 203

PDA polydopamine. 194, 195, 196, 213

PDMS polydimethylsiloxane. 193, 194

PDT photodynamic therapy. 211, 212, 214

PEG polyethylene glycol. 186, 195, 197, 198, 199, 200, 212, 214

PEI polyethylenimine. 195, 202, 212

PET positron emission tomography. 212

PI propidium iodide. 208

PLGA poly(lactic-*co*-glycolic acid). 201, 202, 211

PMAH polymaleic acid n-hexadecanol ester. 187

PSC pluripotent stem cell. 202, 204

PTI photothermal imaging. 212, 214

PTT photothermal therapy. 211, 212, 213, 214

Q

QD quantum dot. 186, 187, 191, 201

R

---

rGO reduced graphene oxide. 192, 195, 203, 204, 207

RNA ribonucleic acid. 190

ROS reactive oxygen species. 207, 208, 209, 213, 214

S

SN-38 7-ethyl-10-hydroxycamptothecin. 200

SPR surface plasmon resonance. 192, 194

ssDNA single-stranded DNA (deoxyribonucleic acid). 190, 193, 196

STED stimulated emission depletion. 188

SWCNT single-walled carbon nanotube. 189, 195, 196, 207, 208, 209

T

TAT trans-activator of transcription. 195

TEM transmission electron microscopy. 193

TMD transition metal dichalcogenide. 200

Tyr tyrosine. 207

U

UV ultraviolet. 187

V

VEGF vascular endothelial growth factor. 205

W

WHO World Health Organization. 208

WST water-soluble tetrazolium salt. 209, 210

Table A.1: Fluorescence imaging.

Material	**Probe**	**Target**	**Cell lines/Animal models**	**Ref.**
Histidine-functionalised GQDs		Cytoplasm	Human ACHN	[328]
Oxide GQDs (O-GQDs); reduced oxide GQDs (R-GQDs)	Functional groups (oxygen-containing for R-GQDs)	Nucleus	HeLa	[329]
CD–silica NP composites	(Phosphorescence-based rather than fluorescence)		EM-6	[330]
CQDs	Strong hydrophobic interactions	Hb	Human blood	[331]
Glucose modified CQDs	Glucose	Cytoplasm	HepG2; HL-7702	[332]
Gold conjugated CDs nano-assembly	Displacement of CDs from AuNP surface with the addition of Cys	Cys	HeLa	[333]
CDs (pork as carbon source)	Quenching due to surface absorption	Uric acid	Human serum and urine	[334]
CQDs (as an antipoisoning drug for heavy metal ions)		Mercury and chemet	Human serum	[335]
iRGD-decorated carbon nanodots	iRGD peptide	NRP-1 and $\alpha_v\beta_3$ integrin receptors	4T1; A2780	[336]
N-doped CDs	Formation of non-fluorescent ground state complex	Cysteamine	MDA-MB-231	[337]
N-doped CQDs	Tyrosinase	DA; alpha lipoic acid	Human blood and urine	[338]
CDs	N–H bonds; electronic transfer between CDs and DA	DA (accumulation in intracellular space)	CRL-5822; HUVEC	[339]
CDs	Reversible transformation between azo and quinone structures induced by protonation–deprotonation	H^+ (pH sensor)	HeLa	[340]

Table A.1: Fluorescence imaging (continued).

Material	**Probe**	**Target**	**Cell lines/Animal models**	**Ref.**
CDs		Intracellular polarity (accumulate in lysosomes and mitochondria)	HepG2; HL-7702	[341]
CB and calcium carbonate incorporated with FITC–PEG 2-aminoethyl ether acetic acid solution		Cytoplasm periphery	A549	[342]
WS_2 QDs	Transformation of Fe^{2+}/Fe^{3+} and the enzymatic reaction	Glucose	Human blood and serum	[343]
Aptamer@AuNCs and aptamer@CdTe QDs cell/tumour-targeting nanostructure		HER2	SK-BR-3; MCF-7 (control)	[344]
AuNCs/N-doped CDs nanohybrids		Cu^{2+}	HepG2	[345]
AuNC embedded in BSA (BSA–AuNCs)	(Interaction between BSA and flavonoids, e.g. aggregation of AuNCs)	Flavonoids (quercetin, apigenin, nobiletin, baicalein, rutin, and wogonin)	Serum, plasma, proprietary Chinese medicine Rutin Tablets	[346]
BSA/3-MPA co-modified AuNCs	Quenched by Fe^{3+} due to strong electron transfer ability	Alkaline phosphatase	Saos-2	[347]
MPA capped CdTe QDs	Quenched ("turned off") by Fe^{3+}, then "turned on" by ascorbic acid	Ascorbic acid	Human plasma	[348]
Dual-mode probes based on mesoporous silica nanomaterials doped with an aggregation-induced emission dye and Gd^{3+}		Accumulation in cytoplasm	L929; DU149	[349]

Table A.1: Fluorescence imaging (continued).

Material	**Probe**	**Target**	**Cell lines/Animal models**	**Ref.**
Coumarin-decorated cationic copolymer functionalised mesoporous silica NPs	5-FU chemotherapeutic agent; p53 tumour suppressor gene (UV-light cross-linked and pH de-cross-linked)	H^+ (triggered by acidic environment)	MCF-7; COS-7	[350]
Oxidised, porous graphitic carbon nitride nanosheets (CNNSs)	Fluorescence quenching of CNNSs due to overlap of FeTMPyP absorbance band and CNNSs emission band; quenched fluorescence "turned on" in response to H_2O_2 (caused by decomposition of FeTMPyP)	H_2O_2	RAW 264.7	[351]
Manganese-fullerenes core–shell nanocomposites	Collapse of the outer MnO_2 shell leading to reconstruction of the nanoprobes after exposure to GSH	GSH	HeLa	[352]
Dual QDs-based fluorescence-linked immunosorbent assay	Amphiphilic oligomers (PMAH)	Inflammation biomarkers (serum amyloid A and C-reactive protein)		[353]

Table A.2: Live cell imaging.

Material	**Probe**	**Detection method**	**Target**	**Cell lines/Animal models**	**Ref.**
GO/Fe_3O_4 hybrids with functionalised polymer	FITC	Fluorescence		BxPC-3	[354]
Ternary complex of GO, Al ions, and alizarin red (GO–Al–AR)		Fluorescence	Lys	Human retinal pigment epithelium	[355]
Multiple-targeted GO nanocarrier	Manganese superoxide dismutase (Mn-SOD); β-actin; control DNA with random sequence	Fluorescence	Intracellular mRNA	MDA-MB-231	[356]
N-doped CDs		Fluorescence	Fe^{3+}	HeLa	[357]
Fluorine and nitrogen co-doped CDs		Fluorescence/STED nanoscopy	Nucleolus; tunnelling nanotubes	4T1	[358]
Carbon nanodots	Hairpin-structured/amino group modified DNA	Fluorescence	miRNA		[359]
CDs		Fluorescence		HeLa	[360]
NIR emissive CDs		Fluorescence	Fe^{3+}; accumulation in cytoplasm	AGS; K562; MGC-803	[361]
N-doped carbon nanodots	Carboxyl/hydroxyl or nitrogen functional groups	Fluorescence	Fe^{3+}	HCT-116	[362]
N-doped CDs	Carboxyl/hydroxyl/amine functional groups	Fluorescence	Au^{3+}	A549	[363]
N-rich metal-free and metal doped CQDs	Phenolic hydroxyl groups	Fluorescence	Fe^{3+}	HeLa	[364]

Table A.2: Live cell imaging (continued).

Material	**Probe**	**Detection method**	**Target**	**Cell lines/Animal models**	**Ref.**
N-doped CDs	Hydroxyl/amine groups	Fluorescence	Fe^{3+}	*C. albicans*; Clone 9 hepatocytes	[365]
N-doped CQDs		Fluorescence	Hg^{2+}; GSH	MCF-7	[366]
N,P-dual doped CDs (A-NPCDs)	Nitrogen, phosphorus and oxygen containing functional groups [for Hg(II) target]; broad absorption band overlapping the emission and excitation spectrum of A-NPCDs [for Cr(VI) target]	Fluorescence	Hg(II); Cr(VI)	HEK-293	[367]
N,S co-doped aminated ligninsulfonate/GQDs	Coordination between sulfonic acid group and Ag^{+}	Fluorescence	Ag^{+}	A549	[368]
Alkyne-functionalised hyperbranched-polyglycerol-coated fluorescent NDs		Fluorescence	Azide-modified membrane proteins; azide-modified Abs of membrane proteins	HeLa; HFW	[369]
Oligonucleotide-functionalised DNA–SWCNTs	$(GT)_n$ oligonucleotides	Visible and NIR fluorescence (observed intracellular fluorescence intensities shown to increase with increasing oligonucleotide length); confocal Raman spectroscopy		RAW 264.7	[370]

Table A.2: Live cell imaging (continued).

Material	**Probe**	**Detection method**	**Target**	**Cell lines/Animal models**	**Ref.**
Prussian blue (PB) microcubes-decorated graphenated CNTs (g-CNTs)-modified electrode	Polycrystalline structure of PB allows small H_2O_2 molecules to pass through but screens other species such as DA and ascorbic acid; negatively charged surface of g-CNTs able to repel negatively charged ascorbate anions	Amperometric experiment	H_2O_2	RAW 264.7	[371]
C_{60}–poly(amino acid) composites		Fluorescence		HeLa	[372]
HA-coated gold nanodot-decorated hollow carbon nanospheres	5'-fluorophore (FAM)-labelled ssDNA probes		miRNA-21	CD44-positive colorectal cancer	[373]
AuNP-based probe	Functionalised hairpin nucleic acid, Cy3 fluorophore	Fluorescence	RNA-induced silencing complex (RISC)	A549; HeLa; MCF-7	[374]
Peptide–gold nanoclusters	Highly metallophilic Hg^{2+}–Au^{+} interactions leading to a significant change of conjugate electron structure in the Hg–Au complex	Fluorescence	Hg^{2+}	NIH-3T3	[375]
AuNCs		Fluorescence		A549; HDFa	[376]
CuNCs–glycol chitosan (GC) nanogel nanocomposite	COO^{-} groups on CuNCs@GC surface; Zn^{2+} acting as a crosslinker to re-aggregate dispersed nanoclusters	Photoluminescence	Zn^{2+}	A549	[377]

Table A.2: Live cell imaging (continued).

Material	**Probe**	**Detection method**	**Target**	**Cell lines/Animal models**	**Ref.**
GSH-coated CuNCs		Fluorescence	H^+ (pH sensor)	HeLa; L-132	[378]
$CuInS_2$/ZnS QDs	Biotin-binding protein traptavidin	Fluorescence	Biotinylated cell surface	MCF-7	[379]
Benzoperylene probe–ZnS QDs nanocomposite		Photoluminescence	hROS ($ONOO^-$, ·OH, H_2O_2, O_{2-}, ClO^-)	HeLa	[380]
Core–shell QDs containing environmentally-benign transition metal ion Mn(II)-doped ZnS as a core material encapsulated within different thickness ZnS shell layers	[Non-specific cellular uptake]; cation-exchange process with metal ions which have a low solubility product constant (K_{sp}) compared with that of chalcogenides	Fluorescence		HeLa, HEK-293; Hg^{2+}, Pb^{2+}	[381]
ZnO NPs		Fluorescence		T47D	[382]
ZnO NPs	Hairpin-structured DNA	Fluorescence	miRNA-21; miRNA-373	HeLa; HepG-2; L-O2	[383]
Gadolinium cluster encapsulated metallofullerene $Gd_3N@C_{80}$	MRI probe [IL-13-TAMRA-$Gd_3N@C_{80}(OH)_{30}$-$(CH_2CH_2COOH)_{20}$]	Fluorescence	Overexpressed IL-13Rα2 receptors	RAW 264.7	[384]
Gadolinium phosphate ($GdPO_4$) nanoprisms doped with lanthanide (Eu^{3+}, Tb^{3+}) ions		Fluorescence		HeLa; L-O2	[385]

Table A.3: Biosensing.

Material	**Probe**	**Detection method**	**Target**	**Cell lines/Animal models**	**Ref.**
Synthetic and biomolecular functionalised graphene-based sensing array	Functionalised graphene nanocomposites	Ultrasensitive electrochemical impedance signal (electrostatic and hydrophobic interactions between probe and target)	Phospholipids, membrane proteins and carbohydrates of the cell surface	A549; HeLa; HepG2; K562; MCF-7; MDA-MB-231; MCF-7/ADR; NIH-3T3; PC-12; HEK-293T; PBMCs	[386]
Carboxy functionalised graphene on Si/SiO_2 substrate	Amine functionalised Abs (anti-JEV for JEV and anti-AIV for AIV) covalently coupled with carboxyl activated graphene	Field-effect transistor-based (monitoring the change in resistance of the graphene channel as a function of time)	Monoclonal Abs of JEV and AIV	JEV; AIV	[387]
Monolayer nanosheets of graphene- and WS_2-coated commercial Au chips	BSA	SPR	Anti-BSA		[327]
ZnO nanowires and graphene nanoplates synthesis on an Au interdigitated electrode		Resistivity-based	Glucose		[388]
Cuprous oxide (Cu_2O) NP and acid-functionalised GO composite		Cyclic voltammetry; amperometry	8-hydroxydeoxyguanosine (8-OHdG)	Biological fluids (blood serum and urine)	[389]
Amine-terminated MWCNTs–rGO–polyaniline–AuNPs modified screen-printed carbon electrode		Cyclic voltammetry; amperometry	Glucose	Human blood serum samples	[390]

Table A.3: Biosensing (continued).

Material	**Probe**	**Detection method**	**Target**	**Cell lines/Animal models**	**Ref.**
Single-chirality DNA–CNT complex (CNTs noncovalently functionalised with specific ssDNA oligonucleotides)	Lipid binding to the ss(GT)6-(8,6) complex reduces the water density near the nanotube surface, thereby lowering the effective local solvent dielectric; the lower dielectric environment corresponds to a blue-shift of the nanotube emission wavelength	NIR hyperspectral microscopy	Lumen of endolysosomal organelles	Fibroblasts from a Niemann–Pick type C patient	[391]
Molybdenum NPs self-supported functionalised MWCNTs (MoNPs@*f*-MWCNTs)-based core–shell hybrid nanomaterial		Electrochemical	DA	Rat brain, human blood serum, and dopamine hydrochloride injection samples	[392]
Magnetised CNT-based lateral flow strip biosensor	Ab-modified magnetised CNTs	Visual detection	Rabbit IgG	Whole blood	[393]
Patterned nano-arrays of carbon nanofibers forming a nanosensor–cell construct		Electrochemical	MB (testing access to cytoplasm)	RAW 264.7	[394]
Ab-conjugated NDs	Maltotriose-conjugated polypropylenimine dendrimers	TEM; fluorescence	Nuclear pore complex	HeLa	[395]
Uniform Pd nanosheets	DNA detection probes with single-stranded sticky end for ssDNA detection	Fluorescence	Single-stranded circulating tumour DNA (ctDNA)		[396]
PDMS herringbone structures made with a ZnO nanorod template	Monoclonal Ab against the hemagglutinin of H5 AIV	AuNP-based colorimetric detection with a silver enhancer	Hemagglutinin of H5 AIV	AIV	[397]

Table A.3: Biosensing (continued).

Material	**Probe**	**Detection method**	**Target**	**Cell lines/Animal models**	**Ref.**
Gold-coated fiber modified with MoS_2 nanosheets followed by bio-functionalisation with anti-BSA Abs	Anti-BSA Abs	SPR	BSA protein		[326]
Ti_3C_2 MXene-based sensing platform and MWCNTs–PDA–AgNPs signal enhancer	Monoclonal anti-CEA antibody (Ab_1) through its F_c region	SPR	CEA		[398]
AuNP–PDMS composite film		Direct assay and sandwich assay	BSA		[399]

Table A.4: Photothermal therapy.

Material	Probe	Method	Target	Cell lines/Animal models	Ref.
Positively charged graphene/Fe_3O_4/PEI nanocomposite	(Positive surface charge increased cellular uptake)	808 nm laser irradiation		MCF-7; U14; mice	[400]
GO–MB nanocomposite		Red LED irradiation		MDA-MB-231	[401]
GO functionalised with an amphiphilic polymer containing [2-(methacryloyloxy)ethyl]dimethyl-(3-sulfopropyl)ammonium hydroxide (SBMA) brushes and loaded with IR780		808 nm NIR laser irradiation		MCF-7; NHDF	[402]
rGO–PEG–folic acid functional nanomaterials		NIR laser irradiation		MDA-MB-231; HUVEC	[403]
PDA-functionalised rGO nanosheets and bimetallic AuPd NP composites		915 nm NIR laser irradiation		MDA-MB-231; L929	[404]
rGO functionalised with oxidised polyphenols		808 nm NIR laser irradiation		A549; MDCK	[405]
Cy7 dye-conjugated SWCNTs bound with targeting IGF-1R Abs	Targeting IGF-1R Ab	785 nm NIR laser irradiation		BXPC-3; PANC-1; ASPC-1; SW1990; BALB/c male mice	[406]
TAT-chitosan functionalised MWCNTs-based drug delivery system for DOX		NIR irradiation	DOX entered cell nucleus; MWCNTs remained in cytoplasm	Bel7402	[407]
Fluorescent-labelled fullerene C_{60}		Visible light irradiation		Jurkat; L1210	[408]

Table A.4: Photothermal therapy (continued).

Material	**Probe**	**Method**	**Target**	**Cell lines/Animal models**	**Ref.**
Water soluble malonodiserinolamide [60]fullerene (C_{60}-ser) conjugated to the surface of mesoporous silica NPs (SiO_2–C_{60})		Radiofrequency exposure	(Smaller cells more susceptible)	HUVEC; HMVEC; primary dermal fibroblast; L939; HeLa; 4T1	[409]
HA-modified SWCNTs, GO, and fullerene		Visible light irradiation	CD44 receptors	MCF-7; female KM mice	[410]
Gold nanocages		Acoustic radiation; 780 nm laser irradiation		MDA-MB-231	[411]
Core–shell multifunctional nanomaterial-based all-in-one nanoplatform composed of gold nanobipyramids@PDA and AuNCs	mucin1 (MUC1) aptamer; ssDNA	808 nm NIR laser irradiation	mucin1 (MUC1); miRNA-21	MCF-7; HepG2; L02	[412]
MB photosensitiser-trapped AuNCs		Dual light irradiation (660 nm for MB, 808 nm for gold)		CT26; female BALB/c mice	[413]
Exosomes mildly functionalised by integration with aptamers and Au nanorods to assemble Apt–Exos–AuNRs combination	aptamer 1 (comprising the HepG2-recognition aptamer (TLS11a) and CD63-recognition aptamer) and aptamer 2 (comprising the nucleolin-recognition aptamer (AS1411) and CD63-recognition aptamer)	808 nm diode NIR laser irradiation		HepG2; MCF-7; A549; HCT116; L02	[414]
Gold–curcumin nanostructure		808 nm NIR laser irradiation; 650 nm laser irradiation		4T1	[415]

Table A.4: Photothermal therapy (continued).

Material	**Probe**	**Method**	**Target**	**Cell lines/Animal models**	**Ref.**
Au/MnO_2 nanocomposite		808 nm NIR laser irradiation		C540 (B16/F10); male BALB/c mice	[416]
DMSA-modified iron oxide-decorated MoS_2 nanosheets with double PEGylation		808 nm laser irradiation		4T1; RAW 264.7; BALB/c mice	[417]
Ultrasmall single-layer MoS_2 nanodots with different phases (1T-MoS_2 nanodots more effective than 2H-MoS_2 nanodots		1064 nm NIR-II laser irradiation)		A549; HeLa	[418]
TaO_2 deposited onto chitosan-coated MoS_2 nanosheet		808 nm NIR laser irradiation		MCF-7; HBL-1000	[419]
Monocomponent hollow Pt nanoframe ("Pt spirals"), whose superstructure is assembled with three levels (3D frame, 2D layered shells, and 1D nanowires)		NIR-II laser irradiation		HeLa; 4T1; mice bearing U14 tumours	[420]
Silica nanostructures on Cu_9S_5 core–shell nanostructures		808 nm NIR laser irradiation		EC109; TE8	[421]
Bismuth sulfide (Bi_2S_3) nanorods with retractable zinc protoporphyrin IX molecules	Zinc protoporphyrin IX	808 nm NIR laser irradiation	oxygenase-1 (overexpressed in cancer cells)	4T1	[422]

Table A.5: Drug delivery.

Material	**Probe**	**Drug**	**Target**	**Cell lines/Animal models**	**Ref.**
Nano GO		MB	Cell cytoplasm	NIH-3T3	[423]
Polyacrylate-grafted GO	"Albumin" surface terminations	DOX		SH-SY5Y	[424]
PEG-modified GO and cobalt NP composites		DOX		L929; 3T3; MG63	[425]
GO–AgNP nanocomposites		Cisplatin		HeLa	[426]
Drug-conjugated CQDs		Metronidazole		*P. gingivalis*	[427]
GQDs-grafted dextran/glycol-polymeric hydrogel		Buprenorphine	Stromal cells (noteworthy infiltration)	L929 (mouse fibroblast); female SD rats with chronic contraction injury	[428]
GQDs	Charge-reversal APTES	DOX	Nucleus	MDA-MB-231	[429]
Nitrogen and sulfur co-doped CDs		Mitoxantrone	Cytoplasm	HeLa	[430]
ND-based composites		DOX	Cytoplasm mainly, some cell nuclei	HepG2	[431]
DOX conjugated with NDs		DOX		Human glioblastoma	[432]
Carbon nanofibers; CNTs		Carboplatin; cisplatin		DU-145; PC-3; EJ28	[433]
Smart freestanding CNTs with hydrophilic core and chitosan surface functionalisation		DOX		MDA-MB-231 TXSA; human foreskin fibroblast	[434]

Table A.5: Drug delivery (continued).

Material	**Probe**	**Drug**	**Target**	**Cell lines/Animal models**	**Ref.**
PEG-coated CNTs		ABT737 nanodrug	Mitochondria (via early endosomes)	A549; NHFB	[435]
C_{60} fullerene		Cisplatin	Three principal plasma membrane transporters involved in the efflux of anticancer drugs (P-gp, MRP-1, and MRP-2)	Human isogenic p54-null, Bax-null, and wild-type HCT-116; HeLa; human Jurkat T-leukaemia; KB-3-1 and KBC-1; HL-60/adr; HL-60/vinc; Lewis lung carcinoma (LLC) C57BL/6J male mice	[436]
C_{60} fullerene and HL1, HL2		HL1 (dimorfolido-N-trichloroacetylphosphorylamide); HL2 (dimorfolido-N-benzoylphosphorylamide)		Human Jurkat T-leukaemia; Molt-16; CCRF-CEM	[437]
Glycine-tethered C_{60} fullerenes conjugated with N-desmethyl tamoxifen		Tamoxifen		MCF-7	[438]
C_{60} fullerene		DOX, cisplatin and landomycin A			[439]
HSA attached to pore openings of mesoporous carbon NPs surface-modified with PEG		DOX	Cytoplasm	4T1; Female BALB/c mice	[440]
CB	Acoustic waves	Calcein	Cell membrane	DU145	[441]
Oxidised carbon nanohorns		Meso-tetra(4-N-methylpyridyl) free base (H2TMPyP4) porphyrin; platinum (PtTMPyP4) porphyrin		HeLa	[442]

Table A.5: Drug delivery (continued).

Material	**Probe**	**Drug**	**Target**	**Cell lines/Animal models**	**Ref.**
Oxidised and unoxidised carbon nanohorns; CNTs		Minocycline		*S. mutans*; *A. actinomycetemcomitans*	[443]
Non-covalently functionalised carbon nano-onions functionalised with a HA–phospholipid conjugate (CNO:f-HA–DMPE)			Cells overexpressing CD44; digestive tract of the zebrafish larvae	MDA-MB-231 (overexpressing CD44); A2780 (control); adult zebrafish	[444]
MoS_2 nanosheets functionalised with lipoic acid-modified PEG		DOX; SN-38; chlorine e6	Folic acid	HeLa; KB	[107]
Single-layer MoS_2 nanosheets decorated with chitosan		DOX		KB; Panc-1; mouse blood samples; male BALB/c nude mice	[108]
TMDs and phosphocholine liposomes hybrids		DOX; calcein		HeLa	[287]
Nano-radiogold-decorated composite bioparticles		DOX	Nucleus; lysosomes	MCF-7; CRL-1790	[445]
Platinum(II) drug-loaded gold nanoshells		DACHPt	Cytoplasm; endo/lysosomes	HCT116; HT29; LS174T	[446]
Rodlike mesoporous silica coated with gold nanoshells, modified with ultrasmall gadolinium-chelated supramolecular photosensitisers		Ultrasmall gadolinium-chelated supramolecular photosensitizers		4T1; human blood; BALB/c and nude mice	[447]
Layered zinc hydroxide		Naproxen		HFFF2	[448]

Table A.5: Drug delivery (continued).

Material	**Probe**	**Drug**	**Target**	**Cell lines/Animal models**	**Ref.**
Hybrid inorganic–organic nanocolloids electrostatically conjugated with DOX		DOX	Cytosol; nucleus	Glioblastoma	[449]
Nanofibrous silica microparticles/polymer hybrid aerogels		Camptothecin		HeLa; SiHa; C33A; HaCaT; L929 cells, ATCC® CCL1; Vero, ATCC® CCL81	[450]
Hydroxy boron nitride nanosheets and Pd nanohybrids		DOX	Cytoplasm; nucleus	MCF-7; female BALB/c mice	[451]
Silver sulfide QDs		^{14}C metformin		SK-Hep-1; HEK293T; male C57/Bl6 mice	[452]
Copper oxide QDs-coated HA/PLGA		Piperine		hCMEC/D3; male Wistar rats	[453]

Table A.6: Stem cell control.

Material	**Probe**	**Cell lines/Animal models**	**Key conclusions**	**Ref.**
Graphene substrates with controlled domain size		Human MSCs	Upregulated neuronal differentiation of human MSCs on small domain graphene compared to large domain graphene	[454]
Pristine GO nanosheets		Rat BMSCs	Pristine GO nanosheets at a concentration of 0.1 µg/mL provide benefits to promote BMSCs proliferation and osteogenesis under a sequential-seeding method	[455]
GO; BMP-2–GO		Rat bone marrow stem cells and chondrocytes; osteoarthritic rats	GO may be potentially used to control the release of carrier materials; BMP-2–GO slowed the progression of NF-κB-activated degenerative changes in osteoarthritis	[456]
A nonviral vector based on Fe_3O_4 NP-decorated GO complexed with PEI (GO–Fe_3O_4–PEI complexes)	Three individual episomal plasmids (pCXLEhOCT3/4-shp53, pCXLE-hSK, and pCXLE-hUL) encoding pluripotent-related factors of Oct3/4, shRNA against p53, Sox2, Klf4, L-Myc, and Lin28	Human PBMCs	Combined effect of magnetic targeting and photothermal stimulation promoted the transfection efficiency of suspension cells; transfected cells show positive expression of the pluripotency markers and have potential to differentiate into mesoderm and ectoderm cells; GO–Fe_3O_4–PEI complex provides a safe, convenient, and efficient tool for reprogramming PBMCs into partially induced PSCs able to rapidly transdifferentiate into mesodermal lineages without full reprogramming	[457]
Phase-engineered GO		Human BMSCs	Transformation results in clustering of oxygen atoms on the GO surface, greatly improving its ability toward substance adherence; results in enhanced differentiation of human BMSCs toward the osteogenic lineage	[458]
BMP-2 immobilised on GO-incorporated PLGA/HA biodegradable microcarriers		MC3T3-E1	The immobilisation of BMP-2 onto the GO–PLGA/HA microcarriers resulted in significantly greater osteogenic differentiation of cells *in vitro* (bone tissue engineering application)	[459]

Table A.6: Stem cell control (continued).

Material	**Probe**	**Cell lines/Animal models**	**Key conclusions**	**Ref.**
Laser-printed GO surfaces with both a local photothermal GO reduction and the formation of nano-wrinkles along precise geometric patterns		Calvarial-derived MSCs (cMSC); MRSA	The morphology of the designed surfaces guided stem cell orientation and the reduction accelerated differentiation; reduced sharp nano-wrinkles were able to enhance the GO antibacterial activity against MRSA	[460]
Micro-sized (1–10 µm) and nano-sized (100–300 nm) GO sheets (MGO; NGO)		Human AMSCs	Human AMSCs grown on the MGO-coated substrates show enhanced cell spreading and proliferation rate when compared with those of NGO counterpart, regardless of their densities	[461]
Bioactive GO-modified titanium implant surface		Rat BMSCs	Compared with the surface type in common use, the GO-modified surface favoured cell adhesion and spreading, and significantly improved cell proliferation and osteogenic differentiation of rat BMSCs *in vitro*; GO modification on titanium implant surface has potential applications for achieving rapid bone-implant integration through the mediation of FAK/P38 signalling pathways	[462]
PCL, rGO/PCL, and GO/PCL nanofibrous meshes via electrospinning		NIH-3T3; human osteosarcoma; MG-63	rGO/PCL fibrous meshes supported improved cell adhesion, spreading and proliferation of fibroblasts and osteoblast-like cell lines; rGO/PCL fibrous meshes enhanced *in vitro* calcium deposition in the extracellular matrix produced by osteoblast-like cells, and human MSCs grown onto the same substrates had an increased expression of the osteogenic markers necessary for mineralisation (bone tissue engineering application)	[463]

Table A.6: Stem cell control (continued).

Material	**Probe**	**Cell lines/Animal models**	**Key conclusions**	**Ref.**
Nanostructured rGO microfibers		RAW 264.7	rGO microfibers inhibit the proliferation of RAW 264.7 macrophages without affecting their viability and cell cycle profiles; rGO microfibers able to support the formation of a highly interconnected neural culture composed of both neurons ($map2^+$ cells) and glial cells ($vimentin^+$ cells)	[464]
Gelatin from cold water fish skin (FG) electrospun microfibers loaded with NDs		Human AMSCs	Increased viability and proliferation profile of human AMSCs in contact with FG/NDs, correlated with very low cytotoxic effects of the materials; human AMSCs developed an elongated cytoskeleton, suggesting that addition of NDs to FG materials encouraged cell adhesion	[465]
Pervasion of beta-tricalcium phosphate (βTCP) with ND particles		Sheep BMSCs; (female merino sheep bone tissue engineering application)	βTCP carrying 4% ND resulted in enhanced attachment of MSCs *in vitro*; ND in βTCP resulted in a consistently steady bone formation when compared to pure βTCP in guided-bone regeneration after lateral augmentation of the mandible in sheep	[466]
ND monolayers with varied surface functionalisations		Human NSCs	Confluent cellular attachment occurs on oxygen terminated NDs (O–NDs), but not on hydrogen terminated NDs (H–NDs)	[467]
Multivalent polyanion-dispersed CNTs for nanostructured fibrous scaffolds		Induced PSCs	Biocompatible platform for promoting the adhesion and proliferation of induced PSCs; immunostaining shows that the nanostructured fibrous scaffolds induce higher neural differentiation efficiency compared to the control substrates; the aligned fibrous scaffolds can guide the orientation of generated neurites	[468]

Table A.6: Stem cell control (continued).

Material	**Probe**	**Cell lines/Animal models**	**Key conclusions**	**Ref.**
Co-engrafted CNTs and human OBNSCs		Human OBNSCs	Engrafted human OBNSCs–CNTs restored cognitive deficits and neurodegenerative changes associated with trimethyltin-induced rat neurodegeneration model; the CNTs seemed to provide a support for engrafted OBNSCs, increasing their tendency to differentiate into neurons rather than into glia cells	[469]
MWCNTs; nano-HAP		Human AMSCs	Cell attachment strength and proliferation on the MWCNTs were better than on the nano-HAP; MWCNTs induced osteogenic differentiation of the human AMSCs better than the nano-HAP; MWCNTs could induce ectopic bone formation *in vivo* while the nano-HAP could not	[470]
Chemically crosslinked CNTs (of various diameters), graphene nanoplatelets, and graphene nanoribbons coatings		Primary human AMSCs	The greatest autodeposition of calcium was observed on graphene nanoribbon surfaces, while MWCNTs of high diameter had the greatest influence on stem cell fate	[471]
Hexagonally arranged gold nanostructures of three different dimensions on silicon		Human AMSCs	Nanostructure size and distance affects the spreading of human AMSCs; an increase of nanostructure feature dimensions corresponded to a decrease of cell size and to the expression of focal adhesions and presence of the small GTPase RhoA	[472]
Metal ion (Zn, Ag and Cu)-doped HAP nano-coated surfaces		Human AMSCs	Results demonstrate that the viability and osteogenic differentiation of the human AMSCs and cell adhesion capability are higher on nanocoated surfaces that include Zn, Ag and/or Cu metal ions than commercial HAP	[473]
AgNPs incorporated VEGF		Human MSCs	AgNPs with VEGF molecules promoted the cell adhesion and proliferation of human MSCs; AgNPs incorporated VEGF material is highly favourable to fracture healing and blood vessel repair	[474]

Table A.6: Stem cell control (continued).

Material	**Probe**	**Cell lines/Animal models**	**Key conclusions**	**Ref.**
Hydrogenated black TiO_2 (H-TiO_2) coating with hierarchical micro/nano-topographies		Rat BMSCs	The fabricated H-TiO_2 coating possessed excellent and controllable photothermal effect in inhibiting tumour growth under 808 nm NIR laser irradiation *in vitro* and *in vivo*; the hierarchical hybrid micro/nanostructured surface and Ti-OH groups improved the adhesion, proliferation, differentiation and osteogenic gene expressions of rat BMSCs	[475]
Nanopatterned Ti surfaces (by electrochemical nanopattern formation, ENF)		Human MSCs	Human MSCs on ENF surfaces exhibit increased proliferation and enhanced osteogenic differentiation compared to the ordered TiO_2 nanotubular and compact TiO_2 surfaces	[476]
Phosphorylated Ti coating (TiP-Ti) with a micro/nano hierarchically structured topography on commercially pure Ti implants		Rat BMSCs; female Sprague Dawley rats	The improved osteointegration mainly benefited from the better spread and adhesion of rat BMSCs on the micro/nano hierarchically structured TiP-Ti surfaces compared to HAP coated Ti (the positive control) and untreated Ti (the negative control)	[477]
Polyether ether ketone (PEEK); Ti_6Al_4V (smooth Ti); macro-micro rough Ti_6Al_4V (Endoskeleton®); macro-micro-nano rough Ti_6Al_4V (nanoLOCK®)		Human MSCs	Incorporation of a hierarchical macro-micro-nano roughness on titanium produces a stellate morphology typical of mature osteoblasts/osteocytes, rapid and random migration, and improved osteogenic differentiation in seeded human MSCs	[478]

Table A.7: Toxicity studies.

Material	**Tests**	**Target/Cell lines /Animal models**	**Key conclusions**	**Ref.**
Fabricated nano GO (NGO) sheets	Extrinsic and synchronous fluorescence spectroscopy; far circular dichroism spectroscopy; molecular docking investigation; cellular assays (trypan blue exclusion, cellular uptake, ROS, cell cycle, and apoptosis); molecular assay	Secondary and quaternary structural alterations of human Hb; human lymphocyte cells	NGOs can unfold the quaternary structure of Hb in the vicinity of Tyr residues; α-helicity of Hb experienced substantial alteration upon interaction with increasing concentrations of NGOs; NGOs interacted with polar residues of Hb; NGOs lead to ROS formation, cell cycle arrest, and apoptosis through the *BAX* and *BCL2* pathway	[479]
AuNPs-decorated rGO nanocomposite	MTT assay; DCF assay; bacterial toxicological evaluation; DIZ and AI evaluation; MIC and MBC determination; GrK and DeK evaluation	A549; HCT116	The synthesised nanocomposite showed significant anti-cancer activity towards A549 cell line and Gram-negative bacterial strain *E. coli* compared to the rest	[480]
rGO; *O. sanctum* rGO (ORGO)	Test for phenols; test for flavonoids; DPPH assay; IC_{50} value determination; haemolysis assay; CCK-8	Hb; Balb 3T3	GO showed higher haemolytic activity of 6.9% and higher inhibition of growth of 3T3 cells at all tested concentrations than ORGO	[481]
SWCNT; MWCNTs; ultrafine CB; crocidolite asbestos		Primary human small airway epithelial cells immortalised with hTERT (SAECs)	Chronic exposure to carbon nanomaterials and asbestos caused substantial DNA damage and p53 dysregulation in human SAECs; exposed lung cells exhibited neoplastic and cancer stem cell (CSC)-like properties, as indicated by anchorage-independent colony formation, spheroid formation, anoikis resistance, and CSC marker expression; high aspect ratio materials including SWCNT, MWCNT and asbestos exhibited strong neoplastic and CSC-like properties as compared to low aspect ratio ultrafine CB particles	[482]

Table A.7: Toxicity studies (continued).

Material	**Tests**	**Target/Cell lines /Animal models**	**Key conclusions**	**Ref.**
Unfunctionalised MWCNTs–ultrahigh molecular weight polyethylene (MWCNT–UHMWPE) nanocomposites	Cellular assays (Trypan blue, calcein AM, cell proliferation, cell adhesion)	HFW	Good cell viability on the surface of MWCNT–UHMWPE composites even after 72 h; nanocomposites showed better cell attachment for fibroblasts than pristine UHMWPE; overall, the results showed that MWCNT–UHMWPE composites displayed good cellular growth and biocompatibility indicating another way CNTs can be nontoxic	[483]
Raw and functionalised MWCNTs (RMWCNTs; FMWCNTs)	Cytotoxicity assays (MTT, NRU); cellular morphology (phase contrast microscope); intracellular ROS generation (DCFH-DA); MMP (Rhodamine-123 fluorescent dye)	MCF-7	Concentration-dependent decrease in cell viability of MCF-7 cells; RMWCNTs- and FMWCNTs-exposed cells found to alter the normal morphology of MCF-7 cells; cells showed significant induction in ROS generation and reduction in MMP level	[484]
Pristine and functionalised MWCNTs	Cell viability (PI); intracellular ROS (DCF-DA, confocal microscopy); MMP (Rhodamine 123); DNA damage (comet assay); phlogistic effect (gene expression analysis and ELISA tests)	Differentiated SH-SY5Y	The neurotoxic and neuroinflammation properties of the examined MWCNTs assessed *in vitro* highlighted the potential pathogenic mechanisms triggered by these engineered NPs; impairment of several molecular pathways could contribute to the onset and progression of neurodegenerative diseases	[485]
Carboxylated SWCNTs and MWCNTs (SWCNT-COOH and MWCNT-COOH)	Cell viability (MTT test); cell motility (evaluated by WHO guidelines); ROS production; NO production	Human spermatozoa	Neither MWCNT-COOH nor SWCNT-COOH exerted negative effect on viability, but motility was significantly dropped in a dose-dependent manner; no significant effect of the type, dose and exposure time of the CNT-COOH on NO production; exposure of sperm cells to both examined types of CNTs at concentrations as low as 0.1 µg/ml caused a significant increase in ROS levels	[486]

Table A.7: Toxicity studies (continued).

Material	**Tests**	**Target/Cell lines /Animal models**	**Key conclusions**	**Ref.**
Eight commercially available CNTs	WST-1 measurement; LDH detection; ROS detection; inflammatory cytokine detection	RAW 264.7	Cellular uptake of CNTs by RAW 264.7 macrophages depends on their sizes, specifically on the widths of their bundles in dispersion, regardless of type or manufacturer; uptake of CNTs increased linearly with dynamic size, and cytotoxicity increased with uptake	[487]
SWCNTs with physicochemical alterations in structure resulting from ball-milling	Evaluation of protein components (proteomics)	Normal and cholesterol-rich mouse serum	Increased ball-milling time of SWCNTs resulted in enhanced structural defects; following incubation in normal mouse serum, differences in the biomolecular content of the biocorona due to the ball-milling process were identified; incubation in cholesterol-rich mouse serum resulted in the formation of unique biocoronas compared to SWCNTs incubated in normal serum	[488]
Pristine C_{60} fullerene aqueous solution (C_{60}FAS); 5-FU and pyrrole derivative MI-1 cytostatic drugs		Colorectal cancer	The number of tumours and total lesion area decreased significantly under the action of C_{60}FAS and MI-1; because these drugs have different mechanisms of action, their simultaneous administration can potentially increase the effectiveness and significantly reduce the side effects of antitumour therapy	[489]
CB particles with primary diameter 56 nm (CB56) and 95 nm (CB95)	Cytotoxicity (trypan blue); 8-nitroG formation (immunocytochemistry); ROS generation (flow cytometry); NO release (Griess method); cellular uptake (DMEM treatment)	RAW 264.7; A549	Both types of CB induced 8-nitroG formation, mainly in the nucleus of RAW 264.7 and A549 cells; CB95 tended to induce more 8-nitroG formation than CB56; CB95 generated larger amounts of ROS than CB56 in RAW 264.7 cells; CB95 produced significantly larger amount of NO than CB56; CB95 was more efficiently internalised into the cells than CB56	[490]

Table A.7: Toxicity studies (continued).

Material	**Tests**	**Target/Cell lines /Animal models**	**Key conclusions**	**Ref.**
MoS_2 functionalised with thiobarbituric acid (TBA)	Cell viability assays (MTT; WST-8)	A549	MoS_2–TBA is less toxic to cells compared to MoS_2	[491]
Boron nitride nanotubes (BNNTs)	Cytotoxicity (WST-8, MTS, MTT assays); cardiomyocyte beating behaviour (novel cardiomyocyte AFM model)	NB4; HepG2; U87	Correlation between tube length and cytotoxicity with longer tubes having higher cytotoxicity; BNNTs exhibit concentration and cell-line dependent cytotoxic effects	[492]
Titanium dioxide NPs modified with noble metals (Au, Ag, Pd, Ag_2O, and PdO)	Cell viability (MTT; flow cytometry, Annexin V-FITC)	Caco-2; BJ; L929	Irrespective of cell line and assay used, NPs of unmodified titanium dioxide as well as those with addition of gold and palladium have a slight impact on cell viability at the investigated concentration range (10–200 µg/mL); NPs with addition of silver (Ag and Ag_2O) were found to have significantly higher toxic effect, the level of which varied depending on the cell line and assay used	[493]

Table A.8: Theranostics.

Material	**Probe**	**Detection method**	**Therapy**	**Target**	**Cell lines/Animal models**	**Ref.**
Highly fluorinated GO (FGO) as a carrier for linoleic acid–curcumin conjugate (FGO–Lino–CUR)		T_2-weighted MRI	Chemotherapy (linoleic acid–curcumin conjugate as an anticancer drug)		MCF-7; MCF10A; 4T1-induced BALB/c mice	[494]
Cyclodextrin-functionalised GO bound to carbon-coated iron NPs (GO-CD/Fe@C)		MRI	Chemotherapy (DOX)	Nuclei (mainly); lysosomes, mitochondria (some amount)	MDA-MB-231	[495]
Fluorescent CQDs		Fluorescence imaging	PDT; chemotherapy (rose bengal)	Mitochondria	MCF-7; HeLa; HepG2; AT II; L02; RAW 264.7	[496]
Protein (urokinase-type plasminogen activator)–CD nanohybrids		Fluorescence imaging	Thrombolysis ability		Human blood clots; male BALB/c mice subjected to 3 h transient middle cerebral artery occlusion (tMCAO) or sham-operated	[497]
PLGA–CDs hybrid		Fluorescence imaging	Chemotherapy (irinotecan); PTT (810 nm laser irradiation)		MDA-MB-231	[498]
Pristine GQDs; GQDs irradiated with gamma rays; GQDs doped with N and N,S atoms	GQDs (GQDs functionalised with urea better for imaging than pristine GQDs)	Fluorescence imaging	PDT (GQDs-U)		HeLa	[499]

Table A.8: Theranostics (continued).

Material	Probe	Detection method	Therapy	Target	Cell lines/Animal models	Ref.
Phycocyanin-functionalised single-walled carbon nanohorns (PC@SWNHs) hybrid	Phycocyanin	PAI; thermal imaging	PDT (SWNHs); PTT (SWNHs)		4T1; MDA-MB-231; mice	[500]
2D BP nanosheets functionalised with positively charged PEG–NH_2		NIR (Cy7)	Chemotherapy (DOX)	Lysosomes	HeLa	[501]
Hollow carbon nanospheres		PAI; NIR	PTT (NIR-triggered)		HeLa; HepG2; MCF-7; male nude BALB/c mice	[502]
C_{60} fullerene-based tumour-targeted PET imaging probe	^{64}Cu; cRGD	Fluorescence imaging; PET	Radiotherapy; radiopharmaceuticals	Integrin $\alpha_v\beta_3$	U87 MG (integrin $\alpha_v\beta_3$ positive); MCF-7 (integrin $\alpha_v\beta_3$ negative)	[503]
GO–GQDs hybrid		Fluorescence imaging	PTT (NIR-triggered)		MDA-MB-231; L929	[504]
PEI- and PEG-modified carbon nano-onion clusters (CNOCs)		Optical (uptake so high that fluorescence labelling is not required); dual-modal PTI/PAI	PTT		AT II; A549; mice	[505]
AuNPs-functionalised hollow P(MAA-*co*-MBA-*co*-AA) nanocontainers		Fluorescence imaging	Chemotherapy (DOX)		MCF-7; HEK-293	[506]

Table A.8: Theranostics (continued).

Material	Probe	Detection method	Therapy	Target	Cell lines/Animal models	Ref.
Structured NP (GNR@HPMO@PVMSN) composed of a gold nanorod (GNR) core, hollow periodic mesoporous organosilica (HPMO) shell and PDA-doped virus-like mesoporous silica NP (PVMSN) outer shell		PAI; infrared thermal imaging	PTT (808 nm NIR laser irradiation); chemotherapy (DOX)	GNR@HPMO@PVMSN is mainly distributed in the liver, spleen and lung	7721; H22 tumour-bearing female BALB/c nude mice	[507]
Fe_3O_4–Au nano-heterostructures		MRI	Magnetic fluid hyperthermia		Huh7; PLC/PRF/5-Alexander	[508]
Folate-modified vincristine-loaded PDA-coated Fe_3O_4 superparticles		MRI	Chemotherapy (vincristine); PTT (808 nm laser irradiation)		HaCat; T24; T24 tumour-bearing BALB/c nude mice	[509]
PDA-modified Fe_3O_4 nanocomposites		T_2-weighted MRI	PTT (808 nm NIR laser irradiation)		4T1; 4T1 tumour-bearing BALB/c mice	[510]
Fe_3O_4@PDA@BSA–Bi_2S_3 composite		MRI; CT	ROS-induced chemodynamic therapy (CDT); PTT (808 nm NIR laser irradiation)	Bi ions largely accumulated in the liver, spleen, and kidneys on the first day, but evidence of excretion over 14 days	L929; HT29 tumour-bearing BALB/c mice	[511]
HA-modified porous carbon-coated Fe_3O_4 NPs	HA	MRI	PTT; chemotherapy (DOX)	CD44 receptors	HeLa; HUVEC; nude mice	[512]

Table A.8: Theranostics (continued).

Material	**Probe**	**Detection method**	**Therapy**	**Target**	**Cell lines/Animal models**	**Ref.**
Boron nitride nanosheets functionalised with tannic acid–Fe^{3+} coordination complex (TA–Fe/BNNS)		T_1-weighted MRI	PTT (808 nm NIR laser irradiation)		KB tumour cells; 5-wk-old female BALB/c nude mice	[513]
2D PEGylated antimonene nanosheets		Multi-modal fluorescence imaging/PAI/PTI	PTT; chemotherapy (DOX)		MCF-7	[514]
Gd^{3+}-doped monolayered-double-hydroxide (MLDH) nanosheets		Dual-modal NIR fluorescence imaging/MRI	Chemotherapy (coloading of DOX and indocyanine green)		HepG2; HepG2 tumour-bearing mice	[515]
Ultrathin nanosheets of CoFe-selenide with a finely controlled structure followed by surface modification with PEG		T_2 MRI	PTT (808 nm NIR laser irradiation)		HeLa; HeLa tumour-bearing mice	[516]
Aggregation-induced emission (AIE) photosensitisers and 2D BP nanosheet compound		Fluorescence imaging (NIR region); PTI (808 nm NIR laser irradiation)	PTT (808 nm NIR laser irradiation); PDT (ROS generation under 808 nm laser irradiation)		4T1; 4T1 skin-tumour-bearing male BALB/c nude mice	[517]
Glucose oxidase-armed manganese dioxide nanosheets (MNS–GOx)		MRI; PAI	PTT (808 nm NIR laser irradiation); self-oxygenation		A375 tumour-bearing mice	[518]

B AFM images and statistics histograms from Chapter 3

In Chapter 3, average values of length (L), width (W), LW (length $\times$ width), and number of layers (N) for each material were needed to normalise the data for nanosheet size. To obtain these average values, the sheetwise data was binned to allow analysis of the distributions. Figures B.1–B.5 show the histograms of L, W, LW, and N obtained from AFM statistics for each material. The insets show example AFM images of a nanosheet for each material; Figure B.6 shows enlarged versions of these AFM images.

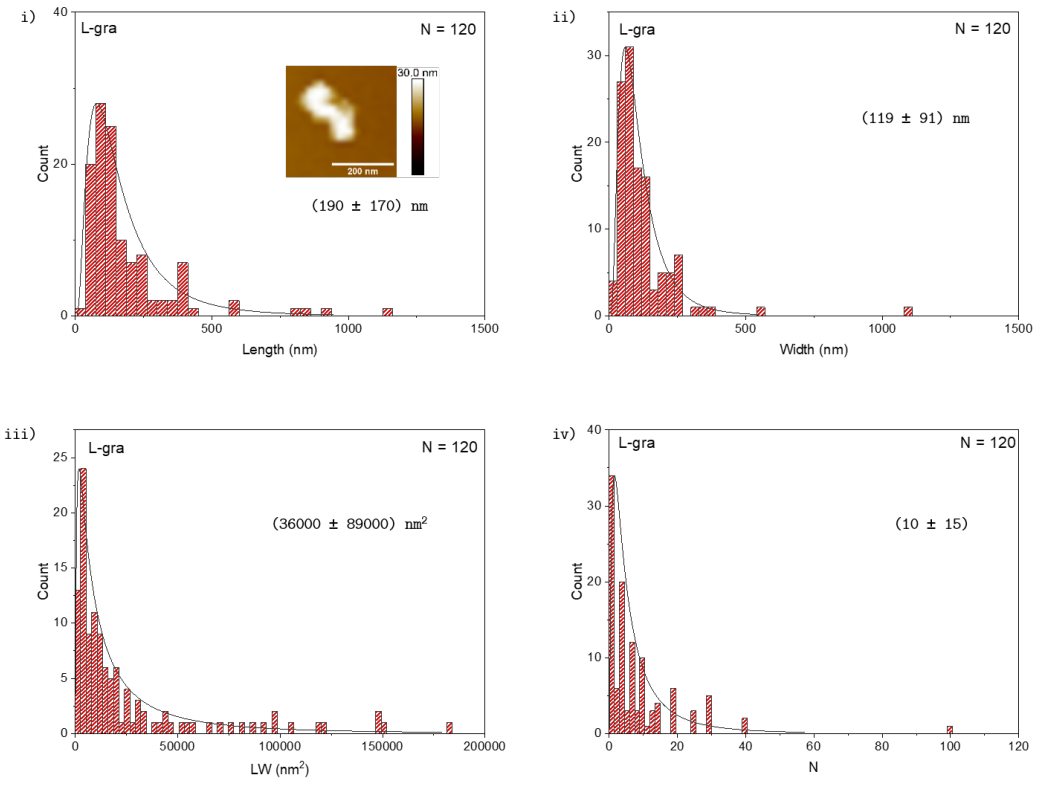

Figure B.1: Histograms of L-gra (i) length; (ii) width; (iii) LW; (iv) N.

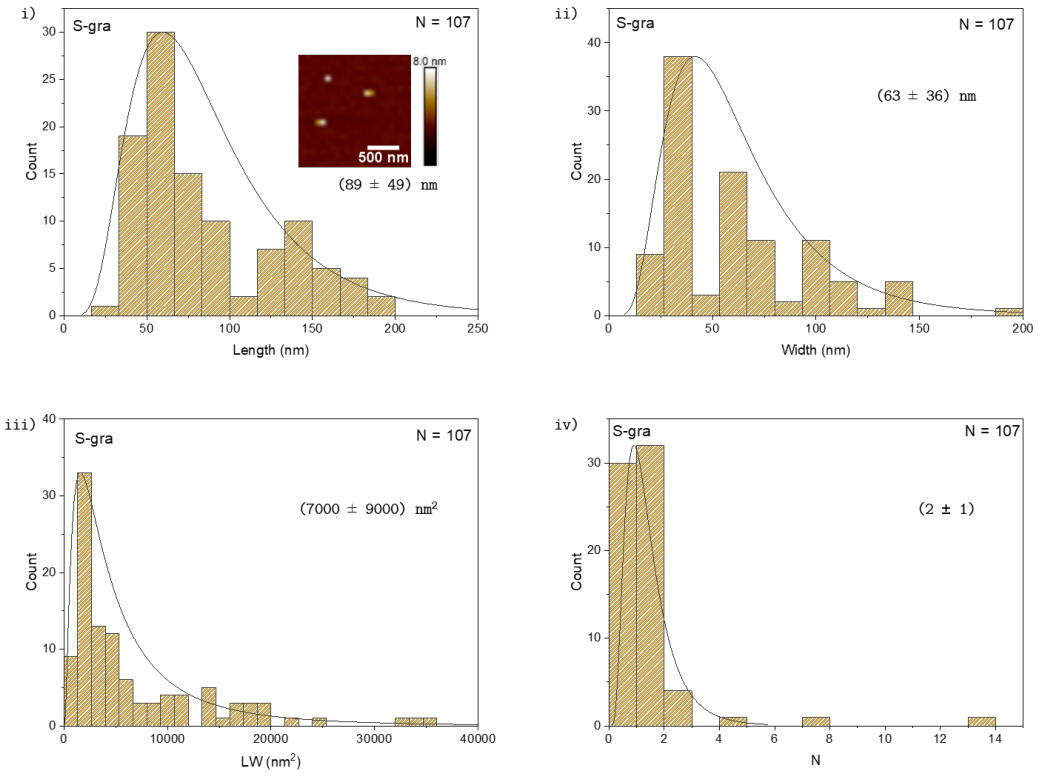

Figure B.2: Histograms of S-gra (i) length; (ii) width; (iii) LW; (iv) N.

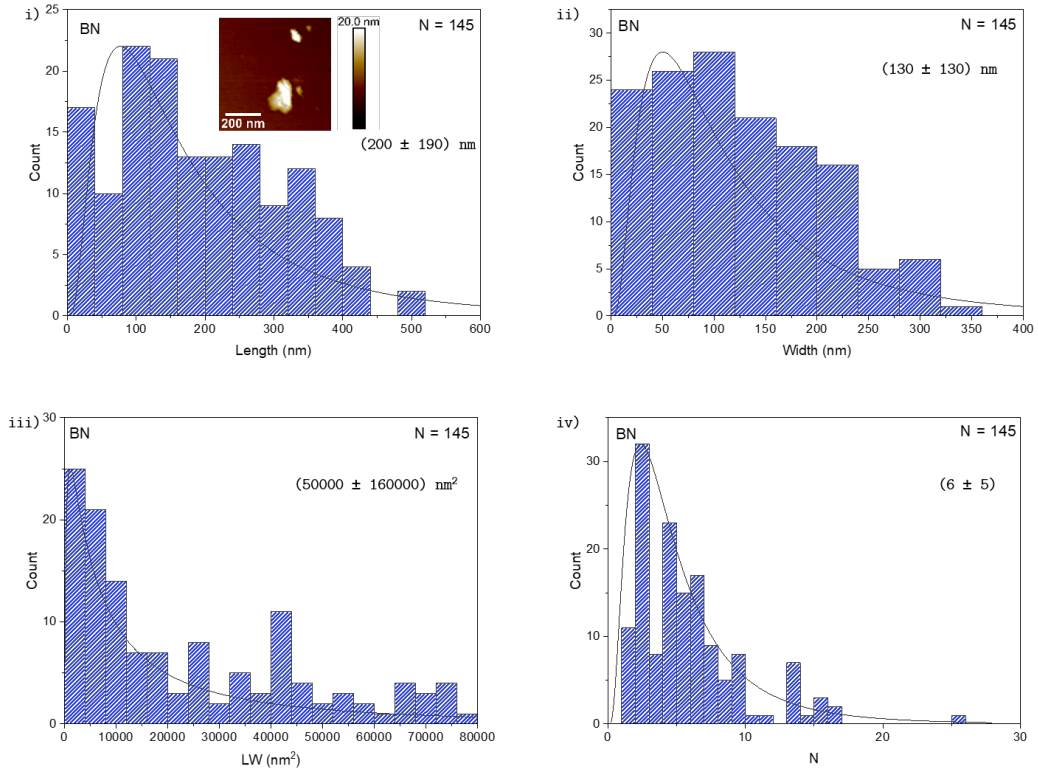

Figure B.3: Histograms of BN (i) length; (ii) width; (iii) LW; (iv) N.

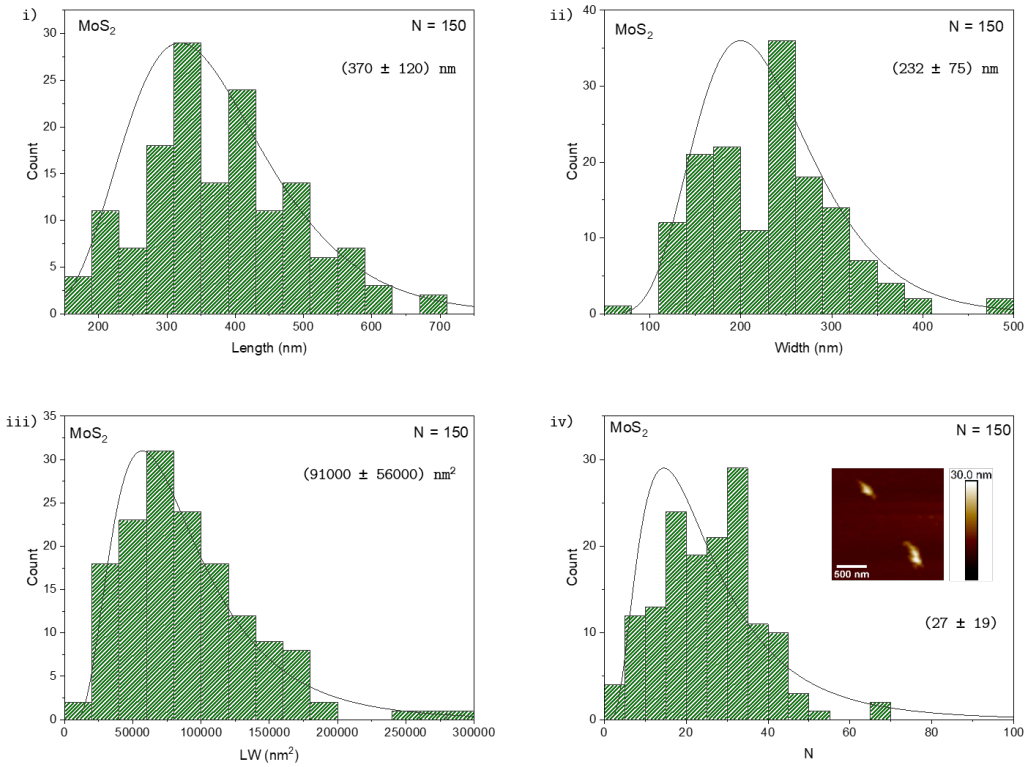

Figure B.4: Histograms of MoS_2 (i) length; (ii) width; (iii) LW; (iv) N.

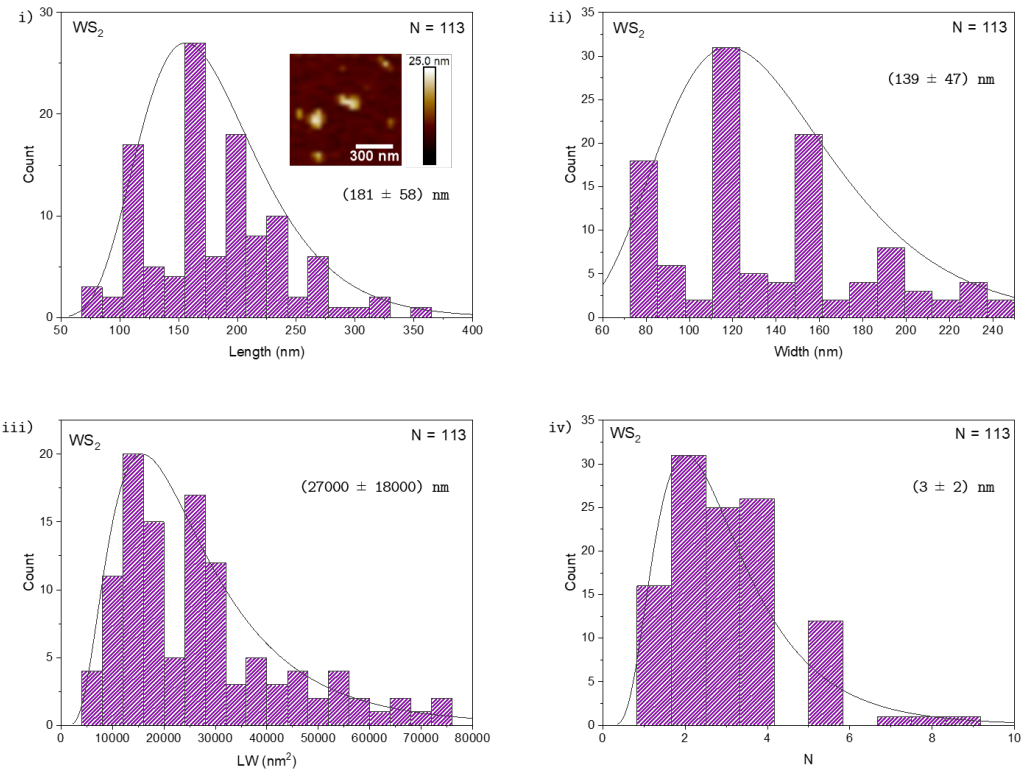

Figure B.5: Histograms of WS_2 (i) length; (ii) width; (iii) LW; (iv) N.

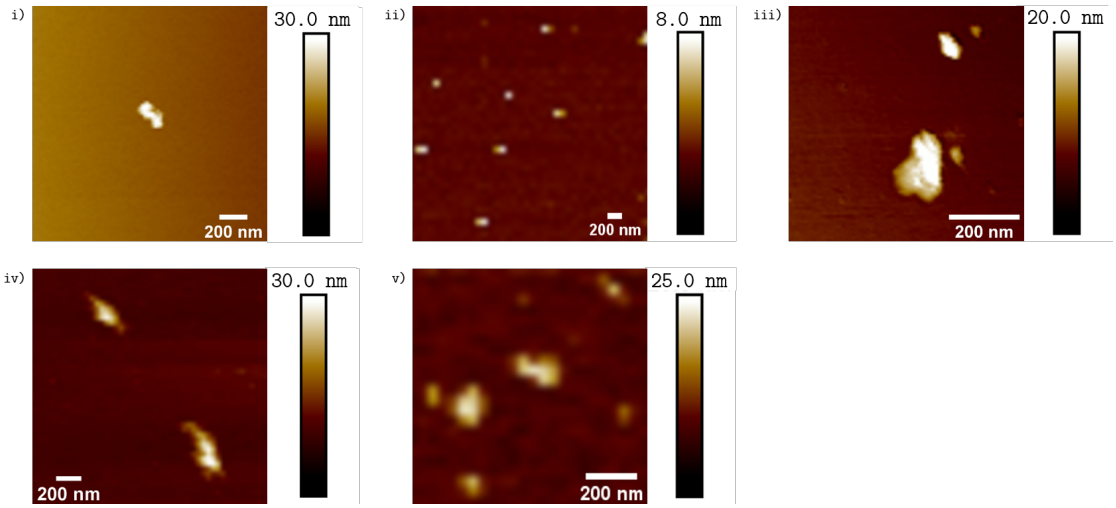

Figure B.6: AFM images of (i) L-gra; (ii) S-gra; (iii) BN; (iv) MoS_2; (v) WS_2.

C Derivation of interparticle distance variable from Chapter 3

The system on the air–water interface can be approximated as shown in Figure C.1. It is assumed that the film comprises uniformly distributed square nanosheets, and that the trough area, A, is also square.

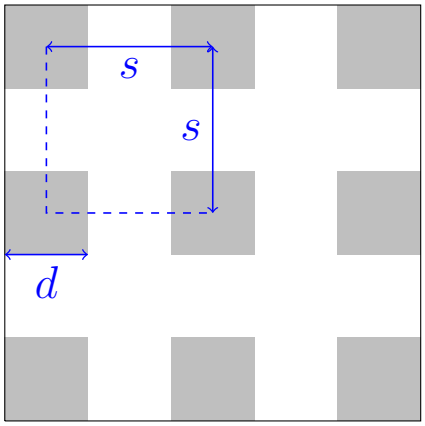

Figure C.1: Top-down diagram of a Langmuir trough with a uniformly distributed film on the air–water interface.

The centre-to-centre interparticle distance, s, and the mean nanosheet diameter, d, are related such that

$$\frac{d^2}{s^2} = \frac{A_f}{A},$$

where A_f is the total film area. This is apparent when considering the square formed by s^2 (shown by the dashed blue line in Figure C.1). As the total film area per trough area gives the surface coverage of the film, Φ, this ratio can be rewritten as

$$\frac{d^2}{s^2} = \Phi.$$

Since the area of a nanosheet has been approximated as $\langle LW \rangle$, the diameter can be taken as $\sqrt{\langle LW \rangle}$. Substituting in this value and rearranging, the interparticle distance can be written as

$$s = \sqrt{\frac{\langle LW \rangle}{\Phi}}.$$

D Additional Raman spectroscopy and mapping for Chapter 4

By mapping the peak intensity of the 405 cm^{-1} A_{1g} mode, and using Raman volumetric mapping, it is possible to determine detailed spatial information for the nanosheet within the cell. Combining multiple overlapping steps gives a z-resolution of < 1 µm, and therefore it is possible to confirm the difference between material internalised within the cell and that above or below the cell. This is shown in Figures 4.5d, 4.5e & D.1.

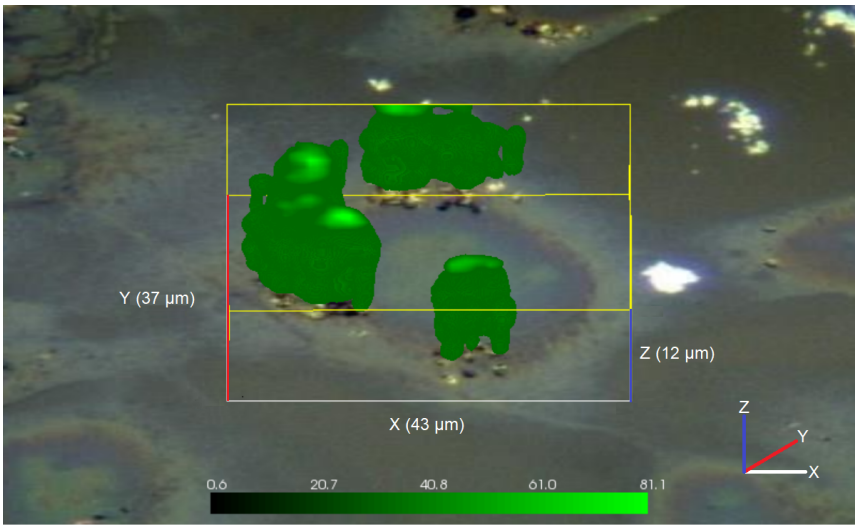

Figure D.1: Raman volume map of the A_{1g} Raman mode for cells after 7 days growth on a MoS_2 substrate.

2D Raman mapping confirms our observations from optical microscopy, showing that the nanosheets are largely internalised in the region around the nucleus (the ER), with some material identified in the cytoplasm. This is seen in Figures 4.5a, 4.5g & D.2.

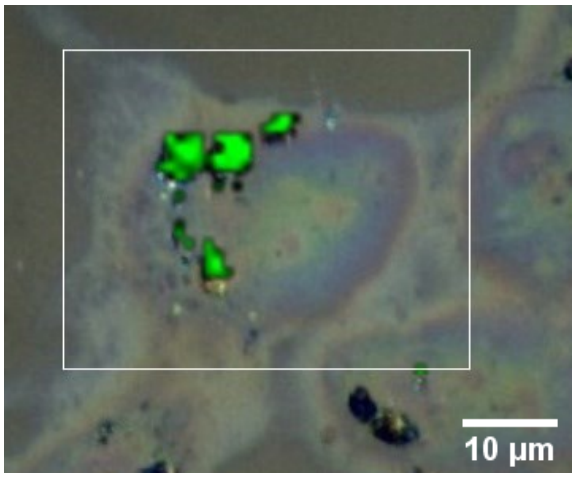

Figure D.2: 2D Raman map of the A_{1g} mode showing MoS_2 localised around the nucleus.

As discussed in the paper, Raman spectroscopy was used to ascertain whether the internalisation process modified the MoS_2. The results shown in Figure D.3 show that there is little to no change to the material.

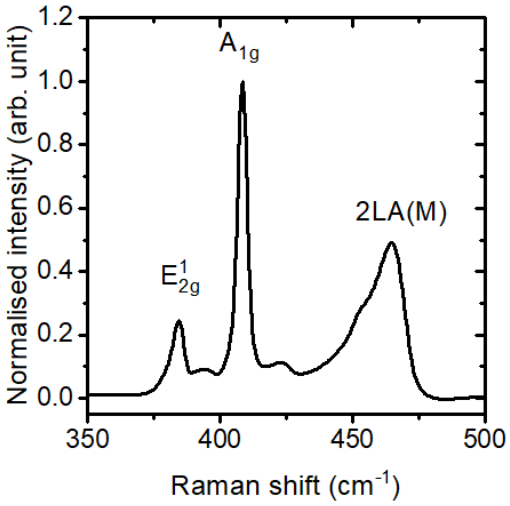

Figure D.3: Raman spectrum from MoS_2 internalised in cells after 7 days growth on a MoS_2 substrate.